

**Modelling Titan's Surface and
Dynamic Simulation and Testing of the
Huygens Surface Science Package
Tiltsensor (TIL)**

Nadeem A.-L. Ghafoor

**A thesis submitted for the degree of
Doctor of Philosophy**

University of Kent at Canterbury

For Mum and Dad

Abstract

The surface of Titan represents the largest surface area in the solar system essentially unexplored. Whilst early models citing global oceans have been all but abandoned, substantial bodies of liquid up to several hundred kilometres in extent are not precluded. If such reservoirs do exist, then in the presence of any surface winds it is expected that wind-driven surface waves will be generated. This thesis considers the adaptation of empirical models used for terrestrial wind-driven sea waves to investigate the properties of such waves on Titan using predicted parameters for Titan's liquids. The wave parameters predicted may have potential surface mission implications for the European Space Agency's Huygens Probe which will land on Titan in 2005. Conversely, their measurement by instruments on board Huygens could yield important planetological information.

One of the sensors partly designed to contribute to such measurement is the Huygens Surface Science Package Tiltensor (TIL). An additional and increasingly important role has also been identified for TIL in contributing to the reconstruction of the Huygens probe descent trajectory and dynamics. Work has been carried out to investigate the sensor's capability in measuring dynamic conditions upon arrival at Titan, and assist in the rapid, accurate determination of dynamics from any data returned. A portable dynamic calibration solution is described and results presented from three experiments investigating the TIL and HASI-ACC sensors' responses under reduced Titan gravity and their combined measurement capability during aircraft flight and simple spin and swing motions. It is found that both sensors will offer information on Probe dynamics during descent, although careful data interpretation is required. Preliminary modelling is carried out towards this end, simulating approximate probe descent dynamics against which the estimated sensor responses may be investigated. Results are presented and recommendations derived for further descent and surface motion modelling and experimentation.

Acknowledgments

I would like to take the opportunity to thank a number of people without this work would have been either incredibly difficult or, in many cases, downright impossible.

To Peter Challenor and Meric Srokosz at the Southampton Oceanography Centre, for their invaluable advice, expertise and assistance concerning the Waves on Titan research. To Yves Gourinat at ENSICA, Toulouse, for his hospitality and limitless offer of support with the reduced gravity flight experiments. He will always be a Big Pilot.

To Ralph Lorenz for his advice and support at numerous points. To the HASI balloon team for their granting a ride to the TIL sensor. And of course to David Atkinson for his friendship and his words of encouragement throughout the whole ordeal.

To Mark Burchell, Prof. Alan Chadwick and Jo Dunn, for their support and understanding during the longest ‘final stages’ ever. To Mark Leese for his friendly advice, support and encouragement, particularly during the lead up to the first reduced gravity flight. To Brijen Hathi for his expert and unquestioning assistance in the field, and for giving a little push when necessary. To Manish Patel, firstly for lending me the HASI ACC unit but, more importantly, for his friendship and for brightening even the darkest days with an amusing tale. And of course to my former supervisor, John Zarnecki, for his academic reviews, his support, his encouragement, (his patience), and for always being there in the end.

To Kathy for her persistent but discreet enquiries into progress during the final stages, and to Nadia Ghafoor for almost the same but without the discretion. To Susan for her words of empathy, and to everyone else at SSTL for their support during the final stages. To Danny, Steve, Steve & Laure, Caroline, Jo, Rachel and the whole Boath family, all of whom did their best to hide their bemusement. And to Faith, who was there in the very beginning, for her kindness and generosity which I truly believe to be without limit.

To Patricia and Dave Hemingway for so many things over the duration I have lost count; mostly for being the closest possible to what was lost and leaving me with the impossible task of ever truly being able to repay them.

To my great friend, Martin Oliver, for his wisdom and clarity of thought, for his words of advice - calming, inspiring and admonishing at all the right times, for his sense of humour and for his wondrous ability with strangely shaped dice. Perhaps most importantly though, because sometimes the only person who can help is the one who has finished and has the scars to prove it.

Lastly and most impossibly to Shauna, who deserves not only a page of thanks but furthermore a book of apologies. For being there when she need not have been, for giving when she need not have, and for so often bearing the unbearable. Again my attempts to fully repay may well be in vain, but here’s to a life of trying.

Contents

Abstract.....	i
Acknowledgements.....	ii
Table of Contents.....	iii
Chapter 1 Introduction.....	1
1.1 Titan.....	2
1.1.1 General Background.....	2
1.1.2 Titan’s surface.....	3
1.2 The Cassini-Huygens Mission.....	4
1.2.1 Cassini Orbiter.....	4
1.2.2 The Huygens Probe.....	5
Huygens Science Instruments.....	6
Huygens Surface Science Package (SSP).....	7
Surface Science Package TIL sensor.....	8
Additional Huygens instruments.....	8
1.2.3 Huygens Probe Mission.....	9
Descent sequence.....	9
Probe Spin.....	10
Huygens Descent Trajectory Working Group.....	11
1.3 Work presented in this thesis.....	12
Chapter 2 Wind-driven Surface Waves on Titan.....	14
2.1 Introduction.....	14
2.2 Titan’s liquid surface environment.....	16
2.3 Surface gravity waves on Titan.....	18
2.4 Wind-waves and the wind-wave prediction model.....	24

2.5 Results	32
2.6 Discussion	37
2.7 Conclusions	39

Chapter 3 The TIL and HASI-ACC

Sensors	41
3.1 TIL Sensor introduction	42
3.2 Tilt Sensor Background	43
3.2.1 Tilt sensors: a general background	43
3.2.2 The SSP Huygens TIL Sensor	44
TIL Sensor structure	45
TIL sensor specifications	45
TIL on board Huygens	46
Electrical interface	47
3.2.3 Tiltmeter principle of operation	47
Orientation of a fluid surface in relative equilibrium	47
Electrolyte resistive potential divider operation	49
3.3 Static Calibrations of the TIL sensor	51
3.3.1 Output vs. angle	51
Measurement axes output	51
Non-measurement axes output	52
3.3.2 Environmental calibrations	53
Vacuum response	53
Temperature response	53
3.4 Dynamic response calibrations of the TIL sensor in 1-g	53
Equilibrium level of the fluid surface	53
Real response to disturbance from equilibrium	54
3.4.1 Laboratory measurements of the TIL sensor step response	54
3.4.2 Simulation of the TIL sensor response from the laboratory measurements	55
3.5 Predicting the dynamic response under Titan gravity	57
3.5.1 Modelling the TIL sensor fluid response and its variation with gravity	57

Standing surface wave.....	58
U-tube fluid.....	60
Semi-torus fluid mass.....	60
3.5.2 Estimating the TIL response time on Titan.....	61
3.6 HASI.....	63

Chapter 4 Design of a TIL and HASI-ACC

Portable Dynamic Calibration Platform.....	67
4.1 Introduction: The need for a portable dynamic calibration platform.....	67
4.2 Platform Requirements.....	69
4.2.1 Parabolic flight experiment opportunity.....	69
4.2.2 Objectives of the Dynamic Calibration Platform.....	72
4.2.3 Dynamic Calibration Platform System Requirements.....	72
4.3 Platform Design.....	74
4.3.1 TIL and HASI-ACC Portable Dynamic Calibration Platform overview.....	74
4.3.2 Dynamic Calibration Platform components.....	76
3 TIL sensors.....	76
TIL Signal conditioning.....	77
HASI-ACC sensor.....	79
Analogue-to-Digital Converter.....	80
Battery unit.....	81
Power Distribution module.....	83
Stepper Motor, Drive Board & Programmable Stepper-Motor Control (PSMC) Board.....	83
Stepper Motor (RS Stock No. 440-464).....	84
Drive Board.....	84
Programmable Stepper Motor Control (PSMC) Board.....	85
4.3.3 Stepper motor selection.....	87
Definitions.....	87
Step resolution.....	88
Torque and speed characteristics:.....	88

Motor mounting and vibration.....	95
Cost.....	96
4.3.4 Programmable motion sequences: s.h.m. simulation.....	96
TIL-Y1 motion requirements.....	96
Program sequences.....	97
4.4 Sample Data from the Portable Dynamic Calibration	
Platform.....	100
4.5 Conclusion.....	101

Chapter 5 Field Experiments with the Dynamic Calibration Platform..... 104

5.1 Introduction.....	104
5.2 Reduced Gravity Simulation: a general background.....	104
5.2.1 Reduced-gravity, microgravity and weightlessness.....	104
5.2.2 Simulation of reduced-gravity and micro-gravity.....	106
Simulation methods.....	106
Robin DR400 Parabolic Flight.....	107
Typical Parabolic Flight Trajectory.....	107
5.3 TIL & HASI-ACC Reduced-Gravity Flight	
Experiment, Castres 1999.....	108
5.3.1 Aircraft and Flight opportunity.....	108
5.3.2 Flight objectives and requirements.....	108
5.3.3 Reduced gravity flight experiment details.....	109
Simulation of Titan's surface level gravity (1/7 th g).....	110
Measurement of TIL and ACC responses: PDCP	
configuration.....	110
Visual representation and measurement of g-level: a	
makeshift g-meter.....	111
Flight profile measurement.....	113
Other supporting equipment.....	114
5.3.4 g-meter calibration.....	114
5.3.5 Instrument calibration settings.....	116
5.3.6 Flight Results.....	116

5.3.7 Data analysis: g-meter curves.....	121
5.3.8 Data analysis: Flight instrument recordings.....	125
5.3.9 Data analysis: TIL sensor response times.....	125
Response time measurement.....	125
Theoretical variation of lag time with gravity.....	126
Comparison of observation and theory.....	127
5.3.10 Data analysis: Flight profile reconstruction.....	130
Conversion between TIL sensor and aircraft axes.....	130
TIL offsets due to linear accelerations during flight.....	131
Calibrated flight profile with annotations.....	134
5.4 Conclusions of the TIL & HASI-ACC Reduced-gravity Experiment.....	143
5.4.1 Experiment conclusions.....	143
5.4.2 Further investigation recommendations.....	145
Flights.....	145
Platform design.....	145
5.5 TIL & HASI-ACC Spin-table test using the PDCP.....	147
5.5.1 Spin Table experiment.....	147
Spin table and PDCP arrangement.....	148
Spin rates.....	150
Supporting equipment.....	150
Experiment.....	150
5.5.2 Spin Results.....	151
5.5.3 Data analysis: Spin vs. TIL output (as measured by HASI ACC).....	156
5.5.4 Spin Table Experiment conclusions.....	156
5.6 TIL & HASI-ACC Swing test using the PDCP.....	158
5.6.1 Swing structure and platform configuration.....	158
5.6.2 Swing Theory.....	158
5.6.3 Swing Results.....	159
5.6.4 Conclusion.....	159
 Chapter 6 TIL sensor aboard the Huygens Probe.....	 164

6.1 Introduction.....	164
6.2 Conversion between TIL angles and Probe axes tilts.....	165
6.2.1 TIL position on Huygens Probe.....	165
6.2.2 Transformation between Instrument and Probe axes.....	166
6.3 Effects of spin on TIL at Titan.....	169
6.3.1 TIL measurement range during probe tilt and spin.....	169
6.3.2 Minimum resolvable spin.....	170
6.3.3 Recognising Spin from the TIL signal.....	171
Spin and tilt about probe centre.....	171
6.4 Investigating the TIL and HASI-ACC measurement capability of parachute descent dynamics.....	174
6.4.1 Introduction.....	174
Spin and tilt about point displaced from probe.....	174
6.4.2 3-d.o.f. parachute model for TIL and HASI-ACC measurement predictions.....	176
6.4.3 TIL and HASI measurements of probe dynamics as generated with by the 3-d.o.f. parachute model.....	180
Spin reconstruction with TIL.....	185
Swing reconstruction with TIL.....	185
Accelerometers.....	185
6.4.4 TIL response time.....	186
6.4.5 TIL Sampling rates.....	186
6.5 Other motions.....	187
6.5.1 Surface Waves.....	187
Probe motion and gravity-wave measurement with TIL.....	187
TIL response time and wave frequency.....	188
6.6 Conclusions.....	188
 Chapter 7 Conclusion.....	 190
 References.....	 194

Chapter 1

Introduction

This thesis focuses on Titan, the largest moon of Saturn, and an instrument onboard the ESA Huygens Probe due to arrive at Titan in 2005, the Surface Science Package Tilt sensor, or TIL. The surface of Titan represents the largest essentially unexplored surface area in the solar system. It is also unique in that it is the only extra-terrestrial surface in the solar system that may feature exposed bodies of liquid. Models have varied over the past two decades, and whilst it is now believed that surface liquids may not be global, substantial bodies of liquid up to several hundred kilometres in extent are not precluded. If such reservoirs do exist, then in the presence of any surface winds it is possible that wind-driven surface waves will be generated. Any such surface dynamics could have potential surface mission implications for the European Space Agency's Huygens Probe which will land on Titan in 2005. Conversely, the measurement of such waves by instruments on board Huygens could yield important planetological information concerning Titan and possibly further our understanding of sea waves here on Earth.

The TIL sensor is one of nine instruments comprising the Huygens Surface Science Package (SSP), whose primary goal when first conceived was to take measurements before, during and after surface impact that would assist physical and chemical characterisation of Titan's surface, almost certainly as a minimum indicating its solid or liquid state. However, whilst the initial main aim of the TIL sensor was to take measurements on the surface, additional significance is increasingly being attributed to TIL sensor descent measurements and their significance to the reconstruction of the probe's trajectory and dynamics, which in turn are required for accurate profiling of the Titan atmosphere. The well established TIL sensor design represents the optimum balance of size, mass, power and performance for static measurements on the surface of Titan, however the performance in measuring the potential probe dynamics during and after Titan descent is not so clear.

This work therefore tackles two main issues. Firstly modelling is carried out for waves on the surface of a liquid expanse on Titan, both to address a gap in the Titan surface literature and to estimate the likely dynamic conditions that may face the Huygens probe upon its arrival at the surface. Focus then shifts to the TIL sensor, with modelling and experimentation described which attempts to offer more conclusive predictions about its performance under dynamic conditions likely during descent and surface phases of the Huygens mission. Significant emphasis has been placed on the need for prompt provision of probe attitude history to all Huygens science teams following the probe's atmospheric descent. Any modelling of the sensor performance in this area is therefore crucial for rapid and accurate data interpretation when finally received from Titan.

This Chapter begins with a brief introduction to Titan and the ESA Huygens mission, before outlining the structure of the thesis and the work presented in subsequent chapters.

1.1 Titan

1.1.1 General Background

With a radius of 2575 km, Titan is Saturn's largest moon and the second largest satellite in the Solar System behind Ganymede. It is unique in that it is the only moon in the Solar System to possess a thick atmosphere and indeed if this were included in its radius then Titan could be considered larger than its Galilean competitor. Titan was first glimpsed as a tiny 'star' accompanying Saturn by the Dutch astronomer Christiaan Huygens in March of 1655. Its atmosphere however was not observed until 1907 by Spanish observer, Comas Solá [Comas Solá, 1908], and confirmed in 1944 by Gerard Kuiper [Kuiper, 1944] who discovered spectroscopically the presence of gaseous methane. Details of the surface were obscured by an aerosol haze even when viewed by Voyager I in 1980, giving Titan its characteristic orange colour, although great leaps were made in the understanding of Titan from other measurements by the spacecraft. Molecular nitrogen was confirmed as the major atmospheric constituent, with methane, hydrogen and possibly argon representing other main constituents. The photodissociation of methane in Titan's atmosphere gives rise to a complex organic chemistry for Titan's atmosphere and surface and a host of complex organic molecules have been detected. The level of nitrogen abundance makes Titan's atmosphere more similar to that of the Earth than any other body in the Solar System and its complex photochemistry has been suggested to offer possible analogues for the prebiotic chemistry of the Earth. Whilst Titan's surface temperature of 94 K is too cold for the evolution of life,

the arrival of Huygens at Titan may present a tantalising opportunity to investigate processes that led to life on Earth several thousand million years ago [Owen et al., 1997]. Table 1 lists some of the physical properties of Titan [Lebreton & Matson, 1997].

Surface radius	2575 km
Mass	1.346×10^{23} kg
Surface gravity	1.345 m s^{-2}
Mean density	1.881 g cm^{-3}
Distance from Saturn ($20.3 R_s$)	1.226×10^6 km
Orbital period	15.95 d
Rotation period	15.95 d
Surface temperature	94 K
Surface pressure	1.496 atm

Table 1.1: Orbital parameters of Titan [Lebreton & Matson, 1997]

Several engineering models for Titan’s atmosphere have been employed over the duration of the Huygens mission development, with that described in Lellouch & Hunten [1997] being used in the probe heatshield and parachute design, although the model described in Yelle et al. [1997] represents the subsequently accepted model.

[Flasar et al., 1997] describes predominantly zonal (east-west) Titan winds and offers a zonal wind profile that was used as an engineering model for the design of the probe-orbiter (see section 1.2 below) radio link. Wind speeds of 100 m s^{-1} at 200 km are considered possible, decreasing down to around 10 m s^{-1} at 10km altitude, although the envelope is as wide as $0 - 20 \text{ m s}^{-1}$. The direction of the wind, east to west or vice versa is not constrained. Atmospheric models suggest wind speeds at the surface of a few m s^{-1} , with the variability unknown [Coustenis & Taylor, 1999].

1.1.2 Titan’s surface

Possibly one of the most exciting aspects of the Huygens mission will be the descent through the haze layer revealing for the first time clear views of the surface. Until this time however the surface of Titan remains the largest unexplored surface area in the solar system, although recent observations from Hubble Space Telescope and ground-based telescopes using adaptive optics have given perhaps the first low-resolution indications of its nature [Smith et al., 1996, Combes et al., 1997].

Models of Titan’s surface, in particular those that invoke the existence of liquid reservoirs, have been the subject of much debate ever since the first Voyager flyby in 1980. Photochemical and thermodynamic models of Titan’s atmosphere based on

early analyses of these data seemed to suggest the presence of a liquid hydrocarbon reservoir at the surface of this clearly unique moon [Lunine et al., 1983]. Indeed, even until perhaps 4 years ago the presence of primarily ethane and methane oceans on Titan's surface was widely accepted as satisfying constraints imposed by these photochemical models, their depth and extent largely constrained by tidal models [Dermott and Sagan, 1995; Sears, 1995]. Whilst radar and infrared observations argued against the presence of such bodies [Muhleman et al., 1990; Griffith et al., 1992], they were not yet judged to be conclusive, and the situation remained at an impasse until perhaps as late as 2 years ago. However, the advent of the Hubble Space Telescope's corrected optics and advances in ground-based observation techniques at last gave rise to new and exciting data, not only challenging previously favoured models but actually making progress toward resolving the issue. Near-infrared images obtained from the Hubble Space Telescope [Smith et al., 1996] and ground-based adaptive optics images [Combes et al., 1997] seemed to corroborate the earlier theories that the surface albedos measured were incompatible with those expected from large-scale bodies of liquid. Even these images, however, were limited in resolution to, at best, several hundred kilometres and, whilst early global ocean theories have now been all but abandoned, the images do not preclude the existence of small (of order 100 km diameter) but significant liquid bodies. Recent modelling [Lorenz et al., 1997] have even suggested that the presence of liquid reservoirs on the surface is not the only solution to the photochemical conundrum posed by Titan's atmosphere and need not necessarily exist after all. The situation is far from resolved, however, and much work remains as theories drift in and out of favour with each new data set. Ultimately, whilst new observations will no doubt continue to reveal further information about Saturn's mysterious moon, many issues are unlikely to be resolved before the arrival of the NASA-ESA Cassini-Huygens mission (see below) at Titan in 2005.

For a detailed discussion of the theories and models mentioned above, the reader is referred to the many review papers which have been published recently [e.g. Lunine, 1994, or the summary by Lorenz and Lunine, 1996]. It is not the intention of the author to debate here the likelihood or otherwise of liquid bodies existing on Titan. Rather, it is recognized that according to current models, ESA's Huygens Probe may encounter a liquid environment upon arrival in 2005, and any work on modelling the behaviour of liquids on Titan is not only of value to the understanding of Titan as a planetary body but moreover potentially vital in the prediction and interpretation of the probe's post impact behaviour. The additional opportunity to take measurements and test terrestrial wave theories over an entirely new measurement regime should also not be overlooked. This is discussed further in Chapter 2.

1.2 The Cassini-Huygens Mission

1.2.1 Cassini Orbiter

The joint NASA-ESA Cassini-Huygens mission comprises the NASA Cassini orbiter, enormous by today's standards having a launch mass of 5650 kg, and the 350 kg (launch mass) Huygens Probe which will descend through the Titan atmosphere. The orbiter is powered by radioisotope thermoelectric generators and features a 4m High Gain Antenna (HGA). The Cassini spacecraft delivers the Huygens probe to Titan, with arrival now scheduled for 2005, and following probe release points its HGA to a predefined location on Titan for 3 hours, during which time it receives data from the probe at 8 kbit s⁻¹ and stores the data in two solid state data recorders. The data is then relayed to Earth as soon as the HGA can be redirected following the completion of the Huygens probe mission. The orbiter is currently scheduled to then remain in orbit around Saturn with a baseline mission duration of 3.5 years.

1.2.2 The Huygens Probe

The Huygens Probe has a launch mass of 350kg, and a landed mass on Titan of 201kg.

Figure 1.1 shows a cut-away model of the Huygens probe with its top cover removed (image courtesy of NASA).

Huygens Science Instruments

The Huygens payload comprises six dedicated science instruments. The Gas Chromatograph and Mass Spectrometer (GCMS) is a highly versatile gas chemical analyser designed to identify and quantify the abundance of the various atmospheric constituents. The Aerosol Collector and Pyrolyser (ACP) is designed to collect aerosols, using a deployable sampling device, for the GCMS which then analyses their chemical compositions. The Doppler Wind Experiment (DWE), as its name suggests, relies on the Doppler shift induced by probe wind drift. The Descent Imager / Spectral Radiometer (DISR) is a multi-sensor optical instrument capable of imaging and taking spectral measurements over a wide range of the optical spectrum, from UV to infrared, 0.3 – 1.64µm. DISR includes an aureole sensor which will measure the Sun's halo, and also a horizon sensor for cloud imaging. DISR has two cameras, infrared and optical, which will allow long awaited imaging of Titan's surface. The light intensity at Titan due to the increased distance from the sun (10AU) and atmospheric absorption and scattering is expected to be approximately 1/1000th that at the Earth, and whilst this is sufficient for imaging, DISR also includes a lamp to provide illumination in the methane absorption bands for spectral reflectance measurements [Lebreton & Matson, 1997].

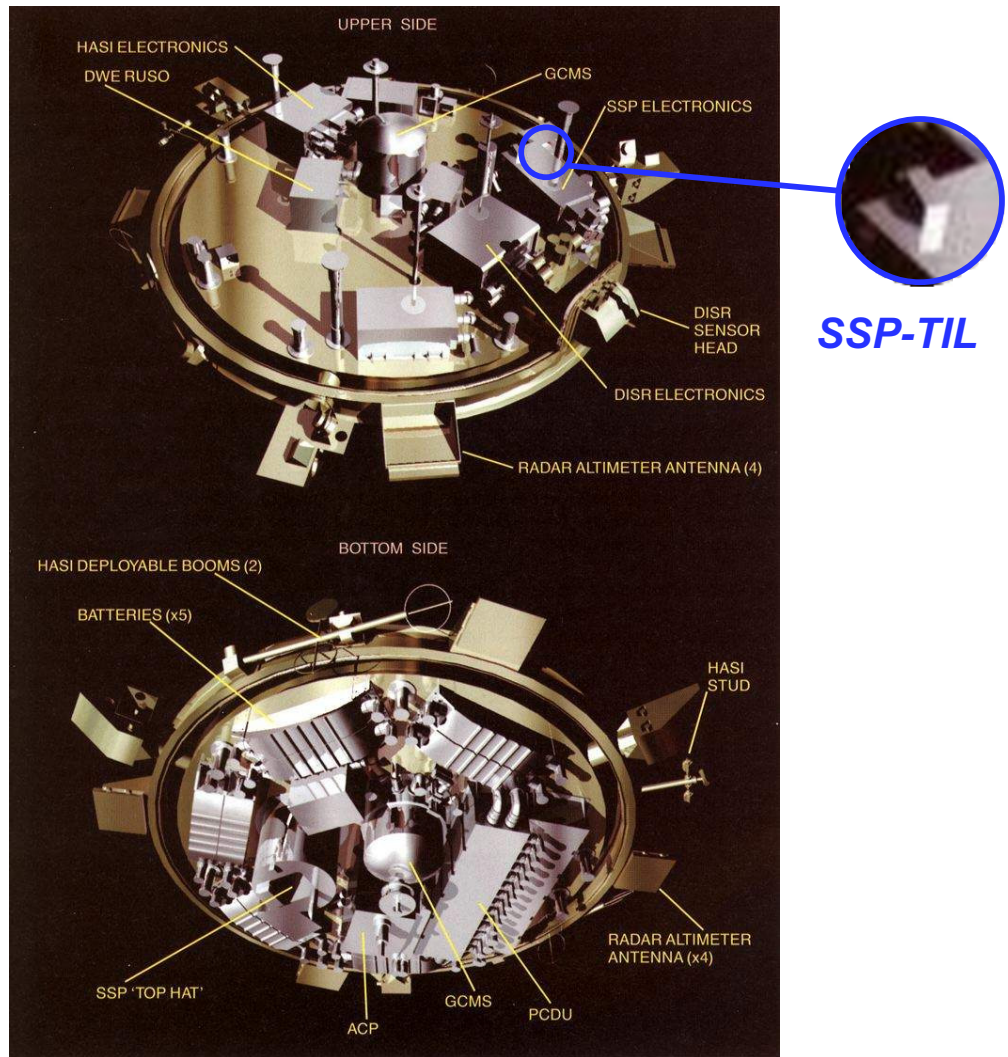


Figure 1.1: Cutaway of the Huygens probe [picture courtesy of NASA], showing location of TIL

The Huygens Atmospheric Structure Instrument (HASI) is a multi-sensor instrument designed to measure the physical and electrical properties of Titan’s atmosphere during the descent. Its sensor suite comprises a 3 axis piezoresistive accelerometer and a more sensitive single axis servo accelerometer aligned with the probe symmetry axis, designed to measure entry decelerations allowing thermal and density profiling of the probe atmosphere during the entry phase, coarse and fine temperature sensors, a multi-range pressure sensor, and an electric field sensor array for measuring the ion conductivity, atmosphere permittivity and detection of atmospheric electromagnetic waves such as those produced by lightning [Lebreton & Matson, 1997]. Work described later in this thesis involved the use of an engineering model of the servo accelerometer, albeit with different gain settings to those of the probe, as detailed later in section 4.3.2. Table 1.2 summarises the characteristics and performances of the four HASI-ACC sensors in their Huygens configuration

[Fulchignoni et al., 1997]. The probe axes adopt the convention of the $+x$ -axis as the downward pointing vector along the probe's line of axial symmetry. Further details of the ACC sensor are discussed in section 3.6.

The sixth Huygens Science instrument is the Surface Science Package and, since it contains the sensor forming a focus for much of this thesis, warrants a separate section.

x-axis servo accelerometer	
<i>High resolution setting:</i>	
Range:	2 – 20 mg
Resolution:	1 – 10 μ g
<i>Low resolution setting:</i>	
Range:	1.85 – 18.5 g
Resolution:	0.9 – 9 mg
Relative accuracy:	1% of full scale
x/y/z piezoresistive accelerometers	
Range:	± 20 g
Resolution:	± 50 mg

Table 1.2: ACC characteristics and performances

Huygens Surface Science Package (SSP)

The Surface Science Package (SSP), as its name suggests, is another multi-sensor instrument and the only one onboard Huygens whose prime focus is the surface mission, although measurement capability of several sensors is retained throughout the descent phase. The primary aims of SSP are to determine the physical nature and condition of Titan's surface at the landing site. In fact many of the measurements of the SSP sensors are biased towards the case of a liquid landing, in which event the aims are to determine the abundances of the major sea or lake constituents, determine the physical and electrical properties of the liquid body, and examine any wave properties and ocean-atmosphere interactions which may be occurring [Zarnecki et al., 2001].

The SSP addresses these aims through a suite of nine sensors, seven of which require intimate contact with the surface and are housed in a 10cm x 10cm square cross-section cavity, known affectionately as the 'Top Hat', cut out of the probe's fore dome and extending to the main experiment platform. The Top Hat may be seen towards the bottom left hand corner of the 'bottom view' in Figure 1.1. The two remaining sensors are housed internally on the SSP electronics box, also visible in

Figure 1.1. The seven sensors housed within the top hat are outlined in turn. An external sensor (ACC-E) based on a piezoelectric force transducer is used to measure the small-scale mechanical properties of Titan's surface. The Acoustic Properties Instrument – Velocity Sensor (API-V) uses two paired piezoelectric transducers for the determination of speed of sound in Titan's atmosphere and any liquid surface, allowing molecular mass to be deduced. The Acoustic Properties Instrument - Sounder (API-S) consists of a sounder for measuring altitude near the surface, liquid depth and possibly some information concerning surface topology. A density sensor (DEN) employs a floating buoy and strain gauge to measure upthrust and therefore density in the event of a liquid surface. The permittivity sensor and refractometer (PER and REF respectively) measure the static permittivity and refractive index of any liquid surface, allowing relative molecular abundances to be determined. The Thermal Properties instrument (THP) consists of two pairs of platinum wire sensors, optimised for atmospheric and surface measurement respectively, and measures the temperature, thermal conductivity and possibly thermal diffusivity of Titan's atmosphere and liquid surface during and after descent. [Zarnecki et al., 2001]. Finally the tilt sensor (TIL) is discussed briefly below.

Surface Science Package TIL sensor

The TIL sensor was initially intended to provide information on ocean wave properties on Titan, whilst in the event of a solid landing it would provide the probe's repose, possibly providing an indication of metre-scale relief. The sensor may also provide information on the Probe's motion during descent, possibly allowing information on winds and atmospheric turbulence to be determined. It has been suggested that, following liquid surface impact, the probe may be considered as a buoy and information concerning probe inclination from the vertical measured by the TIL sensor, together with the vertical acceleration measured by the ACC sensor, may allow retrieval of key wave parameters and testing of the generality of thus far terrestrially derived empirical models of surface gravity waves and wave growth [Zarnecki et al., 1997]. Lorenz [1994] has also suggested the use of TIL data in measuring complex pendulum motions of the probe beneath its parachute and improving the reconstruction of wind gusts from the Huygens DWE experiment. More recently additional requests have been made for TIL contributions to probe attitude history, as mentioned below, and a clear need is identified for verification of the sensor capability in meeting such expectations. Further details on the specific design of the TIL sensor are included in Chapter 3.

Additional Huygens instruments

The probe also has several sensors built into its system, mostly for mission critical activities during Titan entry and early descent phases. These include the Mission

Timer Unit (MTU), involving timers and g-switches sensitive to acceleration above 5.5-6.5g, which activate the probe at a pre-programmed time or in the event of atmospheric entry, whichever occurs first. Also included on the probe are the Radar Altimeter Unit (RAU) which detects altitude below 25km, and the Central Acceleration Sensor Unit (CASU) which is used to calculate the time for parachute deployment [Jones & Giovagnoli, 1997]. The last sensor of particular note for the discussions presented in this work is the Radial Acceleration Sensing Unit (RASU) which measures the probe spin rate up to 15 rpm.

1.2.3 Huygens Probe Mission

Descent sequence

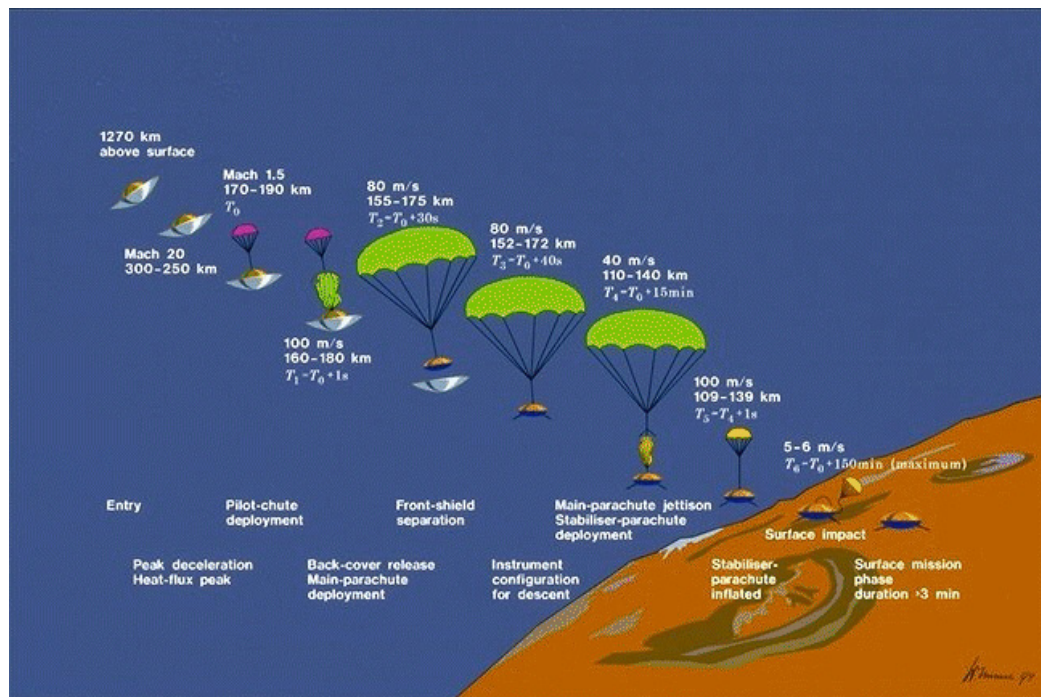


Figure 1.2: The Huygens Probe descent sequence

Figure 1.2 shows the key phases of the Huygens Probe descent [reproduced from Lebreton & Matson, 1997]. The probe separates from the orbiter with a spin rate of 7 rpm for stability during the 22 day coast towards Titan and entry phase. After deceleration during entry from 6 km s^{-1} to 400 m s^{-1} , a pilot chute is deployed to pull away the aft cover and permit inflation of the main 8.3 m diameter parachute. Following main chute inflation the front shield is released and allowed to drift from the probe to avoid sensor contamination before deployment of the HASI booms and the opening of the GCMS and ACP inlet ports. The main parachute is sized to pull the probe away from the front shield, however it is too large for a nominal descent time of less than 2.5 hours, a constraint imposed by a requirement to reach the

surface before batteries are drained. The main chute is therefore jettisoned and a 3.03 m diameter stabilising parachute (inhibiting swings greater than 10° to maintain probe-orbiter link) is deployed to permit descent to the surface and a nominal surface mission of between 3 and 30 minutes. Figure 1.3 shows the envelope of predicted altitude descent profiles for the three atmospheric profiles predicted by the Lellouch-Hunten model [reproduced from Lebreton & Matson, 1997].

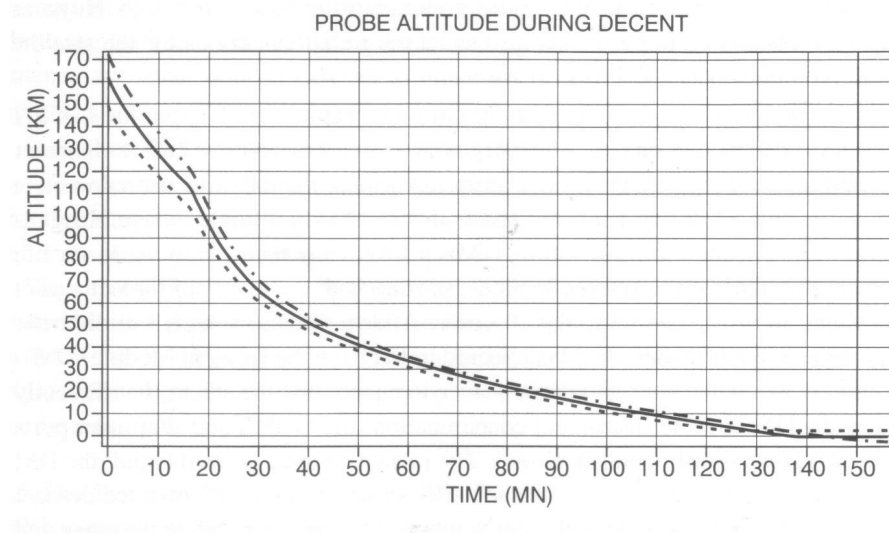


Figure 1.3: The predicted altitude descent profile for the three profiles predicted by the Lellouch-Hunten atmosphere model [reproduced from Lebreton & Matson, 1997].

Probe Spin

While the initial spin induced upon separation from the orbiter was to satisfy stability requirements during coast and entry phases, several sensors require that Huygens spins throughout its entire descent to provide satisfactory azimuth coverage. The DISR required spin rates are particularly strict for the final part of the descent where mosaic images will be taken with the cameras [Lebreton & Matson, 1997]. The necessary spin is induced by a set of 36 vanes mounted on the bottom part of the probe foredome. The probe spin is decoupled from the parachute by means of a swivel using redundant low friction bearings in the connecting riser of both the main and stabiliser parachutes [Jones & Giovagnoli, 1997]. Figure 1.4 shows the envelope for the predicted spin profile during descent.

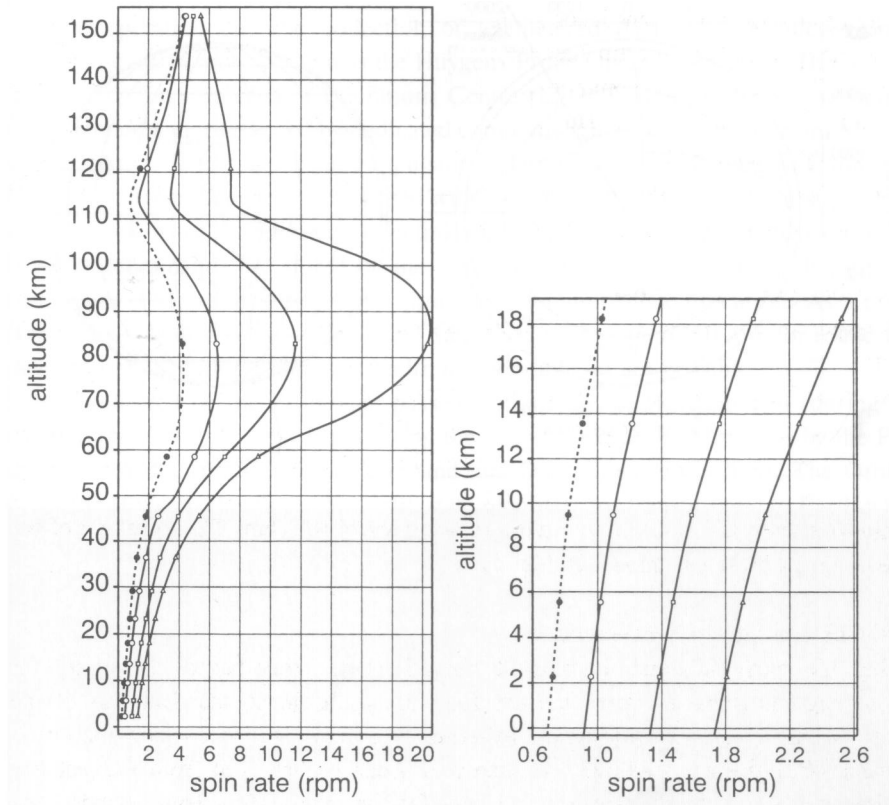


Figure 1.4: Envelope of the expected probe spin profile with altitude [reproduced from Lebreton & Matson, 1997]

Huygens Descent Trajectory Working Group

The Huygens Descent Trajectory Working Group (DTWG), chartered in 1996, includes representatives from each of the probe science instrument teams, Huygens and Cassini Project Scientists and a number of additional ESA engineers. The goal of the DTWG is the development of analysis techniques by which the Huygens probes descent trajectory and attitude may be accurately reconstructed from entry to the surface. Reconstruction will involve accelerometer and telemetry Doppler data, the probe entry position and velocity vector, and contributions from DISR, HASI-ACC, HASI-T&P, SSP API-V and the SSP TIL sensor, with additional contribution at lower altitude from the altimeter [Atkinson, 1998]. The accurate reconstruction of the probe entry and descent trajectory is necessary for the correct interpretation and correlation of results from all the probe science experiments, and to calibrate the remote sensing measurements from the orbiter instruments.

The activities of the DTWG have noticeably intensified as the arrival of Huygens at Titan draws closer. Work is continuing to develop the framework between experiment and project teams for the prompt sharing and exchange of the above information following data retrieval from Huygens in 2005. Additional imperative is

thus given to the verification of the TIL sensor's measurement capability and accuracy for the range of dynamics likely to be experienced throughout the probe descent.

1.3 Work presented in this thesis

As stated at the beginning of the chapter, the work presented in this thesis was carried out largely in response to issues raised in the discussions above, in particular the uncertainty surrounding the dynamics of the Titan surface and the gap in literature surrounding small scale surface-wave motions, as well as the need for clarification of the TIL sensor's predicted response on Titan ahead of its arrival onboard the Huygens Probe early in 2005.

This thesis therefore proceeds initially in Chapter 2 with a presentation of surface wave modelling that has been carried out for the case of liquid expanses on Titan, with predictions made concerning the general nature of Titan surface waves and the generation and growth of waves under the action of a Titan surface wind.

Attention then turns in Chapter 3 to the TIL sensor, with an initial review of the sensor, its operation principles and the state of previous sensor calibrations. Building on this, modelling and predictions are then presented concerning the degradation in response time of the sensor that may be expected under Titan conditions, and the impact on the accuracy of attitude measurement possible with the sensor.

Chapter 4 responds to the need for dynamic sensor tests beyond theoretical modelling with a presentation of a portable dynamic calibration platform design that offers a versatile solution for the remote testing of the TIL and ACC sensors in a range of real dynamic environments.

Experiments conducted to test the reduced gravity performance of the TIL sensor, its spin susceptibility and its ability to represent simplified spin and swing profiles are described in Chapter 5, with the calibration platform described in the previous chapter being used in all three cases.

Chapter 6 draws upon results of the analyses of previous chapters and discusses the implications for TIL measurements of more complex and Huygens representative dynamics. The conversion between probe and instrument axes is quickly described, and discussion briefly given to the retrieval of spin rates in excess of those measurable by RASU from the sensor measurements. Finally a restricted 3 degree of freedom parachute model is used to generate a simplified Titan descent trajectory

against which the TIL and HASI measurement capability can be investigated. Extrapolation to the real Huygens case is discussed and the benefits of a more elaborate model are discussed. The chapter concludes with a consideration of the impact of the TIL sensor sampling rate and response time estimated earlier, and a brief discussion of TIL sensor measurement of the surface wave motions suggested in Chapter 2.

The thesis finally concludes in Chapter 7 with a brief review of the key results, conclusions and recommendations presented in the earlier chapters.

Chapter 2

Wind-driven Surface Waves on Titan

2.1 Introduction

As explained in Chapter 1, the existence of liquid reservoirs at Titan's surface have been the subject of much debate ever since the first Voyager flyby in 1980. Whilst early global ocean theories have now been all but abandoned, the images do not preclude the existence of small (of order 100 km diameter) but significant liquid bodies. The situation is far from resolved, however, and modelling will continue before and long after the arrival of Huygens at Titan in 2005. As explained in the previous chapter, the likelihood or otherwise of liquid bodies existing on Titan is not debated here. Rather it is recognised that any work modelling the behaviour of surface liquids on Titan is of value to the understanding of the moon's planetary processes, vital to the prediction and interpretation of the Huygens probe's post-impact behaviour, and a useful investigation into the applicability of terrestrial wave theories over an entirely new measurement regime. This chapter therefore considers the situation where any liquid body, regardless of size, exists somewhere on the surface of Titan and examines the behaviour of the surface in such a case. The work presented in this chapter was published in [Ghafoor et al., 2000].

Thus far, the most studied aspect of the fluid dynamics on Titan is that of tides, both those arising in liquid bodies at the surface [Sagan and Dermott, 1982, Dermott and Sagan, 1995, Sears, 1995] and those occurring within Titan's interior [Sohl et al., 1995, Dermott and Sagan, 1995]. A surprising gap in the literature occurs, however, where non-tidal processes are concerned, most notably those occurring actually at the surface. It is believed that surface winds exist on Titan, [Flasar et al., 1997] although they

probably do not reach the speeds commonly encountered on Earth. Allison [1992] estimates that surface wind speeds on Titan will be less than 2 ms^{-1} , and whilst this limit might be slightly higher under strongly stable conditions currently preferred estimates are below this value. Nevertheless despite a reduced wind speed, it is reasonable to assume that such atmospheric dynamics near the surface of Titan give rise to wind-driven surface waves just as on Earth. Ori et al. [1997] give an overview of several fluid dynamic processes which would give rise to various types of flow on Titan and include a brief discussion of wind-waves and some predictions based on early wave models as to the wave periods that might be expected. The model employed however is based upon measurements made in the 1950s and much work has been carried out since. Elachi et al. [1991] discuss primarily the nature of capillary waves on Titan and their effects upon radar reflectivity. Whilst the paper also employs an early empirical formula to estimate a minimum wind speed for the generation of gravity waves on Titan of 0.5 ms^{-1} , the theory has since been superseded following advances in the understanding of wind wave generation [Kinsman, 1965] and this is discussed further in section 2.4. Consequently detailed discussion of the likely extent of wind-driven surface wave growth for varying conditions on Titan still remains limited. However as long as the ratio of atmospheric to oceanic densities is similar to the terrestrial value, and ocean viscosity is similarly small, the analysis of the Titan waves could follow a similar approach to that of terrestrial waves and it should be possible to predict, for varying extents of liquid bodies, the scales of waves generated by winds travelling at a particular speed.

The work of this chapter compares and contrasts atmosphere-surface interfaces on Titan and on Earth and adapts, as appropriate, an empirical wind-wave prediction model still used widely today by terrestrial oceanographers to make such predictions about the conditions that might prevail at the surface of a liquid body on Titan. Srokosz et al. [1992] discuss results obtained using a simpler limiting-case wave model, and this treatment is an expansion upon the early work presented therein. It should be noted that the analysis presented here addresses surface wave motion occurring in open expanses of liquid such as oceans or lakes, rather than in fluvial flows over land such as rivers or streams which would be dominated by unidirectional currents rather than gravity waves [Ori et al., 1997].

The following section therefore begins with a consideration of the physical properties of potential liquids on Titan and draws a comparison with the conditions which are commonly observed on Earth. The general nature of Titan waves is derived from a consideration of the controlling factors of general free surface gravity waves and it is found that there are indeed sufficient similarities between the two environments to

warrant an analogous treatment to that used on Earth. The generation of wind-driven surface waves is then discussed, together with the statistical parameters which are often used to describe the spectrum of waves that exist at a sea surface.

Several well established wind-wave prediction models still in use today are then described and their adaptation for the Titan case is carried out. The results are presented and the limitations of the model are discussed. The chapter then concludes with a discussion of further work which is currently underway.

Throughout this chapter, when referring to localised conditions on, or parameters of, liquid reservoirs on Titan, the terms ‘ocean’, ‘oceanic’ or ‘oceanographic’ will sometimes be employed for convenience. Unless specified, however, their use should not be taken as an indication of scale; this parameter remains uncertain and for the purposes of this work can be anything from hundreds of metres to several hundred kilometres.

2.2 Titan’s liquid surface environment

The interface between the atmosphere and any liquid surface that exists on Titan will be very different from that on Earth. The high pressure and low temperature conditions prevailing at the surface (1.5 bar and 95 K), coupled with a chemical make-up of both atmosphere and ocean completely unlike that on Earth, mean that transport properties governing the fluid dynamics of the liquid surface will be drastically altered. The behaviour of such a surface under the action of Titan’s significantly reduced gravity and its interaction with the atmosphere therefore will be considerably different to the equivalent on Earth and before launching prematurely into the application of terrestrial models, care must be taken to assess their applicability.

Table 2.1 lists the relevant conditions and transport properties for Titan from which the expected fluid dynamics of a liquid surface can be derived. The ocean density and viscosity parameters listed range from values for pure methane to pure ethane [Bretsznajder, 1971]. Ori (1997) has calculated the viscosity for the putative ocean composition first suggested by Lunine et al. [1983], i.e. 25% methane, 70% ethane, and 5% nitrogen, as $0.55 \times 10^{-3} \text{ N s m}^{-2}$ using the Peng-Robinson equation of state. The surface tension has been estimated from a calculation of the parachor value, an additive, constitutive and largely temperature independent molecular quantity [Bretsznajder, 1971], for ocean compositions ranging from pure methane to pure ethane.

Parameter	Earth Ocean (at 295 K)	Titan Ocean (at 95 K)	Notes
Acceleration due to gravity, g (m s^{-2})	9.81	1.35	
Atmospheric density at surface ρ_{atmos} (kg m^{-3})	1.2	5.3	
Ocean density, ρ_{ocean} (kg m^{-3})	1025 ¹	430 - 650 ²	¹ salinity 35 parts per thousand, ² densities of pure methane to pure ethane, over temp range 91-105K
Ocean surface tension, τ (N m^{-1})	7.28×10^{-3}	$(1.8 - 3.4) \times 10^{-2}$	Surface tension of pure methane to pure ethane, Bretsznajder (1971)
Ocean viscosity, μ (N s m^{-2})	1.00×10^{-3}	$(0.2 - 1.2) \times 10^{-3}$	viscosities of pure methane to pure ethane, Ori (1997) and Bretsznajder (1971)
$\rho_{atmos} / \rho_{ocean}$	1.2×10^{-3}	$(0.8 - 1.2) \times 10^{-2}$	
Critical wavelength λ_m (m)	1.7×10^{-2}	$(2.8 - 4.8) \times 10^{-2}$	See Section 2.4
Kinematic viscosity, ν ($\text{m}^2 \text{s}^{-1}$)	1.00×10^{-6}	$(0.3 - 2.8) \times 10^{-6}$	$\nu = \mu / \rho_{ocean}$

Table 2.1: Comparison of Earth's and Titan's assumed ocean properties

The parachor may be thought of as the molecular volume of a substance when its surface tension is unity. It is a parameter commonly used in the estimation of surface tension of solvents and mixtures. The presence of suspended hydrocarbons [Lunine, 1993] has been neglected in these values. A simple estimate of the effect upon viscosity due to a suspension of small spherical rigid particles, for volumetric concentration of the solid phase ϕ no more than 2%, can be estimated using Einstein's formula for the effective viscosity, η_{eff} ,

$$\eta_{eff} \approx \eta \left(1 + \frac{5}{2} \phi \right) \quad (2-1)$$

where η is the viscosity of the pure liquid. At the upper limit of 2% concentration for which this simple formula applies the increase in viscosity is 5%. This is however a particularly limiting concentration for application to the Titan case, and Bretsznajder [1971] discusses several formulae applicable to higher concentrations, although the majority of these are still only accurate for relatively disperse suspensions ($\phi < 0.1$). Nevertheless one of the most complex methods described gives, for $\phi < 0.25$, a viscosity increase of less than 50%. Compiling the various methods described by Bretsznajder [1971] it is estimated that for $\phi < 0.5$ the viscosity increase will still be less than an order of magnitude. The significance of viscous effects are discussed further in the next section and for the purposes of this particular treatment the volumetric particle concentration is assumed to be less than 0.5.

Finally, the three parameters at the bottom of Table 2.1 are useful in the consideration of surface fluid dynamics and are simply derived from the parameters that precede them as described in the table.

2.3 Surface gravity waves on Titan

The theory of waves on a free surface has a long history and can be regarded as being well understood [Lighthill, 1978]. It is possible to describe the fluid dynamics of a surface with relatively simple equations by making certain assumptions and the most important of these are investigated here in light of the parameters above.

Firstly it is noted that the ratio $\rho_{atmos} / \rho_{ocean}$ on Titan can be as high as an order of magnitude greater than the value on Earth. Elementary treatment of surface waves on Earth assumes the atmospheric density to be zero, the justification for which becomes apparent by considering the atmosphere as a second fluid of finite density. The result is the inclusion of a factor $(\rho_{ocean} - \rho_{atmos}) / (\rho_{ocean} + \rho_{atmos})$ in the dispersion relation, the neglecting of which leads, on Earth, to a discrepancy of less than 0.3%. On Titan whilst the ratio of densities is less, this discrepancy is still only increased to just over 2% and it is acceptable to proceed as with the terrestrial treatment as far as a theoretical free surface is concerned. It should be recognised that this increased atmospheric density will lead to a slightly higher energy transfer from the atmosphere when considering wind-driven forcing of the surface. However this is left as a topic for discussion at the end of the chapter and is not pursued further here.

Given the above assumption concerning atmospheric density, the controlling factors for waves on the free surface of a fluid are gravity, surface tension and viscosity, the relative importance of these factors determining the form of the waves. For waves on the Earth's ocean, gravity is the dominant influence, acting as the restoring force when the surface is disturbed, while surface tension and then viscosity become increasingly important for shorter waves.

On the basis of linear theory, [Lighthill, 1978], the critical wavelength λ_m divides the *gravity* dominated wave regime from the surface tension dominated *capillary wave* regime,

$$\lambda_m = 2\pi\sqrt{(\tau / \rho g)} \quad (2-2)$$

and from the properties listed in Table 2.1 we see that whilst surface tension effects are slightly more important on Titan than on Earth they still only become significant at wavelengths of a few centimetres or less. These, we shall see, are small compared with typical wavelengths predicted by the wind-wave model. Note that whilst Elachi et al. [1991] obtain the same value as above for λ_m , their calculation of a ‘critical wind speed’, below which only capillary waves are generated (they estimate 1.2 ms^{-1} on Earth, and 0.5 ms^{-1} on Titan), employs an older empirical formula, since superseded by more recent theories of wave generation [Kinsman, 1965]. Essentially energy can be transferred by any turbulent wind to a liquid surface, and waves can still be generated by winds travelling below the ‘critical speed’. There is however a minimum phase speed, c_m , associated with the critical wavelength for gravity-capillary waves (using the values for λ_m contained in Table 2.1 and the dispersion relationships discussed later and given in Table 2.2, one obtains $c_m = 0.23 \text{ ms}^{-1}$ for Earth and $c_m = 0.12 \text{ ms}^{-1}$ for Titan), and problems do exist with the application of wind wave prediction models at very low wind speeds. This is discussed further in the next section.

Again on the basis of linear theory, sinusoidal waves on a water surface suffer attenuation through three main processes of energy dissipation: *internal dissipation* by viscous stresses acting throughout the wave, *bottom friction* where waves induce horizontal motions near the bottom and energy dissipation takes place in a boundary layer between them and the solid bottom, and finally *surface dissipation*, a source of attenuation associated with departures of surface tension from the value it takes during conditions of equilibrium [Lighthill, 1978]. The last is mainly important for liquids covered with a thin film of surface contaminant and is ignored here. Similarly bottom friction effects only become significant when dealing with liquid depths comparable with the wavelength. Since the work of this chapter deals predominantly with deep water waves (see below for details of the depth criterion used) such friction effects are ignored here.

Internal dissipation leads to a loss of wave energy per wave period per unit area in the plane of the undisturbed sea surface, E_{diss} , given by

$$E_{diss} = 8\pi\nu k^2 \omega^{-1} E_{total} \quad (2-3)$$

where ν is the kinematic viscosity (see Table 2.1), k is the wave number ($2\pi/\lambda$), ω is the angular wave frequency, E_{total} is the total wave energy per unit area [Lighthill, 1978]. This is equivalent to saying that the *fractional* loss of energy per wave period is $8\pi\nu k^2 \omega^{-1}$ and Figure 2.1 shows the number of wave periods required for the energy of sinusoidal

waves on deep water to be reduced by a factor of e through internal viscous dissipation for waves on both Earth and Titan.

Note that the figure plots the dissipation against the *kinematic* viscosity, ν , not the viscosity, μ . Two values for Titan are given, representing high and low kinematic viscosity estimates for the Titan ocean. As mentioned in the previous section assumptions have been made regarding the value of the ocean viscosity, namely an ethane-methane composition and volumetric concentration of the solid phase of less than 50%, and therefore results have been plotted for kinematic viscosities two orders of magnitude greater and two orders of magnitude less than the putative Titan ocean estimates to give an indication of the sensitivity of the model. It will be seen that at the wavelengths obtained from the wind wave prediction model, even short waves will have travelled several kilometres before significant dissipation due to viscous effects occurs and this effect is overshadowed by dissipation due to wave breaking. As with surface tension, it is primarily ripples which are susceptible and the effects are pursued no further in this treatment.

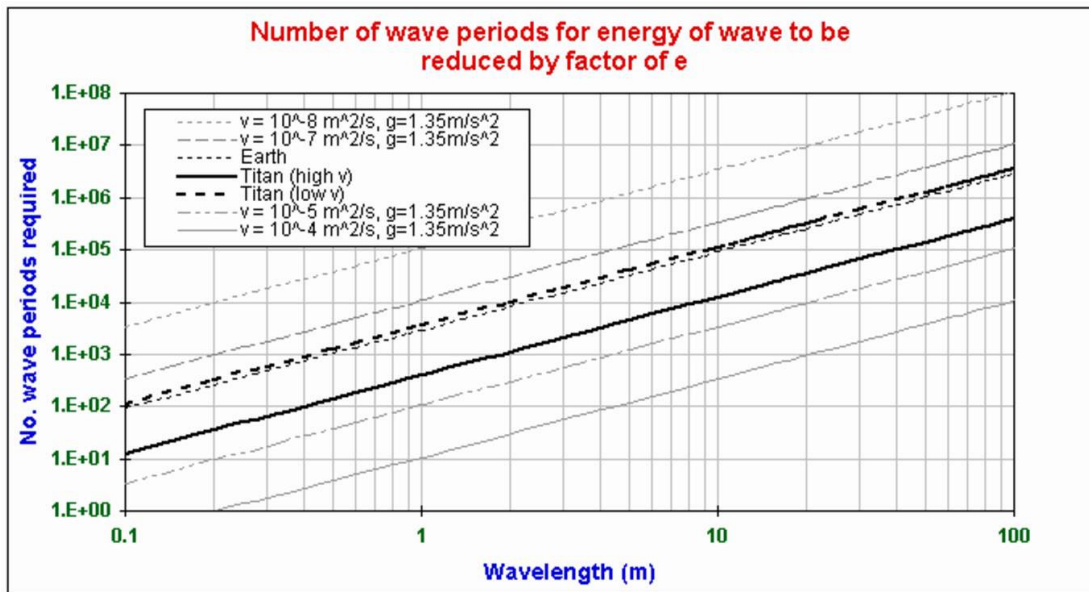


Figure 2.1: Number of periods required for the energy of sinusoidal waves of length λ on deep water to be reduced by a factor e through internal viscous dissipation. ν is the kinematic viscosity (= viscosity / density)

Thus it is seen that surface waves of wavelengths greater than a few centimetres on Titan are largely dominated by gravity just like their terrestrial counterparts. Elementary surface wave mechanics can be applied to consider the behaviour of these gravity waves in the deep and shallow liquid case using linear theory, and the limiting form of the

waves using non-linear theory. It should be noted that the following discussion refers to the monochromatic surface wave and, given the subsequent discussion of wind-wave generation in terms of wave spectra, the direct applicability of such a treatment may initially seem questionable. However, not only does such a consideration give a useful insight into some of the general differences between Titan and terrestrial waves, but the dispersion relations discussed can also be directly employed when manipulating the wave parameters predicted by the wind-wave model. These parameters, detailed in the next section, are statistical parameters used to describe the distribution of waves within the wind-wave spectra. They are also, however, monochromatic and can thus be used to derive, through the dispersion relationships, additional wave parameters not directly generated by the wave model, such as wavelength, phase speed and wave steepness.

These dispersion relationships [Faber, 1995] are summarised in Table 2.2. H is the wave height, c_p is the phase speed, T the period, and d the liquid depth. The deep liquid dispersion relationship applies where the wave amplitude is small compared with the wavelength which is in turn much smaller than the liquid depth. The shallow liquid treatment deals with similarly small amplitude waves but in liquids of depth comparable with the wavelength.

Case	Equivalent dispersion relations		
	Angular frequency	Wavelength	Phase speed
Deep liquid, small amplitude ($H \ll \lambda \ll d$)	$\omega^2 = gk$	$\lambda = \left(\frac{g}{2\pi}\right)T^2$	$c_p = \frac{gT}{2\pi}$
Shallow liquid, small amplitude ($\lambda \gg d$)	$\omega^2 = gk \tanh(dk)$ $\approx gdk^2$	$\lambda \approx \sqrt{gd}T$	$c_p \approx \sqrt{gd}$
Deep liquid, Stokes wave (large amplitude) ($\lambda \ll d, H \sim \lambda$)	$\omega^2 = \left(1 + \frac{(kH)^2}{8}\right)^2 gk$	$\frac{\lambda}{\left(1 + \frac{(\pi H)^2}{2\lambda^2}\right)^2} = \frac{gT^2}{2\pi}$	$c_p = \left(1 + \frac{(\pi H)^2}{2\lambda^2}\right)^2 \frac{gT}{2\pi}$

Table 2.2: Equivalent formulations of the dispersion relationships for small amplitude surface gravity waves in both deep and shallow liquids, and large amplitude surface gravity waves in deep liquid. Expressions are given for angular frequency, wavelength and phase speed.

The exact shallow water dispersion relationship is given in terms of ω and k , but the expression relating λ and T and that giving phase speed are rather more complicated. The shallow liquid approximations given apply in the limiting case of wavelengths large compared with depth – accurate to within 14% for $d < 0.1\lambda$ and to within 6% for $d < 0.05\lambda$. It is also interesting to note that for any given depth there is a wavelength above which the phase speed of the waves remains independent of further increase in wavelength. Naturally the exact shallow liquid dispersion relationship given above tends to the deep liquid expression with increasing depth and it can be shown using linear theory that the deep liquid result requires a liquid depth greater than λ for the approximation to satisfy boundary conditions to better than 1% accuracy. However a more common criterion used is that $d > 0.28\lambda$, which gives accuracy to within 3% [Lighthill, 1978]. This depth criterion is independent of gravity, liquid density, viscosity and surface tension and therefore applies equally well to the case of Titan.

The third row of relationships in Table 2.2 consists of the approximations to second order of the large-amplitude or *Stokes* wave dispersion relationships. These concern the case where the amplitude of a wave is no longer small compared to the wavelength and non-linear terms in the solution of Laplace's equation for the equilibrium distribution of the free surface can no longer be assumed negligible. Taking even just the first few non-linear terms into account it can be shown that a wave profile departs from the simple sinusoidal shape with the troughs becoming flatter and the crests becoming more sharply peaked, as indicated in Figure 2.2.

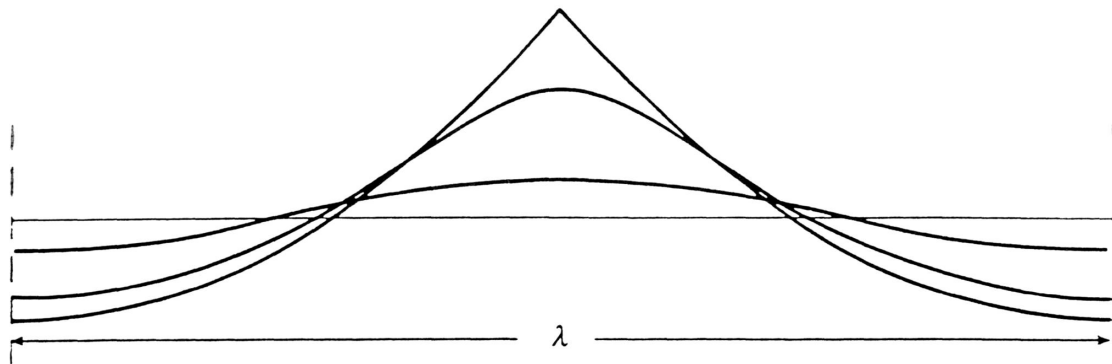


Figure 2.2: Profiles for Stokes waves of steepness $H/\lambda = 0.03, 0.10$ and 0.15 ; the vertical scale shown is twice as large as the horizontal scale for clarity, [Schwarz, 1974]

There is however a limiting value kH at which the peaks become sharp corners and above this value the wave breaks [Lighthill, 1978]. By taking the higher non-linear terms into account this limiting wave height is calculated for deep liquids as close to 0.141λ (approximately one seventh of the wavelength) and the limiting wave speed as 1.092

times the linear wave phase speed [Faber, 1995]. It can also be shown by considering the flow at the surface and the fact that that a particle at the crest of a non-breaking wave cannot be moving faster than the wave itself, that the corner encloses an angle of 120° (Stokes, 1880). The limiting amplitude, corner angle and ratio of Stokes wave phase speed to linear wave phase speed are all independent of gravity [Lighthill, 1978] and therefore, neglecting viscous effects as stated earlier, these results should also hold true on Titan.

From the relationships of Table 2.2 a simple indication is given of the differences between terrestrial and Titan gravity waves. Waves, for example any of those in Figure 2.2, will have a period on Titan approximately $\sqrt{7}$ (about 2.65) times longer than their terrestrial counterparts of similar wavelengths, and will travel $\sqrt{7}$ times slower. Waves of equal wavelength on Titan and Earth will have the same limiting wave height, and waves of equal wave height-to-wavelength ratios will share the same wave profiles shown in Figure 2.2. This will be particularly useful for visualising the wind-waves predicted by the statistical model of the next section.

This section has shown how elementary surface wave theory can be adapted to the Titan case, primarily by adjusting for Titan's reduced gravity. Several other factors which could lead to differences between waves on Titan and those on Earth include Titan's rotation rate, Saturn's tidal influence, the increased atmosphere-ocean density ratio, and sedimentation and suspension in Titan's liquid bodies. The atmosphere-ocean density ratios are discussed further in the next section. For the purposes of this work, the effect of sedimentary particles in suspension on Titan has only been included in the density of the putative ocean. The rotation rate of Titan is believed to be slower than that of the Earth and current observations suggest near synchronicity with Saturn [Lemmon, 1995]. It is assumed therefore that whilst tidal effects may exist on a global scale, for disturbances of the scale considered here, i.e. wavelengths of less than a hundred metres or so, and wind-input over just hundreds of kilometres, their influence will be negligible and they are ignored in this treatment.

This concludes the discussion of the *general* nature of free surface gravity waves that can exist on a liquid Titan surface, regardless of the source of the disturbance. The following section now addresses the more specific and perhaps practical case of waves generated by atmospheric forcing, replacing the monochromatic treatment employed thus far with a spectral approach instead.

2.4 Wind-waves and the wind-wave prediction model

The generation of waves by the wind is a highly non-linear and random process, and our understanding of the exact mechanisms remains poor, being based largely on a mixture of theoretical and observational insights. Not surprisingly a monochromatic treatment is inadequate for representing the sheer diversity of waves which characterise a sea surface and terrestrial oceanography instead describes the waves statistically in terms of a spatially and temporally varying directional wave spectrum, $E(\mathbf{k}, \theta)$. Strictly speaking E is the variance of sea surface elevation, and the energy spectrum is $\rho g E$, but conventionally E is known as the energy spectrum. $E(\mathbf{k}, \theta)$ represents the average amount of energy, at a given wave number, travelling in a given direction. Use will be made in this treatment however of the more conventional *frequency spectrum*, $E(f)$, which is simply $E(\mathbf{k}, \theta)$ expressed in the time domain and integrated over all directions. Note the change in convention from the angular frequency discussed by theoretical consideration of waves to linear frequency, $f (= \omega / 2\pi)$, more commonly used in ocean engineering.

The development of the wave spectrum is described by the wave energy balance equation [Ewing, 1983], expressed here for simplicity in directional wave number space and under the assumption of a deep ocean.

$$\frac{\partial E(\mathbf{k})}{\partial t} + \mathbf{v} \cdot \frac{\partial E(\mathbf{k})}{\partial \mathbf{x}} = S(\mathbf{k}) \quad (2-4)$$

where the left hand side is the rate of change of the spectrum following a wave group with velocity \mathbf{v} . $S(\mathbf{k})$, known as the *source function*, describes the net transfer of energy to, from and within the spectrum and can be expressed as a linear combination of three main component terms.

$$S(\mathbf{k}) = S_{in} + S_{nl} + S_{ds} \quad (2-5)$$

where S_{in} is the atmospheric forcing term, S_{nl} a term representing non-linear wave-wave interactions which transfer energy from the peak to both lower and higher frequencies, and S_{ds} the dissipative term due to wave breaking which becomes significant at higher frequencies. Consideration of the shape of the individual source terms in Figure 2.3 permits a better understanding of several processes involved in wave generation, one of which being the migration of the spectral peak to lower frequencies.

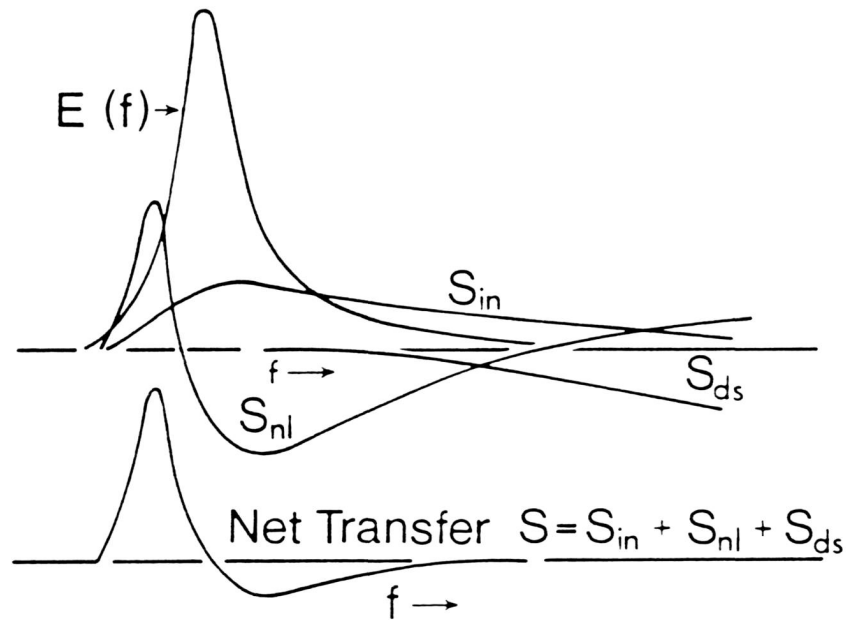


Figure 2.3: Spectral energy balance for wind waves showing energy spectrum, individual source terms and net source function [Ewing, 1983].

Waves of frequency higher than the peak-frequency (to the right of the peak) are shorter and travel slower, those of lower frequency (to the left of the peak) are longer and travel faster. In the early stages of wave growth energy is transferred from the atmosphere to the surface across the whole spectrum. Non-linear wave interactions however transfer some of the energy to lower frequencies and eventually the spectrum develops to the point where energy is no longer being transferred directly from the atmosphere to the spectrum at the peak frequency but is instead maintained by non-linear transfers from slower, higher frequency waves. This transferring of energy is the reason why surface waves increase in both length and period with distance under the action of a constant wind. This leads to the rather counter-intuitive situation where waves at the peak frequency are actually travelling faster than the wind that is generating the sea state, and will continue to accelerate and outrun the wind until they leave the generation area. Such waves are then known as swell.

None of the expressions for the component source terms in Equation 5 are particularly straightforward, and a detailed description of their precise form is not essential to the wind-wave treatment of this work. It should however be noted that each term has been determined semi-empirically for terrestrial application only, and although the prediction model employed here is not explicitly derived from the wave energy balance equation, a consideration of the source terms could give an insight into the applicability of the model to the Titan case beyond mere adjustment for gravity. Unfortunately

environmental parameters other than gravity are not explicitly defined in the expressions for S_{nl} and S_{ds} . S_{in} , however, does contain an exponential growth term which is proportional to ρ_a/ρ_o , the atmosphere-ocean density ratio. It can be shown [Sobey, 1986] using the values from Table 2.1 that this atmospheric forcing term could be as high as an order of magnitude greater on Titan than it is on Earth. However due to the additional source terms S_{nl} and S_{ds} this is unlikely to translate into as great an increase in the energy spectrum and since, as will be shown, the mean elevation of the sea surface is proportional to the square root of the total energy, the implications for the model at the accuracy presented here are limited. A detailed modelling of the individual source terms is presently underway however, and this is discussed later.

The exact form of the wind-wave energy spectrum has been the subject of research for several decades now and several methods exist for its modelling. These range in complexity and accuracy from the first generation models of the early 1960s which were based on often limited observational data and gave limited spectral coverage and little practical applicability, through to the latest generation wave models made possible by recent advances in computing, which can be applied to virtually any problem courtesy of their direct integration of the wave energy balance equation spectrum including explicit modelling of the three main source terms. The model employed here is a second generation model combining observational data and theoretical consideration of wave growth, and whilst not as accurate as the third generation models mentioned above, it is sufficient for the purposes of this work, particularly given the uncertainties surrounding the physical properties on and near Titan's surface.

Two different models are employed to cover the main phases in the evolution of the wind-wave energy spectrum; wave growth and saturation. The sea states corresponding to these two phases are known as the *growing sea* and the *fully developed sea* respectively. In the case of a growing sea, waves increase in size as the distance over which the wind blows (this distance is known as the *fetch*) increases. Here a net increase in the energy spectrum occurs as more energy is transferred from the atmosphere above the surface than is lost through wave breaking and dissipation. The concept of the fully developed sea is employed when, for a given wind speed, a sufficient fetch is reached such that a balance is achieved between wind input and wave dissipation and no further increase in fetch brings about any increase in wave height.

A commonly used spectrum for the growing sea state is the JONSWAP spectrum, obtained during the Joint North Sea Wave Project (JONSWAP) of 1968 and 1969, from

a series of measurements taken 100km off the coast of Denmark [Carter, 1982]. The JONSWAP spectrum, $J E(f)$, takes the form

$$J E(f) = \alpha g^2 (2\pi)^4 f^{-5} \exp\left[-\frac{5}{4}\left(\frac{f}{f_m}\right)^{-4}\right] \cdot \gamma^{\exp[-(f-f_m)^2 / 2\sigma^2 f_m^2]} \quad (2-6a)$$

$$\text{where} \quad \gamma = 3.3 \quad (2-6b)$$

$$\text{and} \quad \sigma = 0.07 \quad f < f_m \quad (2-6c)$$

$$= 0.09 \quad f > f_m \quad (2-6d)$$

The spectrum for the fully-developed sea state is based upon measurements made in the 1950s and early 1960s, prior to the JONSWAP measurements. These measurements, taken in the North Atlantic, led to the derivation of the Pierson-Moskowitz spectrum [Pierson & Moskowitz, 1964], which has since been extensively used in scientific and engineering studies to represent the limiting condition for wave development. The spectrum, $P_M E(f)$, can be expressed as

$$P-M E(f) = \alpha g^2 (2\pi)^4 f^{-5} \exp\left[-\frac{5}{4}\left(\frac{f}{f_m}\right)^{-4}\right] \quad (2-7a)$$

$$\text{where} \quad f_m = 0.816 (g / 2\pi u_{10}) \quad (2-7b)$$

$$\alpha = 8.1 \times 10^{-3} \quad (2-7c)$$

Both spectra contain the two parameters, f_m , the frequency at the spectral peak, and α , a parameter known as Phillip's coefficient. The JONSWAP spectrum however was an improvement over the original Pierson-Moskowitz spectrum, being based upon a mixture of further observations and theoretical considerations of wave growth [Carter, 1982] and as such contains an additional factor modelling the effects of non-linear wave-wave interactions. This important “overshoot” factor is defined by three additional parameters; γ , a peak-enhancement factor and $\sigma = \sigma_a$ or σ_b the spectral width parameters for frequencies less or greater than the peak frequency respectively. For the Pierson-Moskowitz case α is a constant and f_m is defined (Equation 2-7b) for a given wind speed. In this equation u_{10} refers to the wind speed as measured 10m above the sea surface, a commonly used parameter in oceanography. Such simple expressions are not possible for the JONSWAP spectrum, however, as both α and f_m depend upon the fetch as well as

the wind speed. Figure 2.4 illustrates the general shape of the two spectra and, in the JONSWAP case, the development of the spectrum with increasing fetch. Of note is the increase in total energy contained in the spectrum as energy is transferred from the atmosphere, and migration of the spectral peak to lower frequencies as energy is transferred between surface waves.

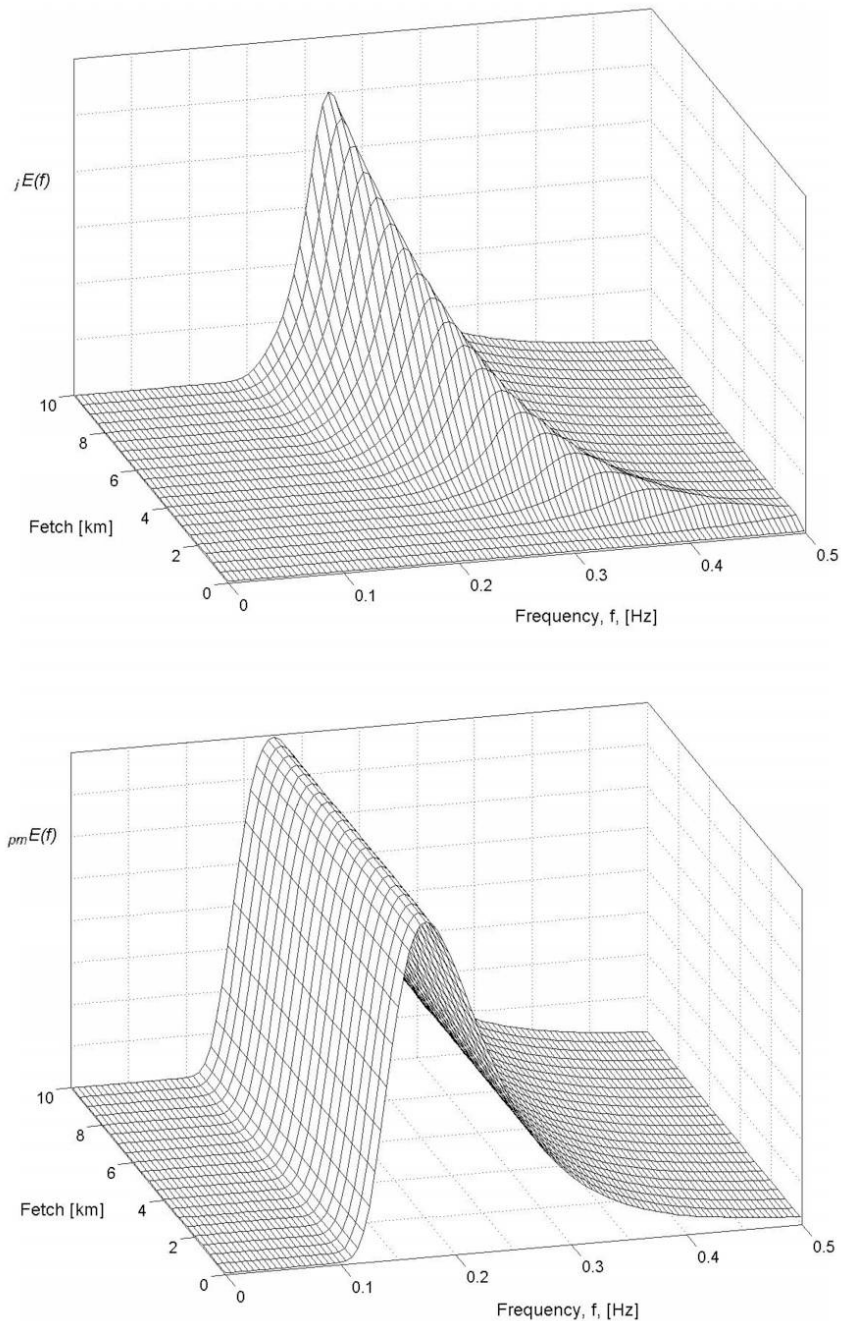


Figure 2.4: General shape and development of the JONSWAP (top) growing sea and Pierson-Moskowitz (bottom) fully developed sea wave spectra (Carter, 1982) with fetch

Essentially, therefore, the problem of wind-wave prediction revolves around the calculation of the defining parameters and the resulting spectrum for a given wind field. Such results do indeed represent characterisation of the sea surface, however it is often useful in practical applications to express the results in terms of parameters providing a more “visual” indication of surface conditions. The model presented here makes use of two commonly used parameters, statistical quantities known as the *significant wave height* and *peak-period*.

The significant wave height, h_s , is defined as

$$h_s = 4\sqrt{\int_0^{\infty} E(f)df} \quad (2-8)$$

i.e. four times the square root of the variance of the sea surface elevation. More practically speaking the significant wave height is close to the mean of the highest one-third of all waves in the spectrum and approximates visual estimates of wave height. For example, on Earth it is generally speaking the height most responsible for damage to coastlines [Allen, 1985].

The peak period, t_m , corresponds to the peak frequency, f_m , of the spectrum:

$$t_m = \frac{1}{f_m} \quad (2-9)$$

In the Pierson-Moskowitz case t_m can be obtained simply from equation 2-7b, and the energy spectrum directly integrated to arrive at an expression for h_s , both expressions depending only upon g and u_{10} . The JONSWAP spectrum, on the other hand, requires numerical integration and the expressions for t_m and h_s depend not only on g and u_{10} but also the fetch, x .

During the early stages of wind-wave modelling it was realised that classical dimensional analysis provided a useful tool for reducing the number of dependent variables to be represented in the equations governing wave parameters. This approach is still viewed as useful even today, and it can be shown [Sobey, 1986] that, for the case of constant wind velocity and deep liquid, it is convenient to represent each of the five parameters - α , f_m , γ , σ_a , and σ_b , as well as the total energy in the spectrum, in terms of the dimensionless fetch parameter, gx/u_{10}^2 . Table 2.3 gives the numerical relationships for dimensionless peak frequency ν , dimensionless surface variance ε , and Phillips’ coefficient α [Carter, 1986].

Dimensionless parameters	Symbol	Definition	Values	
			Pierson-Moskowitz	JONSWAP
Fetch	ξ	gx/u_{10}^2		
Frequency	ν	$u_{10}f_m/g$	0.13	$2.84 \xi^{-0.3}$
Total energy	ε	Eg^2/u_{10}^4	3.66×10^{-3}	$1.63 \times 10^{-7} \xi$
Phillips coefficient	α		8.1×10^{-3}	$0.0662 \xi^{0.2}$

Table 2.3: Non-dimensional frequency, ν , energy, ε , and Phillips' coefficient, α , expressed in terms of non-dimensional fetch, ξ . These expressions can then be rearranged to give the dimensional peak frequency f_m , energy E , and Phillips coefficient α in terms of dimensional fetch, x , and wind speed at 10m above the surface, u_{10} .

The dependence of γ , σ_a , σ_b on fetch and wind speed is not known and the adoption of the constant values of equations 2-6b, 2-6c and 2-6d is said to result in a “mean JONSWAP spectrum” which will simply be referred to as the “JONSWAP spectrum” from here onwards.

Returning to the spectra and the statistical parameters of interest, the peak period t_m can be found from $1/f_m$ and the energy spectra integrated to give h_s , directly for the Pierson-Moskowitz spectrum and numerically for the JONSWAP case. The expressions obtained [Carter, 1982] are

$${}_{PM}h_s = \frac{0.447g\sqrt{\alpha}}{\pi^2 f_m^2} \quad {}_Jh_s = \frac{0.552g\sqrt{\alpha}}{\pi^2 f_m^2} \quad (2-10a,b)$$

where the respective values for f_m and α in each case are given in Table 2.3. Inserting these values it is possible to finally obtain numerical expressions for h_s and t_m in terms of g , fetch x in km, and wind speed u_{10} in ms^{-1} .

Table 2.4 summarises the numerical formula employed, for both Earth and Titan, the latter of which have been adjusted taking into account only the reduced gravity. The ${}_{P-M}$ and ${}_J$ subscripts before h_s and t_m refer to the Pierson-Moskowitz and JONSWAP significant wave height and peak-periods respectively. It should be remembered that these relatively straightforward solutions have relied upon an important assumption which can be considered one of the shortfalls of the empirical approach, namely that the winds are not only constant in direction but also in speed. The constraint on wind direction permits the formulation of the non-dimensional expressions in terms of two

parameters, fetch and wind duration, which to some extent share a certain equivalence. The further constraint on constant wind speed then permits the expression in terms of *either* fetch *or* wind duration alone. In this treatment it was chosen to express the results as a function of fetch, so that they may be discussed more easily in the context of varying Titan sea or lake extent.

	Numerical formulae	
	Earth [Carter, 1982]	Titan
jh_s	$0.0163 x^{0.5} u_{10}$	$0.0439 x^{0.5} u_{10}$
$P-Mh_s$	$0.0247 u_{10}^2$	$0.179 u_{10}^2$
jt_m	$0.565 x^{0.3} u_{10}^{0.4}$	$2.26 x^{0.3} u_{10}^{0.4}$
$P-Mt_m$	$0.728 u_{10}$	$5.28 u_{10}$
X_{lim}	$2.32 u_{10}^2$	$16.8 u_{10}^2$

Table 2.4: Numerical formulae for significant wave height, h_s , peak period, t_m , and limiting fetch X_{lim} separating the growing sea and fully developed sea states on Titan and on Earth, where x is the fetch in km, and u_{10} the wind speed at 10m above the surface

Due to the uncertainties surrounding the level of turbulence and velocity profile of Titan’s surface winds, results are expressed for five wind speeds in the range $0.3 \text{ ms}^{-1} < u_{10} < 5 \text{ ms}^{-1}$, with the upper limit being considered an extreme case for Titan (see section 2.2), particularly sustained across a large fetch. It should be noted that whilst wind speeds lower than $u_{10} = 0.3 \text{ ms}^{-1}$ certainly warrant investigation in the light of current Titan surface wind estimates, such speeds are below the commonly accepted range of applicability of the model. Our understanding of wave generation under wind speeds of less than 1 ms^{-1} on Earth becomes limited as accurate measurement in this regime is difficult (typically open ocean winds are measured to an accuracy of $\sim 1 \text{ ms}^{-1}$). Given that the minimum phase speed (as discussed in section 2.4) of gravity-capillary waves on Titan was calculated as $c_m = 0.12 \text{ ms}^{-1}$, the lowest wind speed considered for this model is $u_{10} = 0.3 \text{ ms}^{-1}$.

Finally it is necessary to define when to employ the JONSWAP formulae and when to employ the Pierson-Moskowitz results instead. Following Carter [1982] the JONSWAP growing sea state is defined as satisfying the condition $\nu \geq 0.14$, and the Pierson-Moskowitz fully developed sea state the condition $\nu < 0.14$, where ν is defined in Table 2.3. This value corresponds to limiting values of fetch, X_{lim} separating the JONSWAP

regime from the Pierson-Moskowitz regime and these are included at the bottom of Table 2.4. It should be stated that Carter [1982] uses $\nu = 0.13$ for the Pierson-Moskowitz non-dimensional frequency, and yet $\nu = 0.14$ in his definition of the fully developed sea state. Here the value of $\nu = 0.14$ has been used in both for consistency, yielding a slightly (approximately 7%) greater peak-frequency for the Pierson-Moskowitz fully developed sea wave spectra. It will be noted from Figure 2.4 that there exists a discrepancy between the asymptotic frequency of the JONSWAP spectra and the peak-frequency of the Pierson-Moskowitz spectra. This is a well recognised problem in oceanography [Tucker, 1991], and is a result of the different aims of the original studies and of the uncertainties in the measurements on which the spectral formulations are based. The results can be reconciled but the method is not trivial and is beyond the scope of this treatment.

Having defined the height and period of a single characteristic wave of the wave spectrum for a given wind input, several other wave parameters are calculated using the wave dispersion relationships discussed in the previous section, assuming a monochromatic wave of wave height h_s at the spectral peak, i.e. having wave period t_m . The calculated parameters are wavelength, λ , phase velocity, c_p , and wave steepness, h_s/λ . The maximum slope of the wave has also been plotted assuming a simple sinusoidal shape to give a practical idea of the slopes that could be experienced by the Huygens probe in the event of an encounter with such a wave. The accuracy of this approximation depends on the steepness of the wave as shown in Figure 2.2, and is discussed further in the next section.

2.5 Results

Figures 2.5 to 2.10 show the results obtained from the model. Each graph displays both Titan and terrestrial case results to aid comparison. Note that the smooth curve at the transition from the JONSWAP to the Pierson-Moskowitz regime is a result of the graphing package.

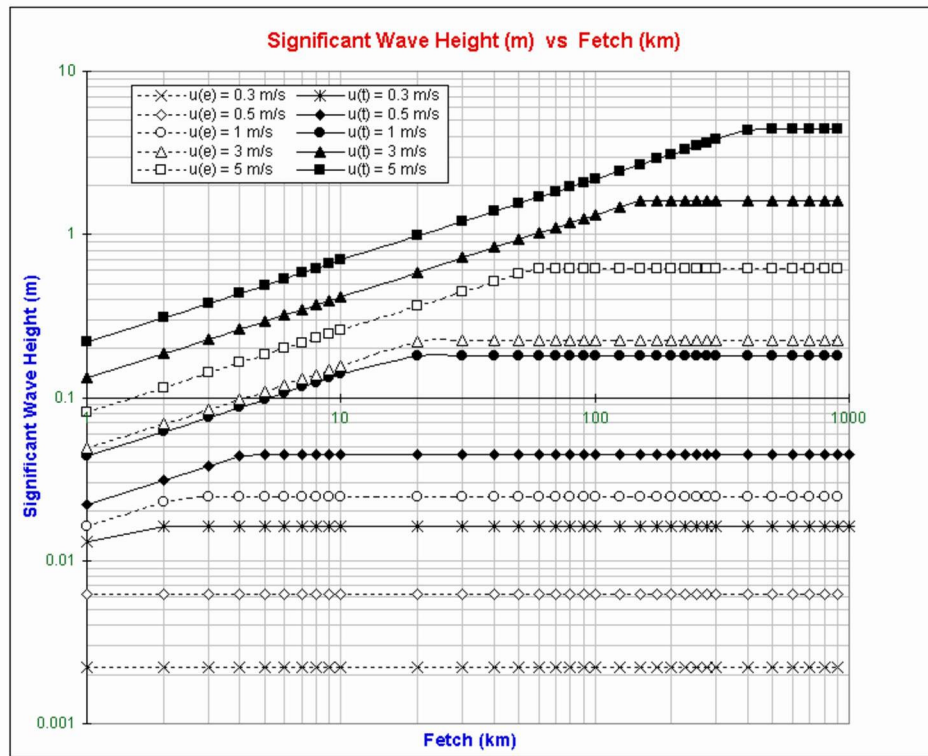


Figure 2.5: Significant wave height, h_s , against fetch, X , for wind speeds $u_{10} = 0.3\text{ms}^{-1}$, 0.5ms^{-1} , 1ms^{-1} , 3ms^{-1} , and 5ms^{-1} on Titan and Earth.

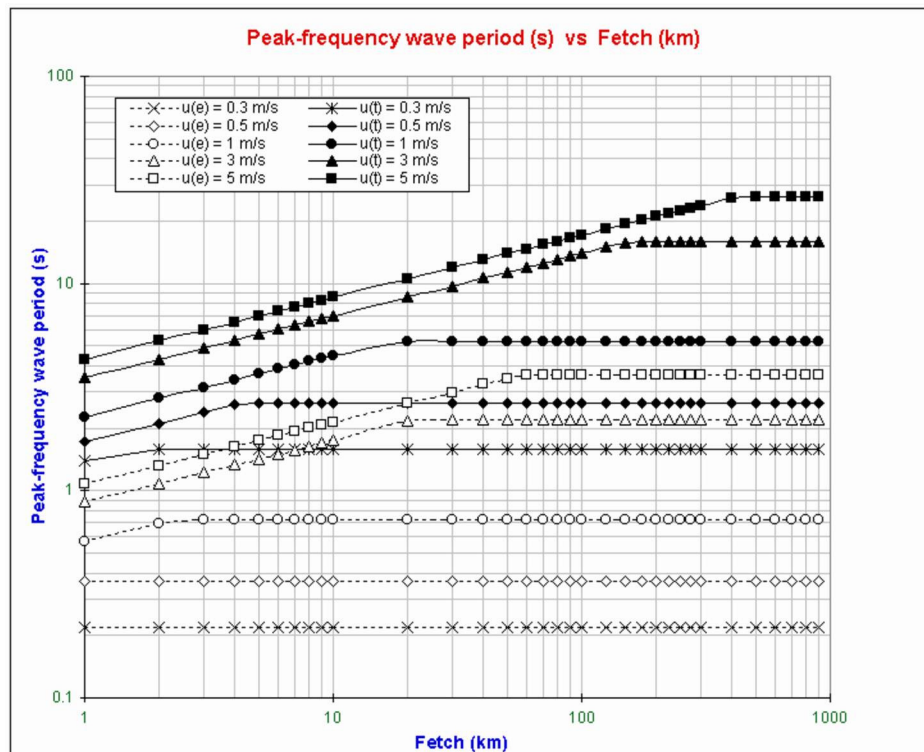


Figure 2.6: Peak frequency wave period, T_m , against fetch, X , for wind speeds $u_{10} = 0.3\text{ms}^{-1}$, 0.5ms^{-1} , 1ms^{-1} , 3ms^{-1} , and 5ms^{-1} on Titan and Earth.

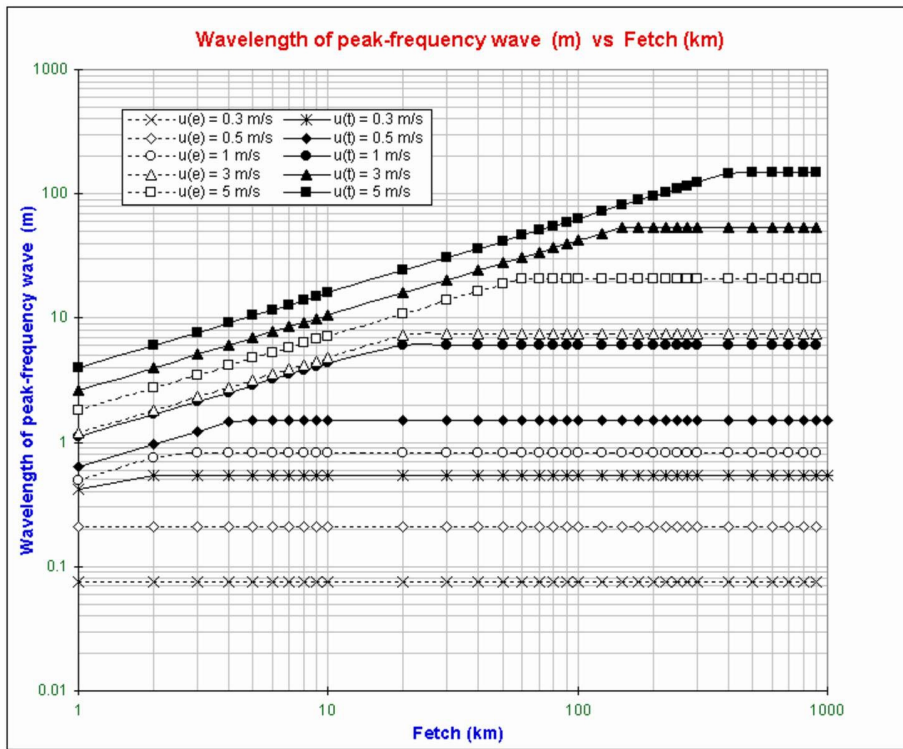


Figure 2.7: Wavelength, λ , of peak frequency wave against fetch, X , for wind speeds $u_{10} = 0.3\text{ms}^{-1}$, 0.5ms^{-1} , 1ms^{-1} , 3ms^{-1} , and 5ms^{-1} on Titan and Earth.

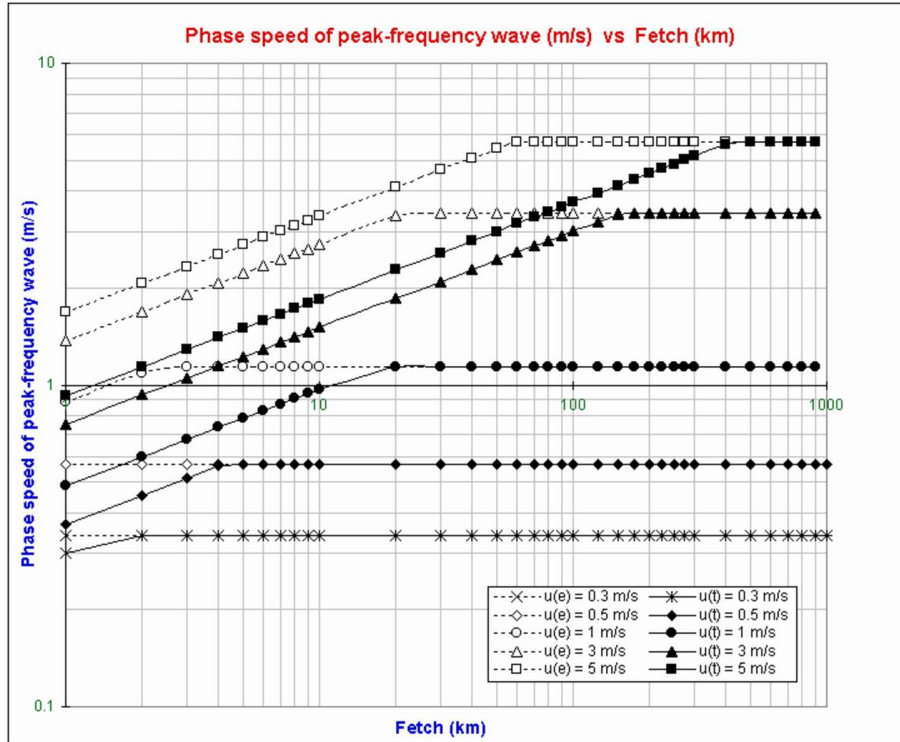


Figure 2.8: Phase speed, c_p , of peak frequency wave against fetch, X , for wind speeds $u_{10} = 0.3\text{ms}^{-1}$, 0.5ms^{-1} , 1ms^{-1} , 3ms^{-1} , and 5ms^{-1} on Titan and Earth.

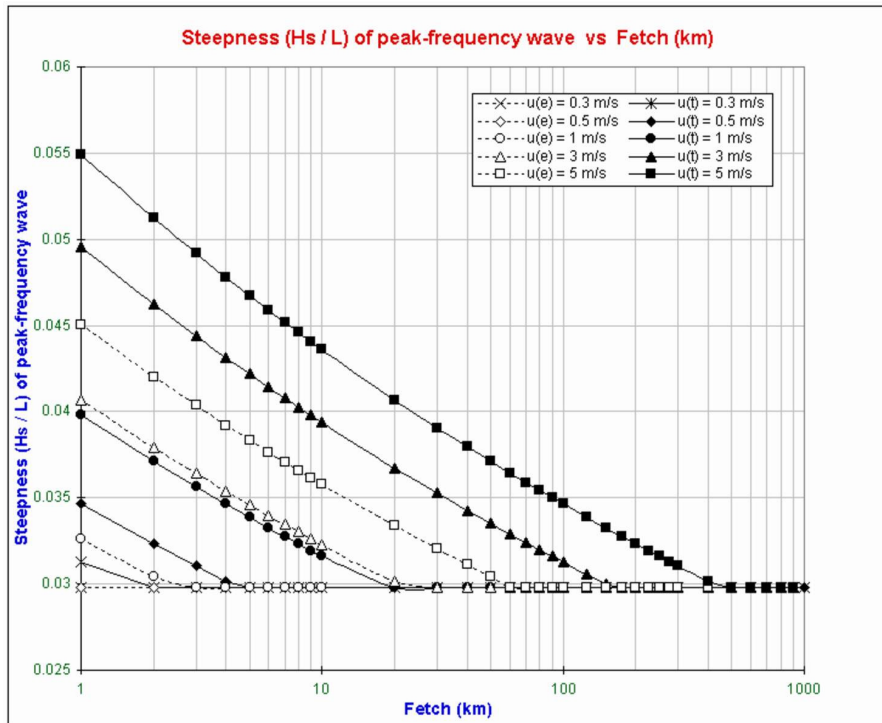


Figure 2.9: Steepness, h_s/λ , of peak frequency wave having wave height H_s , against fetch, X , for wind speeds $u_{10} = 0.3\text{ms}^{-1}$, 0.5ms^{-1} , 1ms^{-1} , 3ms^{-1} , and 5ms^{-1} on Titan and Earth.

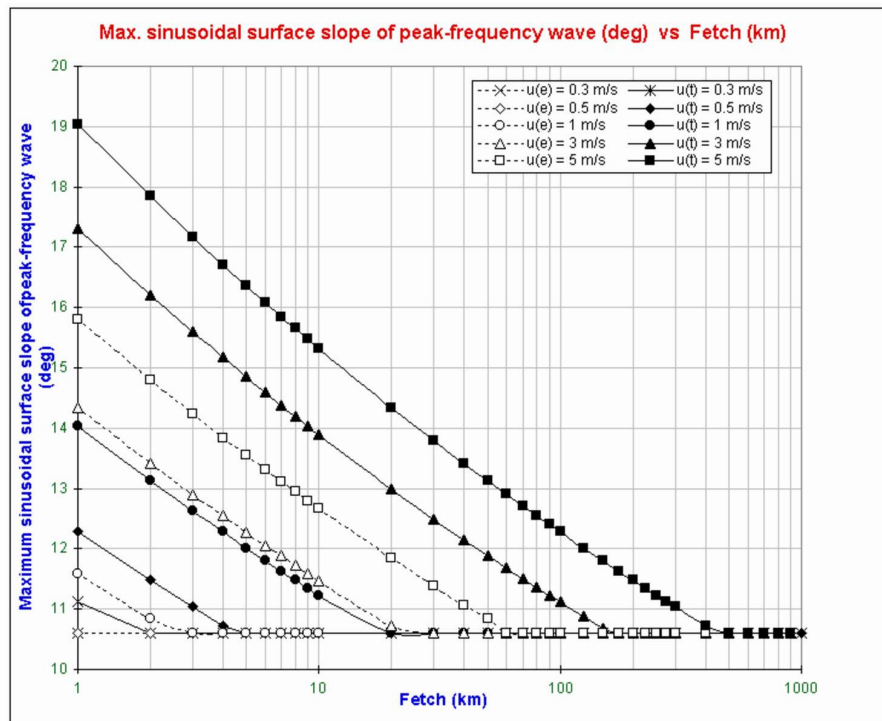


Figure 2.10: Maximum slope θ_{max} assuming sinusoidal wave of peak frequency having wave height h_s , against fetch, X , for wind speeds $u_{10} = 0.3\text{ms}^{-1}$, 0.5ms^{-1} , 1ms^{-1} , 3ms^{-1} , and 5ms^{-1} on Titan and Earth.

Figure 2.5 displays the increase in significant wave height with fetch as expected with energy being transferred to the spectrum from the surface wind until a balance is achieved and the sea becomes fully developed. The fully developed sea value for the Titan surface significant wave height is seven times greater than that on Earth as can be expected (equations 2.7a and 2.10b) by taking gravity alone into account. Interesting and less obvious is the *ratio* of Titan significant wave height to terrestrial significant wave height in the *growing sea* which increases with fetch from as little as 3 to the fully developed sea value of 7.

Figure 2.6 shows the increase in wave period both with fetch and wind speed again as more energy is transferred from the atmosphere to the short period waves and then shifted through non-linear surface wave-wave interactions (equation 2-5) to longer period waves. As with significant wave height the fully developed sea value for the Titan sea is approximately seven times greater than the terrestrial value as predicted by equation 2-7b, whilst for the growing sea the ratio increases from the value of about 4 upwards.

Figures 2.7 and 2.8 show the transfer of energy within the spectra leading to an increase in both wavelength and phase speed with fetch and wind speed. It is found that the peak frequency wavelength of Titan waves increases from twice the terrestrial value to the fully developed sea ratio of 7, whilst the peak frequency phase speed increases from half that on Earth to a fully developed sea value approximately equal to Earth's. Note that as described in the previous section the phase speed of waves at the spectral peak will eventually exceed the generating wind speed itself.

Figures 2.9 and 2.10 show the increase in steepness of surface waves with wind speed but gradual decrease in steepness with fetch, as waves become longer faster than they become higher. Titan waves are slightly greater in steepness compared with their terrestrial counterparts, ranging from 1.2 times steeper down to approximately equal steepness. The steepest estimated Titan wave slopes, assuming wind speeds of up to 5 ms^{-1} gusting over just 1km, are found to be 19° , decreasing down to 11° for lower wind speeds and greater fetches.

The approximation to a sinusoidal wave profile used in the calculation of the maximum surface slope in Figure 2.10 can be seen to be justified by comparing the maximum value of steepness obtained from the model (Figure 2.9) with the non-sinusoidal wave profiles of Figure 2.2. The greatest steepness value obtained is 0.05 and this value corresponds in Figure 2.2 to a wave which is very close to the sinusoidal approximation.

An interesting visualisation which summarises the difference between Titan and Earth surface waves is that, at least in shape, i.e. significant wave height, wavelength and steepness or slope, waves on Titan generated under the action of winds travelling at 1 ms^{-1} appear similar in scale to waves on Earth generated by winds travelling at 3 ms^{-1} . Similarly those travelling at 0.3 ms^{-1} on Titan resemble waves generated by a 1 ms^{-1} wind on Earth. The respective Titan waves, however, will have nearly 3 times the period and travel at one third the speed of those on Earth. Attention is finally drawn to the increased limiting fetch for Titan waves, which separates the growing sea regime from the fully developed sea regime.

2.6 Discussion

As expected the model predicts that waves on a Titan sea will be larger in scale and travel slower than those on Earth, the limiting value for both significant wave height and wave period being inversely proportional to gravity (equations 9 and 10a). The factor of 7 in the ratio of terrestrial to Titan significant wave heights and periods for the fully developed sea can be predicted directly from these equations. Less obvious however is the variation in this ratio for the growing sea state, where there is no such simple inverse proportionality with g , and the model's results in this regime are particularly interesting given the scale of liquid bodies favoured by present surface models for Titan. Thus the model provides a good indication of the effects of the reduced gravity on a liquid Titan surface. However it is important to remember that the approach presented has made several assumptions and there exist certain limitations.

The treatment employed has assumed that effects due to surface tension and viscosity are negligible. Earlier it was shown that this assumption holds for waves of wavelength greater than a few centimetres and therefore for the wind-waves considered here. Figure 2.1 showed the proportional loss of wave energy per wave period due to viscous dissipation, and even though scales of several kilometres would be sufficient for individual waves of the peak-periods predicted to die down, this particular dissipation mechanism is overshadowed by the wave-breaking mechanism for all but the shortest of waves. Figure 2.7 shows, however, that at wind speeds of much less than 1 ms^{-1} the wavelengths generated are of the order of a metre. Remembering that these are wavelengths of waves at the spectral peak and that slower, higher frequency waves will exist which are shorter still, for results at such low wind speeds the accuracy of the model might be questioned. At the wavelengths predicted by very low wind speeds both surface tension and viscous effects will certainly affect the initial wave generation

process and will likely slow the development of the wave spectra with fetch. They may also affect the limiting scale of fully developed sea waves. This however is the subject of more detailed modelling.

The model has also neglected the treatment of suspended particles in both the dispersion relationships and the empirical model, and in calculating Titan's ocean properties a maximum volumetric concentration of the solid phase of 50% has been assumed. Clearly more detailed modelling is required to calculate the viscosity of more concentrated suspensions and furthermore evaluate the precise degree to which suspended particles affect the fluid behaviour and resulting waves beyond that predicted by a simple change in liquid density and kinematic viscosity.

Long wavelength waves arising from tidal effects have not been considered in this treatment. Their dispersion relationships have not been included and the use of the empirical wind-wave model is inappropriate for their treatment as the physical processes involved are completely different. Such waves will exist on Titan however and their modelling remains to be carried out.

Several assumptions have been made regarding the atmosphere-ocean interaction in this particular treatment of wind-waves. Firstly, as was discussed in section 2.3, for the purposes of the dispersion relationships the atmospheric density is taken to be negligibly small as with the terrestrial treatment. As explained earlier this leads, in the Titan case, to an increased but still negligible discrepancy in the dispersion relationships. An improved treatment would account for this but would not significantly improve the overall accuracy of the results in this particular treatment. The increased atmosphere-ocean density ratio is far more important in the atmospheric input source term in the energy balance equation for wind-driven surface waves (equation 5) on Titan. It was explained in section 2.4 that the S_{in} term includes this density ratio, however the empirical model here does not explicitly model the source terms and therefore the enhanced energy transfer from wind to sea surface expected from the increased density ratio is not modelled here. Whilst the effects of this are not likely to change the results significantly, the wind-wave prediction on Titan will not scale precisely by simply adjusting for gravity and such effects demand explicit modelling of the source terms for more reliable results. Similarly the third assumption made in the treatment here is the rather restrictive assumption of constant wind speed and direction, needed for the simplification of the JONSWAP and Pierson-Moskowitz spectral models [Carter, 1982]. Since these models are empirical and do not include a temporal or spatial wind-field term explicitly it is not possible to adapt this particular treatment to incorporate varying

wind velocity which would be an interesting exercise for Titan particularly over the scales considered. Thus a new model which models the atmospheric input explicitly is needed for increased versatility and applicability to Titan. A third generation wind-wave prediction model, as described in section 2.4, would be suitable for this.

Another shortfall of the empirical spectral models employed concerns the locality in which the measurements on which they are based were taken. For the JONSWAP model for example these were taken approximately 100km from a coastline and the applicability of the model to a different locale, such as a bounded lake or near to a coastline, is questionable. Again due to the empirical nature of the model it is difficult to assess exactly how the model might vary without more detailed knowledge and modelling of the local sea or lake bathymetry. This can also be included in a third generation wind-wave prediction model, and whilst preliminary investigation has been attempted using an early model [Ghafoor et al., 1998], mixed results were obtained and it is recommended that advantage be taken of the latest models which are gradually being made publicly available.

Finally, an area that has not been addressed is the phenomenon of wave breaking. This directly affects the development of the entire wind-wave spectrum even out at sea and again explicit modelling of the dissipation source term in the energy balance equation is required for a more accurate model of this on Titan as the empirical models do not include any such term. The treatment of breaking waves near the perimeter of a liquid body is particularly interesting and has potential implications for erosion [Ori et al., 1997] and stirring of sedimentary particles. However the physical processes are slightly different and potential models are not considered further here. They may nevertheless be of considerable value to the modelling of Titan's surface and, whilst beyond the scope of this treatment, do require further attention.

2.7 Conclusions

It has been shown that where liquid bodies exist on the surface of Titan free surface waves will be dominated by gravity, as on Earth, with surface tension and viscous effects only becoming significant below wavelengths of several centimetres. Where a surface wind exists this will give rise to wind-driven surface waves and empirical wind-wave prediction models suggest that such waves will grow to a limiting height, limiting wavelength and limiting period which are all inversely proportional to gravity. On Titan, therefore, the surface waves will grow with fetch to become approximately seven times larger and seven times longer in period than those on Earth. Before reaching this limiting

form the waves will still be larger and slower than their terrestrial counterparts, for a given wind speed and fetch, although the ratio will be less than the fully developed sea value of seven. Titan waves will in general be steeper than their terrestrial counterparts generated under the same wind. For visualisation purposes, surface waves on a Titan sea arising from surface wind speeds of 0.3 ms^{-1} and 1 ms^{-1} will resemble in scale waves on Earth generated by terrestrial winds travelling at 1 ms^{-1} and 3 ms^{-1} respectively. Titan waves will have nearly three times the period and travel almost three times slower than the terrestrial waves however.

Whilst any turbulent surface wind on Titan will generate some surface waves, a problem does exist in the application of terrestrial wind-wave prediction models for wind speeds much less than 1 ms^{-1} since, even accounting for the increased size of Titan waves due to gravity, the wavelengths are low enough for viscous and surface tension effects to influence early stages, and for very low wind speeds later stages, of wave growth. An improved treatment using a third generation wind-wave prediction model is recommended for correct modelling of the atmospheric forcing on Titan. Such a treatment would also permit modelling of crater basin bathymetry, shallow water effects and spatial variation of the surface-wind field.

The modelling of surface waves on Titan is particularly important for interpretation of surface data returned from the Huygens Probe due to land on Titan in 2005 and several of the wave parameters predicted in this work could potentially have surface mission implications. Significant departures from the local vertical of the probe symmetry axis, for example, due to motions induced by the larger waves indicated in Figure 2.10, could have possible consequences for the Probe-Orbiter link. Conversely, careful measurements of the surface waves made by instruments aboard the Huygens probe and Cassini orbiter could possibly be used to retrieve important planetological information about Titan's surface. The potential measurability of surface waves using the TIL sensor is discussed further in Chapter 6.

Chapter 3

The TIL and HASI-ACC Sensors

3.1 TIL Sensor introduction

As described in Chapter 1 one of the aims of this thesis is to consider the capabilities of the SSP TIL and, to a lesser degree, the HASI-ACC sensors, investigate their likely performance on Titan and make predictions as to their usefulness in reconstruction of the probe dynamics both during descent and following impact with Titan's surface. Whilst the previous chapter described the modelling of surface dynamics of potential liquid bodies on Titan, the next three chapters focus on the calibration, modelling and testing of the TIL and ACC sensors (which may indirectly reveal information concerning such surface dynamics), with Chapter 6 attempting predictions as to how well they will actually represent probe dynamics on Titan.

This chapter commences with an overview of the TIL sensor, reviewing its design and principle of operation. A review is made of its laboratory-based calibration with mention of both static and some simple step and frequency response tests. Two key aspects of the TIL sensor response are highlighted: the time response of the sensor in reaching an equilibrium level, and the effect of accelerations on the sensor housing. Modelling of the sensor is carried out using the laboratory-calibration determined parameters and the first of the two aspects above is considered, investigating the response of the sensor to a range of step and oscillatory angular motions about its measurement axis. Extrapolation is made to the case of such motions under Titan gravity and the degradation in response time investigated. The effects of linear accelerations on the sensor housing under Titan gravity are considered in subsequent chapters.

The detailed mechanical design of the sensor housing, the electrical interface and electronics required to support this sensor on Huygens are not relevant to dynamic

response considerations and are not treated here. For such information the reader is referred to the Tilt Subsystem Acceptance Data Package [PY-SSP-UKC-AD-104]. This thesis considers the sensor design only in so far as is needed to simulate its fluid motion, and therefore its projected capabilities and performance on Titan.

3.2 Tilt Sensor Background

3.2.1 Tilt sensors: a general background

As its name suggests, a tiltmeter is an instrument that measures inclination relative to a reference orientation. Frequently the tilt relative to the local horizontal (perpendicular to the gravitational acceleration) is required, but not always. Several systems exist for attitude determination, but most fall into one of three categories; accelerometers, level detectors and what shall be termed ‘relative reference’ based systems.

Accelerometers and level detectors both involve detection of local accelerations, with the former providing both direction and magnitude information whilst the latter provides only direction. Three orthogonally oriented accelerometers provide the magnitude and direction of the sensor accelerations, relative to the sensor housing. Where the sensor is either at rest or moving at constant velocity in a gravitational field then the local acceleration is merely that due to gravity. Thus the attitude can be derived relative to the local gravity vector, and hence the local horizontal plane. Different types of accelerometer are available, with two widely used examples being servo-accelerometers and piezoelectric accelerometers. Both types are described further in section 3.6. The use of accelerometers as tiltmeters does become more complicated when the sensor is subjected to non-gravitational acceleration and this is also discussed later.

Level detecting sensors are so named because of their traditional use in determining orientation relative to the local horizontal. Pendulum type level detectors consist of a mass hanging beneath a reference point by a low friction coupling, and rely on the fact that, in the absence of non-gravitational sensor accelerations, the mass will hang such that the thread by which it is suspended aligns itself with the local gravity vector. Position sensors in the coupling measure the angular position of this vector. Friction and noise issues exist with these sensors however [Shaw, 1997].

The spirit-level sensor relies on the principle of a fluid surface orienting itself perpendicular to the gravity vector (see section 3.2.3) and therefore causing a gas bubble within a fluid vial to rise to the uppermost position, again in absence of non-gravitational

sensor acceleration, thus indicating the direction of the local gravity vector. Spirit-level type detectors are extremely useful for quick and simple manual alignment with local horizontal, however the electronic interfacing required to measure accurately the position of the gas bubble in these sensors is not straightforward [Shaw, 1997].

A variation on this type of sensor is the electrolytic tilt sensor. This also relies on the alignment of a fluid surface with the local horizontal, but within the sensor are three electrodes, as shown in Figure 3.1. The relative resistances between the two side electrodes and the centre electrode vary as a function of the depth of immersion in the electrolyte, and therefore as a function of the fluid surface orientation. This enables a very simple electrical interface by which attitude measurement can be made, with the electrolyte and electrodes acting as a resistive potentiometer. This is explained in greater detail in section 3.2.3. Again, as with the accelerometers, the measurement of attitude is complicated by the existence of non-gravitational sensor accelerations, and this important consideration is also described in section 3.2.3.

The third group of attitude sensors mentioned were termed ‘Relative reference’ systems, and these differ from the previous sensors in that they do not rely on the measurement of local accelerations, gravitational or not, but a variety of other parameters such as light intensity, magnetic field, or electric field, for example. These systems do not directly provide orientation relative to local horizontal, but rather match observed measurements with a database of calibrated values, from which orientation relative to an application specific reference frame may be calculated.

One of the simplest demonstrations of such a system would be the rigid connection of a platform to a potentiometer dial, as in. As the platform is rotated about the axis of the dial, so the dial rotates and a simple linear calibration of attitude, relative to a zero or reference orientation, against voltage is possible. In this way the relative orientation between mechanically connected components is calculable.

More sophisticated, non-mechanical examples of such ‘relative reference’ sensors would include star cameras, sun sensors and 3-axis magnetometers. With each of these attitude is also determined by comparing measured values against a reference database; star field for the star camera, solar angle for sun sensor, magnetic field for the magnetometer. A certain degree of computation is required to actually derive the attitude, far more so that in the example of the potentiometer, and all three calculations require additional knowledge concerning the position of the sensor. Of the examples noted also the star camera and sun sensors rely on the visibility of stars and the sun respectively and the

magnetometer of course is only useful in the presence of a well characterised magnetic field. Where these requirements are met however, these sensors do have the advantage of their measurements being independent of sensor housing accelerations.

Another type of system used in attitude determination involves the use of gyroscopes. These are widely employed in dynamic environments but are slightly different from the above sensors. These can provide extremely accurate information concerning the rate of change of attitude and therefore, by integration, attitude history relative to the sensor housing reference frame. Because these sensors involve continuous integration they do however require information concerning initial conditions and are often used as part of a control loop and not used in isolation.

As shown above a range of tilt measuring techniques are available, each with its own advantages and disadvantages. Other factors such as cost, mass, and power consumption, not just of the sensors themselves but also their mechanical and electrical interfaces, also play a significant role in the selection of the instruments, and again some of these factors are discussed in Shaw [1997]. As concerns this thesis the range of tilt measurement techniques has been discussed primarily for background purposes. The TIL sensor selected for the Huygens Surface Science Package was of the electrolytic type, offering favourable performance to cost, mass and power ratios, long term stability, and broad heritage from civil engineering to aircraft and missile applications [Shaw, 1997]. As a fluid based sensor its use in space necessitated special consideration, as discussed briefly below, however it still represented the best overall value of all options considered at the time of design.

3.2.2 The SSP Huygens TIL Sensor

TIL Sensor structure

The TIL sensor is a slightly modified version of the commercially available Spectron 556A type housing containing two orthogonally mounted L-211U electrolytic tilt sensors. The model is one of a wide range of tilt sensors offered by the U.S. based manufacturer, Spectron Glass and Electronics Inc., who cater for a broad spectrum of static and dynamic applications. Two sensors are required since each is sensitive only to rotation about a single axis, and their orthogonality is necessary for independent measurements.

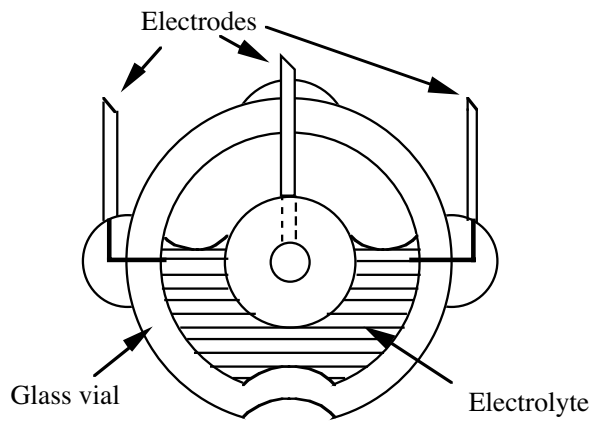
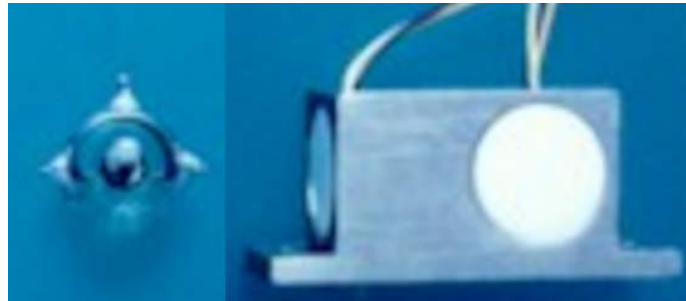


Figure 3.1: Photograph and schematic (front view) of the Spectron L211U Tilt Sensor. The housing shown top right contains two orthogonally mounted sensors.

The sensor transducer consists of an approximately toroidal (but flat on the front and back) shaped high lead-glass Corning Type 0120 vial, vacuum formed around a mandrel coated with a carbon release film. At the bottom of the vial is a damping orifice which controls the fluid response to high frequency motion and vibrations. The platinum contacts lie flush with the glass interior and were plated with platinum black prior to filling with the electrolyte. The electrolyte is methanol with a small concentration of potassium iodide (<.09g/100ml) [Marshall, 2000]. The 556A housing is made of aluminium, finished to MIL spec, and the orthogonally mounted sensors are hermetically sealed in the gyro grade epoxy cement visible in Figure 3.1. The wiring insulation is Space Grade Raychem 55 rather than the standard PVC in accordance with outgassing specifications [PY-SSP-UKC-AD-104]

TIL sensor specifications

Table 3.1 outlines the sensor specifications as provided by the manufacturer on delivery of the sensor.

Manufacturer	Spectron Glass
Sensor Model Number	L211-U
Range	$\pm 60^\circ$
Resolution	30 arc sec
Null Repeat	0.01°
Linearity (1/2 scale)	0.3°
Time constant (at 20°C)	100ms
Null impedance ($\pm 20\%$)	$6\text{k}\Omega$
Operating temperature range	-54° to $+125^\circ$
Housing Model Number	556A
Number of L211U sensors housed	2 mounted orthogonally
Total Mass	25g
Dimensions (housing)	41 x 16 x 18 mm

Table 3.1: TIL sensor specifications [PY-SSP-UKC-AD-104]

TIL on board Huygens

The two orthogonal sensors comprising the SSP TIL sensor on board the Huygens probe are designated TIL-X and TIL-Y. The position of the sensor within the probe is shown in Figure 3.2.

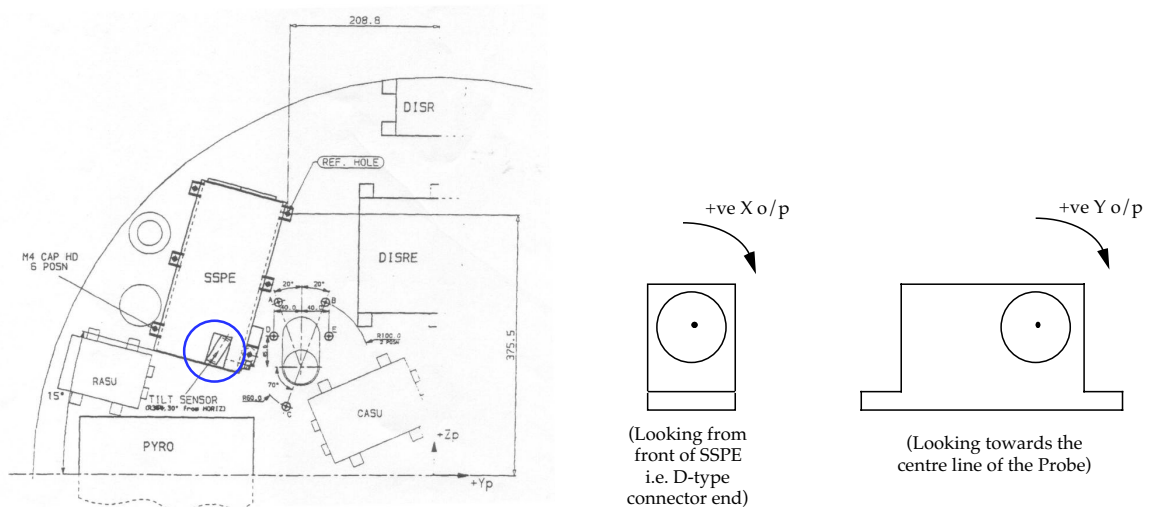


Figure 3.2: TIL positioning on board the Huygens Probe (left) and TIL rotation sense (right)

The sensor is attached to the lid of the SSPE box (see Chapter 1) near the rear of the box. It will be noted that the sensor's internal location within the probe means that temperatures during descent and surface operations will be significantly warmer than those of the Titan environment and calibrations have been performed from -20° to $+60^{\circ}$, well within the sensor's operational range. The sensor is positioned such that the axis of the TIL Y sensor passes through the centre line of the Probe within $\pm 1^{\circ}$ and the TIL X and TIL Y directions are slightly offset from the SSPE unit axes. The sensors are positioned and connected such that a clockwise rotation about the sensor axis (looking at the front of the sensor) gives a positive tilt angle from the electronics [PY-SSP-UKC-AD-104]. The transformation between probe and sensor coordinate systems necessary for the derivation of probe attitude is addressed in Chapter 6.

Electrical interface

Detailed information on the electronic engineering and interface design between the TIL sensor, its electronics and the Huygens probe is summarised in [PY-SSP-UKC-AD-104]. Here discussion is limited to the principles of operation of the TIL sensor, as needed to understand its measurement capabilities during and after Titan descent. One important factor to note however is that the sensor requires square-wave AC excitation. As with all electrolytic tilt sensors a continuous DC voltage would lead to a gradual electroplating of the electrodes thus departing from the initial sensor calibration. Furthermore this could eventually result in irreversible damage to the sensor.

3.2.3 Tiltmeter principle of operation

Whilst the operation of a fluid based tilt sensor as described in the introduction to this chapter may seem straightforward, in predicting the performance of this type of sensor under dynamic conditions it is instructive to review the physical principles behind its operation. In some cases the response to certain dynamic conditions is less than intuitive. This section reviews two key principles of this type of tilt sensor. Firstly how it utilises the fluid surface to indicate inclination, and secondly how it measures this inclination electrically.

Orientation of a fluid surface in relative equilibrium

It is a commonly observed phenomenon that, when at rest, a fluid surface will orient itself horizontally or, more accurately, perpendicular to the local gravity vector. The proof of this can be found in most elementary text books on fluid mechanics, for example Douglas [1985]. The proof actually states that, for any fluid in relative

equilibrium, where shear stresses within the fluid can be neglected, the free surface will lie perpendicular to the resultant vector of all accelerations upon the fluid body.

Figure 3.3 shows a much simplified diagram of the TIL sensor with a body of fluid inside. The sensor, inclined at an angle α to the horizontal, is given an arbitrary acceleration a_s , acting at an angle ϕ to the horizontal as shown. It follows from the fluid mechanics theory of a fluid in relative equilibrium that the angle θ at which the free surface is inclined to the horizontal may be given by

$$\tan\theta = \frac{-a_s \cos\phi}{a_s \sin\phi + g} \quad (3-1)$$

where a_s is an arbitrary acceleration applied to the container, acting at angle ϕ to the horizontal. The TIL sensor measures the angle $(\theta - \alpha)$, that is the inclination of the fluid surface relative to the sensor horizontal, or reference level as shown (this is described further in the following section).

When the sensor is static, or even moving at constant velocity, a_s is zero, θ becomes zero and therefore the TIL sensor measures simply the angle $(\theta - \alpha) = -\alpha$, with the negative sign being a matter of convention. Clearly however the TIL sensor is susceptible to offsets for any non-gravitational acceleration of the sensor housing, as apparent from equation 3-1. This is discussed further in Chapters 5 and 6 when consideration is given to TIL measurements under a more complicated range of dynamic conditions.

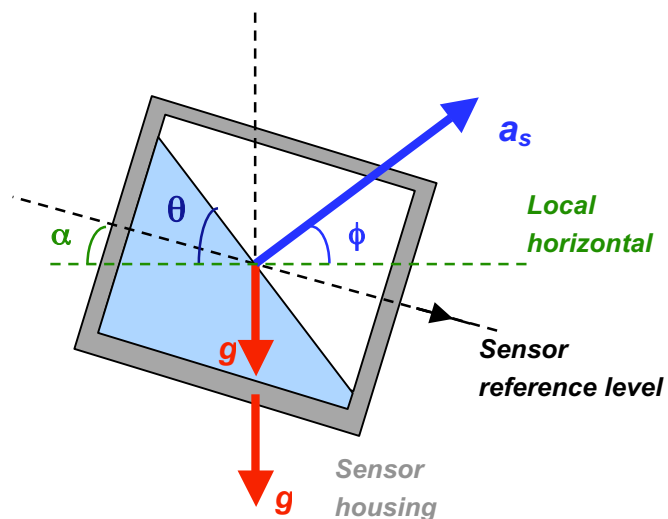


Figure 3.3: Sensor surface inclination for fluid in relative equilibrium

Electrolyte resistive potential divider operation

Figure 3.4 shows another geometrically simplified diagram of the sensor, this time along with an equivalent circuit representation.

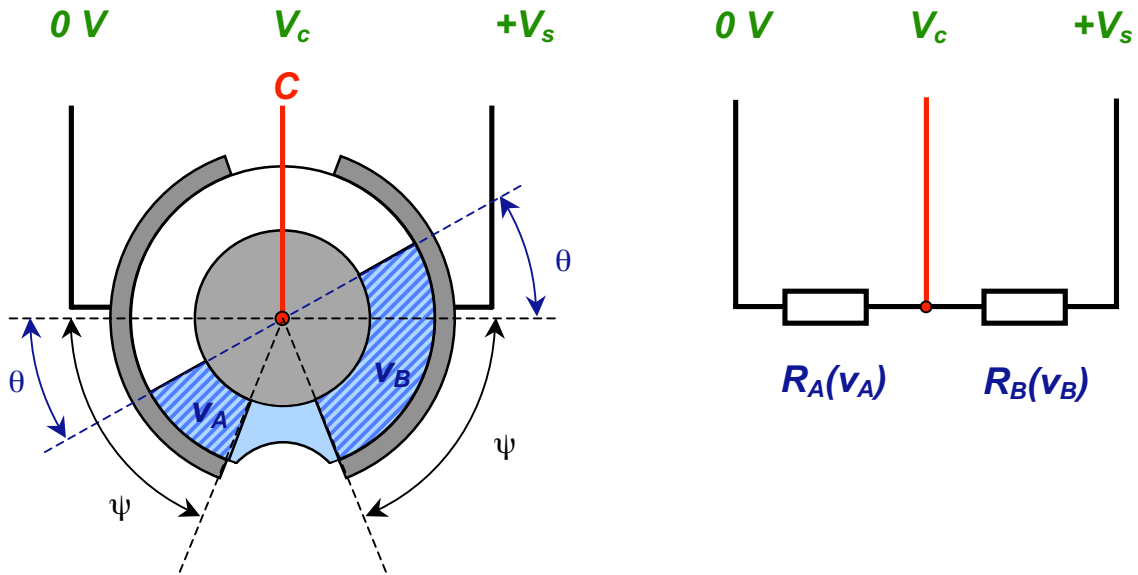


Figure 3.4: Simplified TIL sensor (left) with electrode contacts shown in grey and electrolyte shown in blue. Shaded blue regions show regions of fluid considered in resistance calculation. Also shown (right) is the equivalent circuit representation

As mentioned previously the electrolytic tilt sensor works as a resistive potential divider, with the relative resistances between electrodes A and C, and B and C varying as a function of fluid surface inclination. As also mentioned, the excitation voltage across electrodes A and B must be from an AC source to avoid dissociation effects leading to the electroplating of the contacts, compromising the operation of the sensor. On the Huygens probe this is 5V square wave AC. See [PY-SSP-UKC-AD-104] for further details.

It is possible to show that the V_C variation with angle is approximately linear by considering the volumes of liquid v_A and v_B shown in Figure 3.4. If we assume that the depth of the glass shown two dimensionally in the figure is a constant, d , the electrodes are symmetrical and of identical composition and finish, and that the temperature and conductivity does not vary angularly (for $\theta < \psi$) within the volumes v_A and v_B (even though it may vary radially, [Koryta et al., 1993]), then it is reasonable to assume that the conductances Ω_A and Ω_B , between the centre electrode A and B respectively will vary proportionally with the v_A and v_B , i.e. it is assumed that

$$\Omega_A \propto v_A, \quad \Omega_B \propto v_B \quad (3-2)$$

It is assumed that the central body of fluid in between volumes v_A and v_B contributes equally to Ω_A and Ω_B . The resistances between C and A and B respectively are then given, with k being a constant of proportionality and r_1 and r_2 being inner and outer vial radii, by

$$R_A = \frac{2k}{d(r_2^2 - r_1^2)(\psi - \theta)} \quad R_B = \frac{2k}{d(r_2^2 - r_1^2)(\psi + \theta)} \quad (3-3 \text{ a,b})$$

and V_c is then approximately given by

$$V_c = \frac{V_s}{2} + \frac{V_s}{2\psi}\theta \quad (3-4)$$

i.e. linear variation with angle. It should be noted that the above approximation has assumed no deformation of the fluid surface due to meniscus effects. Unfortunately this and the fact that the conductance will not necessarily vary exactly linearly with v_A and v_B mean that in practice V_c is not completely linear with inclination. Furthermore not only the linearity but the operation of the sensor breaks down at a certain angle as θ increases beyond ψ , and the sensor ceases to act as a potentiometer. These limits to linearity and inclination are represented in the manufacturers specifications.

Signal conditioning devices may adjust the offset and scale factor from the values above, as in some of the experiments described later in this work. However the primary goal of the above derivation is to demonstrate the linearity of the sensor.

Temperature effects will also affect the output of the sensor and whilst the manufacturer also provides specifications on the temperature variation of the sensor scale factors it was necessary to carry out full temperature calibration of the TIL sensor. These results, presented in summary only in the next section, are available in [PY-SSP-UKC-AD-104].

The stability and dynamic response of the sensor are functions of the detailed sensor design (electrodes, contacts, electrolyte fluid parameters). The detailed modelling necessary to confirm the accuracy of the manufacturers specifications is beyond the scope of this thesis, however laboratory based (terrestrial gravity) experimental verification carried out previously is discussed in the next section, before simulations are presented showing the response of the sensor from these values. An experiment that was

carried out to test the true response under reduced gravity conditions is described later in Chapter 5.

3.3 Static Calibrations of the TIL sensor

For several years prior to its launch aboard the Huygens Probe in 1997 the TIL sensor had been the subject of numerous prototype, engineering model and flight acceptance tests and calibrations. Most of these were carried out under static conditions, with the exception of the response time and frequency response measurements described in section 3.4.1. The calibration tests of the flight model included static inclination calibration, vacuum calibration and temperature calibration, in addition to the quality assurance long term charging, EMC and vibration tests. Results from the first three calibration tests are summarised here, with further details being available in [PY-SSP-UKC-AD-104]. The next section then proceeds with a discussion of the dynamic response of the sensor.

3.3.1 Output vs. angle

Measurement axes output

Static calibration of the Flight Model TIL sensor was carried out in 1996 at the University of Kent and again during integration tests in 1997. The sensor output voltages for rotations about the two tilt sensor axes, from -60° to $+60^\circ$, across the temperature range demanded by the design specification are presented in [PY-SSP-UKC-AD-104]. Figure 3.6 shows the sensor outputs for the Flight Model TIL-X and TIL-Y sensors against rotation angle about the measurement axes at 26.5°C , during the 1996 tests. For purposes of clarity Figure 3.5 shows the convention used to define measurement and non-measurement axes for each of the sensors.

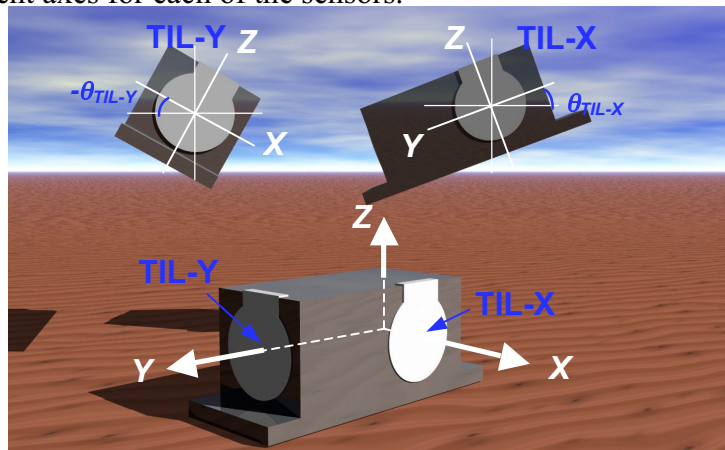


Figure 3.5: TIL sensors and their rotation axes

The Flight Model TIL calibration equations at 26.5°C were found to be [PY-SSP-UKC-AD-104]

$$V_{TIL-X} = [(0.0174 \pm 0.0001) \theta_x + (1.246 \pm 0.001)] V \quad (3-5 a)$$

$$V_{TIL-Y} = [(0.0166 \pm 0.0001) \theta_y + (1.258 \pm 0.001)] V \quad (3-5 b)$$

These calibration equations are for the Flight Model TIL sensor in its flight configuration, interfaced with flight electronics, and are included here both for completeness and to demonstrate the sensor linearity. The scale factors and offsets for the TIL sensors used in the experiments described Chapter 5 differ slightly due to the electrical interface used (see section 4.3.2) There was however no discernible difference in the linearity of the two sensor configurations.

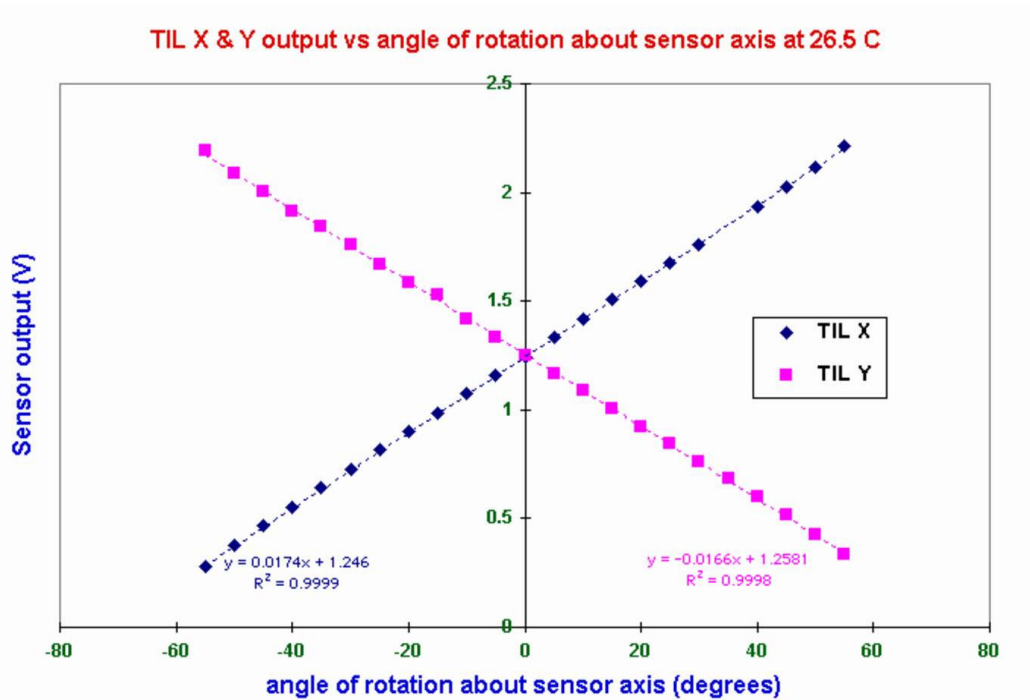


Figure 3.6: TIL-X and TIL-Y outputs against angle of rotation about measurement axes [PY-SSP-UKC-AD-104]

Non-measurement axes output

Calibrations have shown each of the TIL-X and TIL-Y sensors to be reasonably insensitive to inclination about their non-measurement axis. An output of less than $\pm 3\%$ full-scale deflection was measured for inclinations of $\pm 60^\circ$ about the non-measurement axes. However results from later in the thesis show that a useful test that was not performed was the calibration of the sensor about the non-measurement axes whilst the

sensors were simultaneously held at maximum (60°) inclinations about their measurement axes. This would allow a test of the sensor linearity at its extreme inclination of 60° simultaneously about both X and Y axes.

3.3.2 Environmental calibrations

Vacuum response

Vacuum calibration of the TIL sensor was carried out in 1996 prior to delivery of the SSP Flight Model and shows the TIL response to be steady to better than 0.1% during long term vacuum exposure. In any case the TIL sensor will not be required to operate in vacuum and will not be activated, even for cruise checkout tests, until deployment of the main parachute following Titan entry.

Temperature response

The following temperature calibration of the TIL sensor was carried out in 1997 during final testing of the SSP Flight Model [PY-SSP-UKC-AD-104]. The temperature variation of both TIL-X and TIL-Y outputs at several inclinations was tested. The temperatures ranged from -30°C to $+60^\circ\text{C}$ and sensor inclinations ranged from -20° to $+50^\circ$. The tests concluded less than a 0.4% variation in the TIL output across this temperature range. These effects may be considered negligible in the subsequent work of this thesis. Further details of the temperature calibrations for TIL maybe found in [PY-SSP-UKC-AD-104]

3.4 Dynamic response calibrations of the TIL sensor in 1-g

The calibrations reviewed above are sufficient for interpreting the data returned from the TIL sensor on Titan under static conditions (subject to a transformation between the instrument and probe reference axes, as outlined in Chapter 6). Under dynamic conditions however it is necessary to consider two aspects of the sensors performance; (a) an ‘ideal’ response to motion derived from consideration of the equilibrium level of the fluid surface, and (b) its real response.

Equilibrium level of the fluid surface

One the one hand, for any particular type of motion the sensor will be subject to a sequence of accelerations. For any acceleration there will be a relative equilibrium level for the fluid surface, as was described, in the two dimensional case, by equation 3-1. By considering the accelerations associated with the motion sequence, it should therefore be

possible to predict the ‘ideal’ or ‘infinitely fast’ sensor response to the motion that would occur if the sensor had an instantaneous response to varying acceleration. This discussion continues in Chapter 5 where comment is made on TIL measurements made during an aircraft flight, and in more depth in Chapter 6 where an attempt is made at identifying sensor accelerations, and hence corresponding sensor outputs, for a range of possible probe motions.

Real response to disturbance from equilibrium

The second aspect of the TIL sensor performance to be considered is its real dynamic response. It is important to know, in response to a step change in inclination, how quickly the fluid surface adopts its equilibrium level, to what degree the oscillatory motion is damped and the value of the natural frequency of the fluid surface such that any potential resonance arising from probe oscillations may be predicted.

Section 3.4 reviews briefly the dynamic response measurements made in the laboratory with the flight model sensor. Section 3.5 then describes several possible analytical models for predicting how this response may vary under Titan conditions.

3.4.1 Laboratory measurements of the TIL sensor step response

Experiments carried out in 1993, and repeated four years later, investigated the response of the TIL sensor to a step change in inclination. Data from the latter test is currently unavailable, however one of the results graphs available from the previous testing is shown in Figure 3.7 (a) [Brewster, 1991].

The step change was actuated over a 50ms period. The response time in Brewster [1991] is defined as the time lag between the actuator reaching final inclination, and the peak of the overshoot of the fluid surface. Results from several measurements concluded a time lag of (75 ± 2) ms. Figure 3.7 (b) shows the same results approximated in MATLAB by a damped oscillator model with time constant τ (defined more conventionally as the time taken for the amplitude of the oscillations to decay to within $1/e$ of their final value) and natural angular frequency ω_0 . The model suggests experimental values for the TIL sensor of

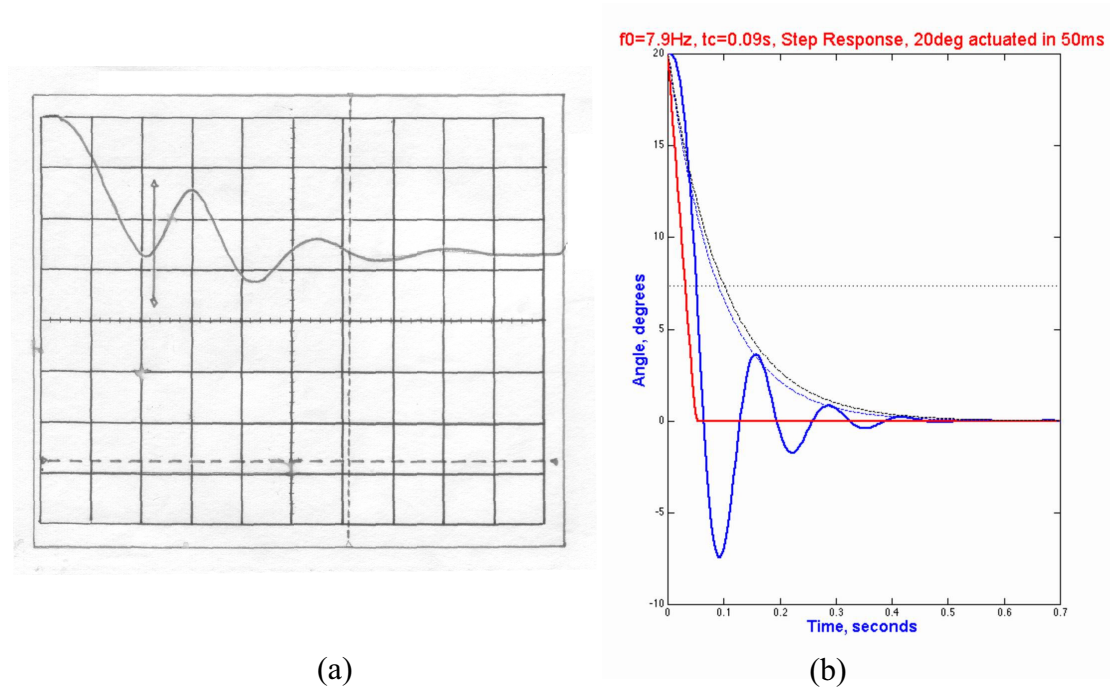


**Figure 3.7: (a) Laboratory-based Measurement of the TIL sensor response time [Brewster, 1991]
 (b) Model fitted to data, actuator position marked in red, TIL output marked in solid blue.
 Dashed blue and black lines are observed and manufacturer's exponential decay.**

$$\tau_{\text{expt}} = (0.09 \pm 0.02) \text{ s and } \omega_{0\text{expt}} = (49.5 \pm 2) \text{ rad s}^{-1} \quad (3-7 \text{ a, b})$$

This gives a natural frequency of approximately (7.9 ± 0.3) Hz with errors being a consequence of the fit of the model. The manufacturer specifies a TIL sensor time constant of

$$\tau_{\text{manufact}} = 0.1 \text{ s} \pm 25\% \quad (3-8)$$

by using a step input of approximately 5 degrees initiated using a relay that actuates in 10ms [Marshall, 2000]. The experimental results are consistent with the manufacturer's specifications.

3.4.2 Simulation of the TIL sensor response from the laboratory measurements

Figure 3.8 (a) shows the response to Gaussian-shaped angular variations with bandwidths (FWHM) of 50ms, 100ms, and 400ms. Figure 3.8 (b) shows the response to sinusoidal variations at 0.5Hz, 2 Hz, and 4Hz. It is assumed here that all rotations occur about the sensor axis, thereby avoiding any linear acceleration on the sensor fluid. Such accelerations will be considered later.

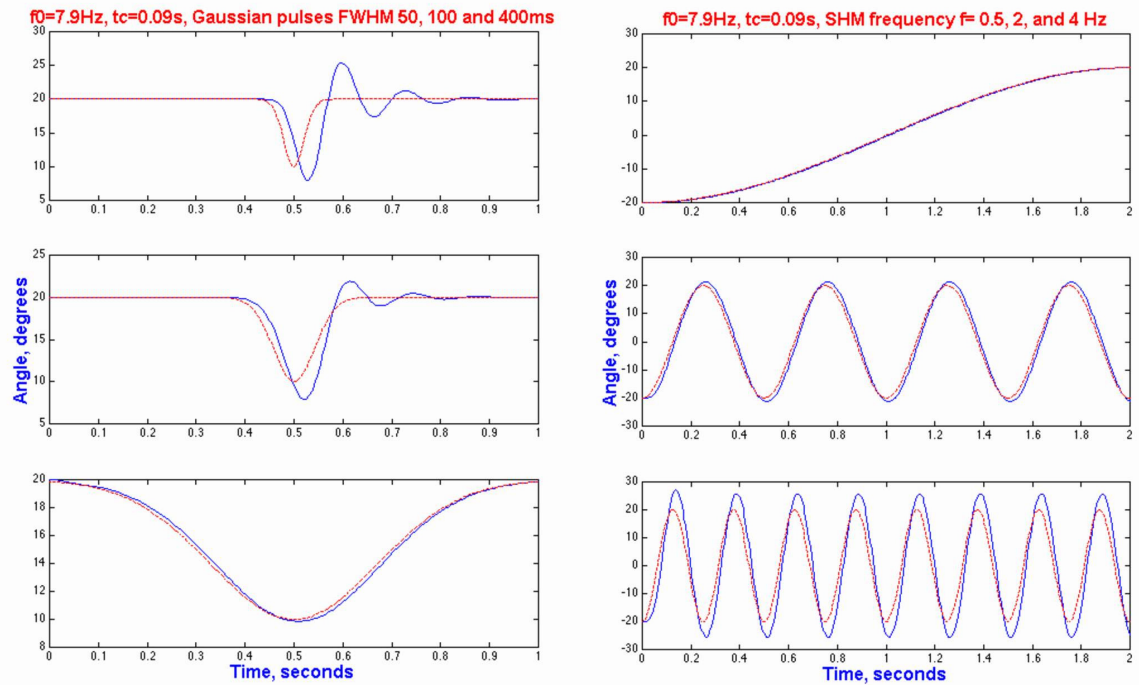


Figure 3.8: Modelled TIL fluid response (in MATLAB), using ω_0 and τ as specified in eqn 3-7, to (a) gaussian angular variations and (b) simple harmonic angular motion about the sensor measurement axis. Terrestrial gravity assumed.

For harmonic motion the theoretical phase lag, ϕ , between the sensor output and the driving motion may be given by

$$\phi = \arctan \left[\frac{\tau (\omega_{shm}^2 - \omega_0^2)}{2\omega_{shm}} \right] + \frac{\pi}{2} \quad (3-9)$$

where ω_{shm} is the angular frequency of the driving motion. Figure 3.9 graphs the amplitude and time lag (ϕ / ω_{shm}) of the sensor, again assuming the values for ω_0 and τ of equations 3-7 a & b.

The phase and amplitude increases are clearly visible as ω_{shm} approaches that of ω_0 . Concerns will of course be raised that such probe oscillations close to the natural frequency could give rise to a resonant peak in the amplitude of the sensor fluid motion. Whilst such motion is not damaging to the sensor it would complicate the accurate measurement of attitude. It will be seen however that such frequencies are above those likely to be experienced by the probe on Titan. This important issue is discussed further in Chapter 6.

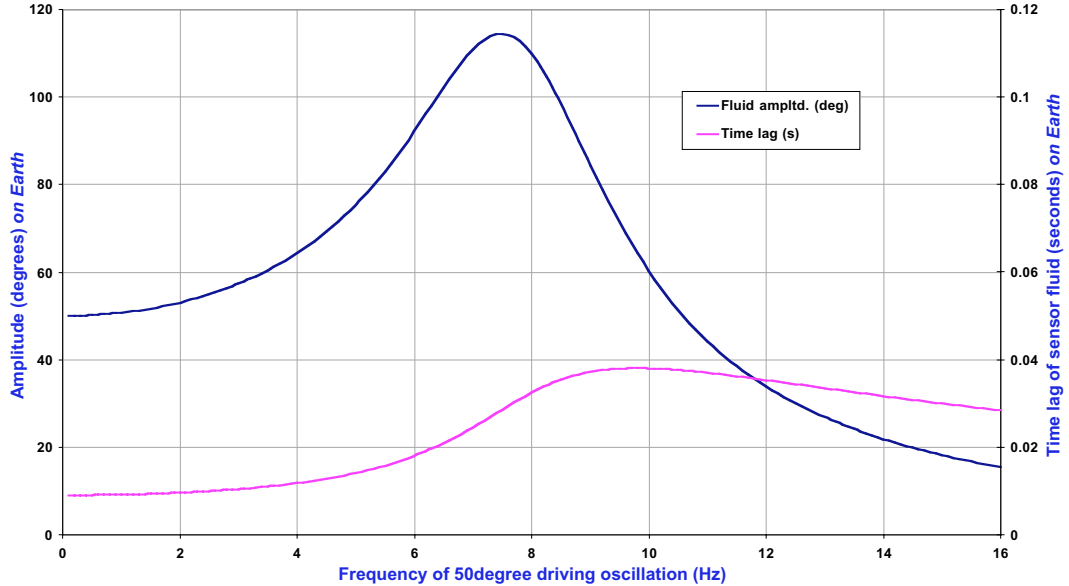


Figure 3.9: Modelled TIL fluid amplitude (°) and time lag (s) against frequency of oscillatory motion, again about the sensor measurement axes. Terrestrial gravity assumed.

3.5 Predicting the dynamic response under Titan gravity

3.5.1 Modelling the TIL sensor fluid response and its variation with gravity

The previous section has characterised the response of the sensor fluid surface when disturbed from its equilibrium orientation, however the experimentally determined values for ω_0 and τ were obtained under specific conditions that will be the same on Titan. These two parameters are no doubt functions of the sensor's internal geometry and surface finishes, and will certainly vary with fluid parameters such as viscosity and surface tension, which are in turn functions of temperature and pressure. Perhaps most significantly however, by the very nature of the sensor's operational principles, i.e. the tendency of the fluid to orient itself perpendicular to the local acceleration, gravity will be a key factor.

The internal geometry and surface finish of the sensor will of course not change, and no deterioration of the sensor structure is expected over the course of the journey to Titan. Since the sensor is hermetically sealed, pressure is also unlikely to be a significant factor. The temperature of the fluid, however, will vary as the internal probe temperature varies on Titan. Whilst section 3.3 has shown that the actual measured static sensor output does not vary significantly with temperature, this yields little information about

the change in the fluid parameters since the calibration was performed under static conditions. Experiments have not yet been carried out to clarify how the sensors response time varies across the operational temperature range of the sensor, and this is an area that would benefit from further calibration. The manufacturer's specifications suggest that the response time will not vary more than $\pm 25\%$ (the accuracy to which the response time is given) over the temperature range -40° to $+80^\circ$ and therefore, for the likely internal probe temperatures over the course of the mission, such effects are not considered further in this work.

The dominant factor therefore is the reduced level of gravitational acceleration on Titan, and it is necessary to take this into account when estimating the response of the sensor to probe dynamics. Such effects will be two fold, as previously mentioned. Firstly the ratio of magnitudes of non-gravitational acceleration to gravitational acceleration on the sensor increase, and therefore the relative equilibrium inclination of the fluid surface will change. A horizontal acceleration on the sensor housing would lead to a greater equilibrium inclination for the fluid surface on Titan than the same horizontal acceleration would on Earth. This is especially significant for spin effects, as discussed in Chapters 5 and 6, and also for other probe motions as shown in Chapter 6.

Secondly since gravity is the restoring force that acts upon the fluid body when disturbed from its position in relative equilibrium the natural frequency and therefore the step response will also vary on Titan. Several theoretical approximations may be used to estimate this effect, although limitations exist for each. Figure 3.10 shows some examples.

Standing surface wave

Figure 3.10(a) greatly simplifies the shape of the fluid vial, assuming a square box of width d housing a fluid of depth h , density ρ , surface tension σ , and viscosity ν . This example approximates the fluid surface motion with the basic sloshing mode ($k=\pi/d$) solution of the linearised, finite depth, gravity-capillary wave equations with zero normal velocity on the boundaries. Such a model is relatively simple for large containers however with the outer radius of the sensor vial being only 5.5mm [Brewster, 1991] in radius this is very much in the regime of capillary waves where surface tension and viscous effects become more significant. Damping occurs due to boundary layers that form at the bottom and side walls, as well as internal dissipative mechanisms similar to those described in Chapter 2 for surface waves on Titan [Srokosz, 2000]. Lighthill [1978] deals with dissipation due to the bottom wall, and the internal dissipation, but not

the side wall and meniscus effects. The fluid surface frequency, ω , and proportional amplitude loss per wave period, are then given by

$$\omega = \left[\left(g + \frac{\sigma k^2}{\rho} \right) k \tanh(kh) \right]^{1/2} \left[1 - \frac{(\nu / 2\omega)^{1/2}}{\sinh(2kh)} \right] \quad (3-10)$$

$$L = \left(\frac{2\pi(\nu / 2\omega)^{1/2} k}{\sinh(2kh)} + \frac{8\pi\nu k^2}{\omega} \right) \quad (3-11)$$

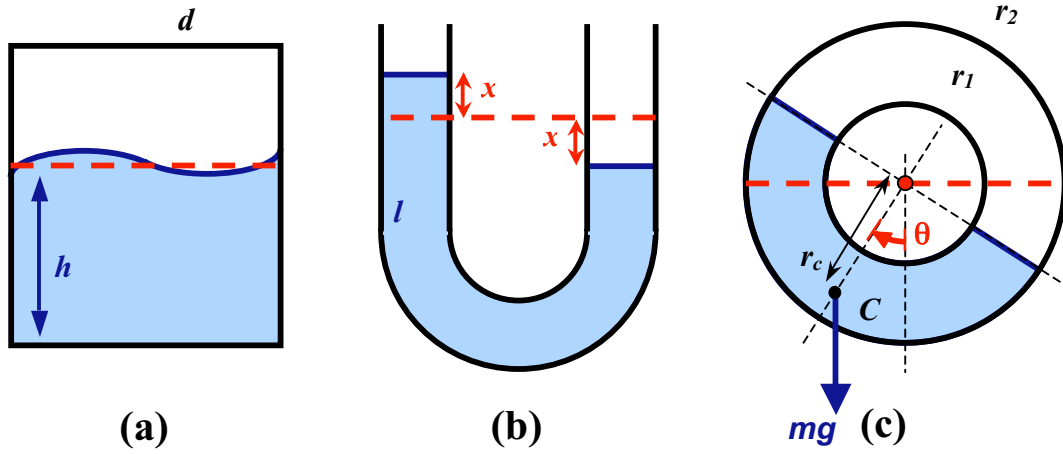


Figure 3.10: Models used in estimating the gravitational variation of the TIL fluid response time
(a) surface wave with $\lambda = d$ atop fluid of depth h , (b) fixed length l of fluid in a U-tube of constant cross section, and (c) semi-torus of fluid, mass m , inner and outer radii r_1 and r_2 .

As far as this discussion is concerned, most important to note is that, for low viscosities, ω has a dependence upon gravity of the form

$$\omega \propto (ag + b)^{1/2} \quad (3-12)$$

where a and b are constants for constant ν and σ . The time constant τ , as defined in section 3.4 is calculated from L as

$$\tau = \frac{2\pi}{\omega \ln(L-1)} \quad (3-13)$$

and is seen to be independent of g .

This model offers some useful insights into the behaviour of the fluid, however the geometry is too significant a departure from the actual geometry of the TIL sensor vial. The wave equations are also intended for small oscillations, and given the sensor range this is too restrictive. Nevertheless it is interesting to compare the g -dependency of ω with that of the other models.

U-tube fluid

Figure 3.10(b) shows the U-tube fluid model, with the equilibrium fluid level indicated by the red dashed line. The equation of motion for the displacements of the fluid arms above and below the equilibrium level is given in equation 3-14, where ρ is the fluid density, l is the length of the fluid in the tube, and k_2 a damping constant which will depend upon the boundary layer effects at the tube walls and other surface tension and viscous dissipation mechanisms. As shown with the previous model, these effects may be assumed to be independent of g .

$$\rho l \frac{d^2x}{dt^2} + k_2 \frac{dx}{dt} + 2\rho g x = 0 \quad (3-14)$$

Here the natural and damped frequencies, ω_0 , ω_d and time constant, τ , of the oscillations are given by

$$\omega_0 = \left(\frac{2g}{l} \right)^{1/2} \quad \omega_d = \left[\frac{2g}{l} - \left(\frac{k_2}{2\rho l} \right)^2 \right]^{1/2} \quad \tau = \frac{2\rho l}{k_2} \quad (3-15)$$

Whilst this model also departs geometrically from the TIL sensor fluid vial, it does represent the movement of the fluid body as a whole more accurately. The model also suggests proportionality between ω_0 and $g^{1/2}$, and τ independent of g .

Semi-torus fluid mass

This model treats the body of fluid as a semi-torus, as shown in Figure 3.10(c) where the red dashed line indicates the equilibrium level of the fluid. The torus is geometrically a close approximation to the sensor vial shape, except for the flat sides and damping orifice shown in Figure 3.1. The equation of motion, that of a rigid pendulum, may be estimated as

$$I \frac{d^2\theta}{dt^2} + k_2 \frac{d\theta}{dt} + mgr_c\theta = 0 \quad (3-16)$$

where r_c is the radial distance of the centre of mass, m the mass of the fluid, and I the moment of inertia of the semi-torus with inner and outer radii r_1 and r_2 . Again the damping constant k_2 will depend upon the boundary layer effects at the walls of the vial and other surface tension and viscous dissipation mechanisms, and is independent of g . The natural and damped frequencies, ω_0 , ω_d and time constant, τ , of the oscillations may then be given by

$$\omega_0 = \left(\frac{mgr_c}{I} \right)^{1/2} \quad \omega_d = \left[\frac{mgr_c}{I} - \left(\frac{k_2}{2I} \right)^2 \right]^{1/2} \quad \tau = \frac{2I}{k_2} \quad (3-17)$$

This model, perhaps the best representation of the movement of the TIL sensor fluid body so far, again suggests proportionality between ω_0 and $g^{1/2}$, and τ independent of g . It should also be possible to estimate a value for ω_0 from the above expression since the I and r_c and m can all be calculated from r_1 , r_2 and ρ for the fluid. However it is not possible to calculate k_2 without more information.

Considering the three models described above it is therefore reasonable to assume a $g^{1/2}$ dependency for ω_0 , τ independent of g , and a g -dependency for ω_d of the form $(ag+b)^{1/2}$ where a and b are constant for given values of v and σ . Computational fluid dynamic (CFD) methods would allow a more detailed and accurate modelling of the specific sensor geometry as well as taking into account the fluid viscosity and surface tension. The necessary time and resources however were beyond those available for this work, and since experimental verification, as described in the next section, was to be undertaken in any case, it was decided that such modelling need only be attempted if the observed results departed significantly from the aforementioned dependency.

3.5.2 Estimating the TIL response time on Titan

Following the discussion of the previous section, the experimentally determined values for ω_0 and τ shown in equation 3-7 are assumed for the TIL sensor under terrestrial gravity. On Titan, assuming the fluid surface tension and viscosity do not change over the predicted internal probe temperature ranges, these values then become

$$\tau_{(T)} = (0.09 \pm 0.02) \text{ s} \quad \text{and} \quad \omega_{0(T)} = (18 \pm 2) \text{ rad s}^{-1} \quad (3-18)$$

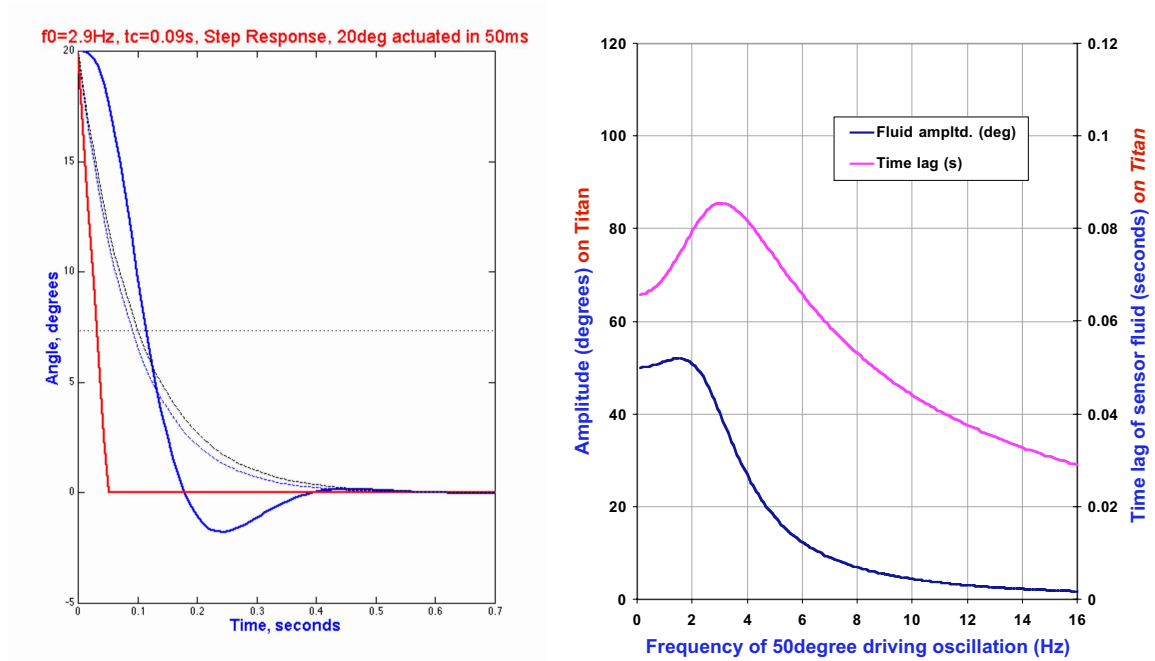


Figure 3.11: (a) Step response (b) Frequency response of TIL sensor fluid under Titan gravity, g_T . Compare these with the graphs shown in Figures 3.7 and 3.9 for the same sensor under terrestrial gravity. Red indicates equilibrium position, blue represents TIL response.

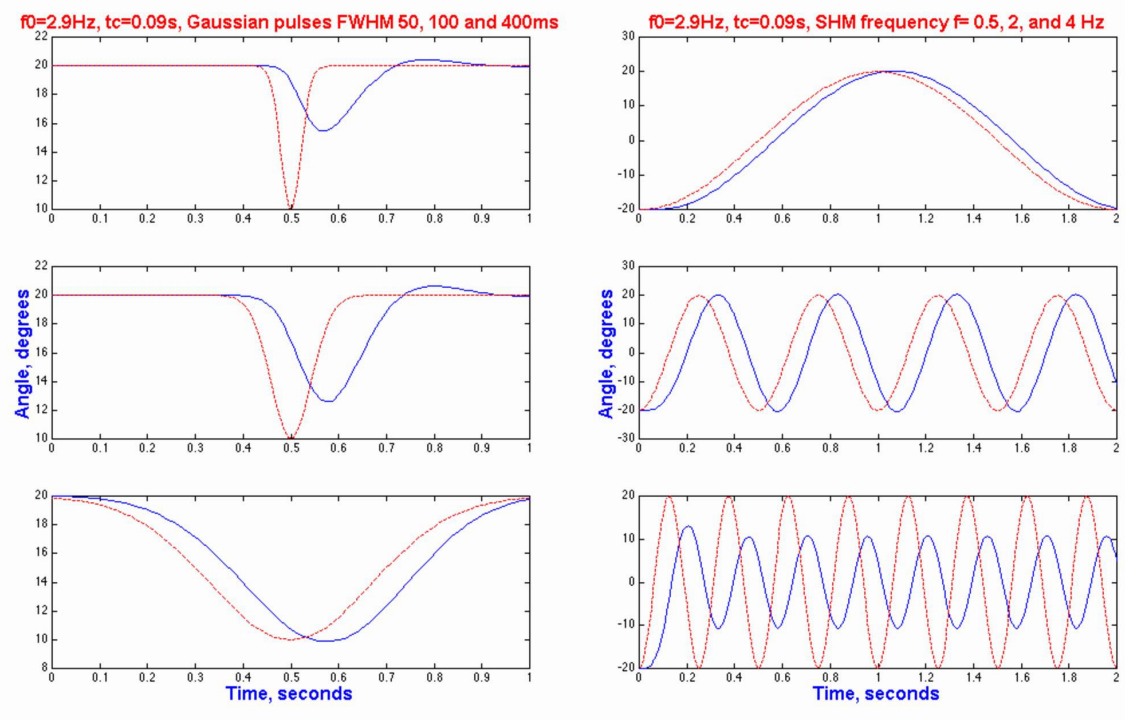


Figure 3.12: (a) time response to gaussian pulse (b) time response to harmonic motion of TIL sensor fluid under Titan gravity, g_T . Compare these with the terrestrial graphs of Figure 3.8. Again red indicates equilibrium position, blue represents TIL response.

Figures 3.11 and 3.12 show the predicted responses to the inputs of section 3.4.2 under Titan gravity.

The specified errors in equation 3-18 will of course increase with any variation of the fluid parameters with temperature. This is an area left to future modelling, perhaps being linked with any CFD analysis of the sensor fluid. However for the relatively slow probe motions expected during the parachute descent on Titan these values are considered to be sufficiently accurate, as discussed in Chapter 6.

Thus the theory, based upon experimentally determined parameters, has been presented for the motion of the fluid within the TIL sensor in response to disturbance from its relative equilibrium orientation. The theory of this relative equilibrium orientation was presented in section 3.2.3 and is applied to theoretical probe motions in Chapter 6.

Before this, chapters 4 and 5 will focus on the design and implementation of an experiment platform for testing the response modelled in this chapter, as well as offering a test of the general performance under real dynamic conditions. Two experiments are described; a reduced gravity flight, and a spin table test, as well as qualitative results from a pendulum-type swing test. Comparison with the above response theory, and consideration of how well motion was reconstructed in each case will then be presented at the end of each investigation.

3.6 HASI

The next chapter will describe an experimental platform designed to allow testing of the TIL and HASI-ACC sensors simultaneously under a range of real dynamic sequences. The sensors are also to be used together in several experiments currently being planned, as mentioned briefly at the end of the thesis. Therefore a quick review is useful of the sensor, its principle of operation, and some existing calibration.

The HASI-ACC sensor suite forms one of four instrument packages that comprise the overall HASI instrument. The accelerometers making up the HASI-ACC suite are three orthogonally mounted piezoresistive accelerometers, each sensitive to acceleration in one of the probe x , y , and z axes, and one servo accelerometer measuring accelerations along the probe's x , or spin, axis. [Fulchignoni et al., 1997]. The measurement specifications of the accelerometers onboard Huygens were given in Table 1.2.

The piezoresistive (PZR) accelerometers consist of a silicon seismic test mass suspended between two strain-dependent resistances. Acceleration of the unit generates a force between the test mass and the resistive elements, and the resulting strain changes their resistances [Fulchignoni, 1997] allowing direct acceleration measurement. These sensors are typical cheap and offer a wide range of measurement. They do however suffer from large temperature drifts and a temperature sensor is incorporated on HASI to account for this.

The servo accelerometer consists also of a seismic mass and a reference plate. A detector senses deviations of the mass from its reference position due to accelerations on the housing, and servo circuitry acts to restore this position by the application of an electromagnetic force. The current consumed by the electromagnet is directly proportional to the force required and is thus a measure of the housing acceleration. Compared with the PZR accelerometers the servo accelerometer output varies very little with temperature, offers good resolution with little noise, suffers less from non-linearity effects, and exhibits high repeatability [Patel et al., 1999]. Unsurprisingly such sensors tend to be much more expensive and heavy than their PZR counterparts.

Calibration of the flight model of the HASI-ACC sensor was carried out prior to delivery in 1997. Interesting wind velocity tests were also carried out using a flight spare model of the HASI-ACC instrument at the University of Kent in 1999 [Patel et al., 1999]. A custom housing for the sensor was built for the experiment and this assembly was also used in the experiments of this work. For the purposes of these experiments however, only the servo sensor was used, while the wind experiment employed both servo and PZR sensors. Two channels, high and low gain, are available with HASI-ACC servo sensor on the Huygens probe, as shown in Table 1.2. The wind velocity experiment also used two channels, but with gain settings of x1 and x4. The gain settings used in the subsequent experiments of this work were unchanged from these values, although as discussed in section 5.4.2, following the failure of one of the channels and saturation of the other channel, it is recommended that future experiments carefully tailor these settings.

Patel et al.[1999] gives calibration settings of the HASI-ACC sensor in its wind velocity experiment configuration as

$$V_{accx1} = [(0.252 \pm 0.001) a + (1.305 \pm 0.002)] V \quad (3-19)$$

$$V_{accx4} = [(0.985 \pm 0.002) a + (1.314 \pm 0.003)] V \quad (3-20)$$

where a is the acceleration along the measurement axes of the sensor. The report also confirms that V_{accx1} and V_{accx4} may both be considered temperature independent between -20°C and $+40^{\circ}\text{C}$. For further details of the HASI-ACC wind velocity experiment and the sensor electronics the reader is referred to Patel et al.[1993].

Finally, before proceeding with the description of the dynamic calibration platform, it is instructive to review the measurement that is actually being made by the accelerometer. This is helpful both for the interpretation of measurements and also in the modelling of predicted outputs of the sensor for simulated probe motions. Figure 3.13 shows a simplified schematic of the servo accelerometer.

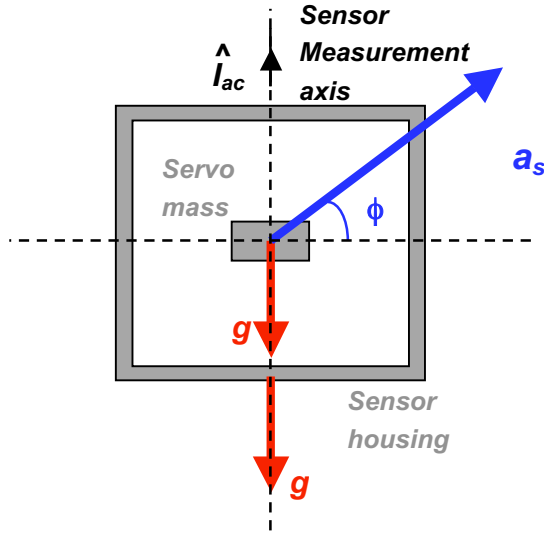


Figure 3.13: Schematic of the HASI accelerometer showing measured accelerations

As mentioned earlier the servo accelerometer measures the relative acceleration between the sensor mass and the sensor housing, and, since both experience gravitational acceleration, the sensor actually measures all non-gravitational accelerations. If a_s is the resultant of all non-gravitational forces acting upon the sensor housing, and I_{acc} is the unit vector along the measurement axes in the direction shown, then the acceleration measured by the sensor, S_{acc} is

$$S_{acc} = -\mathbf{a}_s \cdot \mathbf{I}_{acc} \quad (3-21)$$

Therefore, when the accelerometer sits atop a flat surface, \mathbf{a}_s is that due to the normal force $-m\mathbf{g}$ exerted by the table on the sensor housing, and $S_{acc} = g$. When the sensor is in vertical freefall (with no atmospheric drag) S_{acc} is zero, and when vertical drag \mathbf{D} exists $S_{acc} = D$. When the sensor is at rest upon a surface inclined at angle α , \mathbf{a}_s is due to the

sum of the normal force exerted by the table and the force due to friction, and $S_{acc} = g\cos\theta$. For the sensor acting as a pendulum mass the force (neglecting damping) arises due to tension and again $S_{acc} = g\cos\theta$.

These examples are intuitive, however in Chapter 4 consideration is given to a range of forces acting upon the probe and equation 3-21 is useful in quickly clarifying those measurable by the ACC sensor. This ‘return to first principles’ was found to be surprisingly helpful in the case of both ACC and TIL sensors.

Chapter 4

Design of a TIL and HASI-ACC Portable Dynamic Calibration Platform

4.1 Introduction: The need for a portable dynamic calibration platform

The previous chapter describes the static and environmental temperature and pressure response of the TIL sensor, and experimental values have been obtained for its natural frequency and time constant under carefully controlled laboratory conditions. This then permits theoretical estimation of the TIL output in response to any known orientation or motion through consideration of the particular forces acting on the sensor, as performed in Chapter 6.

Very little practical calibration, however, has been carried out to test the performance of the sensor under such dynamic conditions. As discussed in Chapter 1, several Huygens probe instrument teams have cited the TIL and HASI-ACC measurements as contributing to the interpretation of their expected data sets [Atkinson, 1998], and it has therefore become increasingly important to investigate the real-life performance of both instruments, preferably operating together as will be the case onboard Huygens. Such testing not only permits evaluation of the accuracy of any theoretical sensor models constructed, but also provides a unique opportunity for investigating the true quality of motion reconstruction possible using the sensors together, in an environment of electrical noise, mechanical noise, and other environmental fluctuations such as pressure, temperature and even gravity. Limitations imposed by data handling constraints (such as sampling rate and resolution) could also be highlighted.

Ideally such experimental verification would involve testing of the full sensor suite in flight configuration under Titan representative conditions (pressure, temperature, atmospheric density, gravity) over the full range of motions predicted during the Titan descent and landing. Full coverage of such dynamics would suggest a parachute drop test or a balloon flight to simulate descent dynamics, motion on a static surface (simulating the sliding of the probe down an incline, for example) and motion atop a sea or lake surface.

Unfortunately the financing, logistic and programmatic aspects associated with such endeavours are far from straightforward and very few of these opportunities may be available prior to the arrival of Huygens at Titan. Clearly calibration of the TIL sensor cannot rely solely on the success of such experiments however, and therefore an independent, inevitably lower cost, calibration programme must run in parallel to test the response under controlled conditions that approximate aspects of the probe dynamics. Possible experiments could include the testing of the sensor's response to (a) controlled motions under action of reduced gravity, (b) spin testing featuring a moveable spin axis, (c) linear acceleration testing, (d) swing testing and precession testing. It would also be instructive to subject the sensor to measured, but less regular, motions, and investigate how much information may be derived about the motions from the sensor's output. Any results from such lower cost testing will of course be beneficial prior to the larger scale multi-instrument team tests as and when they arise. A general-purpose portable solution housing sensors, power, data recording and inbuilt attitude control, allowing testing of sensors in unison under a range of conditions was thus identified as being a useful tool.

In 1998 however development was truly catalysed by the announcement of a simple low cost reduced-gravity parabolic flight opportunity [Ghafoor et al, 1999]. The flight would be smaller in scale than a full blown microgravity flight aboard a NASA KC-135, ESA Caravelle or the more recent ESA A300 Zero-G jet [Vago, 1998], using instead a significantly smaller single turbo-propellor powered aircraft, and therefore limiting the periods of reduced gravity periods to several seconds per parabola. On the other hand, the flight itself would be available for next to no cost, and still offered the chance of testing the TIL sensor response under Titan level ($1/7^{\text{th}}$) gravity. In addition it would offer an interesting dynamic environment in which the TIL and HASI-ACC sensor outputs could be investigated, and any platform built for this experiment could be used in future for other dynamic tests.

Consequently a set of requirements were defined for a *portable dynamic calibration platform*. It should perhaps be noted at this point that the initial flight opportunity arose at the last minute, and the time available from concept to delivery was approximately one month. A first design for the platform, whilst tested successfully in the laboratory and on the ground at the remote location, in fact malfunctioned during flight, with the noisy electromagnetic environment of the aircraft being suspected as the cause. Following this initial failure, and benefiting from a longer development and test phase, a more robust solution was constructed, and this is the solution presented in this work. Substantial engineering improvements were made to the platform, however some of the core experiment principles and platform components do have heritage in the rapidly conceived earlier experiment, and subsequent consideration highlights a number of alternative design decisions that could have been made. Nevertheless a successful re-flight was performed in 1999, a year on from the initial flight opportunity.

The parabolic flight opportunity is described briefly first in section 4.2. The section then proceeds with a definition of the platform requirements derived largely in response to the opportunity. The final platform design methodology is then described in depth in section 4.3, with details of the actual experiment reserved until Chapter 5.

4.2 Platform Requirements

4.2.1 Parabolic flight experiment opportunity

As mentioned in the introduction, the development of the dynamic calibration platform was largely catalysed by news of an initial flight opportunity during a week long course in 1998, organized by Terre & Espace, a manned spaceflight education and outreach organisation based in Castres, France, in conjunction with ENSICA one of the largest French aerospace schools, based in Toulouse. The course was designed primarily with students in mind, and aimed to provide education on a wide range of issues relating to manned spaceflight. As part of this education students would be offered the opportunity to experience sensations of weightlessness during a sub-aqua dive in a neutral buoyancy tank and a series of parabolic flights. Continuing the educational theme of the course, students were asked to suggest experiments that would benefit from the reduced-gravity environment and it was in response to this that Ms. Jane Goldsworthy, a University of Kent postgraduate student enrolled on the course, approached the Huygens Surface Science Package team with news of the opportunity. Contact with the organisers of the course was subsequently established and further details were provided, as summarised in

Table 4.1. Some of the details below were only confirmed upon arrival at Castres prior to the reflight.

	Robin DR400	Cap-10B	<i>Notes / impact on experiment design</i>
Date of initial announcement	SUMMER 1998		(first flight opportunity)
Date of initial flight opportunity	4 weeks after announcement		4 weeks to design, assemble, test & deliver
Aircraft description	Single turbo-prop, 180bhp, 4 seats	Single turbo-prop, 200bhp, 2 seats	Greater power results in longer, stabler parabolas
Flight profile	Parabolic trajectory offering reduced gravity simulation		
Lowest g-level attainable & duration	~ 6 sec, ~ 0.1 g	~ 6 – 10 sec, <0.1g	
Number of parabolas	Approximately 20 – 30, time & weather permitting		
Seat allocation	Pilot + co-pilot + 2 rear passengers side by side	Pilot + co-pilot / passenger, side by side	Co-pilot / 2 nd passenger can video g-meter & a/c instruments
Space available on aircraft for equipment	Floor, 2 nd passenger seat, large rear shelf	Floor, small rear shelf	Space required for battery pack & calibration platform
Flight recorder onboard?	No	No	Would provide reliable pitch, roll, airspeed & g-level data

Table 4.1: Details of experiment opportunity assuming flight on either Robin DR400 or Captan B aircraft [Gourinat, 1998]

As seen from the table, two aircraft options were offered, with a small possibility of a Cessna 182 being a third. Photographs of the Robin and the Captan are shown in Figure 4.1. Unfortunately flights aboard the Cessna and Cap-10B could not be guaranteed until closer to the flight date due to aircraft and pilot availability. Aside from this uncertainty the primary trade-off in aircraft selection was one of engine power versus cabin space. The theory of parabolic flight is discussed further in the next chapter but in general, the more powerful the aircraft the longer the parabola and hence longer the duration of reduced gravity. In addition the more powerful the aircraft the lower the gravity level attainable.



Figure 4.1: (a) Robin DR400 (b) Cap-10B

The Cap-10B is an extremely well established aerobatic trainer, and initially it seemed that this more powerful aircraft would be favourable, however upon first-hand inspection of the aircraft it became clear that the Robin DR400 offered far greater flexibility in allowing a third passenger in addition to more room for the experiment and support equipment while still providing 6 seconds of reduced gravity. The aircraft was selected and the running of the experiment is described later in Chapter 5.

4.2.2 Objectives of the Dynamic Calibration Platform

In response to the announcement of the flight opportunity the following primary and secondary experimental goals were identified to satisfy the outstanding calibration requirements highlighted during meetings of the DTWG [Atkinson, 1998], with particular focus on the TIL instrument.

- **Primary objectives**

- a) Examine the response of the tiltmeter under real conditions, in particular measuring the response time of the sensor as defined in Section 3.4.
- b) Investigate how this response time varies with gravity

- **Secondary objectives**

- a) Investigate the performance of the ACC sensors under real conditions
- b) Test the correlation between ACC and TIL sensor measurements
- c) Investigate the degree to which, from the ACC and TIL measurements alone, general motions can be reconstructed
- d) Where problems or limitations are discovered in such reconstruction, identify the additional information required and ascertain whether this will be available from other instruments onboard the Huygens probe

4.2.3 Dynamic Calibration Platform System Requirements

From the primary and secondary goals listed above, and the details of the flight opportunity described in Table 4.1, it was possible to define a more detailed set of requirements for the experiment. These are listed below, and it was primarily from these that the design of the TIL and ACC Calibration Platform was derived.

- a) Primary TIL sensor as close as possible in design to that flown on the Huygens probe
- b) Signal conditioning unit (MUPI) required to convert AC TIL output into measurable DC signal
- c) Analogue to Digital Converter to allow data recording
- d) Common housing for as many of the individual experiment components as possible in the interests of experiment portability
- e) Laptop computer to provide portable experiment control and data acquisition
- f) Portable power supply to provide the necessary input voltages for experiment components without relying upon mains power, thus incorporating batteries, power regulation and power distribution components.

At this point, an experiment defined by the above requirements alone is merely a portable tilt sensor and data recording system. To measure the response of the sensor a known change in orientation of the primary TIL sensor had to be applied, for example a step or well characterized continuous motion, against which the primary TIL sensor output could be compared.

- g) Motion generation system to apply to the primary TIL sensor a known motion, calibrated relative to a particular reference frame. For portability it would be desirable to incorporate this into the common housing, also providing a convenient reference frame. Preferably such a system should have the versatility to provide a range of motions, and ideally be capable of simulating motions analogous to those expected for the Huygens probe upon arrival at Titan
- h) Positional feedback within motion generation system, providing the actual position of the primary TIL sensor such that a comparison can be made against

its measured position, and an evaluation be made of the sensor response, a primary goal outlined in the previous section. It will be shown that the available data recording system at the time of the experiment necessitated certain design decisions concerning the way this was achieved, and this is highlighted as an area requiring improvement in section 5.3.9.

- i) Secondary, fixed tilt sensor (experiment control) The primary TIL sensor was to be evaluated on how well it measured a known motion relative to the experiment housing yet the sensor itself measured orientation relative to the local horizontal (as explained in chapter 3). It would therefore be necessary to know the orientation of the housing reference frame, relative to the local horizontal, a second tiltmeter (measuring tilt in two orthogonal directions) being needed for this purpose. This would also offer an additional TIL data set to compare with that obtained using the primary TIL sensor.

- j) G-Level measurement In order to evaluate the response time of the tilt sensor under reduced gravity conditions it is obviously necessary to measure the ‘effective’ gravitational acceleration (discussed in the next chapter) experienced by the sensors. Assuming the platform does not move relative to the aircraft body the g -level measured by a g -meter onboard the aircraft would be sufficient for this purpose. Unfortunately no integral g -meter was available onboard any of the low cost flights offered and therefore it was necessary to rely upon the simple yet less accurate system of a “mass-and-spring meter”. This is described further in section 5.3.3 of the next chapter.

- k) HASI-ACC sensor incorporation, thus serving two purposes. Firstly, to evaluate the performance of the HASI-ACC sensor in accordance with the secondary goals outlined above. Secondly, the HASI-ACC sensor could provide additional information regarding the g -level experienced by the tiltmeter sensors, assuming it is mounted in a fixed position relative to them, as would be the case with a common platform. Such a measurement however, would again require knowledge of the platform orientation since the g -level in the aircraft is defined relative to the vertical (again, discussed in Chapter 5) whereas the HASI-ACC measures acceleration along a sensor axis. This doubled the benefit of flying the second tiltmeter, fixed relative to the platform, as in (i).

Thus are defined a set of requirements for an experiment that is to satisfy the above objectives. The following section describes the final solution designed in response to these requirements.

4.3 Platform Design

4.3.1 TIL and HASI-ACC Portable Dynamic Calibration Platform overview

Figure 4.2 shows a photograph and a diagram of the final design arrived at for the dynamic calibration programme. As can be seen, a platform configuration was employed. Before describing in detail the individual components, some general advantages of the design are of note:

- a) *Compactness and portability:* Firstly all of the instruments are mounted together on a common platform forming a neat and robust arrangement (both mechanically and electrically, see below) with no separate boxes other than a battery pack, thus reducing the likelihood of damage or loss during transport, vital for any portable solution. In the original 1998 design for example, the HASI-ACC (PZR in the original design) box was attached a separate unit and convenience was noticeably impacted. The sizing of the platform necessitated consideration of the available cabin space outlined in Table 4.1 and the resulting design (450mm x 600mm x 200mm for main platform and 250mm x 250mm x 100mm for the battery pack) permitted seating of the platform either on a passenger's lap, in place of a passenger, or in either of the rear shelf spaces of the Cap 10-B or Robin DR-400.



Figure 4.2: The Portable Dynamic Calibration Platform: early assembly close-up (left), platform on ground at airfield (right)

- b) *Stability*: The platform base was comprised of two layers. Firstly a 5mm thick sheet of aluminium provided a strong, smooth, electrically conducting surface into which mounting holes could be drilled and subsequently tapped. The second layer, whilst being made of light wood, was much thicker at 20mm and therefore provided much improved rigidity and stability without compromising the weight of the platform.
- c) *Common reference frame* : By fixing all of the experiment components to a single platform, all of the sensors shared a common reference frame. Therefore measurements could be made of various motions without having to consider relative motions between the sensors, only their relative fixed positions within this reference frame. This was particularly important when attempting correlation between the tiltmeter and accelerometer data, and parallel or orthogonal alignment of the sensor axes simplified considerations of the differences in force experienced by individual sensors.

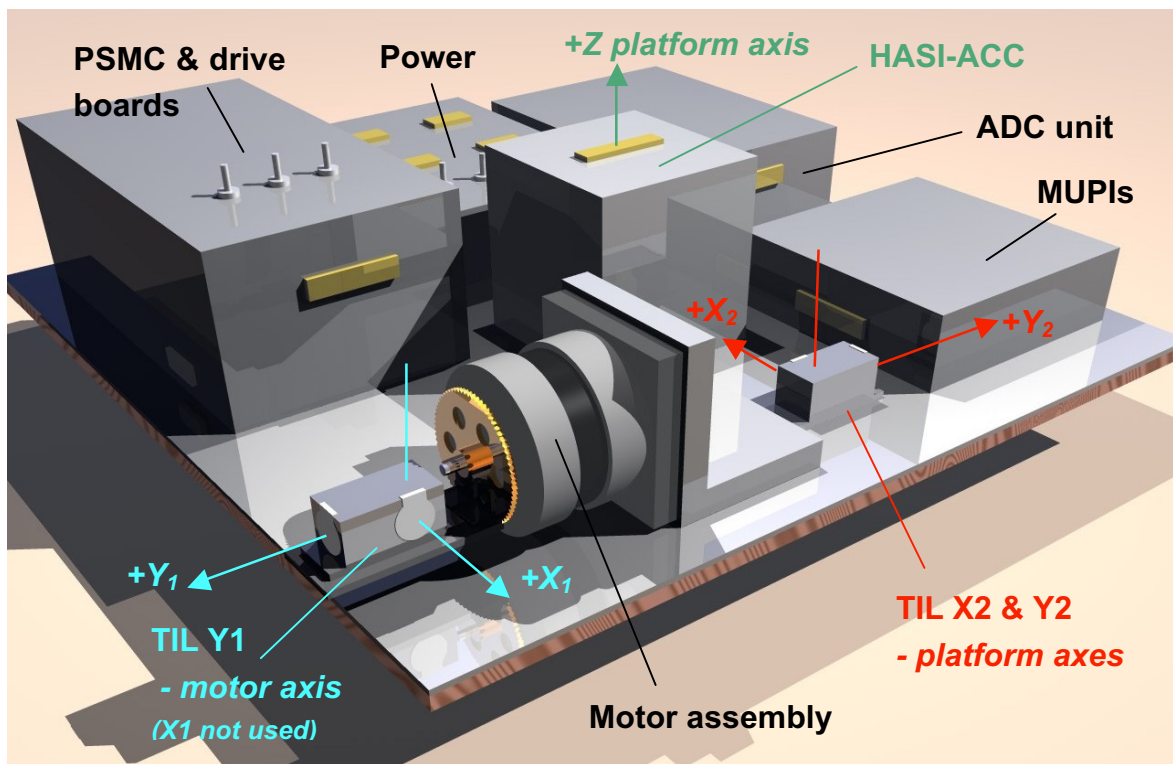


Figure 4.3: The Portable Dynamic Calibration Platform: diagram of flight model platform indicating axis conventions and key components

- d) *Die Cast Aluminium Housing* : The initial 1998 design housed all experimental components, except for the accelerometers, in a single wooden box with a clear

plastic lid. The design whilst compact and quick to assemble, housed less instrumentation, was less sturdy, physically, and most significantly offered little electromagnetic shielding from the external environment. In addition the decision to house the motor, which tended to radiate a considerable amount of heat as well as electromagnetic noise from the drive wires, in the same container as the supporting electronics gave rise to thermal and electromagnetic concerns internally. These issues when coupled with the adverse electromagnetic environment experienced within an aircraft cabin are considered prime factors which led to the failure of the controlling electronics in the initial design of the experiment platform during the 1998 flight. Consequently these issues represented a major focus for the improvements made during the design of the succeeding platform and in the final platform design the motor was housed externally. This isolated it both thermally and electromagnetically from the sensitive supporting electronics, all of which were now housed in individual high-temperature die-cast aluminium alloy boxes providing optimum physical, thermal and electromagnetic shielding. Each box had a wall thickness of 1.9mm and in addition to the physical protection, according to manufacturer's specifications, provided electromagnetic/RF screening better than 40dB at 10MHz and 76dB at 100kHz when the lids were sealed [RS stock numbers 225-237, 225-243, 225-265, 225-271]. The aluminium base plate of the platform tied each box to a common ground and the interface to each box was via either a 9-way or 25-way D-type connector, with connections between boxes using shielded multi-core cable.

4.3.2 Dynamic Calibration Platform components

3 TIL sensors

As explained in the requirements discussion above three TIL sensors were used in the final design for the calibration platform: one (TIL-Y1) mounted on an oscillating tilt plate undergoing a programmed motion sequence, and two (TIL-Y2 and TIL-X2) fixed to the calibration platform, orthogonally oriented with one sensor's measurement axis aligned with that of the oscillating TIL sensor. TIL-Y2 and TIL-X2 provided the platform reference orientation with respect to the local gravity vector but were subject also to inertial effects as described in section 3.2.3, thus providing a reference against which the effects of the programmed oscillating motion of TIL-Y1 could be compared.

The three sensors were provided by two individual Spectron Dual-Axis Tiltmeters, as described in section 3.2.2, with the TIL-Y1 measurement relying on only one of the two

sensors housed within the tiltmeter. The tiltmeter used for this TIL-Y1 measurement was in fact the Huygens Surface Science Package flight spare and was identical to the sensor flown onboard Huygens. TIL-Y2 and TIL-X2 used a similarly designed Spectron sensor, but an earlier prototype, manufactured prior to the flight versions and therefore not to MIL spec. The only differences were possibly in the fluid parameters of the sensor electrolyte although these were considered as negligible, and less shielding on the wires leading out from the TIL-Y2 and TIL-X2 sensors. Each sensor was calibrated individually and at the temperatures and pressures experienced during the reduced gravity calibration programme, the response times of the sensors were found to be the same, to within the experimental error, for each sensor.

It should also be noted at this point that the platform possesses additional versatility by allowing the TIL-Y1 sensor to be mounted in several orientations on the TIL sensor plate. Figure 4.4 shows possible variations. By adjusting the length L it is possible to introduce different accelerations on the sensor housing. By orienting the sensor as in (b) and adjusting the length D centrifugal effects may be further investigated. For the experiments described in this work insufficient flight opportunities were available to test the effect of varying either of these parameters, however, particularly in the case of varying L , it is recommended that use be made of this additional variable in subsequent experiments.

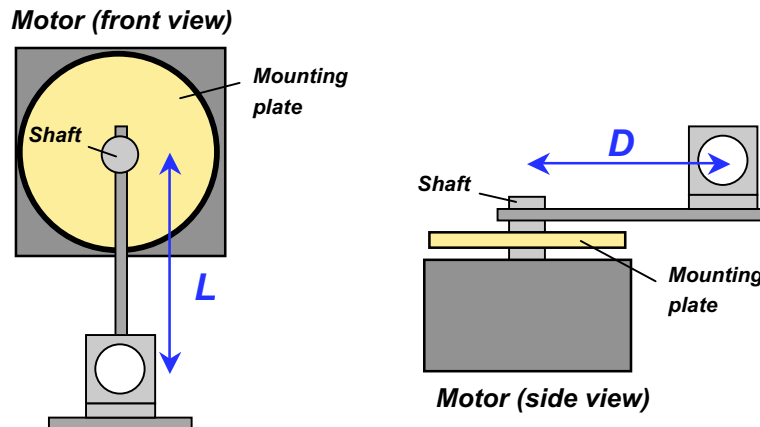


Figure 4.4: Different TIL mounting orientations to test the effect of different accelerations

TIL Signal conditioning

As previously mentioned the Spectron Glass tilt sensors were necessarily AC voltage driven to avoid electrolyte dissociation effects. On the Huygens Probe this is handled by the SSP electronics box. This driving electronics is somewhat complex however as it is necessarily designed to be integrated closely with the overall probe's onboard data handling subsystem. As such the design is larger, heavier, more complex, power-demanding and expensive than is needed for simply driving and measuring the TIL

sensor and its output. Fortunately Spectron offer a much simpler signal-conditioning unit designed specifically for their electrolytic tilt sensors known as the MUPI. The MUPI is conveniently d.c. powered and both supplies the necessary a.c. driving voltage to the tilt sensor electrodes and converts the a.c. voltage at the centre electrode into a polarised d.c. signal proportional to the sensor tilt.

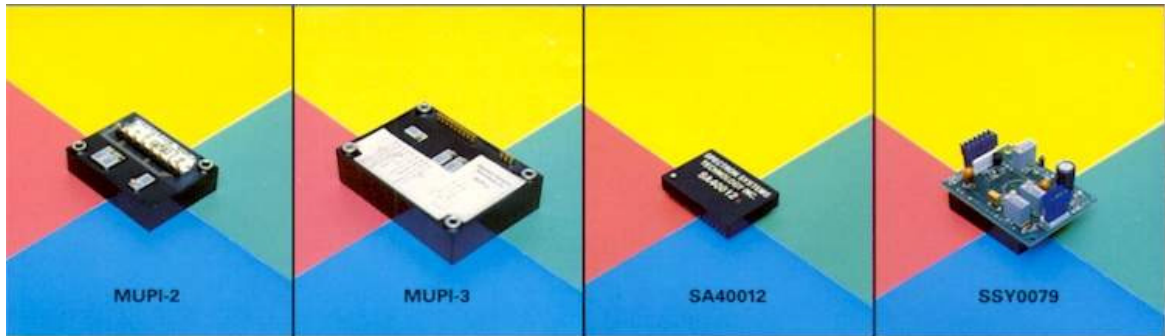


Figure 4.5: (left to right) MUPI-2 and MUPI-3, and two low mass, low power PCB mountable units for future consideration (<http://www.tiltsensors.com/oneaxisig.htm>)

At the time of the experiment two MUPI models exist, the MUPI-2 and MUPI-3, the latter being the newer model of the two, only slightly larger, and possessing improved built-in temperature compensation. Figure 4.5 shows the two MUPI units, and Table 4.2 summarises the specifications for each.

	MUPI-2	MUPI-3
Supply voltage range (bipolar) (d.c.)	$\pm 10\text{ V to } \pm 16\text{ V}$	$\pm 11\text{ V to } \pm 16\text{ V}$
Output signal (d.c.)	$0\text{ to } \pm 7\text{ V}$	$0\text{ to } \pm 7\text{ V}$
Supply current (at 12V)	20 mA	20 mA
Dimensions (mm)	51 x 39 x 20	70 x 50 x 21.5
Adjustments available:	Null, + & - gain	Null, + & - gain Temp. compensation
Connections	Soldering pins	Soldering pins
Advantages	Plus and minus gain separately adjustable	Plus and minus gain separately adjustable Temperature compensation

Table 4.2: MUPI-2 and MUPI-3 specifications (details from Spectron, see [Marshall, 2000] or <http://www.tiltsensors.com/oneaxisig.htm>)

At the time of the experiments two MUPI-3 units and one MUPI-2 unit were available. The MUPI-2 unit was used with the TIL-Y1 sensor and the two MUPI-3 units with the TIL-Y2 and X2 sensors. Each of the MUPI-2 and MUPI-3 units' gain settings were set to their minimum values. Calibration values of the TIL-Y1, Y2 and X2 sensors for each of the experiments carried out are given prior to the respective results sections.

HASI-ACC sensor

As mentioned previously the initial 1998 design was forced to use PZR accelerometers due to availability problems with the servo sensor. This was not the ideal solution since they demonstrated insufficient resolution and too high a temperature variability to be of use in measuring the acceleration ranges expected during flight, between -1 and $+1.5g$. By the time of the 1999 experiment however these had been resolved and the servo, in the housing designed by Patel et al. [1999] (see section 3.6) could be integrated directly into the platform design with no change in its settings.

Figure 3.13 showed a schematic of the HASI-ACC sensor. As with the TIL sensor the choice of orientation for the sensor housing, i.e. with the measurement axis horizontal or vertical, depended upon the calibration being performed. As shown in Figures 4.2 and 4.3, for the reduced-gravity flights the HASI-ACC housing was mounted such that this axis was aligned perpendicular to the platform base. This ensured that for the most common orientations of the platform – horizontal or close to horizontal since the aircraft pitch was not expected to exceed 45° [Gourinat, 1998] – the sensor is optimally aligned to measure the gravitational acceleration experienced by the TIL sensor housing and fluid. For spin-table tests the sensor housing was turned on its side with the measurement axis horizontally aligned, parallel to the direction of centrifugal acceleration, the optimum orientation for spin-rate measurement using the HASI-ACC sensor.

In retrospect, following analysis of the flight results, two issues are noted. Firstly, in the absence of any flight computer giving an accurate time history of the aircraft trajectory to compare the TIL and HASI-ACC measurements against, it would have been preferable to have three orthogonally mounted ACC sensors. Thus the attitude and trajectory of the aircraft could have been derived accurately. It is strongly recommended that future flights involve an aircraft with a flight computer for this purpose.

Secondly, as will be seen in the next chapter, reasonable success was achieved in using the HASI-ACC sensor to record the reduced-gravity levels. However it became immediately apparent that full reconstruction of the flight profile was limited by saturation of the sensor during periods of g -level greater than 1. This was an unforeseen shortcoming in the retention of Patel's gain settings for this particular application. Any future experiments should carefully consider the range of likely accelerations and tailor the sensor gains appropriately.

Analogue-to-Digital Converter

Two analogue-to-digital converters were readily available at the time of the experiment, both made by the same manufacturer, the Pico ADC-11 and the Pico ADC-16. Both units have since been superseded by more capable units, most significantly with respect to sampling frequencies and number of channels that can be sampled simultaneously. This is highlighted as one of the most significant areas for improvement in future experiments. Nevertheless at the time of experiment the ADC-16 unit was chosen since, of the two units, its featured the wider input voltage range, including the handling of negative input voltages, and superior bit resolution, as summarised in Table 4.3. The negative voltage issue was particularly important in the case of the TIL sensor outputs, since it allowed direct measurement without the need for scaling circuitry.

<i>Parameter</i>	<i>ADC-16</i>
Input range (V)	± 2.5 V
Resolution (bit)	8 – 16 bit
Max. no. input channels	8
Conversion time per channel:	
8 bit	6.6 ms
9 bit	8.9 ms
10 bit	14 ms

Table 4.3: Pico ADC-16 specifications.

Channel	Sampling resolution (bit)	Conversion time (ms)
TIL-Y1	9	8.9
TIL-Y2	8	6.6
TIL-X2	8	6.6
ACC x1	8	6.6
ACC x4	8	6.6
PSMC O/P (see <i>control board</i> description)	9*	8.9
	Total	44.2

Table 4.4: Channels with conversion times (* note: during this experiment the PSMC O/P channel was erroneously set to 9-bit resolution rather than 8-bit)

Six of the available eight channels were used, as shown in Table 4.4 above. The ADC-16 permitted software-controlled allocation of different sampling resolutions for each channel, however each improvement in channel sampling resolution carried an associated penalty in sampling time, and these summed together gave an overall sampling period for a single ADC measurement cycle. Thus maximization of the

sampling rate necessitated a compromise in resolution of several instrument measurements, and these are also summarised in Table 4.4.

The total conversion time leads to a maximum sampling rate for the experiment of 22Hz. Whilst the experiment was successful, clearly this was too slow a sampling rate to fully characterise the sensor response time when its time constant was of the order of 100ms. Again, it is recommended that future experiments consider faster options.

The ADC-16 was PC-controllable via a standard 9-pin RS-232 interface. A laptop was used to maintain portability and the Pico developed ‘Picolog’ software was employed to sample, record and display the data in 2 minute cycles, i.e. every two minutes the data was saved to disk. The Picolog software permitted real-time graphing for instrument monitoring during data capture, whilst writing to a text file for tabulation and analysis later. As with the actual hardware selected, more advanced software has since been developed by Pico however at the time, and given the laptop specification then available, the DOS-based Picolog program represented the best choice.

One final issue concerning the data recording, noted only after analysis of the results was the time lag between successive data recording cycles. The software allows automatic continuation of the next cycle after having completed the previous cycle, however it was noted with alarm that some data was lost in between cycles. Careful examination of the PSMC ‘clock signal’ used to report the position of the TIL-Y1 motor driven plate allowed this time lag to be calculated as 1.475 seconds. This adjustment was made and corrected a mysterious inconsistency in the measured flight timelines.

Battery unit

Table 4.5 summarises that input voltages demanded by the platform, and Figure 4.6 shows the arrangement chosen to satisfy these power requirements.

Unit	Input voltages required	Current drawn (mA)	Notes
Motor Drive Board Board alone With motor	0V, +12V _(board) , +6V _(motor)	60 4000 max	Current drain highest when motor energised but stationary (6V chosen to minimise vibration)
Motor Control Board	0V, +5V	600	
MUPI-2	0V, ±12V	20	
MUPI-3	0V, ±12V	20	
ADC	0V	0	
ACC	0V, ±15V	100	

Table 4.5: Power and voltage line requirements

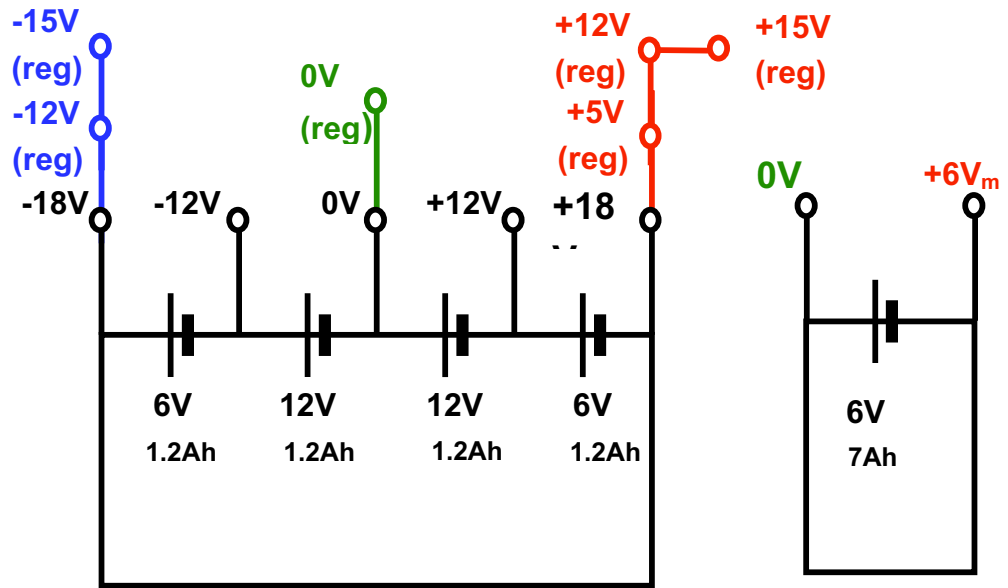


Figure 4.6: Calibration Platform battery arrangement indicating regulated line voltages and separate high capacity motor battery

The housing of the batteries separate from the main platform was necessary for space and mass considerations. With the total mass of batteries required being over 5kg any attempt to house them on the main platform would have seriously compromised the portability of the unit and would have made more serious demands on the platform structure. Clearly the necessary size increase of the platform would also have compromised portability. The batteries were thus housed in a single, separate die cast box with four banana plug interfaces, and rubber feet. The choice of banana plug interface was to promote quick and easy installation and disassembly. The rubber feet were added since the box would most likely be seated, due to its bulk and mass, on the floor of the aircraft where it would likely experience a harsher vibration environment.

As can be seen from Table 4.5, most of the platform components were of low power consumption, with the exception of the 4A at 5V maximum drain of the motor drive board (see later this section) whilst the motor was energised, and the 0.6A drain of the PSMC. Consequently the majority of the batteries selected were of 1.2Ah capacity, the main trade offs being capacity versus price and mass.

The capacity requirement budgeted a total flight duration of up to 2 hours. As seen from the table, for the low power consumption components capacity was not a major concern. For the motor, assuming maximum power drain, that is approximately 2A, this would

require capacity of over 4Ah to avoid the need to recharge between two potentially adjacent flights. Such capacities proved to be sufficient however by incorporating a switch into the power distribution module which allowed individual powering on and off of the each of the main components, as described below.

Power Distribution module

As shown in Figure 4.6, 0V, $\pm 18V$, and +6V lines were fed out from the battery unit into a power distribution module containing regulators. The interface into the power distribution module was again via banana plug to facilitate set-up. The +6V line was fed unregulated to the motor drive board, whilst all other voltages were regulated to the values shown. Harness connections between the power distribution module and the individual module boxes was via shielded D-type connectors.

Switches were inserted on the Power Distribution Unit to allow individual module activation to prevent unnecessary power drain when the experiment was not running, or when choosing to isolate any particular module not being used. This was particularly important in the case of the motor which uses power to provide the required detention torque to hold the TIL sensor in a fixed position (see next section). This avoided the necessity of repeated connection and disconnection of the banana plug cables between battery unit and the platform during any experiment.

Stepper Motor, Drive Board & Programmable Stepper-Motor Control (PSMC) Board

As described above the experiment required a calibrated tiltable platform for the TIL-Y1 sensor and this was achieved by mounting the sensor on a small plate in turn mounted on the shaft extending from a unipolar 4-phase stepper motor. The stepper motor is driven by a drive board which provides power to the appropriate motor windings according to the clock rate set either on board or from an external clock source. Since oscillations, rather than complete revolutions, of the TIL-Y1 sensor were required a variable and programmable step rate was needed. The complex clock pulse sequences necessary for this were provided to the motor drive board from a programmable stepper-motor control board, which in turn was programmed by PC through an RS232 interface. The motor, drive board, and programmable control board were all commercially available units and their specifications are summarised below. RS Stock Numbers are included for reference.

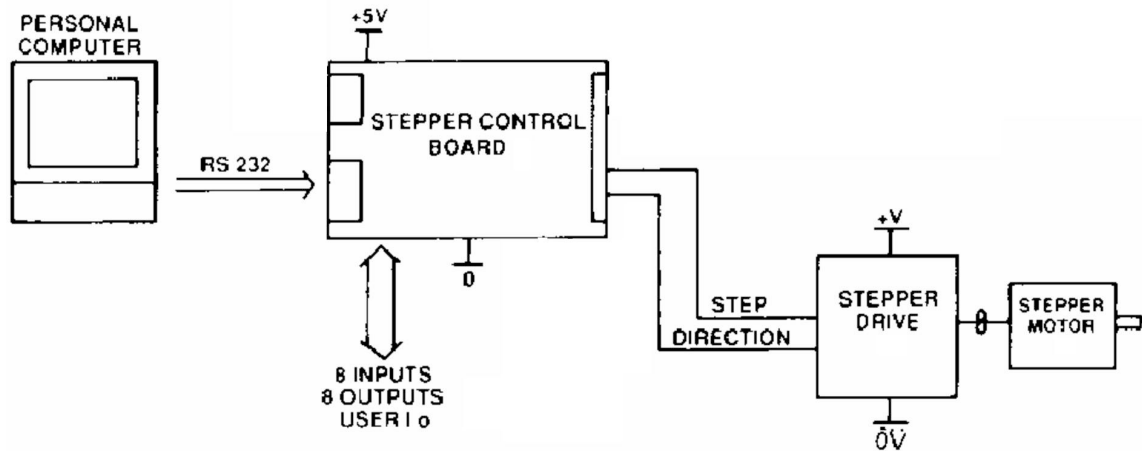


Figure 4.7: Schematic of how the motor, drive board and controller board fit together (data from RS Datasheet)

Stepper Motor (RS Stock No. 440-464)

A stepper motor is a special kind of DC motor that can be rotated in precise increments, or steps, in either direction. The step size of a stepper motor is the highest precision by which one can position the stepper motor shaft and common step sizes vary between 1.8° and 30° . Each incremental step is achieved by a single input pulse and thus the position of the motor shaft is proportional to the number of input pulses sent to the motor. This key property of stepper motors is the main reason for their repeatability and positional precision; by their very principle of operation each step has a *non-cumulative* positional error of only 3-5% of the step angle. It also means that the motors respond to digital pulse trains and therefore they are often easily be driven by computers with very little additional circuitry. Stepper motors can generally start and stop ‘on a dime’, and they possess high durability and reliability since they do not have any slip rings or brushes, their lifetime being limited only by that of the bearings [Yeadon & Yeadon, 2001]. All of the above characteristics make stepper motors popular with a wide range of high-precision, low-torque applications, and a wide selection was commercially available for the calibration platform. Section 4.3.3 describes calculations carried out in selection of the stepper motor for the calibration platform.

Drive Board

The drive board simplifies the driving of the stepper motor by applying correctly sequenced voltage pulses to the motor windings. The resulting motor step rate (essentially its speed) is governed by the drive board according to a clock input. Whilst it is possible to construct one’s own clock input, the degree of motion control required of

the TIL-Y1 plate here was sufficiently complex that the variable clock input was automatically provided to the board by the Programmable Stepper Motor Control board (see below). The drive board is the Unipolar 2A Eurocard model, and is directly compatible with the range of motors being considered and could share the same power supply. The board offers a virtually ‘plug and play’ solution between the versatile control board and the stepper motor. Details of the board may be found in RS Datasheet 232-5435.

The drive board receives two voltages, +12V to power the board’s drive functions, and $+V_m$, where V_m is the motor voltage (selectable according to torque performance requirements). Initially values of 24V and 12V were used for V_m however during final pre-flight testing this was reduced to 6V to reduce heat dissipation, current drain and vibration levels. For the experiment configuration used in this particular flight the torque performance remained satisfactory. Increasing the moment of inertia of the TIL-Y1 assembly (by introducing a radial extension rod, for example) would probably have necessitated a higher V_m setting.

Whilst it is possible to drive the motor in half-step mode to improve step-angle resolution (see Yeadon [2001]), this was not done for the flight experiment due to the penalty paid in torque performance.

Programmable Stepper Motor Control (PSMC) Board

The control board controls the stepper motor position via stepper motor drive boards. Whilst the drive board translates clock sequences into motor steps, the control board is responsible for generating the clock sequence according to a program which is loaded via an RS-232 serial link from an ASCII compatible device, in this case a laptop PC. The program language is a proprietary language, which can be written using any text editor. The main commands used in the program specifies a target direction and the number of steps to be actuated, along with a maximum speed and both acceleration and deceleration profile. Programs can also use loops, therefore allowing complex motion sequences to be initiated. Section 4.3.4 shows how, with careful selection of the motion parameters, it is possible to program an approximation to simple harmonic motion, paving the way for probe swing simulations, using appropriate radial extension rods for the TIL-Y1 platform. As has been mentioned previously this was not performed in the experiments described in this work but certainly remains an avenue for further investigation.

Several additional features of the PSMC are made use of in the calibration platform design. The board is supplied as standard with 20KB of user RAM, with an option to add 32KB non-volatile RAM if stand-alone operation is required. The programming language allowed for auto-execution of program loaded in the non-volatile memory. This upgrade was essential in the 1998 flight since the experiment was to be flown by an engineer not directly involved in the design process and therefore reprogramming in the field would be almost impossible. In the 1999 flight when the experiment was carried out personally by the author, the auto-execution was not only convenient for avoiding repeated cable-changing and reloading, but also permitted powering down of the PSMC during flight outside periods of motor activity.

A second feature of the board are the programmable input and output channels. The inputs were used to control the speed of the motor and the output capability was used to report the position of the TIL-Y1 plate. Since each channel is only single bit resolution (i.e. on/off, true/false, 1/0, etc.) representation of graduation requires the use of multiple channels. In principle this is not an issue and allows for an enormous range of applications, however since the ADC unit currently used could only spare a single channel for the PSMC output a limitation was imposed on the reporting of the TIL-Y1 position. As described in section 4.3.4, every time the TIL-Y1 plate reached its point of maximum inclination during the simulated simple harmonic motion sequence, a change of state of the PSMC output was executed. This was an unfortunate limitation of the hardware available. This was less of a limiting issue with the input switches, since the use of two switches allowed the selection of four separate motions sequences without the need to reprogram the control board. In this case four simple harmonic motion frequencies were selectable, one of which was zero, i.e. stationary. These command sequences are described further in section 4.3.4.

The last two features used with the PSMC board were the status LEDs and Clear Memory commands. Two LEDs, a red and a green, gave an indication of the status of the board: steady green showed program executed successfully, flashing green showed program being executed, flashing red and green showed a syntax error in the program, and steady red showed an error during execution and a crash. Many a desperate hour were spent battling the unblinking red light with this board. Nevertheless in the event of an irrecoverable loop being entered or a crash, a jumper setting was available to clear the memory. This posed a problem once the board was sealed in its Die Cast box, and therefore a push button switch was inserted into the side of the box, allowing completion of the jumper connection within the box from outside. Similarly two tiny holes, small enough so that EMI/RFI screening was not compromised, were cut into the box to

permit visibility of the status LEDs.

One limitation of the PSMC board was its inability to recognize the absolute position of the motor shaft, but only the specified number of steps that had been sent to it by the control board. This meant that in the event of externally forced of step angle increments, the PSMC would not accurately report the angular position of the shaft. In practice this proved to not be a major issue since the measurements of the TIL-Y1 response time during reduced gravity flight, relied only on the time of maxima and minima of the TIL-Y1 inclination, rather than the absolute angular values. Ambiguities raised about the absolute bank angle of the aircraft were resolved courtesy of the TIL-Y2 measurement which was fixed relative to the platform (although, as will be seen from the flight results, it does appear that the platform shifted position during the flight).

Further details of the PSMC may be found in RS Datasheet 232-3692.

4.3.3 Stepper motor selection

Definitions

A comprehensive treatment of stepper motor characteristics may be found in [Yeadon, 2001] whereas here it will be sufficient to define only a few terms as relevant to the motor selection. For an excellent introduction to stepper motors however above the above reference is highly recommended.

The *step-angle* of a stepper motor is the smallest step size executable by the motor and is a function of the internal motor design. Several methods exist for increasing the step resolution, one of which is a technique known as *half-stepping*, however this is usually accompanied by a decrease in the torque performance of the motor. The *working torque* is the maximum torque obtainable from the motor. The *holding torque* of a stepper motor is the external torque required to overcome the magnetic torque holding the rotor in a particular orientation, when the motor is energised, thus externally forcing an angular step. The *detention torque* is the de-energised holding torque even when the motor windings are not energised. The *maximum pull-in rate*, the maximum switching rate (speed) at which an unloaded motor can start without losing steps. *Hybrid* stepper motor rotors feature a permanent magnet core with a ferromagnetic teathed surface offering the fine resolution of variable reluctance motors, whilst also offering the detention torque, holding torque and improved accuracy of a permanent magnet motor [Yeadon, 2001].

As noted previously, a wide selection of stepper motors was commercially available for the calibration platform and to maximize the versatility of the motion control feature of the calibration platform care was needed in selecting the appropriate specification. The trade off was a common one; performance, in this case step resolution, torque and speed characteristics, against size, mass, power and cost.

Step resolution

To permit maximum control of the programmed motion sequences, the angular step size of the stepper motor should be as fine, that is as small, as possible. Typical step sizes range from 1.8° to 30° . Two readily available step angles were 7.5° and 1.8° , equating to 16 or 66 steps respectively to cover the TIL measurement range of -60° to $+60^\circ$, and consequently the 1.8° step angle was selected. As mentioned previously half stepping was not used to decrease the step angle further due to the penalty paid in the torque – speed performance of the motor when using this method.

Torque and speed characteristics:

Before selecting a motor according to its torque performance it was obviously necessary to have some estimate as to the torque requirements of the experiment. Figure 4.8 shows a diagram of the motor and TIL-Y1 plate assembly. Included in the diagram is an extension rod of adjustable length to introduce a variable offset of the TIL-Y1 sensor from the rotation axes thus permitting investigation into effects of carefully controlled non-gravitational sensor accelerations on the fluid surface. This final element of the design was not included in the flight tests described in this thesis, however as mentioned previously it does represent an important area to address any subsequent experiment involving the platform. The effects of the introduction of up to a 20cm radial offset between the TIL plate and the rotation axis are considered at the end of the moment of inertia calculations below since they impacted the choice of motor, as will be seen.

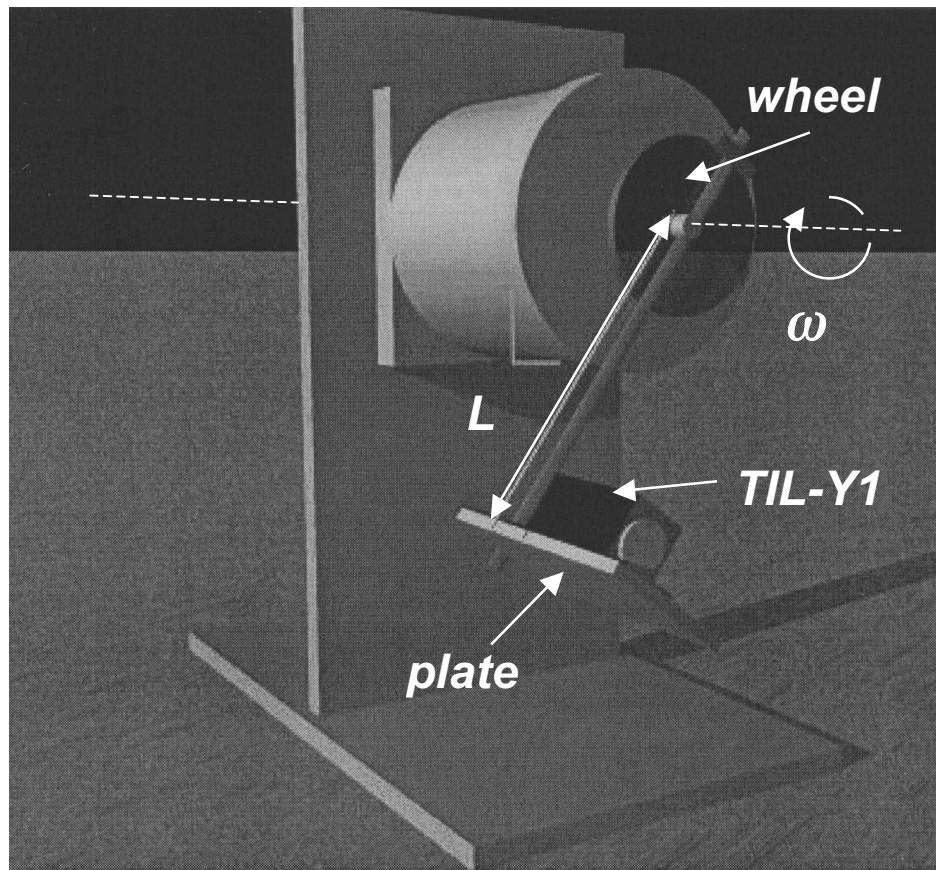


Figure 4.8: Close-up 3-d model of TIL-Y1 plate assembly, indicating sensor assembly, wheel, plate, and $\omega=d\theta/dt$ as referred to in calculations

The torque, T , required of the motor in rotating the TIL sensor assembly could be obtained using

$$T_{total} = (I_{assembly} + I_{rotor}) \frac{d\omega}{dt} \quad (4-1)$$

where $I_{assembly}$ is the total moment of inertia of the complete TIL sensor assembly shown in Figure 4.8, I_{rotor} is the moment of inertia of the rotor (dependent on motor selection), and ω is the angular velocity of the assembly about the rotation axis. As discussed the sensor assembly motion would approximate simple harmonic motion, and therefore it was possible to estimate the maximum torque required using $I_{assembly}$ and $(d\omega/dt)_{max}$, the maximum value of the angular acceleration. At the time of motor selection the TIL-Y1 motion sequences had not yet been finalised, and it was thus necessary to estimate the frequencies that would be required. It was judged unlikely that the calibration program would demand a frequency greater than twice that of the equivalent natural simple harmonic pendulum motion frequency, $f_{pend-shm}$, for any given radial offset (with $f_{pend-shm}$ being the natural frequency of an equivalent simple pendulum of length equal to the radial offset, acting under terrestrial gravity) and therefore this was used as the baseline

for motor selection. Such oscillations having maximum angular displacements of $\pm 60^\circ$ (equal to the manufacturer's specified limits for the TIL sensor) give a maximum angular acceleration of

$$\left(\frac{d\omega}{dt}\right)_{\max} = \frac{4\pi^3 f_{\text{pend-shm}}^2}{3} \text{ rad s}^{-2}. \quad (4-2)$$

Note that this maximum acceleration (and hence maximum torque requirement) occurs at the maximum platform inclinations where the angular velocity, and hence motor speed, is zero.

<i>Component</i>	<i>Approximation</i>	<i>I estimate</i> (<i>g cm</i> ²)	<i>Notes</i>
Meccano wheel	2 hollow cylinders. For each cylinder $I_{\text{cyl}} = m (r_o^2 + r_i^2) / 2$, where m is mass, and r_i and r_o are inner and outer radii	91	
TIL plate	Thin plate, mass m (see notes), width w , radial offset r_{plate} , $I_{\text{plate}} = m(r_{\text{plate}}^2 + w^2/12)$	250	Plate mass includes mass of nuts, bolts and mounting brackets. No extension bar offset included.
TIL sensor	Box, mass m , width w , height h , radial offset of box top r_{box} , $I_{\text{TIL}} = m(w^2/12 + r_{\text{box}}^2 + r_{\text{box}}h + h^2/3)$	335	No extension bar offset included.
<i>I_{assembly}</i>		676 g cm²	sum of components above

Table 4.6: Estimation of the moment of inertia, I_{assembly} , for the TIL-Y1 platform assembly, with no extension rod.

In order to estimate I_{assembly} the sensor assembly was broken into geometrically simpler components and the moments of inertia for each of these were summed. Note that for the purposes of this calculation several approximations were made and judged to be satisfactory:

- i. The individual moments of inertia of the nuts, bolts and mounting brackets between the wheel and sensor plate were not calculated. Instead their combined mass was included in that of the sensor plate. This would only lead to an overestimation of the moment of inertia and therefore was not a matter for concern.

- ii. The moments of inertia of the TIL sensor wires (six in all) were not included, but were not judged to affect the result significantly.

The calculations in Table 4.6 do not include any additional TIL plate radial offset from the rotation axis provided by the extension rod (its length, L , being assumed zero). Whilst unfortunately the experiments of this chapter were not able to include this extension rod, Figure 4.9 shows the effects upon $I_{assembly}$ for extensions up to 30cm. Whilst it would not be difficult to do so, these calculations do not include the additional moment of inertia of the extension rods.

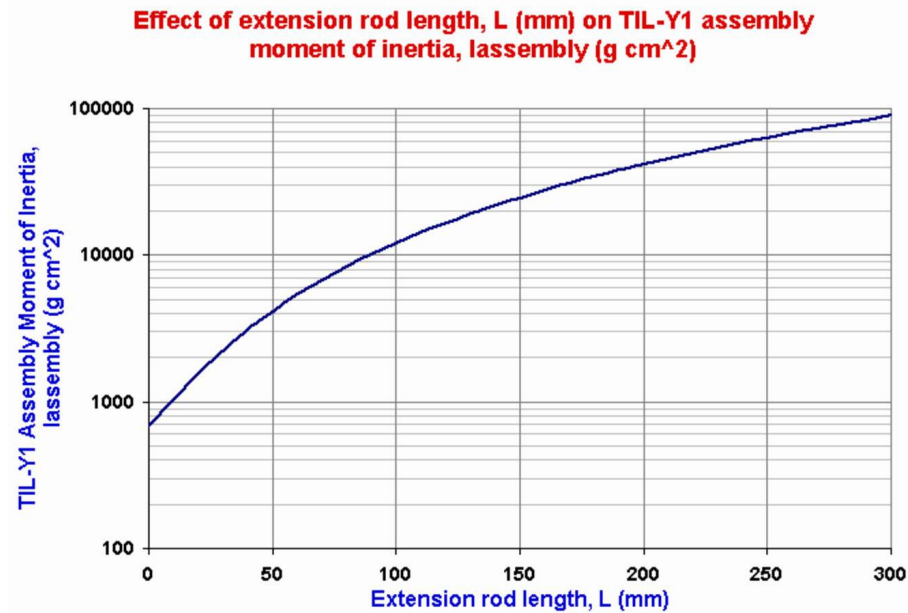


Figure 4.9: Graph of $I_{assembly}$ vs extension rod length, L .

Stepper motor type	Permanent magnet		Hybrid	
Size classification	1	2	23	34
Step angle	7.5°	7.5°	1.8°	1.8°
Detention torque (mNm)	n/a	n/a	30	100
Holding torque (mNm)	10	85	500	1100
Max working torque (mNm)	6	57	320	650
Max pull-in rate (steps s ⁻¹)	350	130	880	800
Rotor inertia, I_{rotor} (g cm ²)	2.6	45	135	640
Motor power consumption (W)	2	5.3	not avail.	not avail.
Mass (g)	80	300	600	1350

Table 4.7: Summary of motor characteristics [RS Datasheet 232-5749]

Values of I_{rotor} were available in the numerous motor datasheets and values for prime motor candidates are summarised in Table 4.7. Several larger motors, not listed here, were available but also significantly more expensive. The size 1 and size 2 permanent magnet 7.5° stepper motors are included here to indicate relative performances, however these were discounted as described earlier due to their poorer angular resolution.

Table 4.8 below summarises the moments of inertia for several extension rod lengths graphed in Figure 4.9 and, comparing these with the specified values of Table 4.7 above, it can be seen that only from the size 23 1.8° hybrid stepper motor upwards are the I_{rotor} values of a similar order of magnitude. It would thus be expected that these motors would represent the minimum specification if departure from the specified torque-speed curve (inertially unloaded) is to be minimised. Furthermore, Table 4.8 shows the maximum torque levels demanded of each of motor in simulating simple harmonic motion at twice the natural pendulum frequency, $f_{pend-shm}$, as per equation 4-2, for each of the extension rod lengths.

Extension rod length, L (mm)	$I_{assembly}$ (g cm ²)	f_{shm} (Hz)	T_{max} required for s.h.m. ($\pm 60^\circ$, f_{shm} and $2f_{shm}$), mNm							
			Size 1		Size 2		Size 23		Size 34	
			f_{shm}	$2f_{shm}$	f_{shm}	$2f_{shm}$	f_{shm}	$2f_{shm}$	f_{shm}	$2f_{shm}$
0	676	3.15	28	112	30	119	33	133	54	216
45	3,578	1.88	53	210	53	213	55	218	62	248
75	7,539	1.58	77	310	78	312	79	315	84	336
100	12,076	1.41	99	397	100	398	100	401	105	418
150	24,526	1.19	144	576	144	577	148	579	148	591
200	41,476	1.05	189	758	190	758	190	760	192	769
300	88,876	0.87	281	1124	281	1124	281	1125	283	1132

Table 4.8: Sample $I_{assembly}$, and required T_{max} values for each motor for approximating simple harmonic motion at 1x and 2x the natural frequency for several extension rod lengths, L . Greyed out areas indicate regions beyond the performance capabilities of that motor, assuming manufacturers specifications.

Note that the lengths 45mm, 75mm and 150mm have been included in the table to show the extension rod lengths (to the nearest millimetre) at which the torque demanded of particular motors exceeded their specified available working torque.

It can be seen that the size 2 7.5° permanent magnet stepper motor was the smallest motor satisfying the non-extended TIL assembly requirements for $f = f_{pend-shm}$, however with a 5cm extension rod, or for any extensions at $f = 2f_{pend-shm}$ the size 23 motor was

needed. For TIL platform oscillations up to the natural pendulum frequency for a particular radial offset the size 23 motor would have sufficed, however for oscillations at twice this frequency – the criteria used for motor selection – and extension rod lengths above 7.5cm the size 34 motor represented the minimum motor specification. With this motor it should have been possible to approximate simple harmonic motion at twice the natural pendulum frequency of a 15cm extension, but beyond this required a more powerful motor. For purposes of testing centrifugal effects upon the TIL sensor however this would neither be necessary nor justify the additional expense and inconvenience of a larger, costlier and more power-hungry motor.

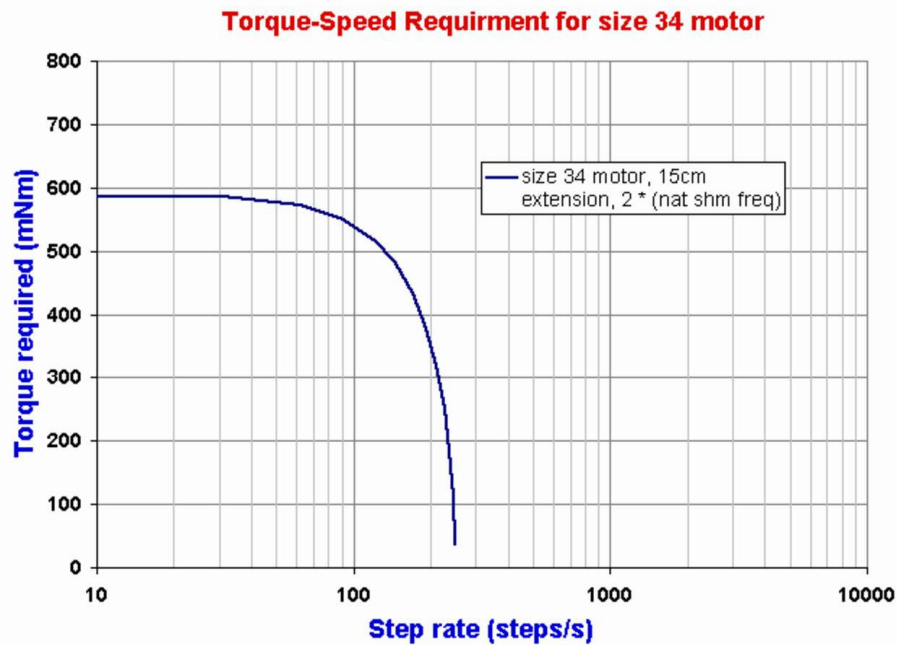


Figure 4.10: size 34 motor, $L=15\text{cm}$, $f=2f_{\text{pend-shm}}$ torque speed requirements

Note that for the purposes of this analysis it was sufficient to consider only the specified ‘Maximum working torque’, rather than the overall torque-speed curve since, for simple harmonic motion, $(d\omega/dt)_{\text{max}}$, and hence T_{max} , occurs at zero step-rate. Figure 4.10 shows this for the size 34 motor with a 15cm extension rod length, executing simple harmonic motion at frequency $2f_{\text{pend-shm}}$, the limiting case for that motor. Comparing this with the manufacturers torque-speed curves it can be seen that the use of T_{max} for selection was justifiable.

The other requirement of the motor was the maintenance of positional integrity not only throughout the motion sequence but in between cycles when the motor would be energised but stationary, and also whilst the motor would be de-energised, perhaps for power conservation purposes. Thus it was necessary for the motor to possess sufficient

holding and detention torques to hold the TIL assembly at its maximum inclination (when its weight would exert the maximum moment about the shaft axis) without slipping. Using the parameters defined in Table 4.6 the required holding torque can be given by

$$T_h = g \sin\theta (m_p r_p + m_{TIL} (r_{TIL} + h/2)) \quad (4-3)$$

where it is assumed that r_{TIL} includes the extension rod length L . Figure 4.11 shows the holding torque requirements for 60° maximum TIL assembly inclination for L between 0 and 30cm. Comparing these results with the specifications provided in Table 4.7 it can be seen that, only the hybrid motors provide suitable levels of holding torque, and only the size 34 motor provides sufficient detention torque for any extension rod length of more than a few centimetres. Even then, for the size 34 motor, the maximum L value for the TIL assembly that can be held steady when the motor is de-energised is 12cm.

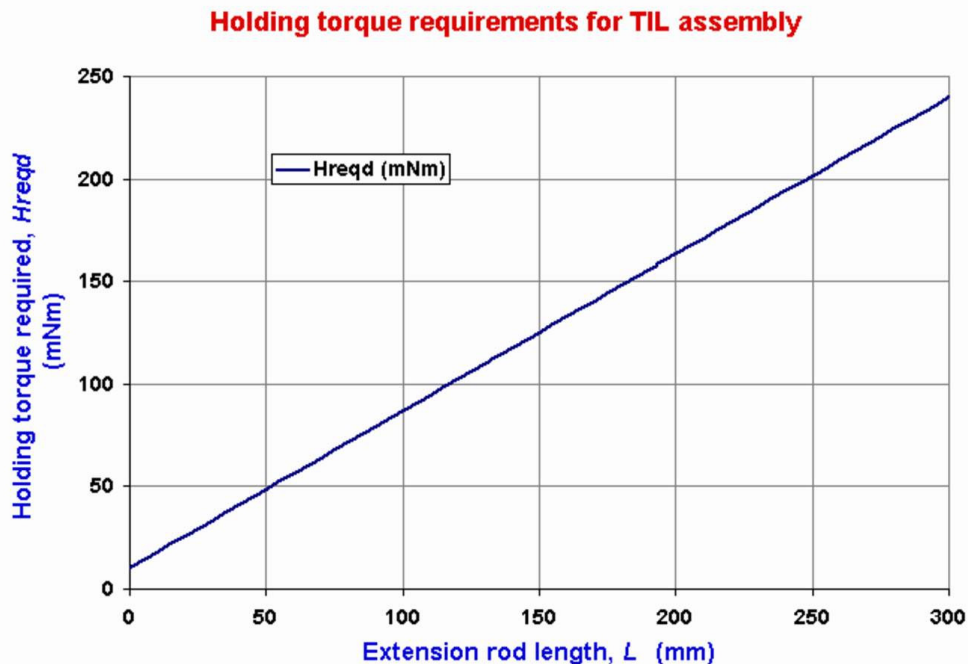


Figure 4.11: Holding torque requirements calculated from $I_{assembly}$, for 60° inclination, with extension rod length L (mNm)

From the evaluation of experiment requirements and motor performance issues above, it became clear that the Size 34 hybrid stepper motor represented the most appropriate choice. The only issues that needed to be traded-off against the clearly superior performance were the added bulk, extra cost and higher power requirements. The size of the motor was not of great concern since it was smaller than many of the electronics

boards that drove the motor itself and as such did not add significant size to the TIL sensor set-up, as can be seen in Figures 4.2 and 4.3.

The mass of the motor was a more serious issue, 1.35kg representing a significant addition to the experiment mass. Nevertheless since the motor represented the heaviest component of the platform the total mass of the experiment remained within manageable limits, remembering that the platform would ideally at least need to be comfortable in the lap of an experimenter.

Motor mounting and vibration

One definite impact of the size 34 motor's bulk, however, was the need for a strong mounting frame, and a 10mm thickness aluminium bracket, as shown in Figure 4.2, was manufactured specifically for this purpose. For the experiments detailed in this work, a basic L-shape design was employed for the bracket due to time constraints.

Unfortunately, as will be seen from the results this mounting solution, while robust, failed to satisfactorily reduce the vibrations transmitted to both the TIL and most significantly the ACC sensors. This significantly increased the noise in the sensor outputs and the specific vibration damping features of an improved motor mounting design would have been valuable. A finite element structural analysis (e.g. a simple NASTRAN model) of possible options could not be employed since the appropriate tools were not readily available within budget and time constraints. Nevertheless the reduction of vibration through an improved mounting represents another vitally important area for further analysis before future reduced gravity experiments are performed.

The use of gears may also be considered for providing a smoother profile, although these would also affect the torque performance of the system and this trade-off should be considered with care.

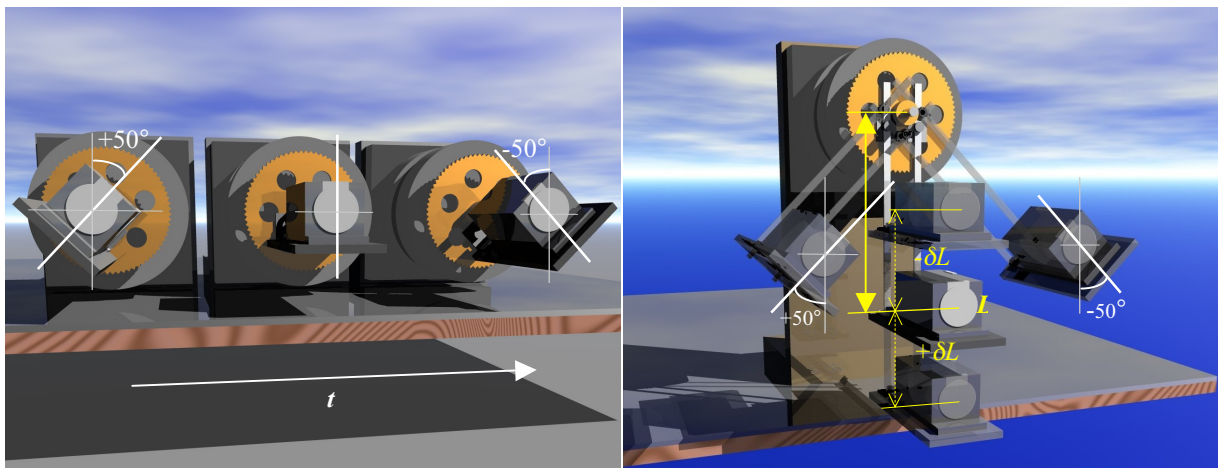
With the existing system, attempts were made to reduce vibration by reducing the motor voltage from 24V down to 12V initially, and then again to +6V. As has been mentioned, the reduced torque performance remained sufficient for the purposes of the experiments described here since no radial offset of the TIL-Y1 plate was introduced. Interestingly, vibration was found to decrease significantly with increasing motor speed and hence frequency of approximated simple harmonic motion.

Cost

The final issue surrounding motor selection was one of cost, and for the size 34 hybrid stepper motor this was not a prohibitive issue. Larger motors were available, at greater expense however, and the performance benefits to this experiment, given the requirements outlined above, did not justify the additional expense.

4.3.4 Programmable motion sequences: s.h.m. simulation

TIL-Y1 motion requirements



(a) Standard PSMC motion

(b) Extended PSMC expt

Figure 4.12: (a) shows the standard motor motion sequence. (b) shows the extended experiment, not flown during the reduced gravity flight. Motion of the TIL-Y1 plate is indicated.

An ideal test for the tiltmeter performance under Titan conditions would be to measure damped simple harmonic motion under Titan gravity simulating the sensors' response to parachute swing. Several problems present themselves with this however. Firstly, in order to evaluate the sensor response, it is necessary to know the actual motion undergone by the sensor so that it can be compared with the measured motion. Simply swinging the sensor on the end of a piece of string will not permit this without some form of tilt sensor which does not suffer the same inertial effects as the fluid based tilt sensor. Therefore it was decided to use the programmable capability of the motor control board to generate an approximate simple harmonic motion sequence for the TIL Y1 sensor. Thus the true motion sequence, even if not precise simple harmonic motion, can

be calibrated prior to flight and, since it is by definition fully repeatable, therefore provides a reference against which the TIL-Y1 output can be measured.

The second problem is that to properly simulate the forces experienced by the Huygens TIL sensor during parachute swing, it would be necessary not only to simulate Titan gravity but also displace the TIL sensor from the point of rotation in order to generate the appropriate accelerations on the TIL fluid that arise from the accelerating sensor reference frame, as shown in Figure 4.13(b). Obviously it was not practical to reproduce the actual Huygens value for the probe-parachute separation distance. A compromise would be to use a more manageable, both in terms of size and motor torque requirements, distance and scale the effects accordingly. Unfortunately at the time of the experiment only the standard, zero displacement configuration, as in Figure 4.13(a) was employed due to the limited number of free flight opportunities. The extended experiment configuration was reserved for a future flight and is highlighted as an avenue for future investigation.

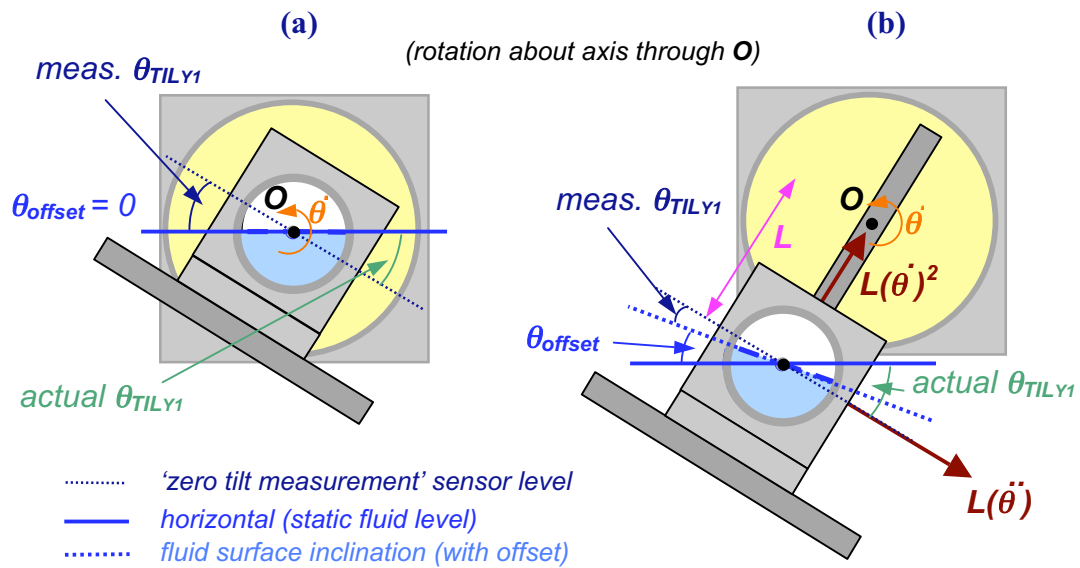


Figure 4.13: showing schematic of sensor fluid in vial with a) zero displacement and b) radially offset sensor. Indication is given in the radially offset case of the underestimation of tilt.

Program sequences

As described in section 4.3.2, the control board could be programmed via a language which, although nowhere near as extensive as Fortran or C for example, nevertheless offered sufficient versatility to generate some useful motion sequences. Below are described the principal commands that were used in generating the motor motion sequences. Further details of these may be found in the PSMC board datasheet. Note that each command actually included an additional parameter specifying which one of two

axes the command was referring to, since the PSMC board was designed to control up to two axes simultaneously. This is not shown in the descriptions below since this experiment required control in only one axis.

`cmove(x,y)`

This moves the motor from position x to position y at a constant speed (stepping rate) as specified by the `cvel()` command (see below)

`cvel(v)`

This sets the step rate of the constant motion executed under the `cmove()` command (see above) to v steps per second.

`move(x,y)`

This moves the motor from position x to position y , smoothly accelerating and decelerating as specified by the `param()` command (see below)

`param(base,top,accel,decel)`

This sets the parameters of the accelerated motion executed under the `move()` command (see above). The parameters *base*, *top*, *accel* and *decel* refer to the starting speed (steps/sec), top speed (steps/sec), acceleration rate (steps/sec²) and deceleration rate (steps/sec²) respectively.

`prescale(factor)`

This command caused all subsequent parameters to be divided by the specified factor, thus allowing fractional values to be used.

An approximation to simple harmonic motion can be attained using a sequence of motor ‘move’ commands, each characterised by carefully selected values of x , y , *base*, *top*, *accel*, *decel*, calculated according to the desired simulated simple harmonic motion frequency.

Figure 4.14 shows an example of the simple harmonic motion to be approximated, $\theta_{shm}(t)$, along with the associated angular rate, $d[\theta_{shm}(t)]/dt$, and angular acceleration, $d^2[\theta_{shm}(t)]/dt^2$. The motion approximation attainable using the PSMC control language is also shown in blue. The approximation specifies constant levels of angular motor acceleration thus generating a ‘triangular’ approximation to the true sinusoidal angular velocity, with the resulting PSMC position profile as shown, and periods $T_{approx} = T_{shm}$.

It should be noted at this point that a small discrepancy was observed in between the motor period and the target simple harmonic motion period being approximated by the parameters specified above. This discrepancy was measured at between 2% and 5% for motion frequencies of 0.25 and 1Hz respectively. It is believed that this was in part due

to the approximation employed, part due to the processing and execution time of the PSMC board, and part due to the accuracy to which the *base*, *top*, *accel*, and *decel* parameters were specified within the program.

Fortunately, for the purposes of this experiment, the consequences were not serious enough to compromise the results. It was simply necessary to be aware of the error range in the motion frequency when comparing the observed TIL-Y1 response with the theoretical TIL SHM response which has been shown to vary with motion frequency in Chapter 3.

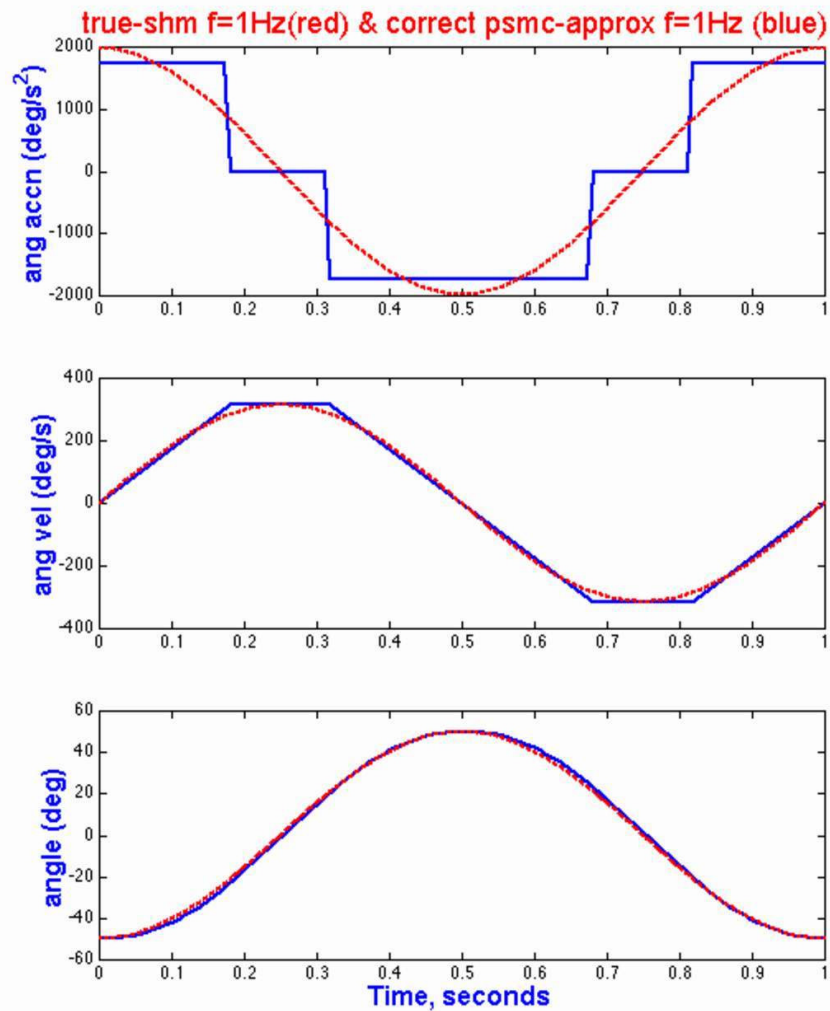


Figure 4.14: PSMC approximations to simple harmonic motion at 1Hz. Red dashed line indicates true SHM, blue solid line indicates PSMC approximation

Also built in to the PSMC program was the ability to select one of four frequencies for the approximated simple harmonic motion. This involved reading the state of two switches (housed on the PSMC board die cast box) thus permitting two-bit speed

selection. Since a noticeable delay was found to accompany the reading of the switches, continuous monitoring of the switch states was not appropriate. Therefore the program was written to run ten full oscillations at the selected frequency, then pause, check the switch states, and then resume the next cycle of ten oscillations. In retrospect and in light of the flight results, it is felt that the pause time was longer than necessary and in some instances occurred during a flight parabola, reducing the amount of reduced gravity dynamic response data. On a more positive note it was originally hoped that such ten-period cycles would aid the time correlation of commentary during flight with observed data features. This did in fact bear fruit when a timeline inconsistency arose due to the time delay between successive data-recorder file saves every 2 minutes. Such cycling significantly helped resolve ambiguities in the timing of the data and conclude a value for the time delay. Consequently the program has since been revised to retain the ten-period motion cycles but reduce the pause time between successive cycles.

One final feature of note in the PSMC simple harmonic motion program involved the switching of a PSMC board output channel (see section 4.3.2) to allow determination of the position of the TIL-Y1 plate. One of the objectives governing the design of the experiment was the measurement of the theoretical response of the TIL sensor fluid to simple harmonic motion. The theoretical response of the TIL sensor to simple harmonic motion was modelled in section 3.4.2, and as shown in the next chapter the response time of the sensor in the experiment would be calculated from the time lag of the TIL fluid surface relative to the actual calibrated platform motion. In order to provide a reference point from which the actual TIL-Y1 plate position could then be determined an output termed PSMC, with two states (call them HI and LOW), was incorporated into the program, switching states each time the motor position reached maximum inclinations $\pm A$, where A is the amplitude of simple harmonic motion being approximated. As has been mentioned previously, this was a limitation imposed by the number of channels that could be recorded by the ADC unit.

4.4 Sample Data from the Portable Dynamic Calibration Platform

Figure 4.15(a) shows a sample raw data file from the calibration platform. The platform was on level ground, and it can be seen that the TIL-Y1 plate executed two cycles at 1Hz and three cycles at 0.5Hz before switching to a 0.25Hz oscillation. Figure 4.15(b) magnifies an 18-second segment of the data for a clearer view of the PSMC clock and the lag of the TIL-Y1 output. As discussed in the next chapter the TIL-Y1 time lag was

measured from the switching of the PSMC output signal to the peak of the TIL-Y1 signal. Also noticeable in Figure 4.15(b) is the noise in the ACC(x4 gain) signal.

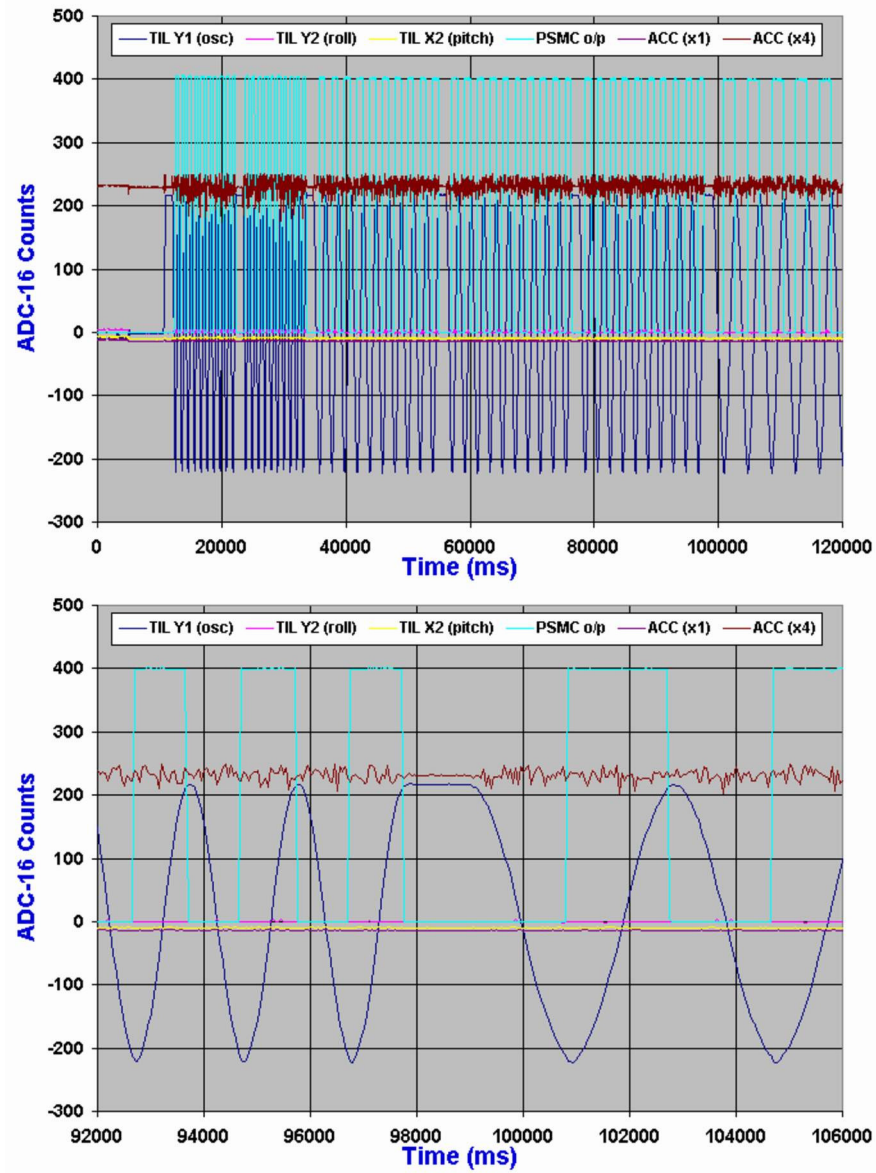


Figure 4.15: (a) Sample raw data file from the calibration platform with the TIL-Y1 plate executing motion at frequencies 1, 0.5 and 0.25Hz, and (b) magnified segment of data file showing PSMC position indicator signal, TIL-Y1, and noise in ACC(x4 gain) signal

4.5 Conclusion

This concludes the discussion of the engineering and mechanical design methodology for the TIL and HASI ACC dynamic calibration platform. As measure of the platform's success to date, three experiments - the reduced-gravity flight, a spin table and brief

swing experiment - are all detailed in the next chapter, along with their results and analysis. The performance of the platform, observed both during and in light of the results, are discussed at the end of the next chapter. Design issues and recommendations for future development are also highlighted.

PAGE INTENTIONALLY BLANK

Chapter 5

Field Experiments with the Dynamic Calibration Platform

5.1 Introduction

As detailed in the previous chapter, whilst the design of the Portable Dynamic Calibration Platform was catalysed by the announcement of a reduced gravity flight opportunity [Ghafoor et al, 1999], it also satisfied an existing need for a method of testing the TIL and HASI-ACC sensors in complement outside the laboratory environment under a range of dynamic conditions. This chapter describes the two experiments performed to date with the platform: the reduced-gravity flight test to investigate the deterioration of the TIL sensor response time under Titan gravity, and a spin-table test to verify the response of the sensor to spin rates likely to be experienced by the Huygens probe on Titan. A brief impromptu pendulum-type swing test was also carried out with the platform immediately after the spin test, and this is also described in this chapter.

Each experiment is described in turn, together with a presentation and discussion of the results analysis. Limitations of each of the experiments are discussed in turn, along with recommendations for design improvements of the calibration platform and suggested avenues of investigation for future experiments.

The details of the reduced-gravity flight opportunity were summarised in Table 4.1. Before proceeding with a description of the experimental set-up for the 1999 flight a brief review is offered of the principles behind the term ‘reduced gravity’ and its simulation through parabolic flight in section 5.2 below.

5.2 ***Reduced Gravity Simulation: a general background***

5.2.1 **Reduced-gravity, microgravity and weightlessness**

A person, like all matter, has mass, measured of course in kilogrammes. Whilst the term mass and weight are often used interchangeably in everyday English, the weight is actually the force exerted upon a mass when placed in a gravitational field, and as such is measured in Newtons. Immediately, from this definition, a problem is presented with the term ‘weightless’ as commonly used. Any object, assuming it has mass, can clearly not exist within a gravitational field and yet have no weight. Here is where care must be exercised with terminology. Weightlessness in the truest sense, from the above definition, cannot actually be achieved in a gravitational field. Instead, only the sensation of weightlessness, or apparent weightlessness of an object, can be achieved.

Consider a person standing in a stationary lift. He or she senses their weight through the reaction force that is exerted upon them by the ground and which in turn is transferred up through the body. He or she also senses the ease with which limbs can be lifted. A car passenger senses their weight similarly by the reaction force exerted upon them by their surroundings, in this case the car seat, and the ease with which arms and legs are lifted. However if the car crests the bridge at speed, safety aspects aside, inertia will briefly carry the passenger upwards in relation to the car and the reaction force felt by the passenger will temporarily decrease. A similar inertial effect occurs with limbs which will feel easier to lift, and the overall result is a stomach-churning sensation of lightness. In this case the passenger *feels* as though they weigh less, even though their actual weight is of course unaltered. An analogous sensation of lightness occurs for the person in the lift when it begins to move. At the beginning of a descent or the end of an ascent inertia carries passengers slightly upwards relative to the lift itself. Conversely, at the start of an ascent or the end of a descent passengers are pushed downwards slightly relative to the lift and thus feel a sensation of increased weight.

Clearly situations b), c) and d) all involve accelerating frames of reference. Objects within such reference frames perceive an ‘effective’ force in the opposite direction to that of the frame acceleration and where this acceleration has a component in the local vertical direction, so too will the effective force experienced within the reference frame. Depending upon the direction of acceleration this will either act against or alongside the gravitational force and, since both forces are indistinguishable to an observer, the result is a sensation of decreased or increased weight, respectively.

It can thus be seen that where the frame acceleration is equal to that of gravity the effective force felt within the frame will exactly cancel the gravitational force and the weight of objects within the frame will appear to decrease to zero. This is regularly referred to as *weightlessness* even though this is clearly not actually true. The conditions within such frame of reference are also often referred to as *zero-gravity*, whilst again this is certainly not the case in truth. Any accelerating frame which experiences no forces other than gravity is said to be in a state of free fall and will, by definition, give rise to the above conditions.

Reduced-gravity conditions occur whenever the frame acceleration is in the same direction but of lower magnitude than that of gravity, such that a residual gravitational force is perceived and objects in such a frame appear to be of reduced weight. *Micro-gravity* conditions are when the ‘effective gravity’ experienced within the accelerating frame is of the order of 10^{-6} times the normal gravitational acceleration at the Earth’s surface.

5.2.2 Simulation of reduced-gravity and micro-gravity

Simulation methods

Since any state of freefall will simulate reduced gravity conditions, several methods may be employed and the choice will depend on a number of factors, including the gravity regime required, the period of simulation required, scale requirements and of course cost.

- a) *Drop towers*, or drop shafts, typically permit reduced-gravity conditions of between 2 seconds, as for a 24m structure at NASA Lewis, and 10 seconds for a 490m mine shaft in Japan that has been converted into a drop facility, offering the longest drop time in the world.
- b) *Parabolic flight aircraft* are so named due to their achievement of reduced gravity conditions through flight of a carefully defined parabolic trajectory, during which a period exists where centrifugal force counters the gravitational force. Parabolic flights can offer periods of up to 20 seconds, as for the Novespace Airbus A-300 Zero-G, depending on the thrust capability (required to overcome aerodynamic drag) and the structural reinforcement of the aircraft. Parabolic flights also offer the significant advantage of being able to control the level of reduced gravity by selection of an appropriate trajectory. Parabolic flight campaigns offer a significant cost advantage over the other options.
- c) *Unmanned orbital platforms* such as the European retrievable carrier, Eureka, can offer weeks or months of relatively stable micro-gravity conditions.

Naturally these are heavily size and mass constrained and expensive and require autonomous experiments

- d) *Manned orbital platforms* such as the US Space Shuttle or the International Space Station can offer micro-gravity conditions of weeks, months or even years, although stability of the micro-gravity is inevitably compromised due to manned activity.

Robin DR400 Parabolic Flight

Against this background, this treatment now focuses upon the parabolic flight simulation utilized in this experiment. Furthermore it should be recalled from section 4.2.1 that a significant factor for this experiment was the low cost associated with the opportunity. This is reflected in the use of a much smaller aircraft, the Robin DR400, to achieve shorter periods of reduced gravity than those reflected above. Also, due to both thrust and structural limits, the Robin DR400 was not capable of sustaining true micro-gravity conditions. This of course was of little concern for an experiment requiring only reduced gravity levels down to 1/7thg.

Typical Parabolic Flight Trajectory

The principles behind the parabolic flight trajectory is the same for a two seater aircraft as for a structurally reinforced Airbus A300 Zero-G aircraft. Values will differ for the dive and climb angles, the speed and size of the parabolas, and the length of the resulting g-profiles, however Figure 5.1 shows the key features general to any reduced gravity parabolic flight trajectory.

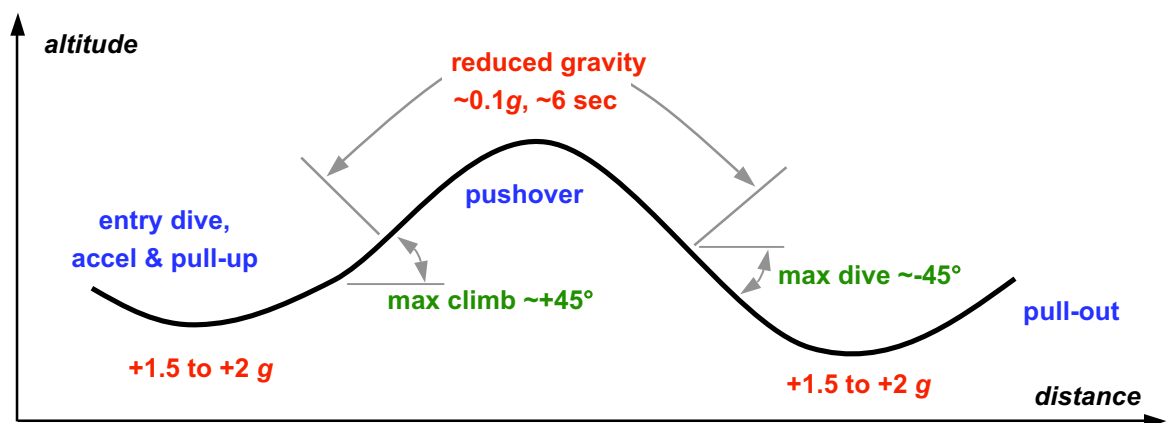


Figure 5.1: Key features of reduced-g parabolic flight trajectory (inc. parameters for RobinDR400)

Before parabola entry the aircraft throttle is increased to give sufficient airspeed to complete the manoeuvre, diving slightly if necessary (as with the Robin DR400). The aircraft then commences the entry pull-up phase, taking on a positive-g load factor. The throttle is then considerably reduced to the point where the thrust just

overcomes aerodynamic drag and the pilot kills the lift. The nose is allowed to progress downwards, and since the thrust still countering aerodynamic drag the aircraft simulates freefall and reduced gravity conditions are achieved. The aircraft completes the parabola with a symmetrical pullout phase. Typical g-levels during pull-up and pull-out may vary between +1.5 to 2g

One other key difference that also varies between aircraft is the stability of the reduced-gravity conditions. As would be expected, reduced-gravity flights aboard larger KC-135 and A-300 aircraft benefit from both longer and more stable g-levels. This again, however, is reflected in significantly higher cost associated with such flights. Nevertheless, discussions are currently underway to follow up the investigations presented in this work with a future flight aboard a full-size KC-135 or A-300 Zero-G aircraft. Figure 5.2 illustrates the stability of g-levels attained during a flight of the Ilyushin 76-MDK of the Cosmonaut Training Centre of Star City. Of note are the 1.8g levels preceding and following the 0g level [Plester, 1994].

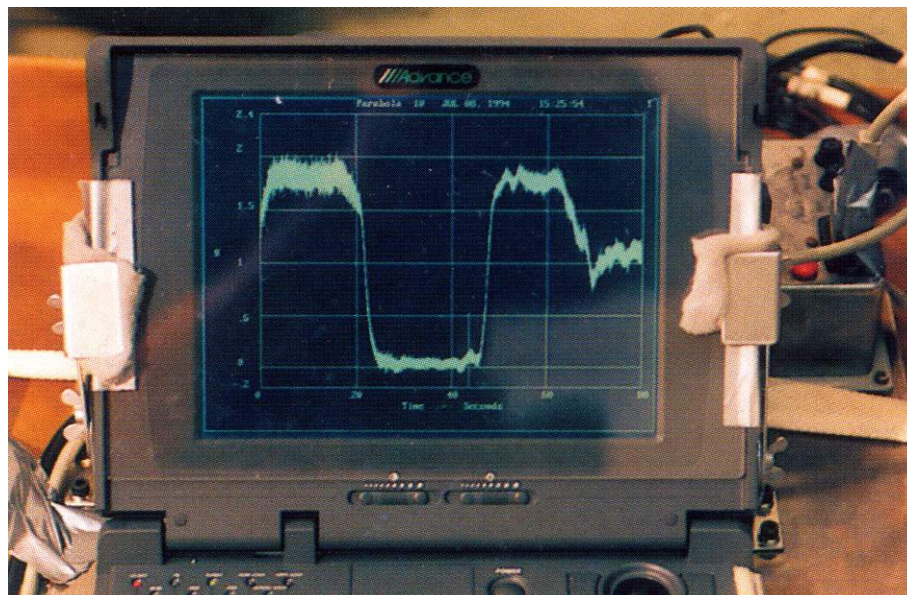


Figure 5.2: Residual acceleration level profile of a parabola as displayed by an ESTEC computer during parabolic flight of an Ilyushin 76-MDK aircraft [photo adapted from Plester, 1994]

5.3 TIL & HASI-ACC Reduced-Gravity Flight Experiment, Castres 1999

5.3.1 Aircraft and Flight opportunity

Details of the Robin DR-400 aircraft and the parabolic flight opportunities between 1998 and 1999 may be found in the earlier discussion of the history of the Portable Dynamic Calibration Platform, in section 4.2.1.

5.3.2 Flight objectives and requirements

Principal and secondary objectives of the flight were identified as follows:

- 1) Principal goals of the flight were
 - a) To test the operation of the TIL and HASI-ACC sensors under real dynamic conditions
 - b) To test the degradation in TIL sensor response time during periods of reduced gravity equivalent to that expected at the surface of Titan
- 2) Secondary aims of the experiment were:
 - a) To investigate the measurement of reduced gravity levels by the HASI-ACC (servo) sensor and compare with actual g -level.
 - b) To investigate the recording of the flight profile by the TIL sensors, including both pitch and roll
 - c) To evaluate the quality of flight history reconstruction made possible by the combined measurements of TIL and HASI operating in complement
 - d) To test the operation and usability of the Portable Dynamic Calibration Platform during field experimentation

Requirements necessary to fulfil all of the above objectives were then:

- i. Parabolas be executed that offer reduced gravity levels of $1/7^{\text{th}}$ g , being of sufficient duration to permit several measurements the TIL sensor response time at this g -level
- ii. Measurement be made of both TIL and ACC sensor outputs throughout the flight, and measurement of the sensor response time be made throughout the parabolas.
- iii. Some method of targeting and maintaining the required $1/7^{\text{th}}$ g be available, either by flight instrumentation or otherwise
- iv. A record be taken of the g -profile throughout the parabolas
- v. A record be taken of the flight profile for the duration of the flight, including airspeed, altitude, pitch and roll.

5.3.3 Reduced gravity flight experiment details

This section describes the experimental set-up used to meet the requirements identified above. It will be seen that some aspects of the experiment were influenced by resources aircraft instrument availability, rather than representing optimum

technical solutions, and in some cases this demanded a certain degree of improvisation.

Simulation of Titan's surface level gravity (1/7th g)

As described in section 4.2.1 the low cost Robin DR-400 flight opportunity was able to offer approximately 6 seconds of Titan *g*-level gravity per parabola. This was executed by flying an approximation to the parabolic trajectory described above. The Robin DR-400 flight profile would involve an initial dive followed by a pull-up entry climb of approximately +45°, followed by a maximum dive angle of -45° [Gourinat, 1999]. The predicted range of load factors would be from 0.1*g* during the parabola to +2*g* during parabola pull-out.

A two-day window was available between Saturday and Sunday 17th – 18th July 1999 for the flights to be conducted. The specific timing would depend upon weather conditions, pilot and aircraft availability and the commitments of the Terre-Espace / ENSICA course. Normal procedure was to minimise the level of reduced gravity rather than sustain a particular *g*-level, and consequently an initial flight was performed on the morning of Saturday 17th July, where practice parabolas were executed to give the pilot a chance to improve the accuracy of 1/7th *g* simulation using the simple instrument described in section 5.3.3. Data was taken during this flight however due to a problem with the recording of the aircraft profile, as well as reduced accuracy of 1/7th *g*-simulation, this data is not presented here.

Unfortunately weather conditions prevented flight throughout the afternoon causing great concern, however cleared just in time for a late evening flight. The final flight, from which data here is presented, therefore successfully took place at approximately 21:15 on Saturday 17th July. The flight duration, due to the late take off, from ignition to cut-off was approximately 30 minutes, during which a short flight and sequence of ten parabolas was possible.

Measurement of TIL and ACC responses: PDCP configuration

The reduced gravity flight represented the maiden voyage of the Portable Dynamic Calibration Platform. As described in the previous chapter the recorded outputs of three tilt sensors and the HASI-ACC servo accelerometer. The PDCP, in its configuration shown in Figures 4.2 and 4.3, was mounted on one of the rear passenger seats, secured by straps, so that the operator (the author, in this case) could easily energise / de-energise the motor and switch frequency settings throughout the flight. The battery pack, due to its weight, occupied the most stable and least hazardous position on the cabin floor. The platform was oriented as shown in Figure 5.3, such that the HASI-ACC sensor was aligned with the aircraft yaw axis, and the motor shaft axis (and hence TIL-Y1 measurement and oscillation axis) were aligned

with the aircraft roll axis. This was chosen so that during parabola execution, the only attitude measured by the TIL-Y1 sensor would be due to the TIL-Y1 plate oscillations. Also, since the parabolas would have a maximum inclination of 45°, the yaw axis represented the most useful alignment for the HASI-ACC sensor. In this orientation, the TIL-Y2 output therefore measured aircraft roll, and the TIL-X2 output measured aircraft pitch.

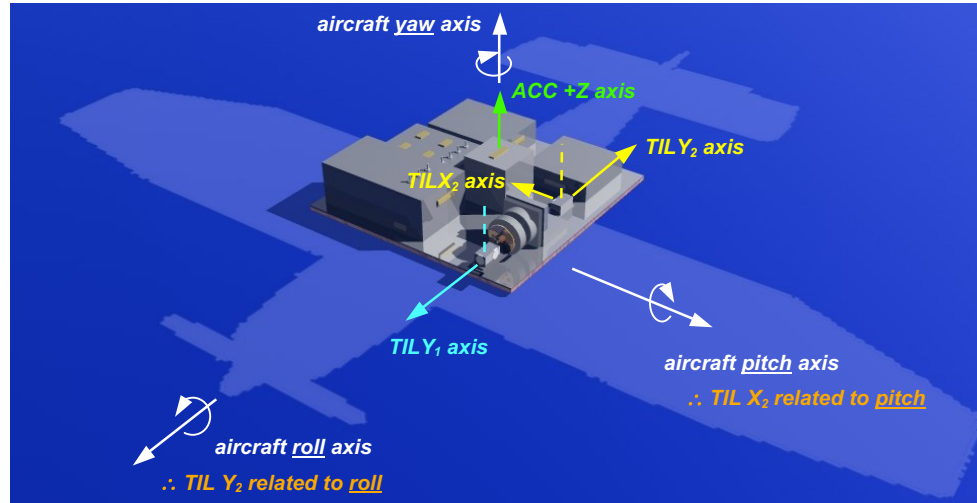


Figure 5.3: Orientation of the Portable Dynamic Calibration Platform relative to aircraft axes.

The measurement of TIL-Y1 response time is described in section 5.3.10.

Visual representation and measurement of g-level: a makeshift g-meter

As mentioned previously, the need to sustain a constant reduced *g*-level, rather than trying to completely eliminate it, was a relatively rare request for the organisers of this low-cost opportunity. Unfortunately this meant that the aircraft in question did not have a built in G-meter at the time of flight. Therefore, to satisfy experiment requirements (iii) and (iv) an alternative was required. Time and financial resources restricted the number of options, and therefore a makeshift *g*-meter was constructed from a simple spring balance, as shown below in Figure 5.4(a).

The length of the spring, x , which in turn adjusts the position of the indicator, is of course given simply by

$$x = \frac{mg}{k_1} + x_0 \quad (5-1)$$

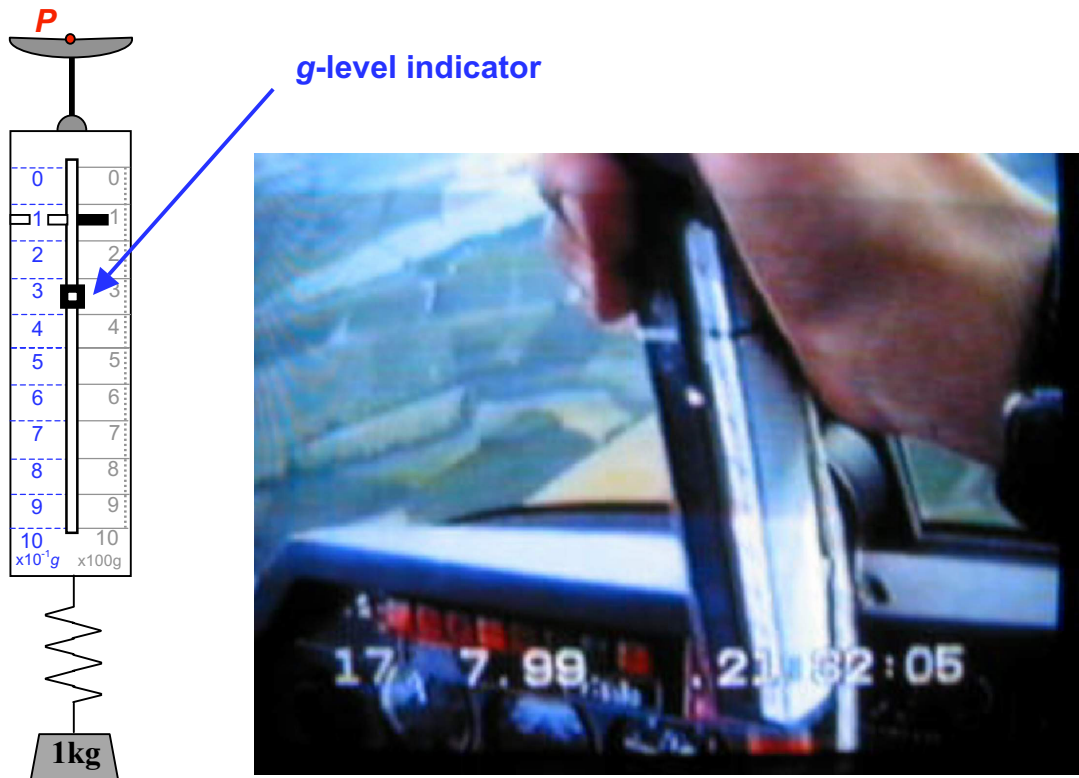


Figure 5.4: (a) Diagram of the spring balance g -meter (note scales), and (b) the meter in flight. Note the strip indicating clearly the target $1/7^{\text{th}}g$ level for the pilot

where x_0 is the unloaded extension length, m the mass of the weight block, g the local gravitational acceleration, and k_l the spring constant. Conveniently the scale on the spring balance read from 1 to 10 $\times 10^{-2}$ kg, and of course was calibrated under $1g$ conditions. Therefore for a mixed mass, x is proportional to g , assuming x_0 is the point of minimum spring length and therefore is constant for $g < 9.81\text{ms}^{-2}$. Using a 1kg mass, under regular terrestrial- g conditions, the mass would hang at the 10 mark at the bottom. By re-marking the scale from 0 to 1 therefore, the equilibrium position of the reading indicator gave a measure of the local g -level. For the ease of visibility by the pilot, who would use this to guide his control of the flight trajectory, the $0.135g$ (Titan gravity) mark was highlighted on the meter. Figure 5.4(b) shows the g -meter during flight.

An important consideration in the use of the spring-balance was the dynamic response inherent in the use of such system. The method described in the previous paragraph is straightforward for static conditions, however for a time varying g -level the equations of motion of the damped spring system must be considered. This calibration is described in section 5.3.4.

It should finally be noted that the meter was free to pivot about its point of suspension and therefore automatically aligned itself with the gravity vector, thus

removing the need to consider a $\cos\theta$ term, where θ is the pitch of the aircraft. This proved useful in comparing with the acceleration measured by the HASI-ACC sensor which, since the platform was fixed relative to the aircraft axes, did vary with the cosine of the aircraft pitch. In the absence of accurate flight instrument based pitch data (see below) this also removed the need to rely on the TIL-Y2 pitch data, which was strongly affected by aircraft accelerations, as described in section 5.3.11.

Flight profile measurement

Ideally the aircraft would have featured a flight computer which could provide a full history of the aircraft pitch and roll, as well as its altitude (or most importantly vertical speed) and airspeed. Unfortunately, such no such computer was available, and therefore an attempt was made to record as much information as possible using a video camera trained on the g-meter and analogue flight instruments. Figure 5.5 shows an example shot from the video.



Figure 5.5: Flight instrumentation recorded using VHS-C video

Time correlation and qualitative comparison of TIL and HASI-ACC results was theoretically possible. Unfortunately only one camera (and one camera operator, occupying the co-pilot seat) was available, and attempts to simultaneously record flight instruments and the g-meter achieved mixed results.

Other supporting equipment

In addition to the video recording shown above, a cassette dictaphone was used to permit flight commentary by the experiment investigator (again, the author). This

proved very useful in comparing noteworthy flight events (including take off, taxiing, banking, climbing, reduced gravity conditions, approach and landing) with observed signals from TIL and HASI-ACC.

Of course the last item of equipment used was a Toshiba laptop computer. It is perhaps ironic that of all items this represented the most significant experiment risk, due to a faulty power system. A spare battery was available to extend the lifetime, but even then very poor total measurement time was offered by the unit which, again, was selected for its availability rather than technical specification.

Clocks built into the laptop and video camera were carefully synchronised, and regular time reporting of the audio commentary permitted time synchronisation of the digital audio files following conversion to .AIFF (Mac), .WAV (PC) and .MP3 (universal compression) file formats using an Apple Powerbook G4.

5.3.4 g-meter calibration

As noted above the g-meter indicator naturally exhibited oscillatory behaviour due to the time-varying local g-level experienced within the aircraft cabin. Therefore an instantaneous snapshot of the g-meter (as taken from the video) did not necessarily give an accurate representation of the actual g-level at that time.

From the equation of motion of a forced damped harmonic oscillator, with varying $g(t)$

$$\frac{d^2 x(t)}{dt^2} + \frac{k_2}{m} \frac{dx(t)}{dt} + \frac{k_1}{m} (x(t) - x_0) = g(t) \quad (5-2)$$

where $x(t)$ is the position of the mass (represented for example by the indicator shown in Figure 5.4), $g(t)$ is the *effective* gravitational acceleration experienced inside the aircraft, m is the mass attached to the spring, and k_1 and k_2 are the spring stiffness and damping constant respectively.

k_1 can be found from the equilibrium position, x_{eqm} , of the spring marker with mass m attached, under the action of constant terrestrial gravity, g_e . If x_0 is the position of the spring marker for the unstressed spring,

$$k_1(x_{eqm} - x_0) = mg_e, \quad \Rightarrow \quad k_1 = mg_e / (x_{eqm} - x_0) \quad (5-3)$$

k_2 can be found from the damped response of the spring. For constant gravitational acceleration,

$$\frac{d^2 x(t)}{dt^2} + \frac{k_2}{m} \frac{dx(t)}{dt} + \frac{k_1}{m} (x(t) - x_0 - g_e) = 0 \quad (5-4)$$

Assuming light damping, i.e. $k_2 \ll k_1 m$, and neglecting non-linear damping terms,

$$x = Ce^{(-t/\tau)} \cos(\omega_0 t + \varphi) \quad (5-5)$$

where

$$\tau = \frac{2m}{k_2}, \quad \omega_0 = \sqrt{\frac{k_1}{m}}, \quad (5-6)$$

and C and φ are constants. Thus k_2 is found by measuring the time constant of the decaying response of the spring under constant gravitational acceleration.

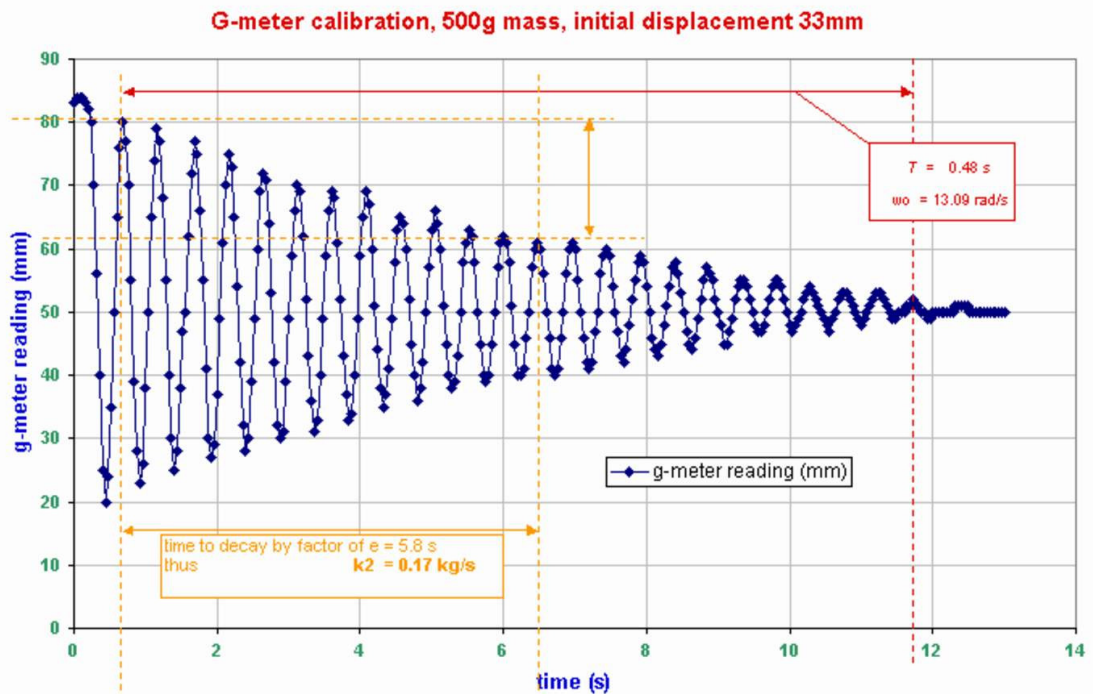


Figure 5.6: Oscillations of the g-meter spring when loaded with a 0.5kg mass, used to determine the g-meter damping constant

Figure 5.6 shows a graph of the g-meter's spring oscillations measured with a 0.5kg mass (used since a 1kg would obviously not permit oscillatory motion due to the g-meter design) from an initial 33mm displacement.

The results suggest values for the spring stiffness, k_1 , and damping constant k_2 , of

$$k_1 = 98.1 \text{ kg m s}^{-2} \quad \text{and} \quad k_2 = 0.17 \text{ kg s}^{-1} \quad (5-7)$$

Using these values a straightforward MATLAB routine was then written to calculate $g(t)$ from $x(t)$. The resulting profile required smoothing to remove numerical spike

artefacts. The differences between the indicated g -level and the derived actual g -level are shown for several parabolas in the results presented in section 5.3.6.

5.3.5 Instrument calibration settings

Calibrations for the sensors flown during the experiment, established during the development of the platform, are shown below.

$$\begin{aligned}
 \text{TIL-Y1:} & \quad V_{Y1} = (\quad 0.021 \quad \pm \quad 0.001 \quad) \times \theta_{Y1} \text{ (}^\circ\text{)} + (\quad -0.020 \quad \pm \quad 0.002 \quad) \quad V \\
 & \text{(motor)} \\
 \text{TIL-Y2:} & \quad V_{Y2} = (\quad -0.034 \quad \pm \quad 0.001 \quad) \times \theta_{Y2} \text{ (}^\circ\text{)} + (\quad -0.003 \quad \pm \quad 0.005 \quad) \quad V \\
 & \text{(pitch)} \\
 \text{TIL-X2:} & \quad V_{X2} = (\quad -0.034 \quad \pm \quad 0.001 \quad) \times \theta_{X2} \text{ (}^\circ\text{)} + (\quad 0.090 \quad \pm \quad 0.005 \quad) \quad V \\
 & \text{(roll)} \\
 \text{HASI-ACC:} & \quad V_{acc4} = (\quad 0.985 \quad \pm \quad 0.001 \quad) \times a \text{ (}ms^{-2}\text{)} + (\quad 1.314 \quad \pm \quad 0.002 \quad) \quad V \\
 & \text{(x4 gain)}
 \end{aligned}$$

With these settings, and the ADC sampling resolutions as described, it is therefore possible to interpret the raw data recorded throughout the flight. Note that calibration settings for the HASI-ACC x1 gain setting have not been included since this channel did not respond during the flight and was not used. This along with other discussion of the results follows in the next section.

5.3.6 Flight Results

The graphs presented on the next few pages show the raw data recorded by the PDCP throughout the final reduced gravity flight. As previously mentioned the ACC (x1 gain) channel failed during flight. As can also be seen during the flight the ACC (x4 gain) channel, scaled to give optimum resolution of the reduced gravity levels, saturated for levels of gravity significantly over 1g. Thus the failure of the ACC(x1 gain) channel was especially unfortunate as this would have given, albeit at a lower resolution, an indication of the flight profile throughout these ACC (x4) saturation periods. The ADC sampling resolutions for each instrument were as specified in Chapter 4.

Take off is mid way through the data file TILFLT12, and landing mid way through TILFLT18. Each data file is 120s long, and a break of 1.45s has been calculated between consecutive data files (section 4.3.4).

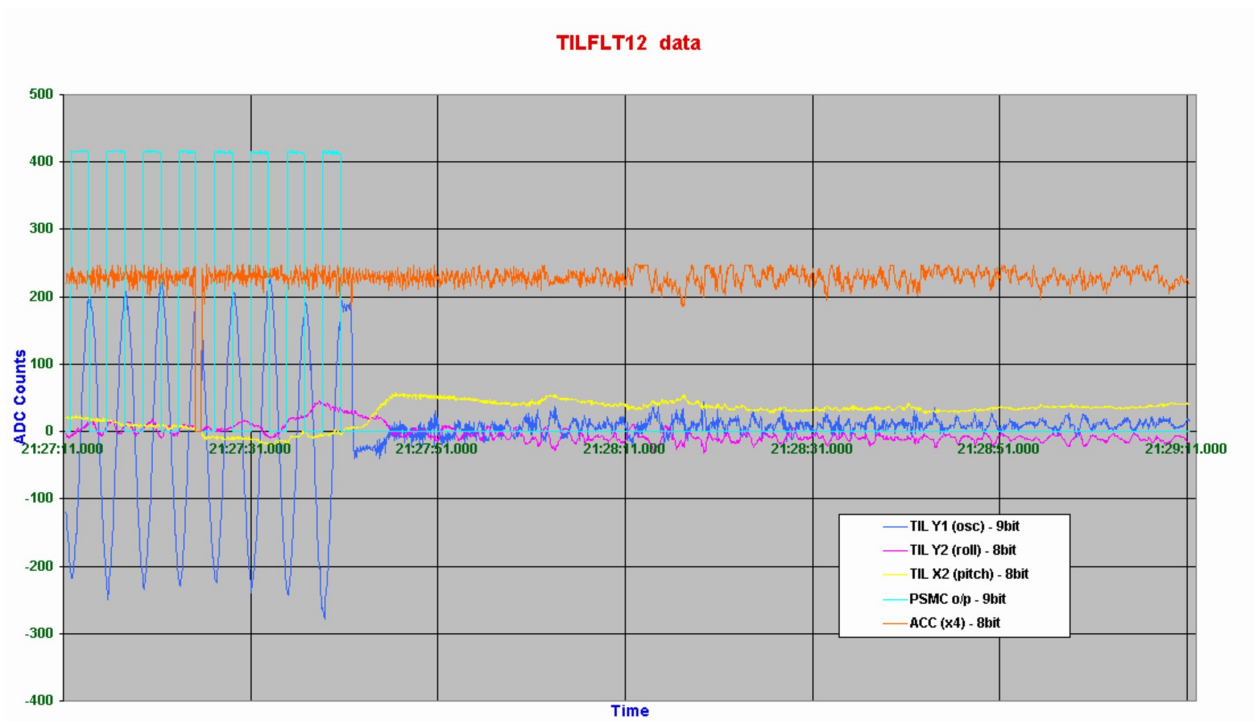


Figure (a): TILFLT12 raw data. See Figures 5.20-5.27 for calibrated results.

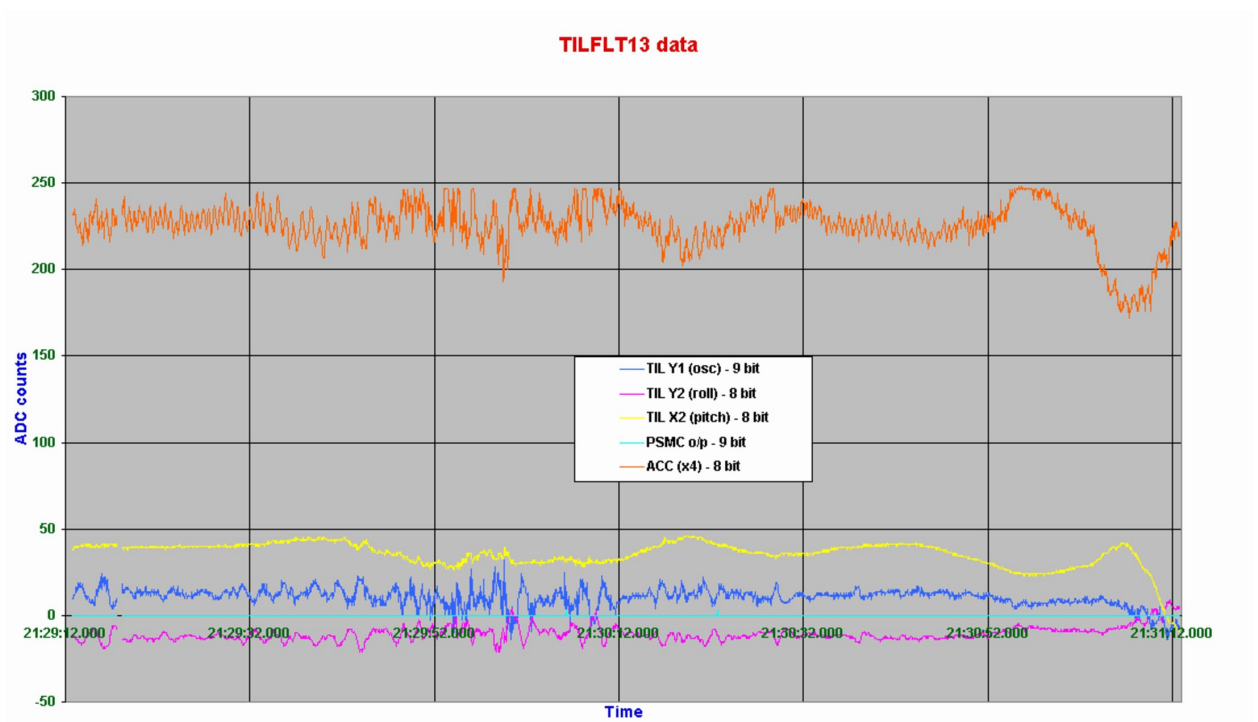


Figure (b): TILFLT13 raw data. See Figures 5.20-5.27 for calibrated results.

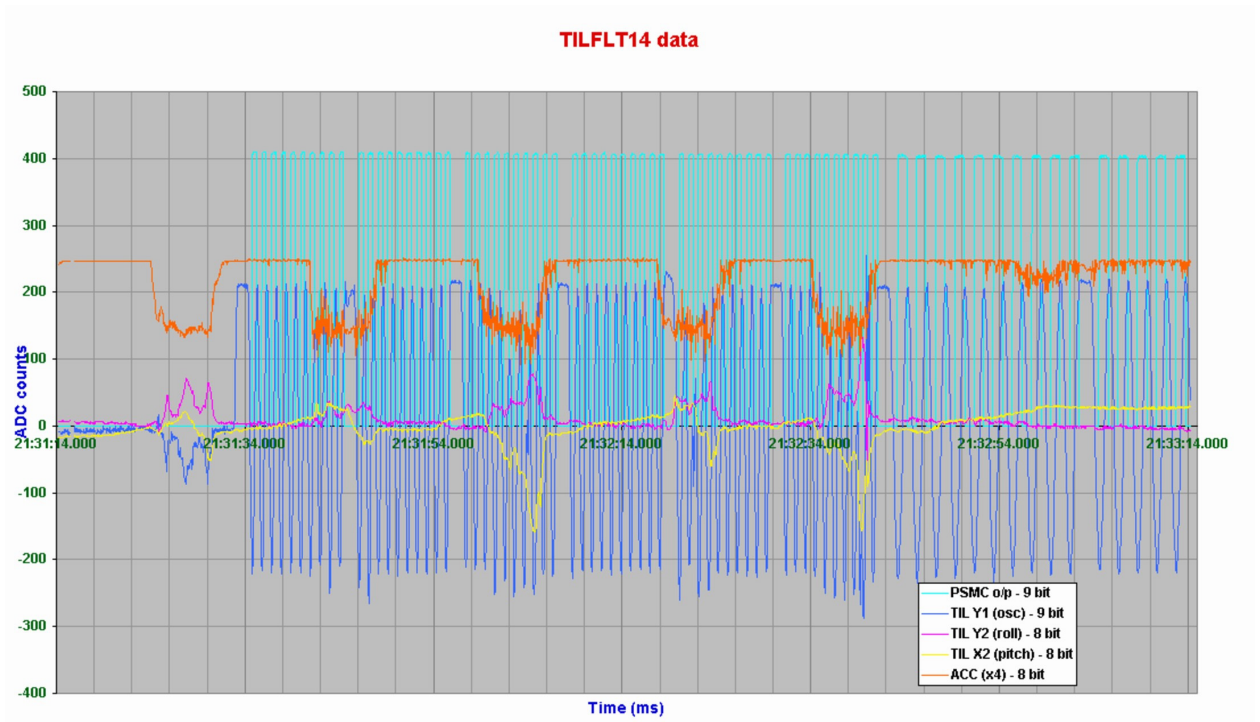


Figure (c): TILFLT14 raw data. See Figures 5.20-5.27 for calibrated results.

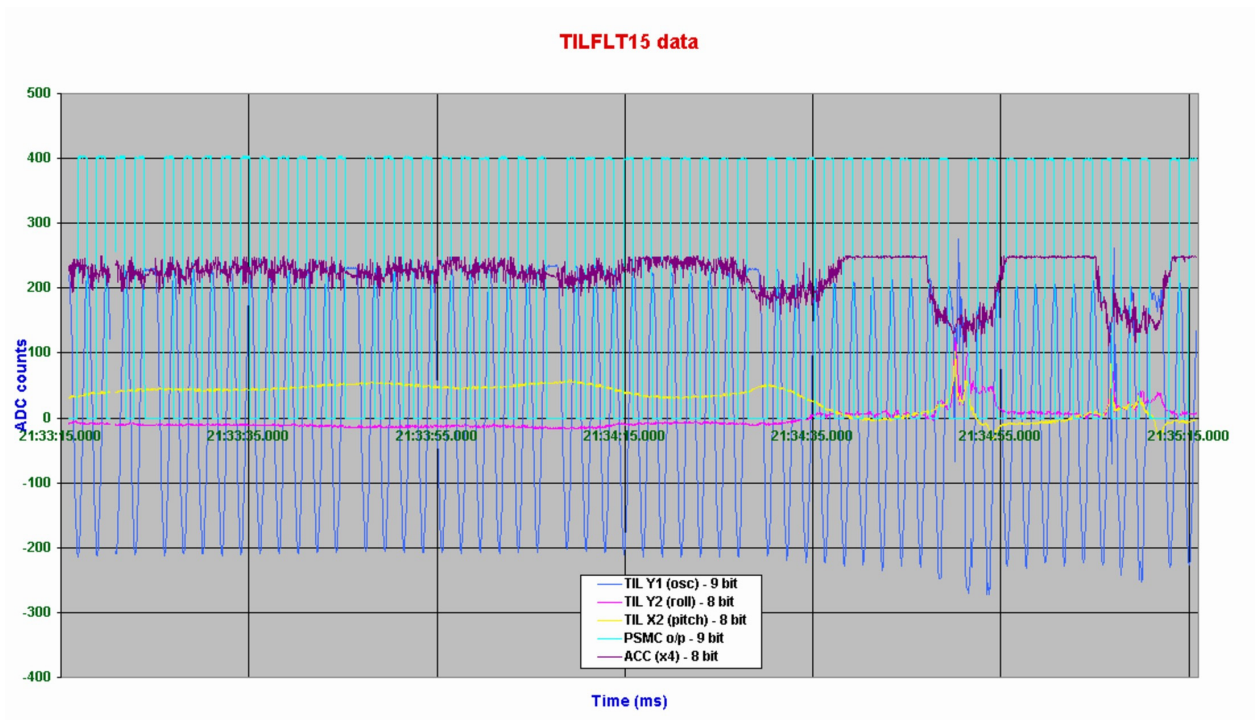


Figure (d): TILFLT15 raw data. See Figures 5.20-5.27 for calibrated results.

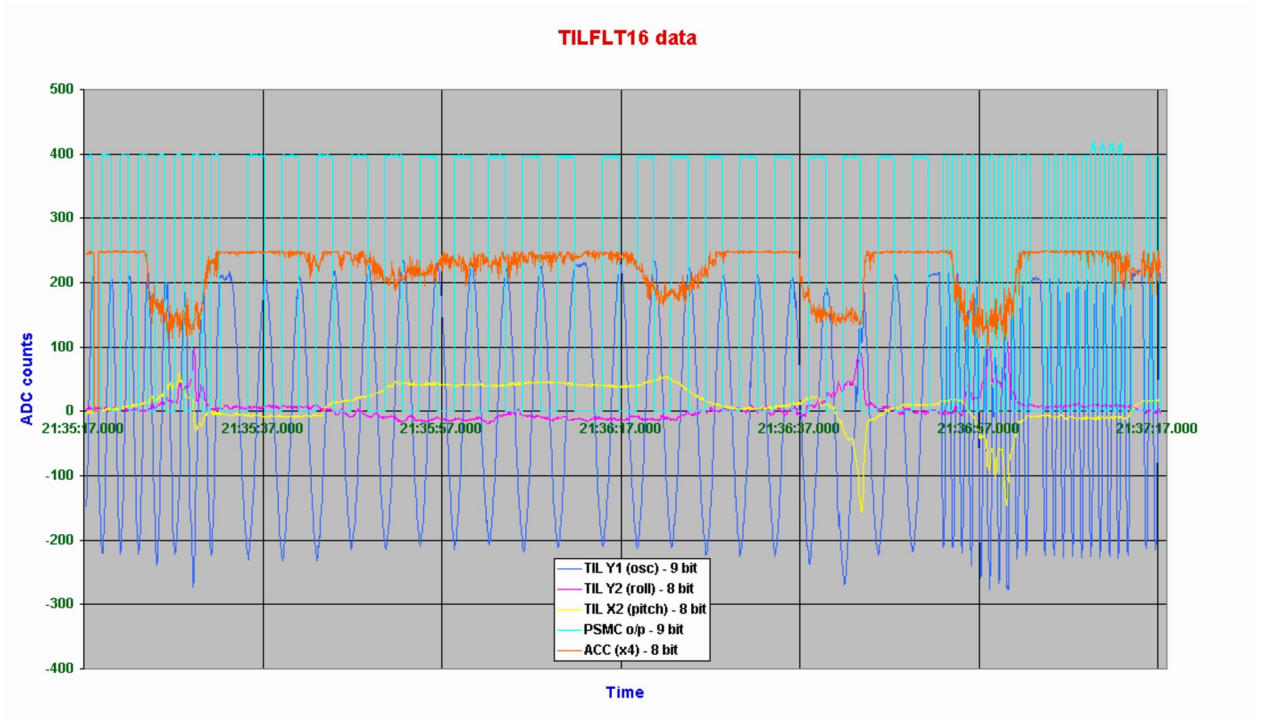


Figure (e): TILFLT16 raw data. See Figures 5.20-5.27 for calibrated results.

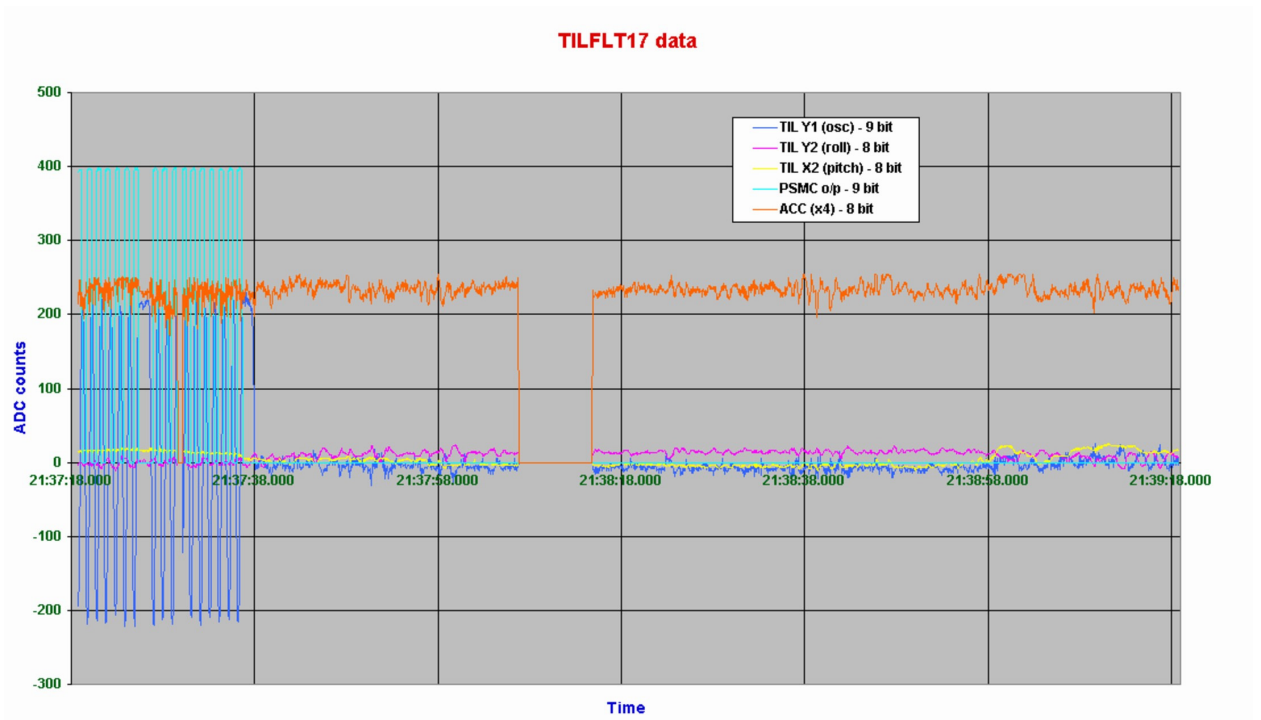


Figure (f): TILFLT17 raw data. See Figures 5.20-5.27 for calibrated results.

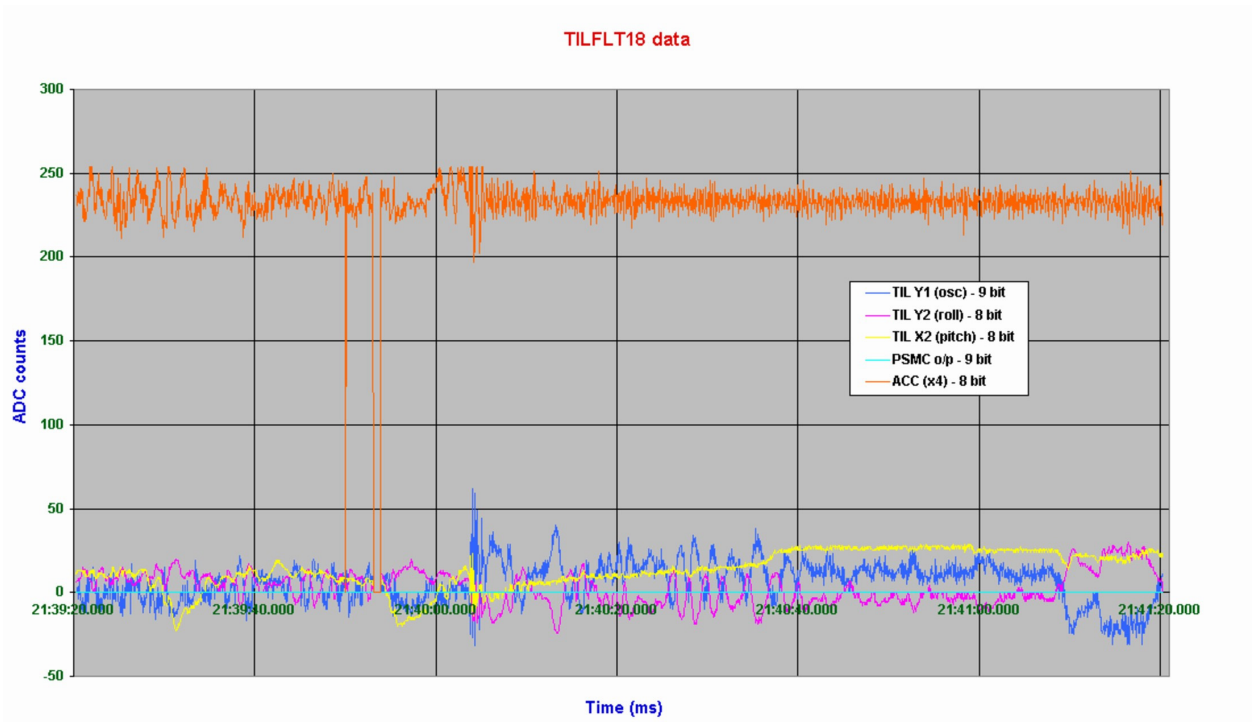


Figure (g): TILFLT18 raw data. See Figures 5.20-5.27 for calibrated results.

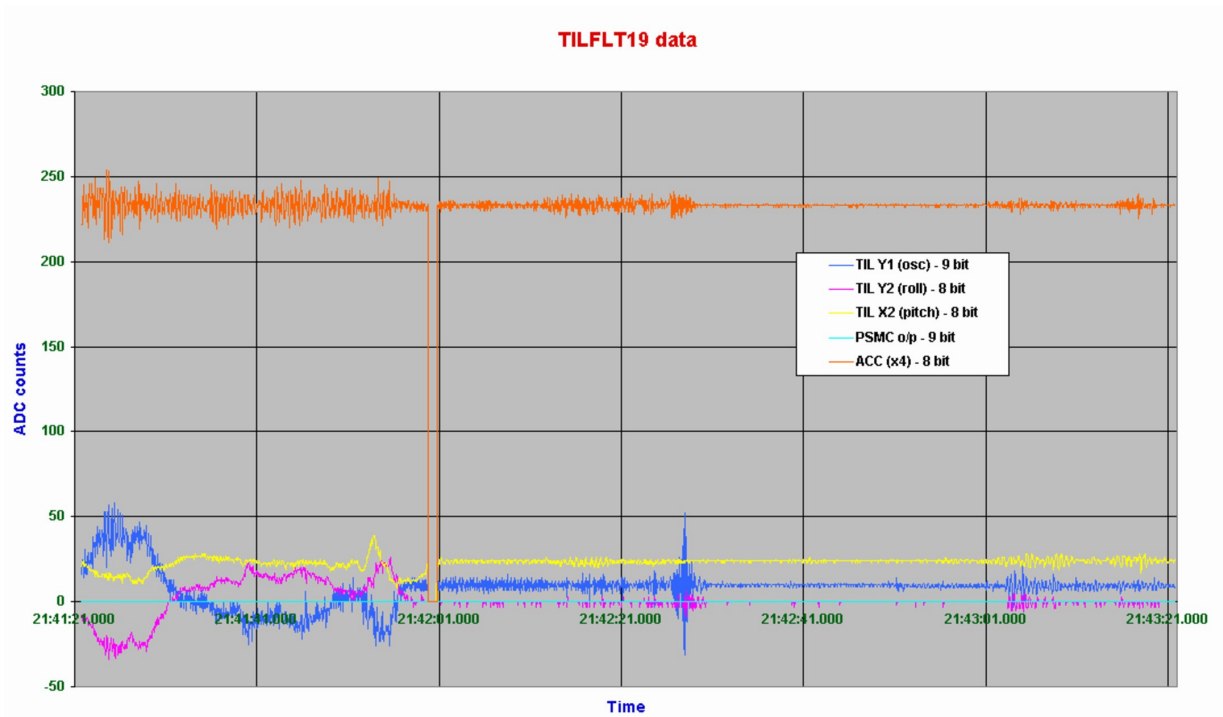


Figure (h): TILFLT19 raw data. See Figures 5.20-5.27 for calibrated results.

5.3.7 Data analysis: g-meter curves

Figure 5.7 shows the results from a simple MATLAB routine written to check the reconstruction of g-level from the g-meter. The graphs show a gaussian dip in the g-level, and a theoretical response of the g-meter spring. The algorithm is then tested to check the reconstruction of the original g-profile. It is seen to leave a residual oscillatory component however it is small enough to be neglected. Small spikes are also noticeable due to the numerical method employed and the flight g-meter signal was therefore smoothed.

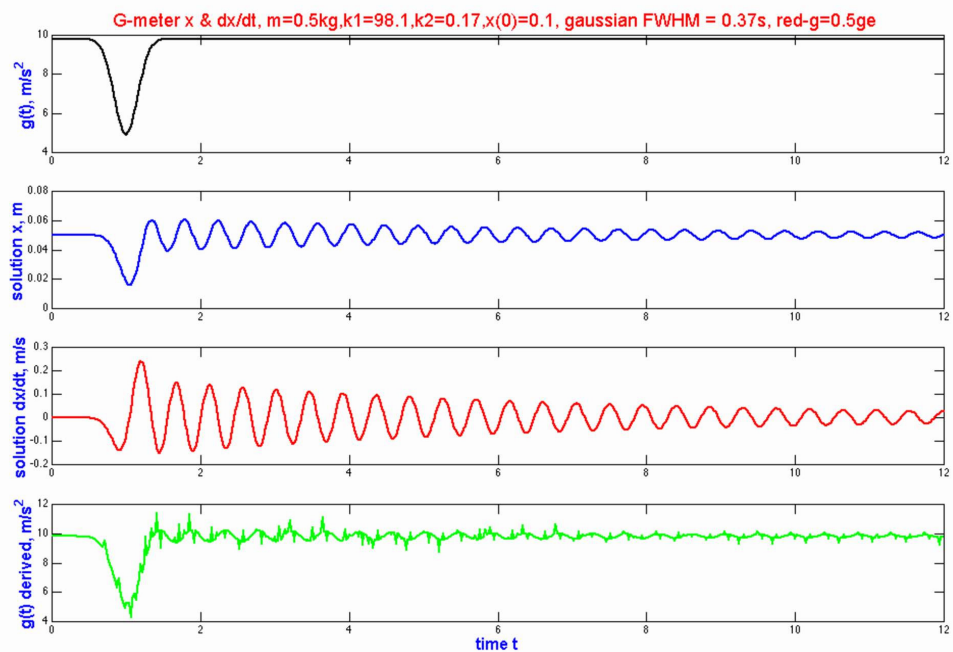


Figure 5.7: Simple test to check the g-meter algorithm, reconstructing a gaussian dip in g-level from the theoretical spring extension profile

Figures 5.8 to 5.12 present magnified views of five of the parabolas, and show the raw HASI ACC measurements, the derived g-level from the HASI-ACC measurements corrected for pitch as measured by the TIL-X2 sensor (see below), the raw g-meter measurements, and finally smoothed and unsmoothed g-level calculations from the g-meter algorithm. Both HASI-ACC/TIL-X2 and g-meter algorithm smoothing were carried out using an 8-pt moving average. The HASI-ACC derived, raw g-meter, and smoothed g-meter algorithm g-level results are used later in the plot of response time against gravity.

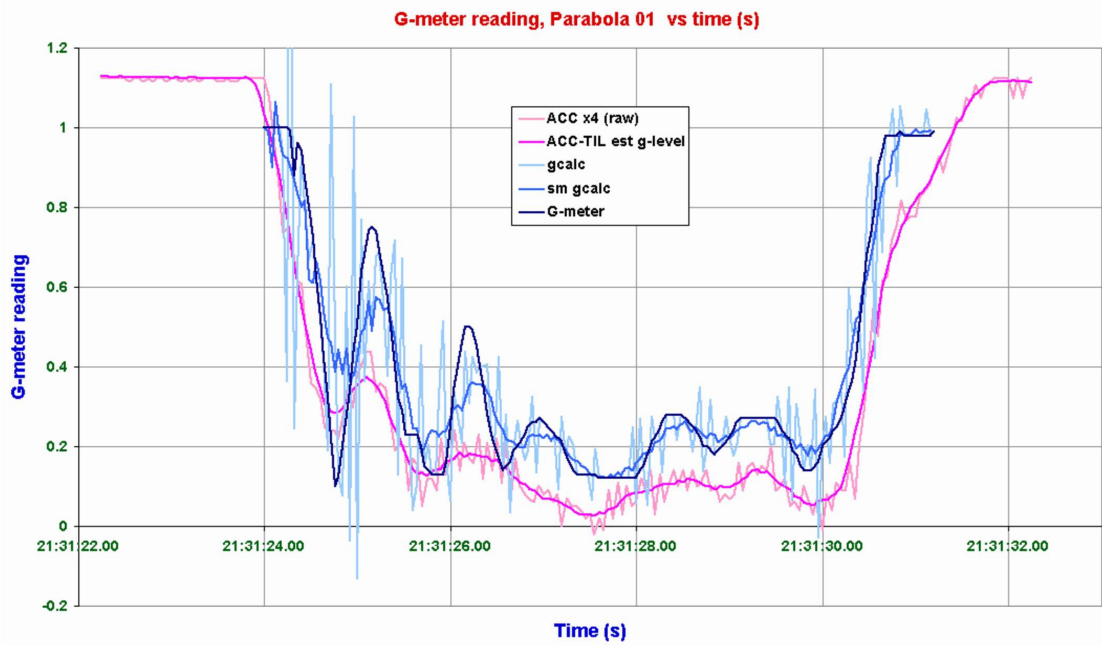


Figure 5.8: Parabola-1 g-levels

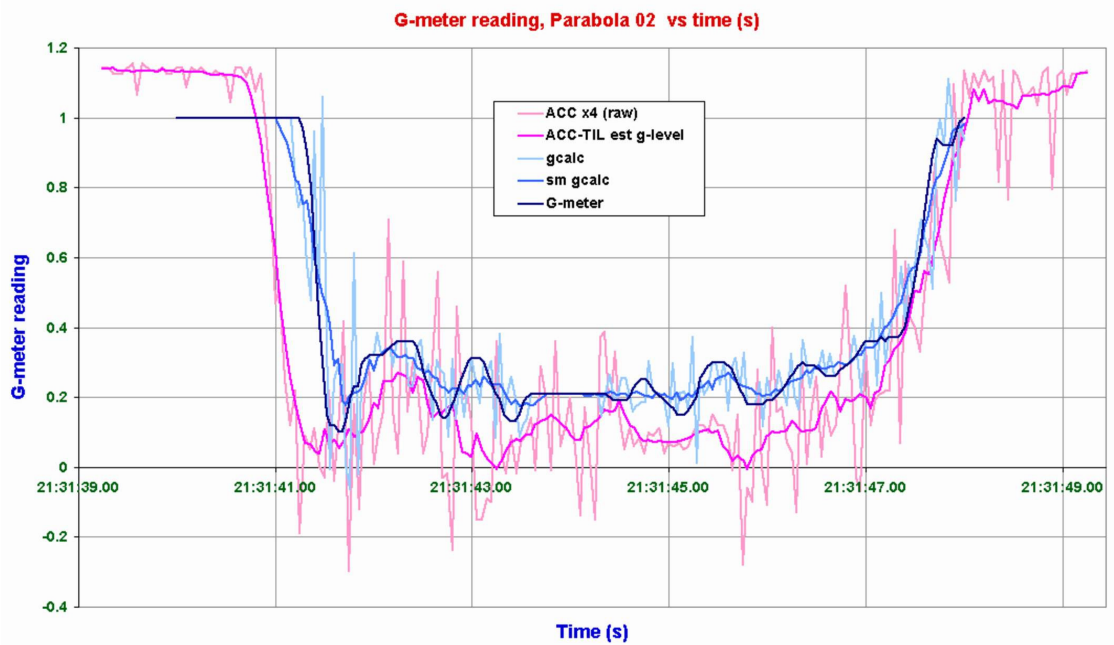


Figure 5.9: Parabola-2 g-levels

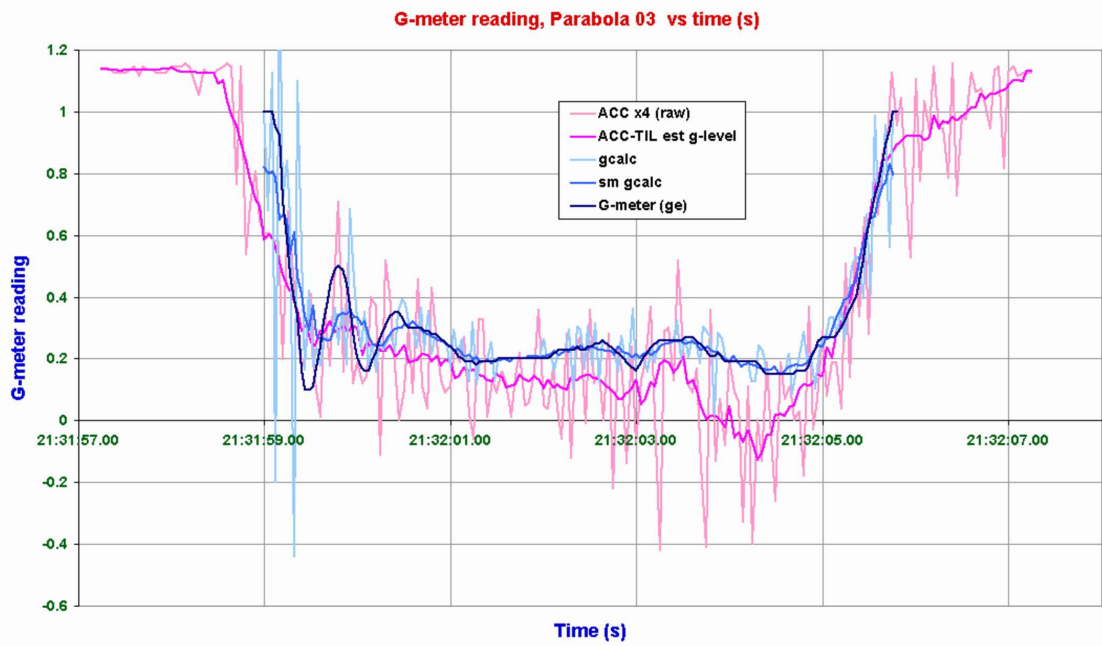


Figure 5.10: Parabola-3 g-levels

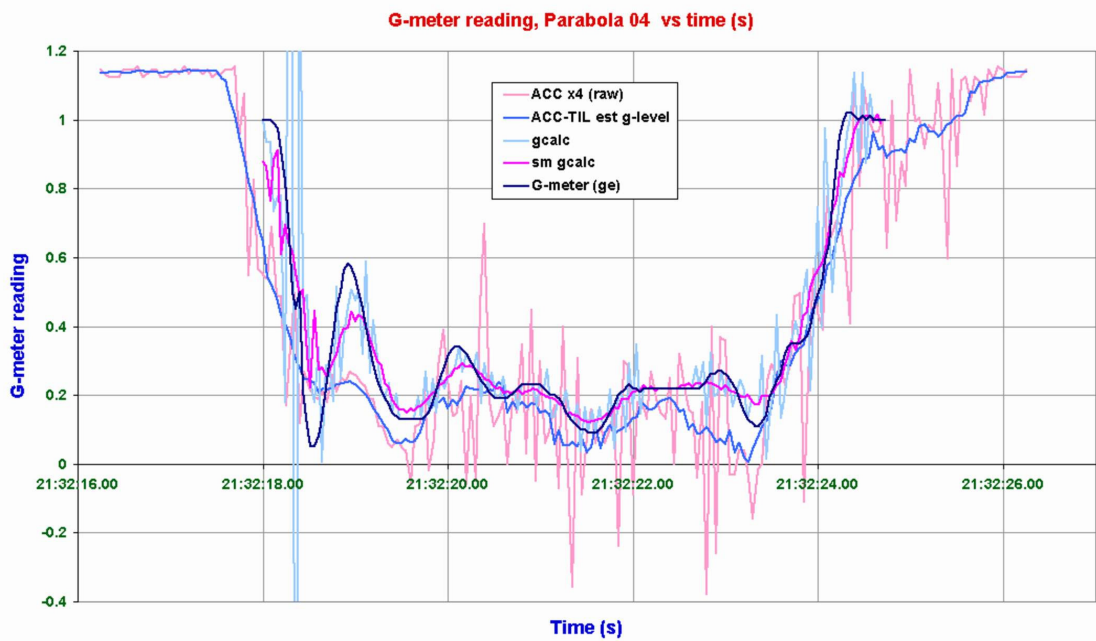


Figure 5.11: Parabola-4 g-levels

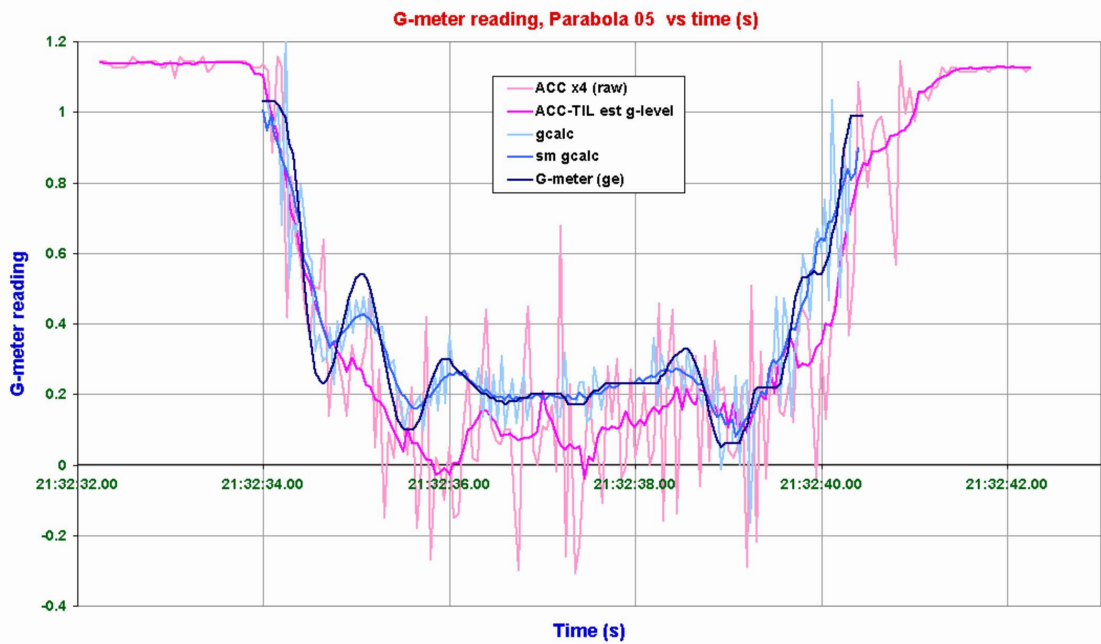


Figure 5.12: Parabola-5 g-levels

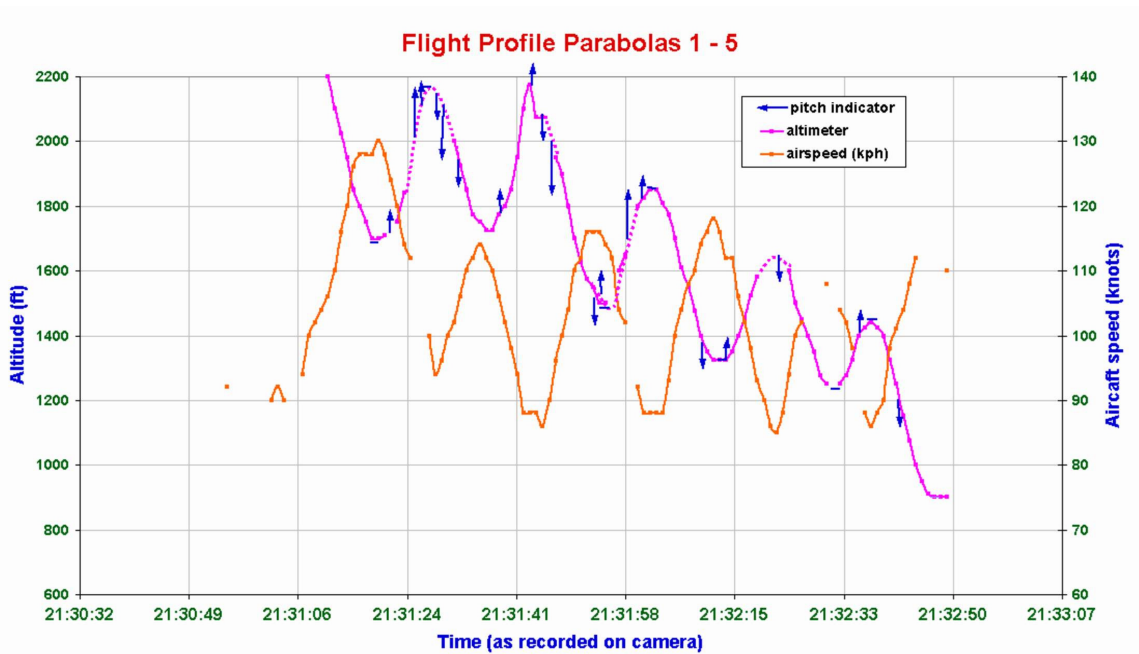


Figure 5.13: Airspeed (knots) and Altitude (ft) during parabolas, read from the analogue flight instruments

5.3.8 Data analysis: Flight instrument recordings

For interest, Figure 5-13 plots the aircraft altitude as recorded from the analogue altimeter using the VHS-C camera. Qualitative aircraft pitch is represented with arrows, however video resolution and instrument obscuration meant a more accurate pitch profile was unfortunately not possible without additional instrumentation (see discussion section 5.4).

5.3.9 Data analysis: TIL sensor response times

Response time measurement

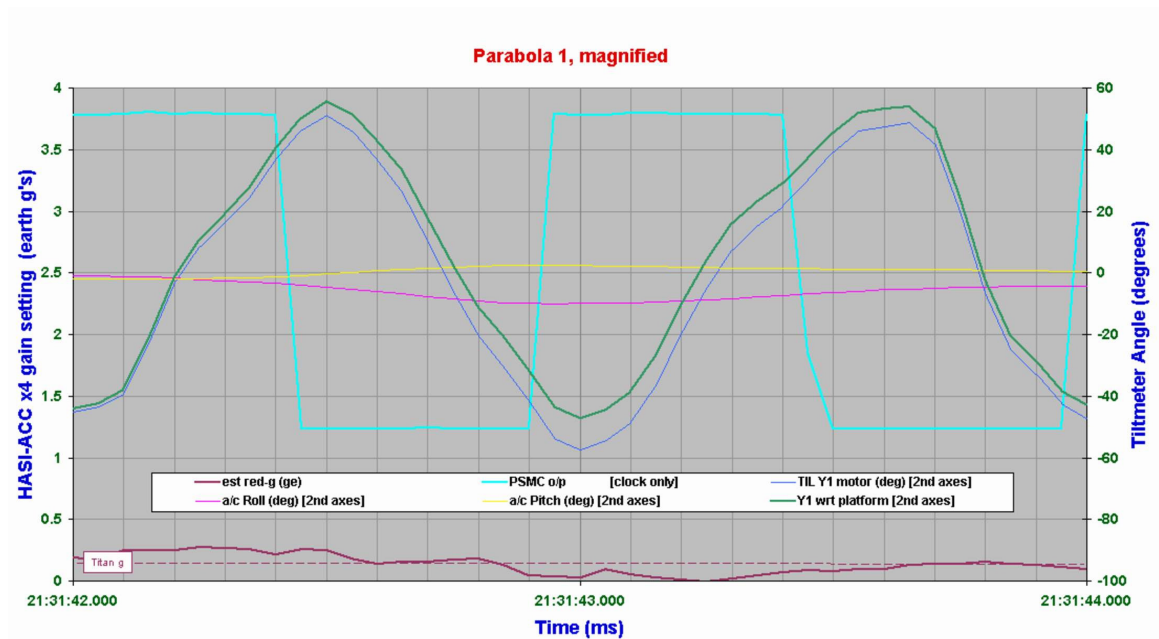


Figure 5.14: Close-up view of TIL-Y1 and PSMC output during parabola (some data removed for clarity)

Figure 5.14 shows a close-up of the calibrated data during one of the parabolas. For clarity some data has been removed from this picture. Figure 5.15 shows a diagram representing the PSMC output, the approximated simple harmonic motion of the TIL-Y1 plate, and the TIL-Y1 sensor output. Shown in the illustration are the phase lag between the TIL-Y1 plate position and the TIL-Y1 measurement, ϕ_{lag} , measured in rad s^{-1} , and the time lag, t_{lag} , measured in seconds.

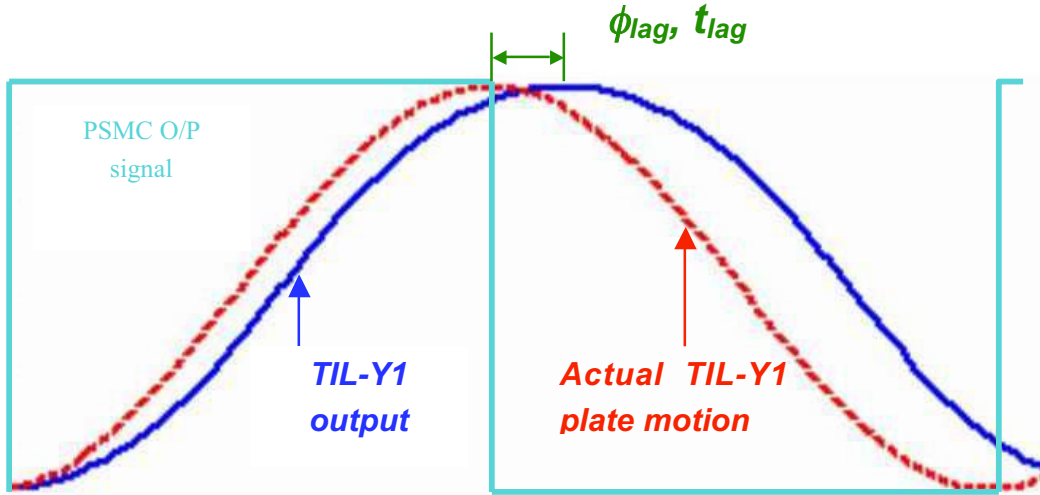


Figure 5.15: Diagram showing measurement made of time lag, t_{lag} , between TIL-Y1 sensor output and the actual TIL-Y1 plate motion, indicated during the experiment by the PSMC clock signal (PSMC O/P)

Theoretical variation of lag time with gravity

As shown in section 3.4, theoretical values for ϕ_{lag} and t_{lag} are given by

$$\phi_{lag} = \arctan\left[\frac{\tau(\omega_{shm}^2 - \omega_0^2)}{2\omega_{shm}}\right] + \frac{\pi}{2} \quad (5-8(a))$$

and

$$t_{lag} = \frac{\phi}{\omega_{shm}} \quad (5-8(b))$$

where τ and ω_0 are the time constant and natural frequency of the TIL-Y1 sensor fluid, and ω_{shm} is the angular frequency of the TIL-Y1 plate motion.

Recalling the discussion of section 3.5, where it was shown that ω_0 could be considered approximately proportional to $g^{-1/2}$, then for a general g-level g_g measured in ms^{-2} , the natural frequency of the fluid under conditions of that g-level, ω_{0g} may be written

$$\omega_{0g} = \left(\frac{g_g}{g_e}\right)^{1/2} \omega_{0e} \quad (5-9)$$

where g_e is $9.81ms^{-2}$ and ω_{0e} is the natural frequency of the fluid under 1-g conditions. Thus t_{lag} may be rewritten as

$$t_{lag} = \frac{1}{\omega_{shm}} \left\{ \arctan \left[\frac{\tau(\omega_{shm}^2 - [g_g/g_e]\omega_{0e}^2)}{2\omega_{shm}} \right] + \frac{\pi}{2} \right\} \quad (5-10).$$

Comparison of observation and theory

Figure 5.16 shows a plot of measured TIL-Y1 t_{lag} values, against g -level as derived using three different methods, the HASI-ACC measurement corrected for aircraft pitch, the raw g -meter reading and the processed g -meter measurement. The Figure also illustrates the comparison with the theoretical variation represented by equation 5-10.

Whilst a similar trend in the increase of response time with decreasing g -level is clearly observed, the correlation with theory is perhaps disappointing. The HASI-ACC derived g -level measurement depended upon TIL-X2 measurement of pitch which, as discussed below, is strongly susceptible to aircraft accelerations. Nevertheless the HASI-ACC / TIL-X2 measurements, as shown in Figures 5.8 – 5.12, did not depart significantly enough from those of the g -meter to explain the discrepancy between observation and theory of Figure 5.16. Since the 1- g values for t_{lag} were most severely underestimated, it is considered most likely that the measurement sampling rate possible with the available data recorder, a maximum rate for six channels of 20Hz, was simply insufficient to more accurately resolve the time lag of the sensor fluid. This again has been highlighted throughout this work and is recommended as a key issue for future investigations.

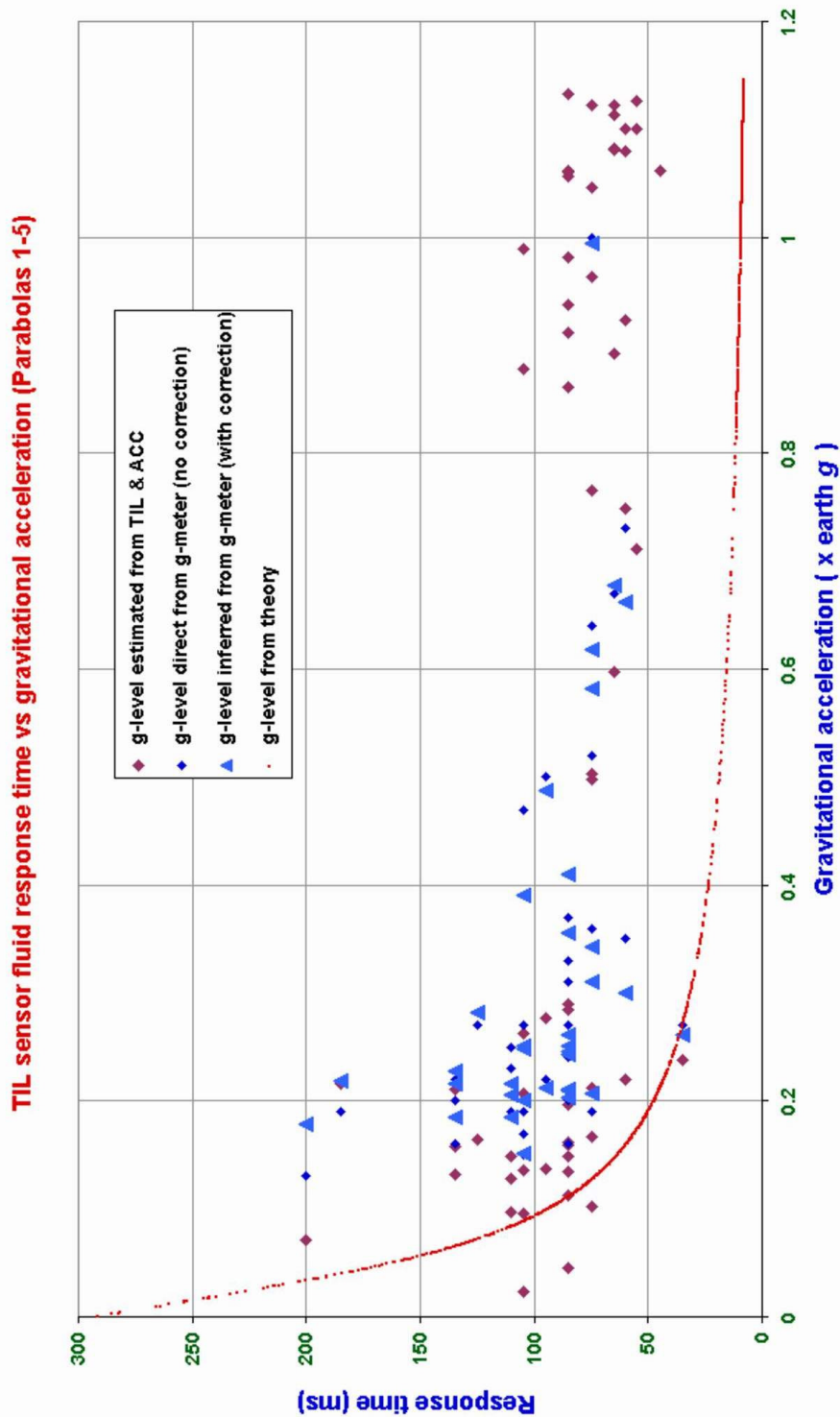


Figure 5.16: TIL-Y1 time lag plotted against g-level

Another source of error is the accuracy of the approximated simple harmonic motion of the TIL-Y1 plate. The theory above assumes perfect simple harmonic motion is achieved which, as shown in section 4.3.4, was not quite the case. A more accurate

method of determining the TIL-Y1 plate position would be to use some form of relative inclination measurement tool, such as was described in section 3.2.1. With a continuous record of the TIL-Y1 plate a more complicated calculation of the theoretical time lag would be possible, rather than having to assume perfect simple harmonic motion. This set-up however would still necessitate a higher sampling rate than 20Hz.

Vibration effects and slight radial offset of the centre point of the TIL-Y1 sensor from its oscillation axis may have also contributed to the discrepancy between observation and theory, and whilst these effects are believed to have been less significant these are important areas of focus for any further investigation in future.

Such discussions as those of the previous two paragraphs have focussed on the correlation with theoretical variations of the TIL-Y1 response, and whilst this is clearly important it can lead to oversight of an important achievement of the experiment. As outlined in the requirements of the experiment, a principal aim was to investigate the deterioration of the TIL sensor response under Titan-representative gravity levels. From the results shown in Figure 5.16 it may be said that an observed upper limit of 200 ms can be offered for the time lag of the sensor to oscillatory motion at 1Hz, at the levels of gravity expected on Titan. Furthermore it is strongly suspected that this is a conservative value due to possible errors described above. Considering the predicted frequency response of the sensor shown in Figure 3.11, this suggests that a maximum time lag of no more than around 300ms for 4Hz oscillations may be expected under Titan gravity and, as will be shown in Chapter 6, oscillations likely to be experienced by the Huygens probe after parachute deployment are unlikely to approach this high a value.

Whilst it is acknowledged that the time lag measured in this experiment may be an overestimate, it is interesting to attempt to see the implications for the TIL responses modelled in section 3.5 assuming these observed values. It was found that by assuming ω_0 for the fluid surface to be 0.6 times its measured value in section 3.4.1 under more tightly controlled experimental conditions, the flight observed time lag t_0 could be simulated. Figure 3.17 shows the responses to simple harmonic motion, a gaussian pulse and a step change in inclination, assuming the flight derived value of ω_0 . Again it must be stressed that these responses may only be considered worst-case estimates due to the inaccuracies inherent in flight derived values. Theory still predicts the responses shown in section 3.5. As shown from the Figure, even if the flight derived response times were correct, the TIL sensor would still achieve its equilibrium orientation in under 1 second. For very rapid motions it is shown that the TIL sensor would not accurately represent the amplitude of pulse or oscillatory

inclination changes, however the speed of such motions are above those likely to be expected on Titan.

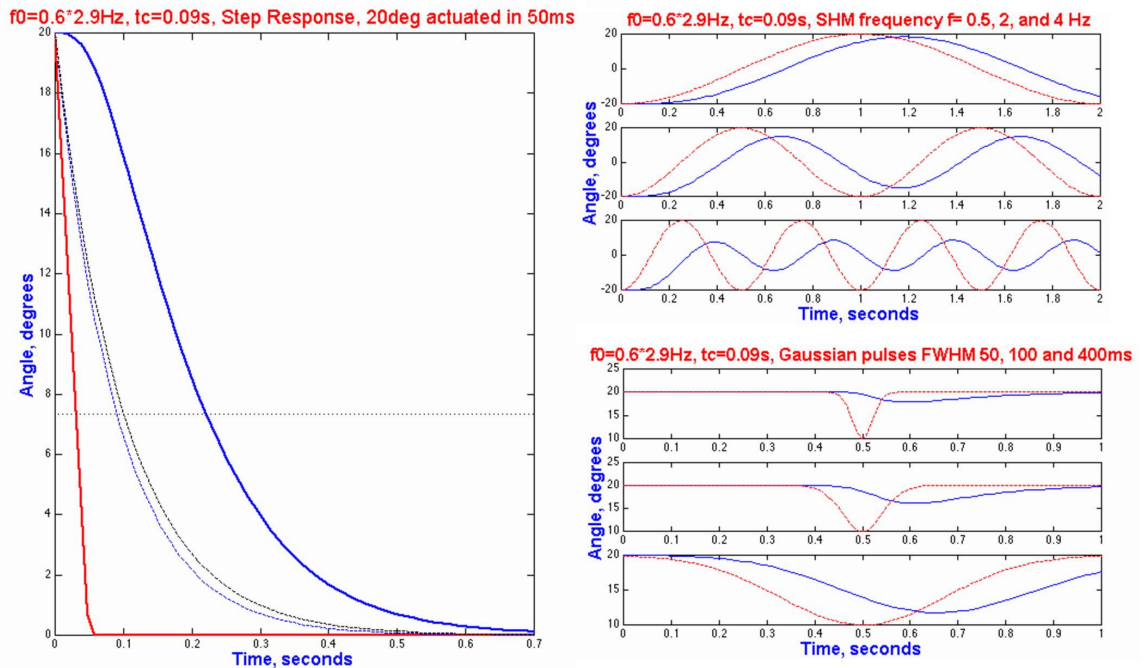


Figure 5.17: Step, simple harmonic motion and gaussian pulse responses of the TIL sensor if flight derived g-response were taken to be accurate.

It should be noted when considering these time response values, such responses are representations of the time lag between the sensor output and the equilibrium orientation of the sensor fluid surface. As shown in the next chapter, this is however only part of the story in evaluating the TIL sensor’s general response. As illustrated in the next section, and modelled further in Chapter 6, the effects of linear accelerations upon the TIL sensor fluid are strongly significant.

5.3.10 Data analysis: Flight profile reconstruction

Conversion between TIL sensor and aircraft axes

A secondary aim of the experiment was to investigate the outputs of the TIL and HASI-ACC sensors acting in complement throughout the dynamic environment of aircraft flight. Using the calibration settings as shown in section 5.3.5, the raw data was converted to the parameters being measured and the TIL-Y1, TIL-Y2, and TIL-X2 and HASI-ACC data were smoothed using an 8-pt moving average. This resulted in profiles of platform z-axis acceleration, TIL-Y1 plate tilt relative to the local horizontal, and platform pitch and roll relative to the local horizontal from the TIL-X2 and TIL-Y2 sensors respectively. Whilst perhaps useful in its own right, this was not the information required and conversion to aircraft axes was required to permit interpretation of the flight profile. Additionally the correct measurement of the TIL-

Y1 plate position relative to the platform, hence giving more accurate indication of the motor step position, required conversion from earth axes (i.e. measurements relative to the local horizontal) to platform axes.

The conversion of the TIL-Y1 signal to platform axes was achieved through subtraction of the TIL-Y2 measurement, as designed. This successfully showed oscillations of fixed amplitude between $+50^\circ$ and -50° , to within $\pm 2^\circ$, relative to the platform z-axis.

In order to obtain the aircraft pitch and roll it was necessary to remove the inclination of the platform relative to the horizontal which was a function of its mounting in the rear seat and the orientation of the aircraft seat relative to the horizontal. Consequently measurements taken with both TIL-X2 and TIL-Y2 when the aircraft was not only on the ground but also stationary, to eliminate any linear accelerations on the fluid, were then subtracted from the TIL-X2 and TIL-Y2 profiles. This method assumed that the ground at the point of measurement, the pan just outside the airfield hangar, had zero gradient. In the absence of linear accelerations therefore TIL-X2 and TIL-Y2 were then measurements of aircraft pitch and roll. Knowing the static values for the platform orientation relative to local horizontal, the angle between the platform z-axis and the local vertical was calculated. This in theory then allowed the HASI-ACC acceleration measurement to be resolved into components along the aircraft roll and yaw axes, where it was assumed that the platform roll axis lay within the plane containing the aircraft pitch and yaw axes. Put simply, this meant assuming the platform was pointing forwards, even though possibly inclined downwards and tilted sideways. Figure 5.3 summarised these platform and aircraft axes conventions.

TIL offsets due to linear accelerations during flight

Clearly however a limitation exists in the accurate use of TIL-Y2 and TIL-X2 as indications of roll and pitch, since any linear acceleration along either the pitch or roll axis respectively will induce an offset in the sensor fluid inclinations, as shown in section 3.2.3. Figures 5.18(a)-(c) illustrate, with some simplification, the effects of linear accelerations associated with the aircraft flight.

Assuming the straight and level flight of Figure 5.18(a), for an acceleration a (with a being the resultant of acceleration due to engine thrust minus acceleration due to drag), the TIL sensor fluid will exhibit an inclination offset θ given by the inverse tangent of (a/g) , as per equation 3-1. During periods of constant speed therefore such offset is zero and the TIL-X2 sensor gives a good indication of pitch. Clearly however horizontal accelerations were experienced during flight and it is useful to consider the levels of TIL offsets likely to have existed throughout the flight.

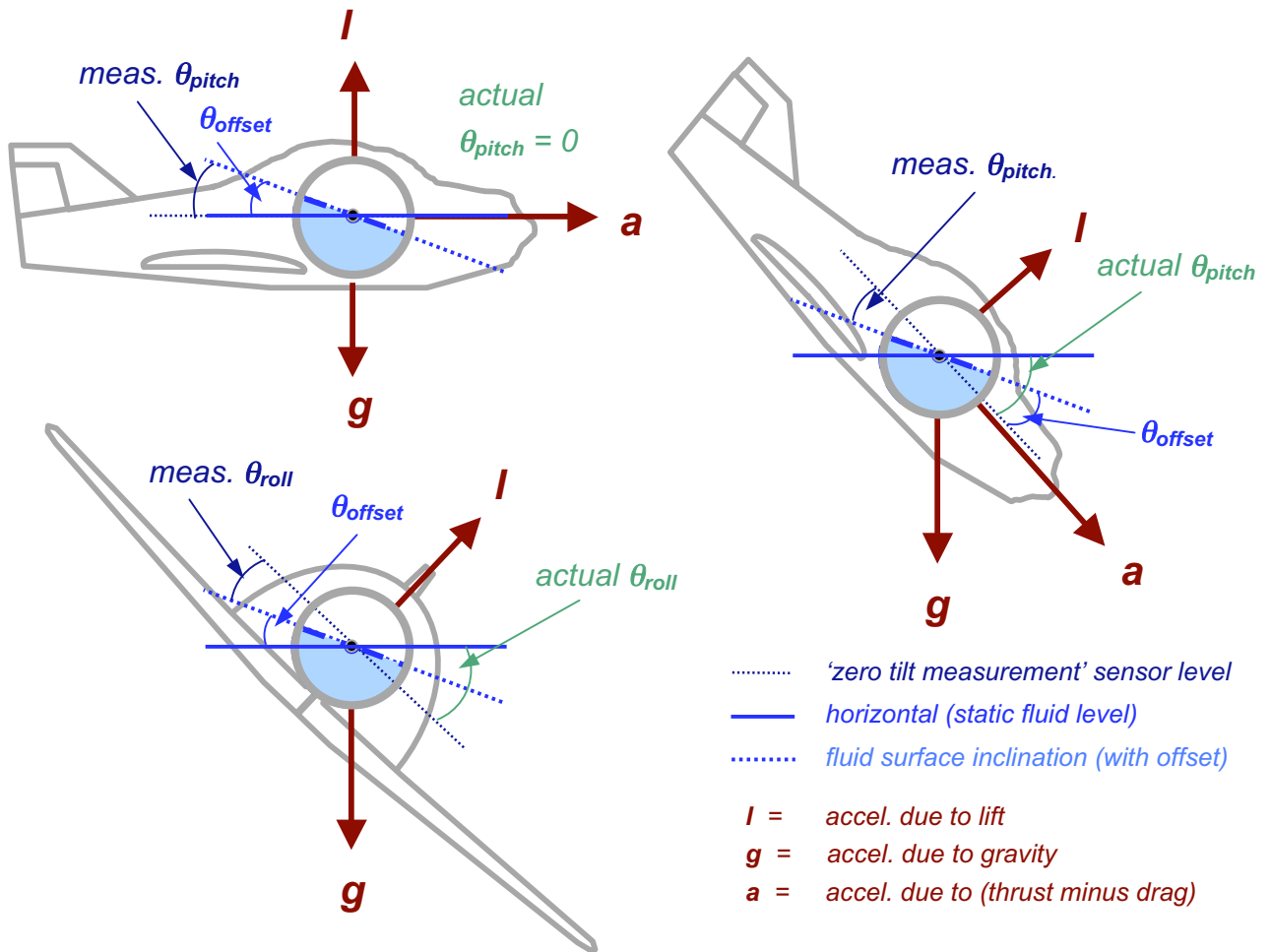


Figure 5.18: Influence of linear accelerations on the TIL-X2(pitch) measurement (a) during horizontal acceleration, and (b) during a dive, and on the TIL-Y2(roll) measurement (c) during banking

Unfortunately flight computers would have been useful for this, however for certain phases of the flight some data is available from the video camera. Figure 5.19 shows a graph similar shown previously for the parabolas, showing the altitude and airspeed during descent, final approach, and landing, as measured from the analogue flight instruments using the camera.

Assuming the pitch was small such that component of gravity along the flight vector was also small, and the aircraft was aligned with the runway direction throughout, maximum values of a during the descent can be estimated at $\pm 1 \text{ kph s}^{-1}$, or approximately $\pm 0.3 \text{ m s}^{-2}$. This would suggest TIL-X2 offsets of around $\pm 2^\circ$. Higher levels of horizontal acceleration did occur during the flight, as indicated by the audio commentary, however if it is assumed that these were unlikely to have exceeded $\pm 2 \text{ kph s}^{-1}$ then offsets during approximately straight and level flight can be considered to be less than 5° .

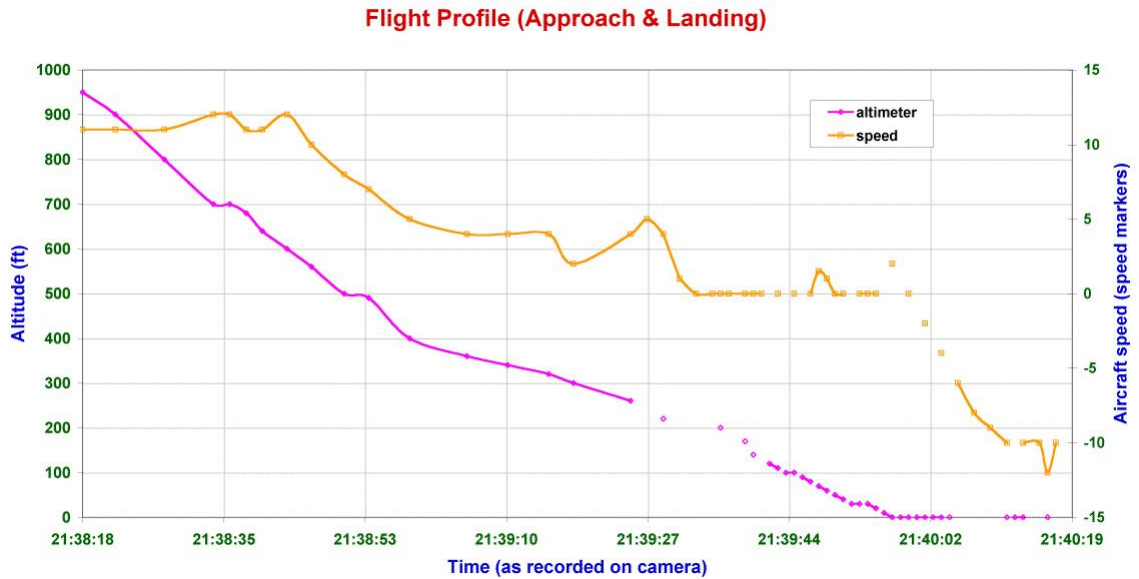


Figure 5.19: Airspeed (knots) and Altitude (ft) during final approach and landing, as read from the analogue flight instruments

During climbing or diving the offset is perhaps less obvious, however its existence can be understood by considering the forces indicated in Figure 5.18(b). The TIL sensor measures the angle of inclination by measuring the angle between the fluid surface and the sensor reference level. For static conditions the fluid surface would of course adopt the solid blue line, perpendicular to gravity. When the acceleration due to lift and any acceleration a , due to the resultant force of thrust and drag, are considered, equation 3-1 suggests that the offset will be given by

$$\tan\theta_{offset} = \frac{(L \sin \alpha + a \cos \alpha)}{g} \quad (5-11).$$

This would lead to a reduced tilt being measured since the sensor will now, erroneously, indicate a pitch measured by the angle between the dashed blue line and the sensor reference level in Figure 5.18(b). (It is clear from this diagram and equation 5-11 how the pilot may create zero-g conditions, by zeroing both the lift and balancing thrust and drag). Unfortunately from the data available it is difficult to estimate the TIL-X2 offset θ_{offset} during the parabolas without more flight data giving information on the aircraft pitch, allowing the accelerations in Figure 5.13 to be resolved into the gravitational component and the thrust related component. The steepest accelerations were observed immediately before and after the parabola, with airspeed accelerations being measured at approximately $\pm 10 \text{ kph s}^{-1}$, or around 3 m s^{-2} . If pitch had been assumed to be small, then these values would have suggested offsets of around $\pm 15^\circ$, however it is well known that the profile was such that these accelerations had a significant gravity component and the offset will be less than this. More information is required about the pitch however to calculate an

actual offset. An attempt was made to use the HASI-ACC data, which measured acceleration in the aircraft z-axis, to resolve the gravity component however without information about the elevator controls it was difficult to remove the lift component acting along this axis. Attempts to use the altimeter data yielded mixed results and would benefit from more accurate flight control data.

During banking, shown in Figure 5.18(c) a similar effect to that during the climb or dive is observed, but with the TIL-Y2(roll) sensor. It is a common experience that the steepness of an aircraft turn depends on the lift generated in the direction indicated. Similarly the offset of the TIL sensor will increase with the lift generated, and as shown above the TIL measurement of aircraft bank will be an underestimation of the true level. As mentioned above, attempts to use the analogue altimeter data yielded mixed results and more accurate information was required.

Finally, an ambitious attempt was made to consider the aircraft whilst taxiing. Under these conditions the pitch angle was known to be zero, and therefore by using the TIL-X2(pitch) offset data it was hoped that the forward acceleration could be deduced, and integrated to obtain the velocity and even displacement profile. Furthermore using the derived velocity data it would theoretically be possible to use the TIL-Y2(roll) offset data to deduce information regarding the turning profile during taxiing. The only available boundary conditions were the final velocity when the aircraft came to rest outside the hangar.

Unfortunately due to noise and the cumulative errors inherent in this calculation, a touch-down velocity of over 230 kph was derived which was more than a factor of two higher than the value of the airspeed indicator prior to touchdown of around 60 knots or 110kph. The exercise illustrated some interesting reconstruction possibilities however. A horizontal accelerometer could have reduced the level of uncertainty surrounding certain measurements, and the entire exercise highlights the iterative nature of motion reconstruction using these sensors.

Calibrated flight profile with annotations

Having made attempts to quantitatively reconstruct elements of the flight profile with mixed results, reasonable success was achieved with a qualitative reconstruction and signatures of several key flight events are well represented in the data. The smoothed flight data, processed to give estimations of the aircraft flight profile and the TIL-Y1 motion relative to the platform axes, is shown in Figures 5.20 to 5.27 over the following pages. Again file names are included for reference, each representing a 120 second data sample with a gap of 1.45s between adjacent files. Annotations highlight areas of interest. Also of note is the signal noise due to engine vibrations, aircraft buffeting, and platform motor vibrations which further inhibit a more quantitative reconstruction.

**TILFLT12 calibrated flight data, 2nd reduced gravity flight, Sat 17th July 1999
(taxi, take-off and climb)**

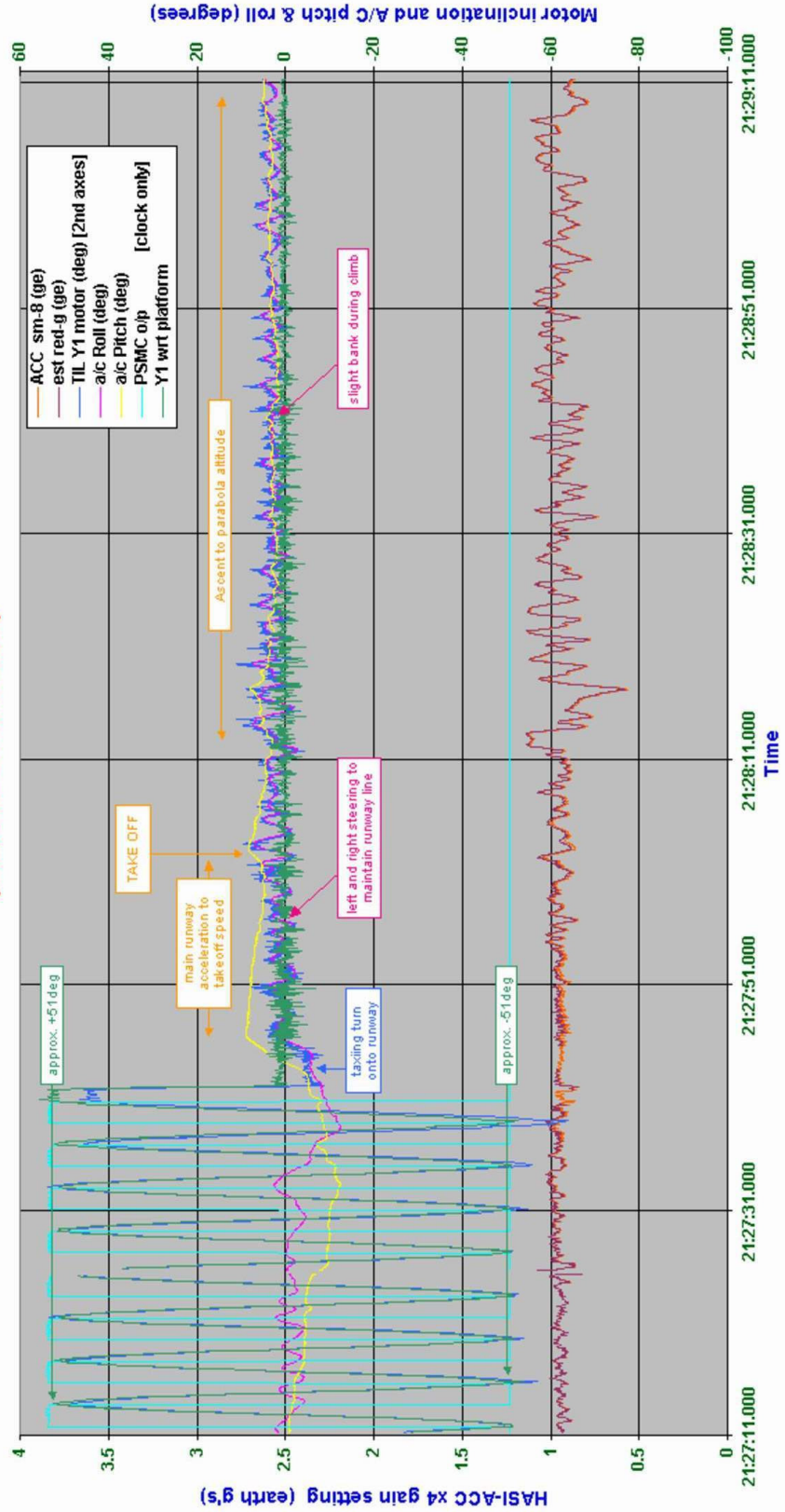


Figure 5.20: TILFLT12 flight profile , featuring taxi, take off and climb (21:27:11 to 21:29:11)

**TILFLT13 calibrated flight data, 2nd reduced gravity flight, Sat 17th July 1999
(preparing for parabolas)**

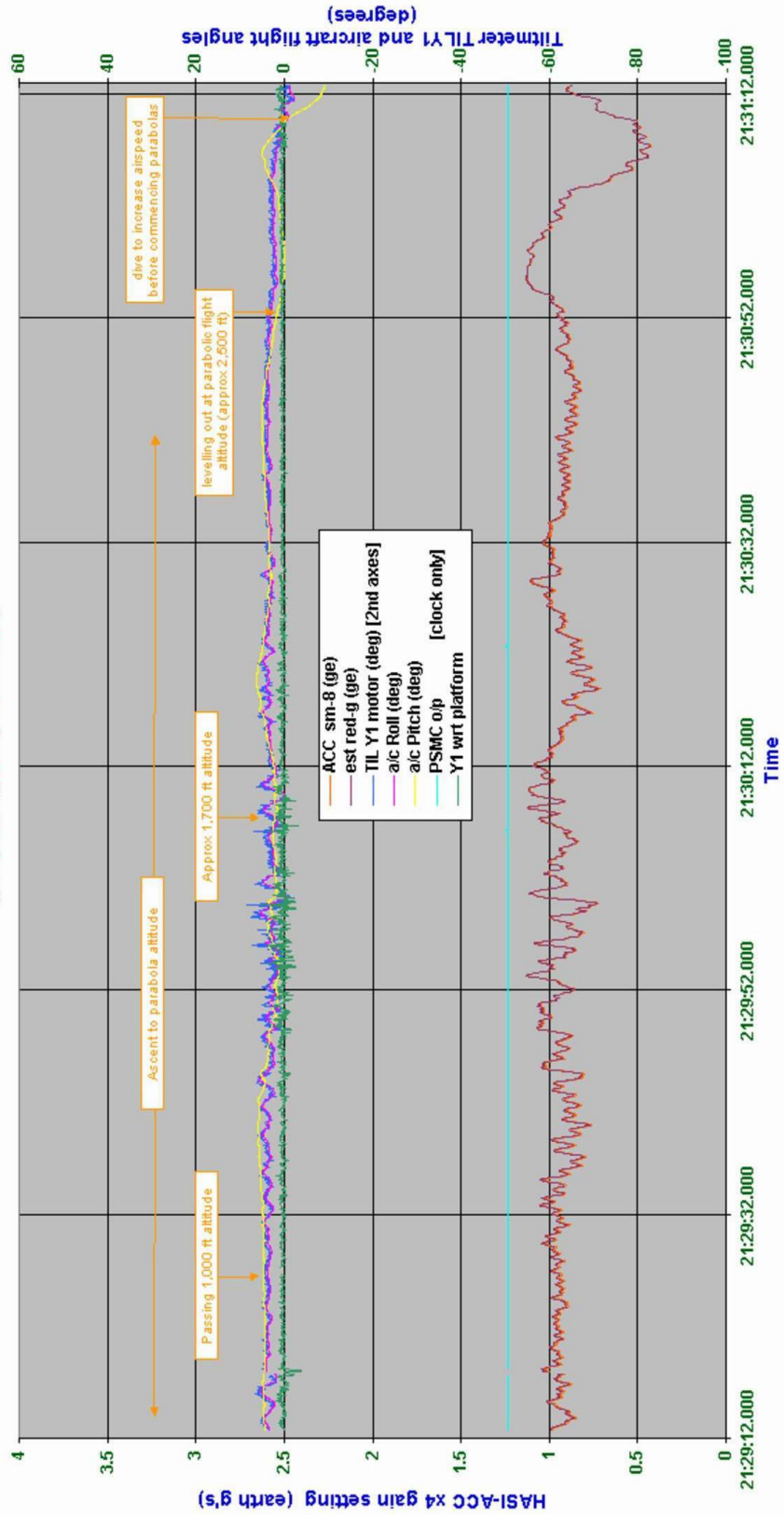


Figure 5.21: TILFLT13 flight profile, featuring flight pre-parabolas (time 21:29:12 to 21:31:13)

**TILFLT14 calibrated flight data, 2nd reduced gravity flight, Sat 17th July 1999
(parabolas 1,2,3,4,5)**

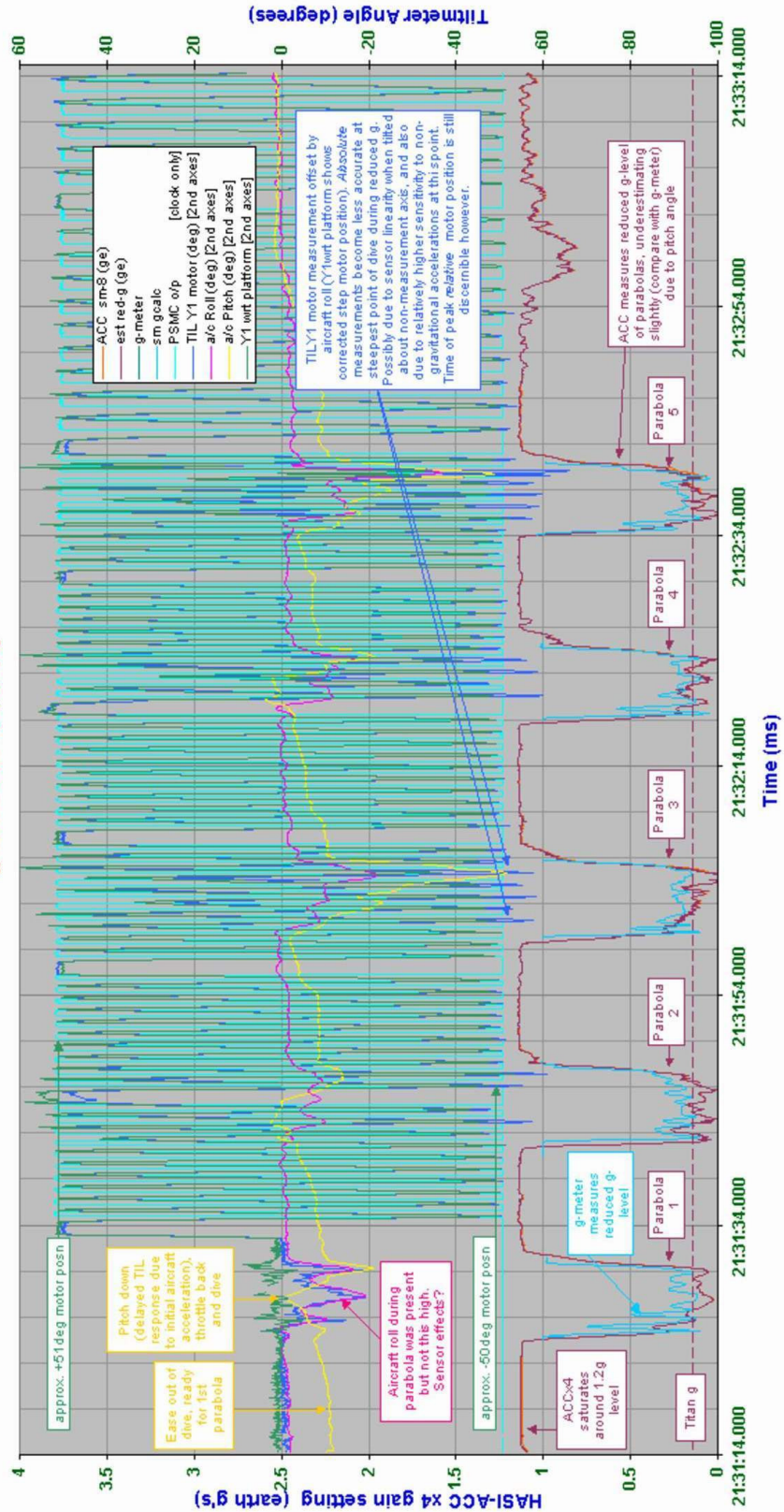


Figure 5.22: TILFLT14 flight profile, featuring parabolas 1-5 (time 21:31:14 to 21:33:14)

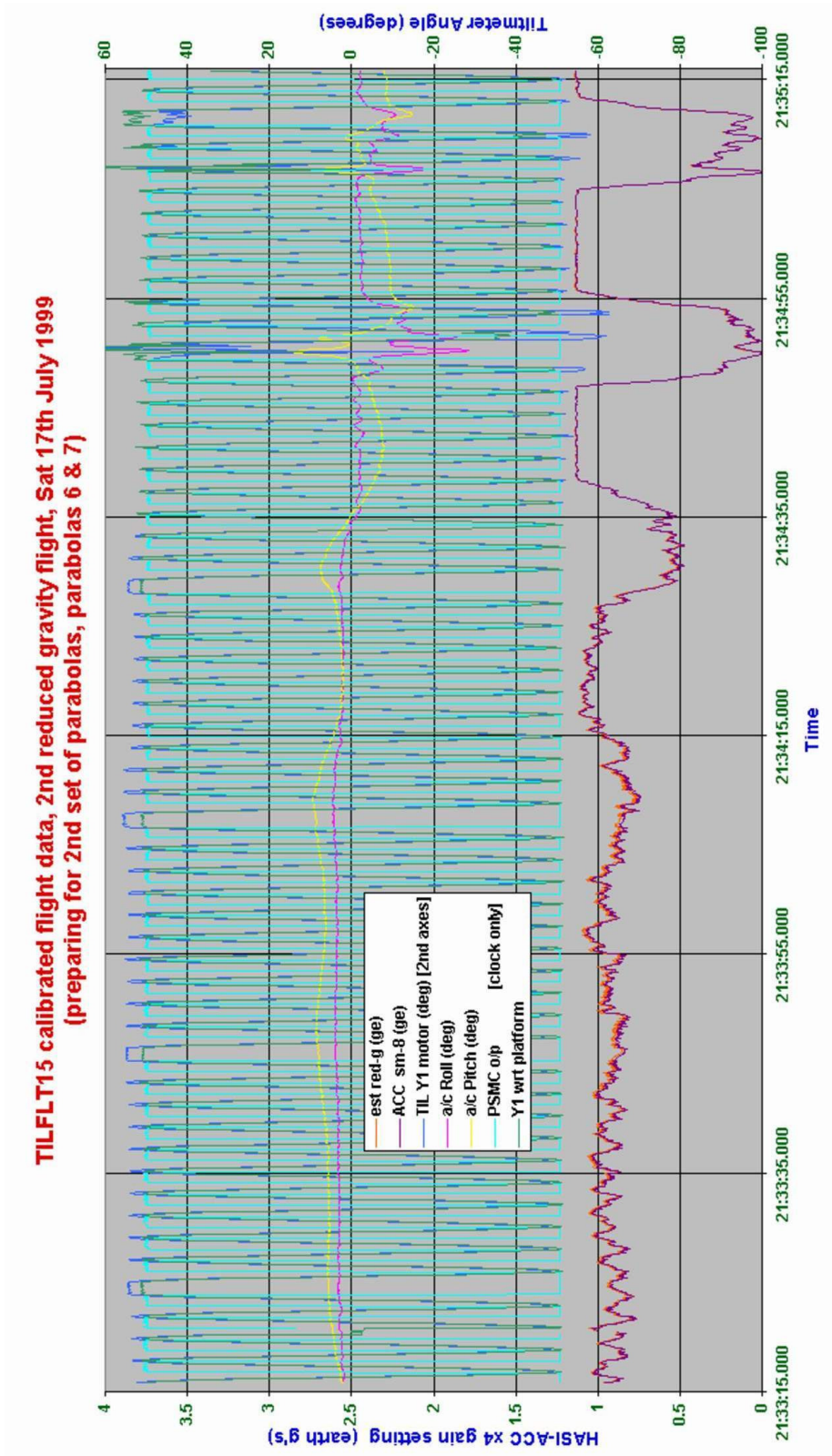


Figure 5.23: TILFLT15 flight profile, featuring ascent and parabolas 6 & 7 (time 21:33:15 to 21:35:16)

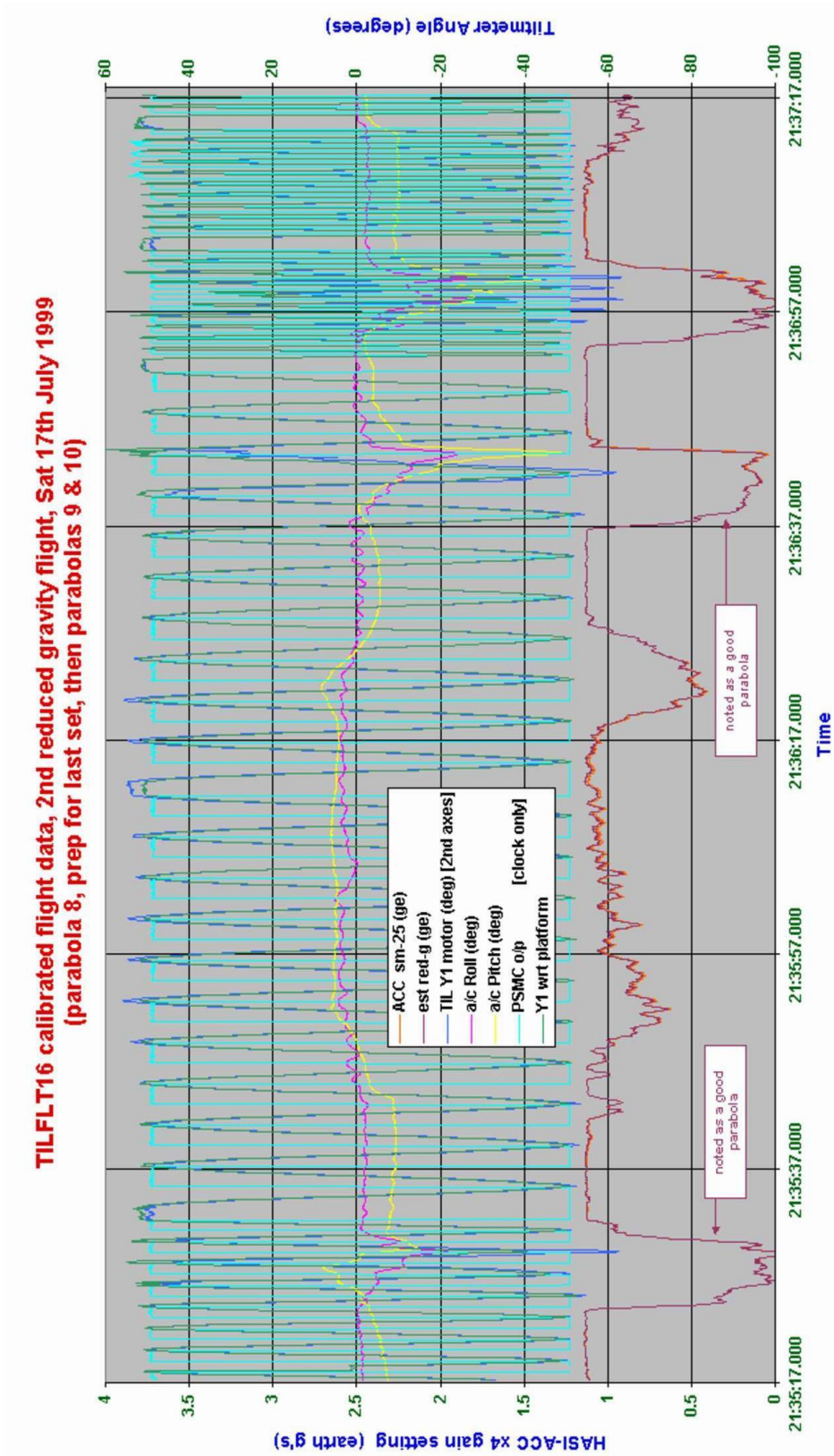


Figure 5.24: TILFLT16 flight profile, featuring parabolas 8, 9 and 10 (time 21:35:17 to 21:37:17)

**TILFLT17 calibrated flight data, 2nd reduced gravity flight, Sat 17th July 1999
(flight after parabolas)**

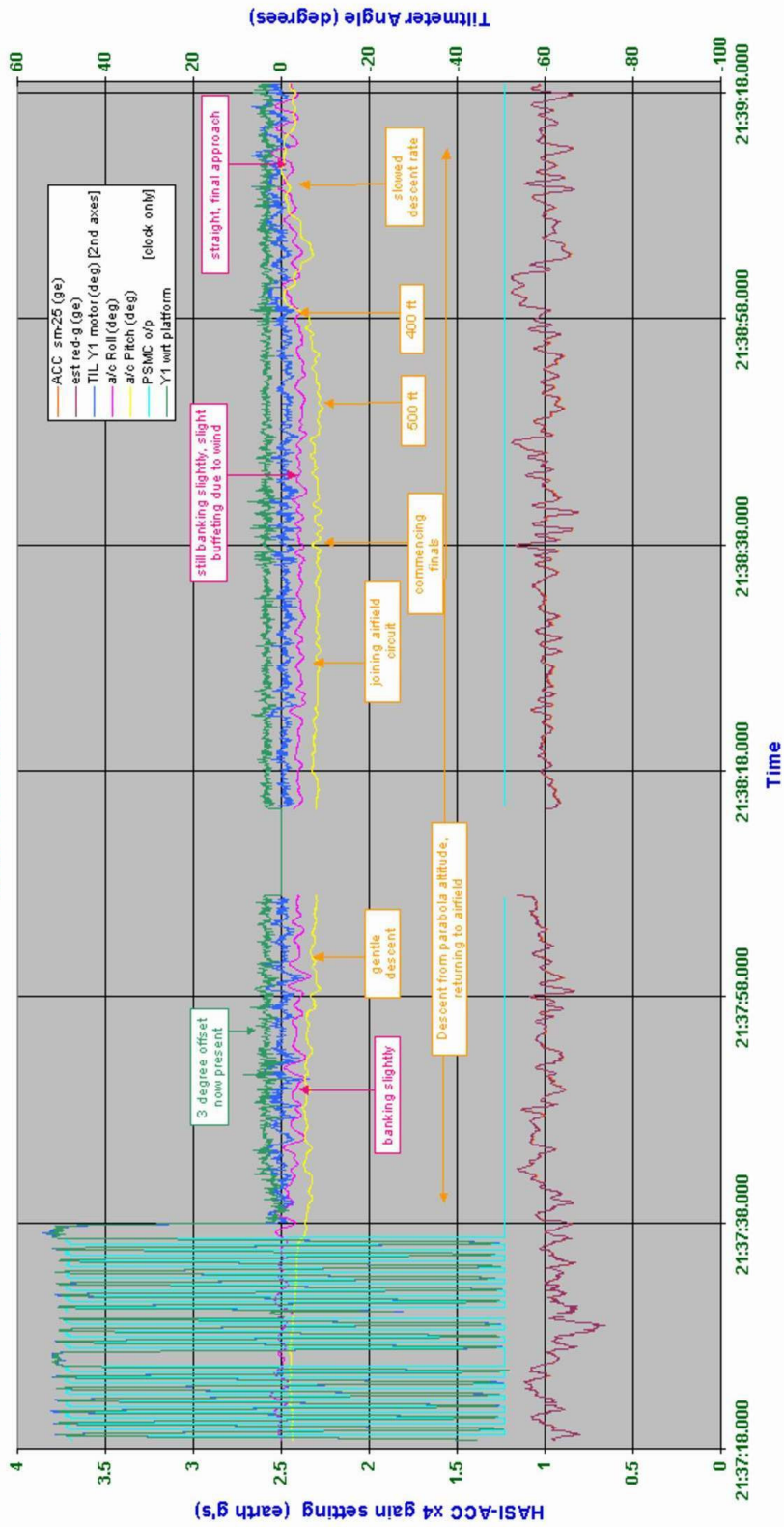


Figure 5.25: TILFLT17 flight profile, featuring post-parabola flight and return to airfield (time 21:37:18 to 21:39:19)

TILFLT18 calibrated flight data, 2nd reduced gravity flight, Sat 17th July 1999
 (descent after parabolas)

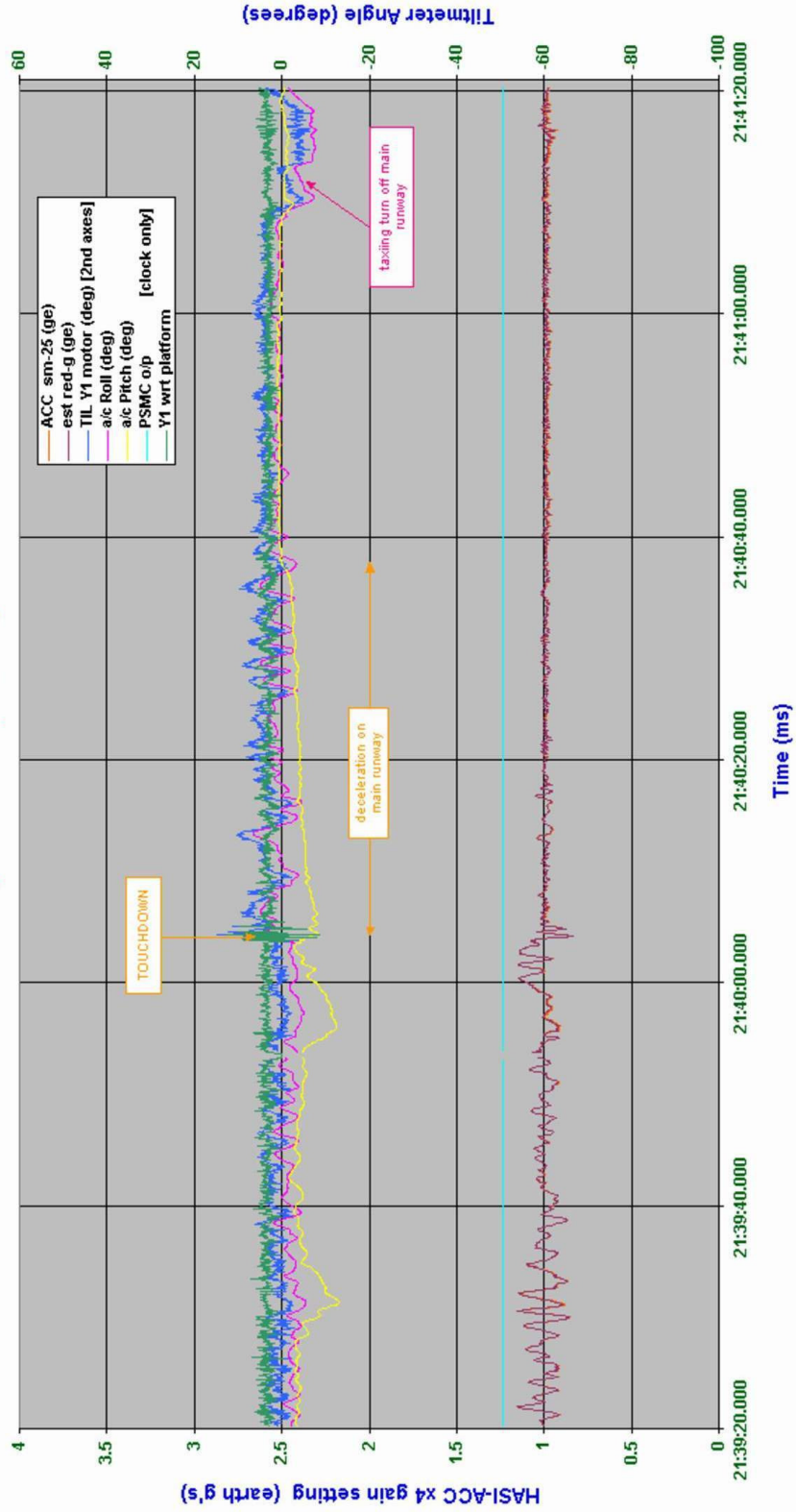


Figure 5.26: TILFLT18 flight profile, featuring final approach, landing and taxi (time 21:39:20 to 21:41:20)

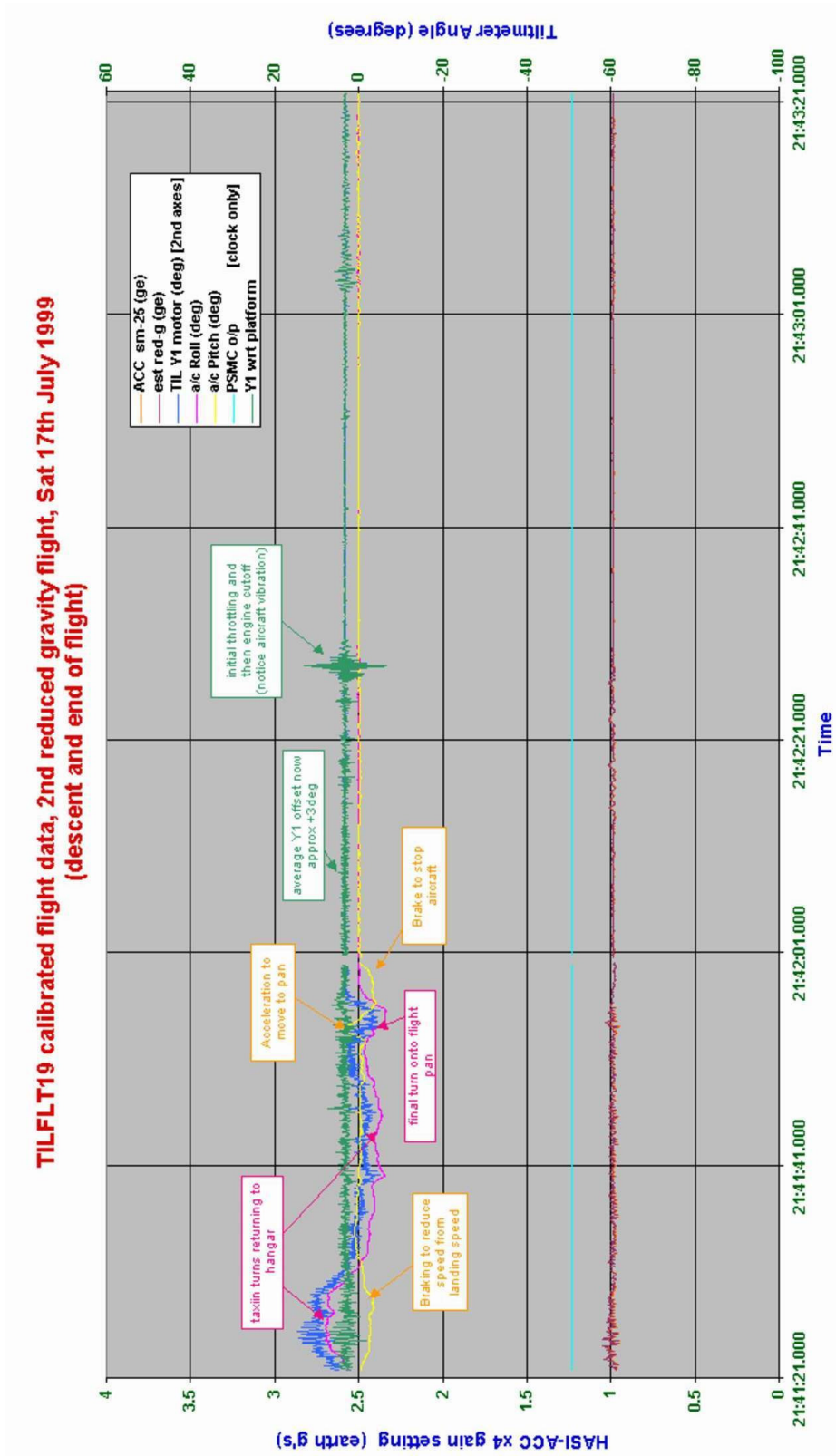


Figure 5.27: TILFLT19 flight profile, featuring taxi to hangar, engine cut-off and shutdown (time 21:41:21 to 21:43:22)

5.4 Conclusions of the TIL & HASI-ACC Reduced-gravity Experiment

5.4.1 Experiment conclusions

Recalling the objectives outlined in section 5.3.2, the principal goals of the TIL & HASI reduced-gravity flight experiment were:

- a) to test the operation of the TIL and HASI-ACC sensors under real dynamic conditions, and
- b) to test the degradation in TIL sensor response time during periods of reduced gravity equivalent to that expected at the surface of Titan

Both of these objectives were satisfactorily met. The operation of the TIL and HASI-ACC sensors was observed and useful data was returned. Although one of the HASI-ACC channels failed, this was due to supporting electronics rather than the sensor itself. The TIL response time under reduced gravity was observed and, as predicted, seen to increase with reducing gravity level. The sensor response time at Titan gravity level seemed to be longer than that predicted by theory, by around 60%, with the discrepancy increasing for higher gravity levels, although this is considered partly due to the slow sampling rates available from the data recorder. From these values an upper limit of 300 ms was concluded for the time lag, under Titan gravity, in response to oscillations about the sensor measurement axis. The experimental values suggested that the TIL sensor fluid would still achieve relative equilibrium orientation in under a second. Prediction of this relative equilibrium orientation, however, requires consideration of the linear accelerations on the sensor housing.

The experiment also had a series of secondary objectives.

- a) To investigate the measurement of reduced gravity levels by the HASI-ACC (servo) sensor and compare with actual g -level.
- b) To investigate the recording of the flight profile by the TIL sensors, including both pitch and roll
- c) To evaluate the quality of flight history reconstruction made possible by the combined measurements of TIL and HASI operating in complement
- d) To test the operation and usability of the Portable Dynamic Calibration Platform during field experimentation

As shown in the graphs of section 5.3.8 the HASI-ACC sensor was useful in correlating measurements made with the g-meter and represented the reduced g-levels well. Unfortunately the combined accelerations due to the platform motor vibrations and aircraft engine vibrations significantly increased the noise in the HASI-ACC signal. Such vibrations were unique to the experiment and would likely be significantly lower during parachute or balloon tests. The use of a single axis sensor complicated interpretation of the acceleration data, and this would have been improved by information concerning accelerations in the remaining two orthogonal axes.

Section 5.3.11 has discussed the limitations of the TIL sensor in accurately representing flight inclination in the presence of any non-gravitational acceleration on the sensor housing. The sensor is *strongly* susceptible to such accelerations (approximately 5° offset per 0.1g of horizontal accelerations less than 0.7g) and further information on these is required to accurately reconstruct sensor orientation. Alternatively, if the sensor orientation may be constrained by some other means then information may be derived concerning the sensor accelerations.

From combined interpretation of the TIL HASI-ACC flight data, several key flight events were identifiable from signature profiles in the data. Quantitative reconstruction was hindered by the noise arising from aircraft engine noise, buffeting, and platform motor vibrations. For more accurate quantitative analysis of the flight angles, and flight profile, additional information on the accelerations experienced during flight were required. Without additional accelerometers, for an aircraft this would require information concerning the aircrafts drag and lift coefficients, as well as throttle, elevator and aileron profiles throughout the flight. In absence of these, direct flight profile information as would be provided by a flight computer would have permitted more quantitative reconstruction analysis, and this is an important consideration for future flights.

The Portable Dynamic Calibration Platform operated as designed, proved straightforward to use, and permitted valuable testing of the TIL and HASI-ACC sensors together in a unique dynamic environment. The versatility of the control board, in providing controlled motion of the TIL-Y1 sensor, successfully permitted the estimation of TIL response time, with the use of the secondary sensors successfully removing the effect of platform orientation. Unfortunately the limited flight opportunities did not permit, on this occasion, the introduction of radial offset of the TIL-Y1 from its axis of rotation. This is an area that strongly warrants investigation, particularly under reduced gravity conditions and should be addressed in any future flight plans.

Several areas of improvement were highlighted for the platform during the experiment. The ADC unit and data recording computer offered insufficiently high sampling rates for accurate measurement of parameters varying over timescales under 50ms, and for the purposes of more accurate TIL response time measurement this was inadequate. The ACC(x1 gain) channel unfortunately failed in flight and since the ACC(x4 gain) setting was geared towards measurement of accelerations of less than 1g, this led to saturation of the sensor in between flight parabolas. A significant area for improvement with the platform is in vibration damping. Any sensitive measurement made with the accelerometer is complicated by the motor, and some way of isolating these would be beneficial. The use of gears has also been suggested in reducing the vibrations transmitted to the TIL-Y1 sensor. Any efforts to isolate the sensors from external vibration would also be beneficial.

5.4.2 Further investigation recommendations

Recommendations from this experiment for future investigations may therefore be summarised as follows:

Flights

- i. For improved measurement of the TIL response time, a reflight under more stable reduced gravity conditions is recommended. This would most preferably be aboard a larger aircraft such as the Novespace A-300 Zero-G.
- ii. Tests involving non-gravitational accelerations on the TIL sensor, and their increased significance under reduced gravity, are also recommended.
- iii. Any testing aboard an aircraft must have made available to it details of the flight profile, including attitude, g-level, pitch, roll, airspeed and vertical speed, as a minimum. Such information would also need to be accurately synchronised with any data taken.
- iv. Stable mounting of the platform is required, and if possible this should also isolate the sensors from any external vibrations.
- v. For flight profile reconstruction an aircraft represents a particular type of dynamic environment and, for reduced gravity tests, is the only option. A more stable environment is that offered by a balloon flight. Any such flight should have as a minimum three-axes acceleration measurement capability, and as a backup some form of camera or GPS system able to constrain the linear accelerations experienced by the TIL sensor.

Platform design

- vi. A faster sampling rate (100Hz recommended) from the ADC and data recorder is essential.

- vii. Consideration of the full range of accelerations involved in any experiment needs to be given so that the ACC channels may be scaled appropriately.
- viii. Noise and vibration reduction through motor mounting redesign or gears, as well as some method of damping external vibrations should be incorporated.
- ix. Future experiments should include investigations with radial offset from the motor shaft axis.

5.5 TIL & HASI-ACC Spin-table test using the PDCP

As mentioned throughout the previous sections of this work, the TIL sensor surface is susceptible to linear accelerations and this therefore includes centrifugal forces associated with the probe spin. Accurate measurement of the probe attitude using the TIL sensor therefore requires removal of this spin component, for example using the spin rates measured by the Huygens system radial acceleration sensor unit (RASU). The measurement of spin aboard the Huygens probe is discussed further in Chapter 6.

This section briefly details the spin test carried out with the TIL and HASI-ACC sensors, using the Dynamic Calibration Platform. Afterwards a very brief mention is made of a swing test involving the platform carried out immediately after the spin test. Recommendations are also made at the end for future testing.

5.5.1 Spin Table experiment

As shown in section 3.2.3 when subjected to a horizontal acceleration a , under conditions of relative equilibrium the TIL sensor fluid surface will be inclined at an angle θ , given by the inverse tangent of (a / g) where g is the local gravitational acceleration.

Where this acceleration is due to spin rate, Ω , as shown in Figure 5.28, the TIL offset is given by

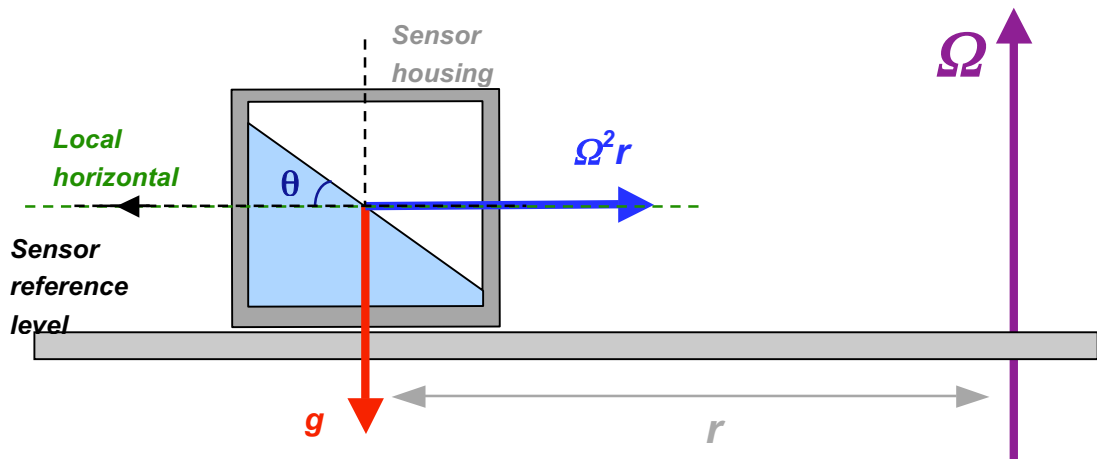


Figure 5.28: TIL sensor distance r from spin axis

$$\tan\theta = \frac{\Omega^2 r}{g} \quad (5-12)$$

where r is taken to be the radial distance between the centre of the sensor and the rotation axis.

Spin table and PDCP arrangement

Figure 5.29 shows a video camera still of the experiment set-up used. As may be recognised the experiment took advantage of a, quite simply a children's roundabout, in a local recreation park. Tests with the TIL sensor showed that the rotation axis was indeed vertical, to better than 0.5° , and therefore represented an adequate test platform. Of course more controlled test facilities are available however these were beyond the resources available at the time of experiment, and for the purposes of this particular experiment the set-up shown here would suffice. One restriction imposed was the inability to incline the rotation axis with respect to the local gravity vector. As discussed later this is an important test, and at a remote facility where a subsequent test was carried out.

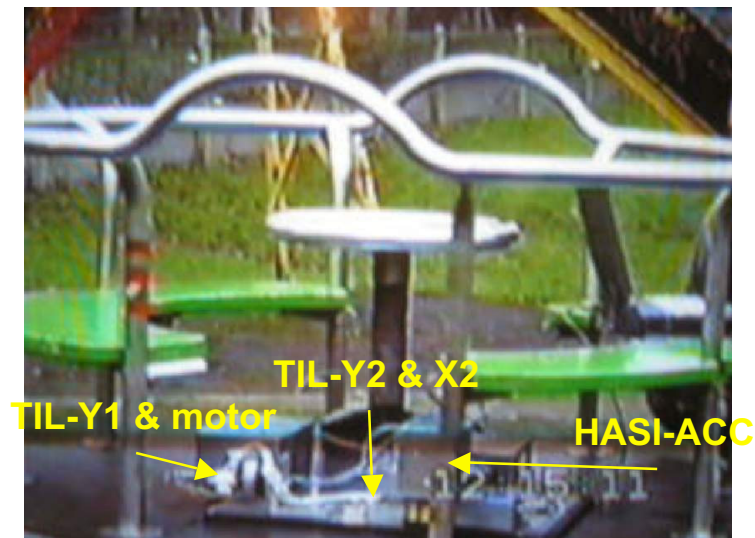


Figure 5.29: Video still of the spin platform, showing the PDCP and laptop computer mounted on the table. Visible on the platform are the motor and oscillating TIL-Y1 sensor, the TIL-X2&Y2 sensor and the HASI-ACC sensor mounted horizontally.

The PDCP represented a ideal solution for taking these measurements by virtue of its stand-alone capability. With the battery and laptop computer housed on the rotating platform the need was avoided for rotating contacts connecting power and data lines to the sensors. The PDCP was used in a similar configuration to that described in the reduced-gravity flight experiment, except for a rotation of the HASI-ACC sensor to allow horizontal alignment of its measurement axis. Due to mounting issues on the platform, the TIL-X2 and HASI-ACC sensors were fixed parallel and opposite, as were the TIL-Y1 and TIL-Y2 axes. The platform was oriented such that the TIL-X2 axis was aligned with the radial vector making it insensitive to radial centrifugal accelerations. This then introduced a misalignment between the HASI-ACC axis and the radial vector. A similar misalignment existed between the line perpendicular to the TIL-Y1 axis and the radial vector. The ACC misalignment was estimated at approximately 24° and needed to be taken into consideration when using the ACC

sensor to measure the spin rate. Finally the ACC sensor was oriented such that a positive acceleration was indicated during spin.

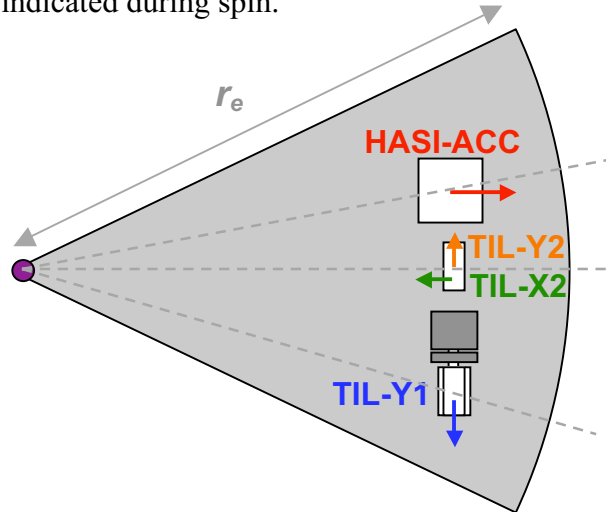


Figure 5.30: Sensor arrangement indicating axes. Note the slight misalignment between the HASI-ACC and the radial axis, and also for the orthogonal line to the TIL-Y1 axis and the radial axis

Figure 5.30 shows the sensor arrangement on the spin table. It was desired that the TIL offset against rotation rate be confirmed, and investigation be made into how well the spin profile was represented during a TIL measurement sequence. It was also desired that Huygens representative spin rates be used, and this therefore required scaling to counter the effects of the Earth's higher level of gravitational acceleration.

If θ is the TIL angle offset due to centrifugal acceleration, then the same angle θ would be generated by radial displacement and spin rate under Titan gravity g_t of r_t and Ω_t , as would be generated for radial displacement and spin rate under terrestrial gravity g_e of r_e and Ω_e , where

$$\frac{\Omega_e^2 r_e}{g_e} = \frac{\Omega_t^2 r_t}{g_t} \quad (5-13).$$

Therefore to simulate similar offsets as would be experienced by a Huygens probe spin rate on Titan of Ω_t , two options were available. To keep the spin rates during simulation the same as on Titan, it would either be necessary to use a radial displacement for earth testing of r_e

$$r_e = \frac{g_e r_t}{g_t} \quad (5-14).$$

Alternatively, a Huygens representative radial displacement could be used and to induce the same centrifugal offset as would be seen for a Titan spin rate of Ω_t , an increased spin rate on earth would be necessary, equal to

$$\Omega_e = \left(\frac{g_e}{g_t} \right)^{1/2} \Omega_t \quad (5-14).$$

Scaling of the radial displacement would have necessitated a spin table of radius greater than 2.6m, beyond that available, the option to scale the spin rates was chosen.

Spin rates

The spin profile predicted on Titan was shown in Chapter 1 and suggested a maximum expected descent spin rate of 20 rpm. Consequently spin rates of up to 54rpm would ideally have been tested. The experiment performed spin rates as high as 40rpm however, equivalent to 14rpm on Titan.

At this maximum spin rate (on earth) of 40rpm, the predicted TIL offset would be 32.6°. Since the maximum fluid angle measurable by the TIL sensor is specified as 60° this would limit the measurement by any sensor with its measurement axis tangentially aligned to approximately 28°. This would be observed by the TIL-Y1 sensor whose oscillations, as for the previous experiment, were between ±50°. Theoretically the highest rate at which the sensor could still be used to accurately measure inclination, with spin effects removed, would therefore be when the centrifugal angle offset was 10°, at 21rpm.

Supporting equipment

To measure the spin rate independently of the HASI-ACC and TIL sensors, the table use was made of the 8 radial ‘arms’ of the roundabout, as shown in Figure 5.29. A rod was fixed to the ground just beside the edge of the table, and as the table rotated, every time one of the radial arms connected with the rod a distinct click was audible. By synchronising these clicks with the audible pulses of an electronic metronome approximate spin rates were calculable. This would be used to provide calibrated spin rates. As with the previous experiment a cassette based dictaphone was also employed for audio commentary.

Experiment

The plane of the table surface was verified as being perpendicular to the gravity vector by checking the static table TIL output following rotation about the spin axis by 45° (using the symmetric arms of the spin table as a guide of angle). A complete spin up of the table was then executed, to as fast a spin rate as was manageable, to test correlation between TIL-Y2 and HASI-ACC outputs as the table spun down smoothly. Several spin cycles were then attempted, and a few sample results are presented in the next section.

5.5.2 Spin Results

Figures 5.31 to 5.38 show the calibrated sensor outputs of the experiment, along with a plot of spin rates as measured by the HASI-ACC sensor against the TIL-Y2 measured angle. Some known spin rates are provided from the audio commentary.

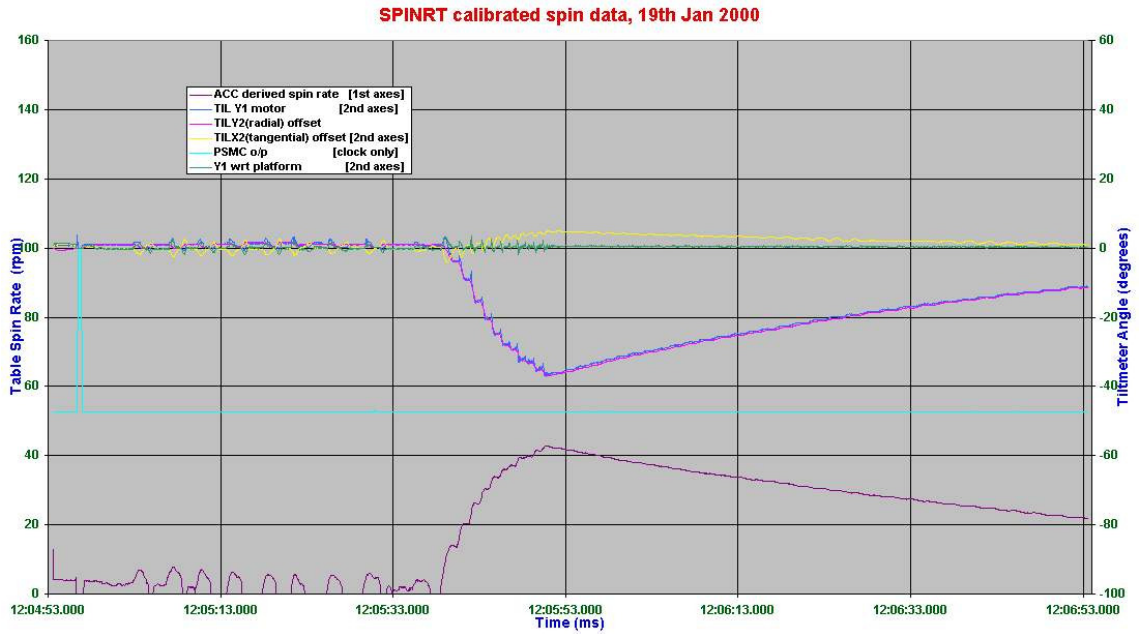


Figure 5.31: SpinRT0 results showing spin up and spin down results. Note the small accelerations registered in both radial and tangential sensors during spin rate increases

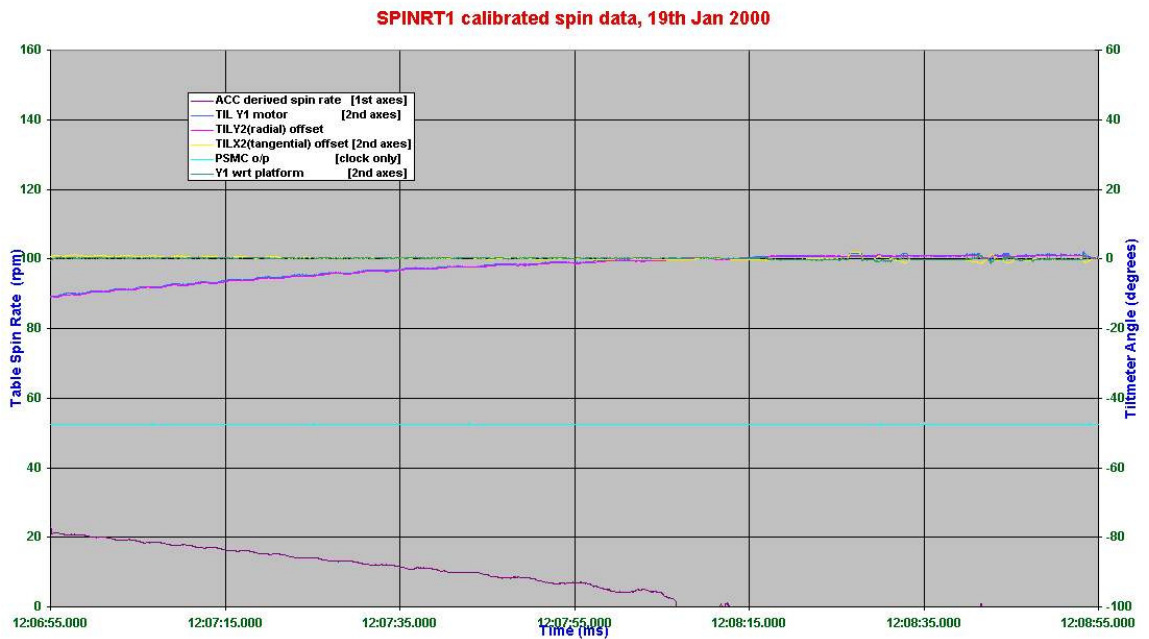


Figure 5.32: SpinRT1 results showing smooth spin down

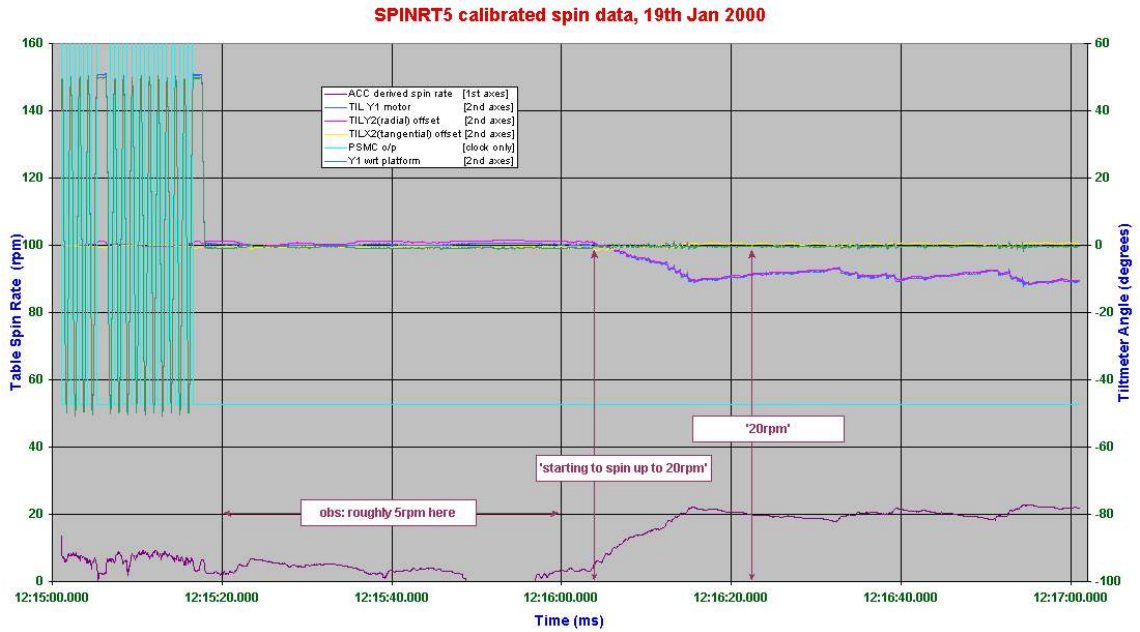


Figure 5.33: SpinRT5 results showing correlation between HASI-ACC measured spin rates and actual spin rates during slow spin and spin up, and note spin profile represented in TIL signals

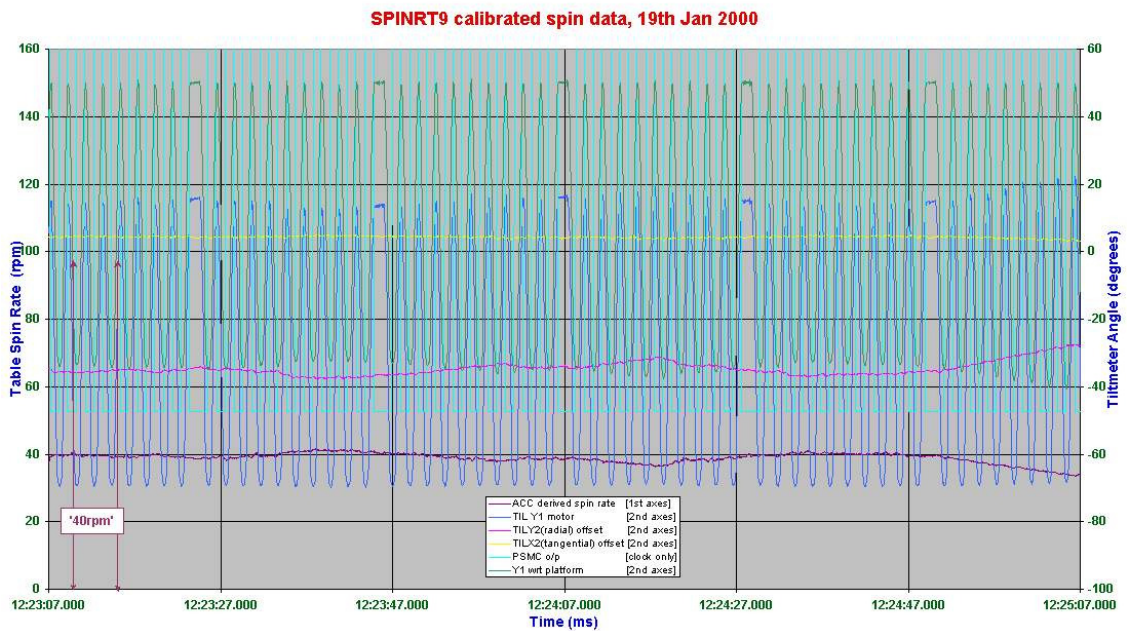


Figure 5.34: SpinRT9 results showing correlation between HASI-ACC measured spin rates and high spin rate of 40rpm. Note TIL-Y1 position (green) no longer accurately represented by TIL sensor

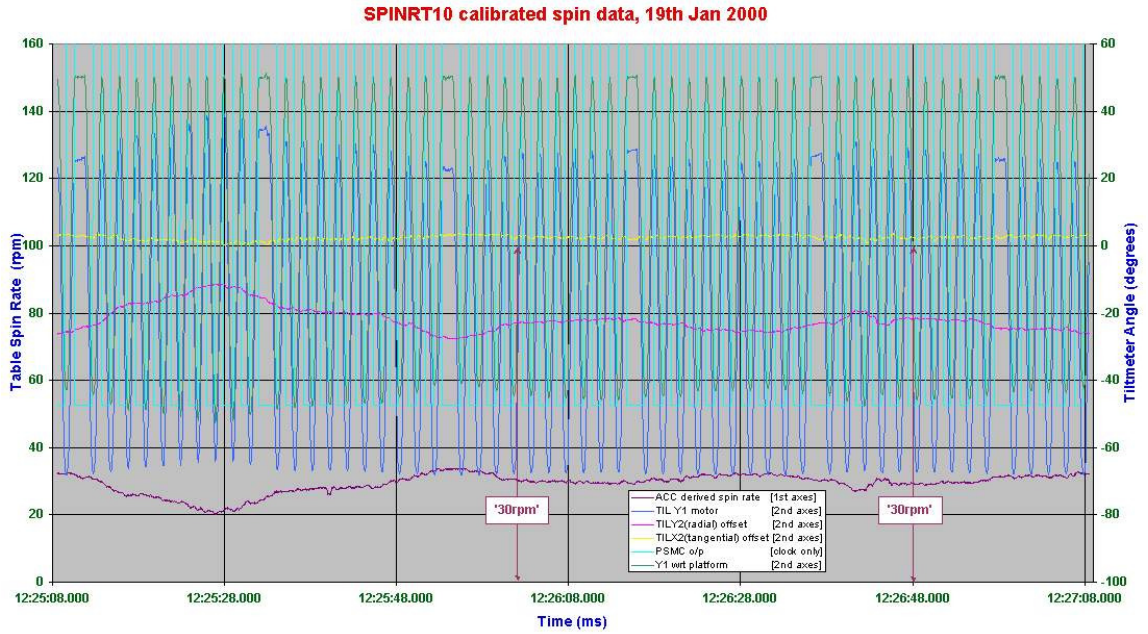


Figure 5.35: SpinRT10 results showing correlation between HASI-ACC measured spin rates and actual spin rates of 30 rpm. Note TIL-Y1 position (green) only accurately represented by TIL sensor at 20rpm

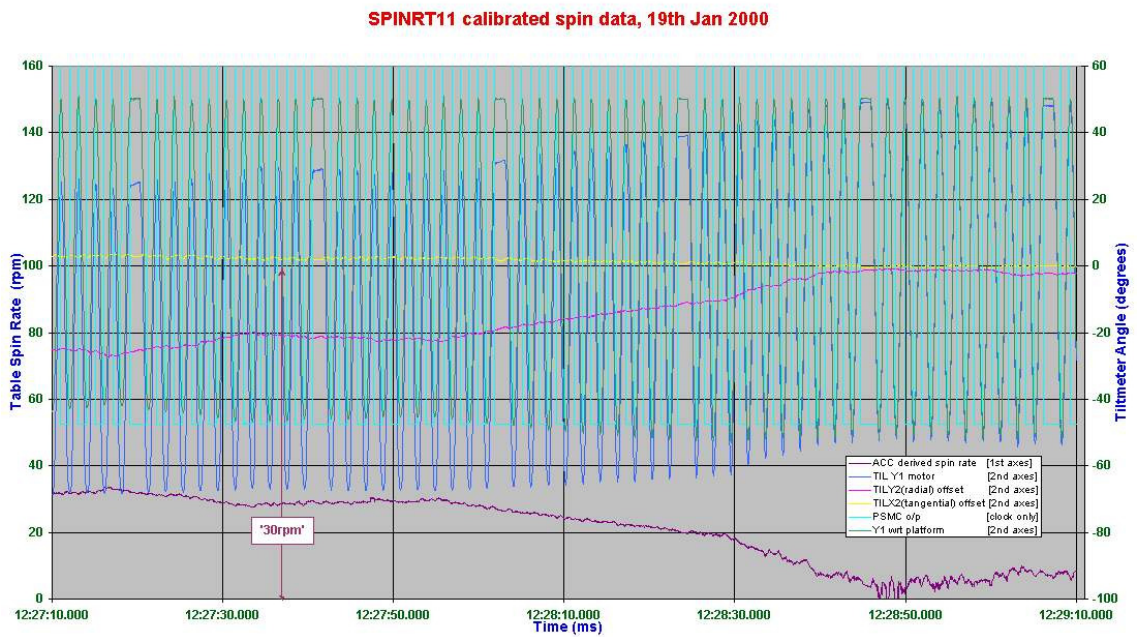


Figure 5.36: SpinRT11 results showing correlation between HASI-ACC measured spin rates and actual spin rates of 30 rpm. TIL-Y1 position (green) only accurately represented by TIL sensor below around 20rpm

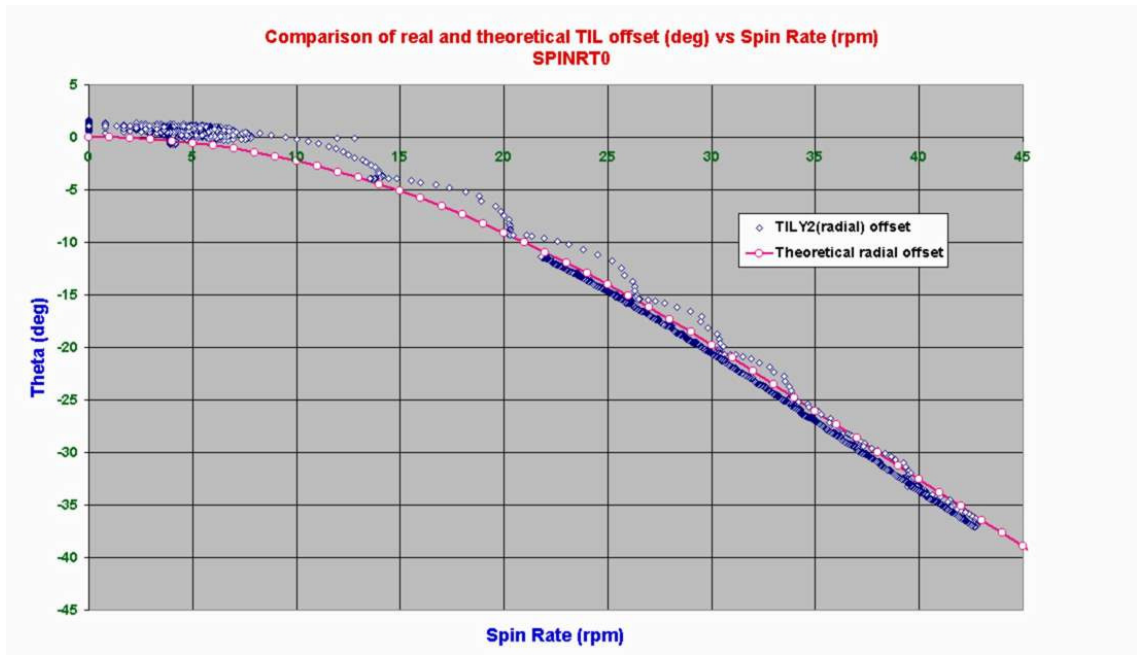


Figure 5.37: SpinRT0 results showing good correlation between spin offset and theory, once the misalignment of the ACC sensor had been taken into consideration

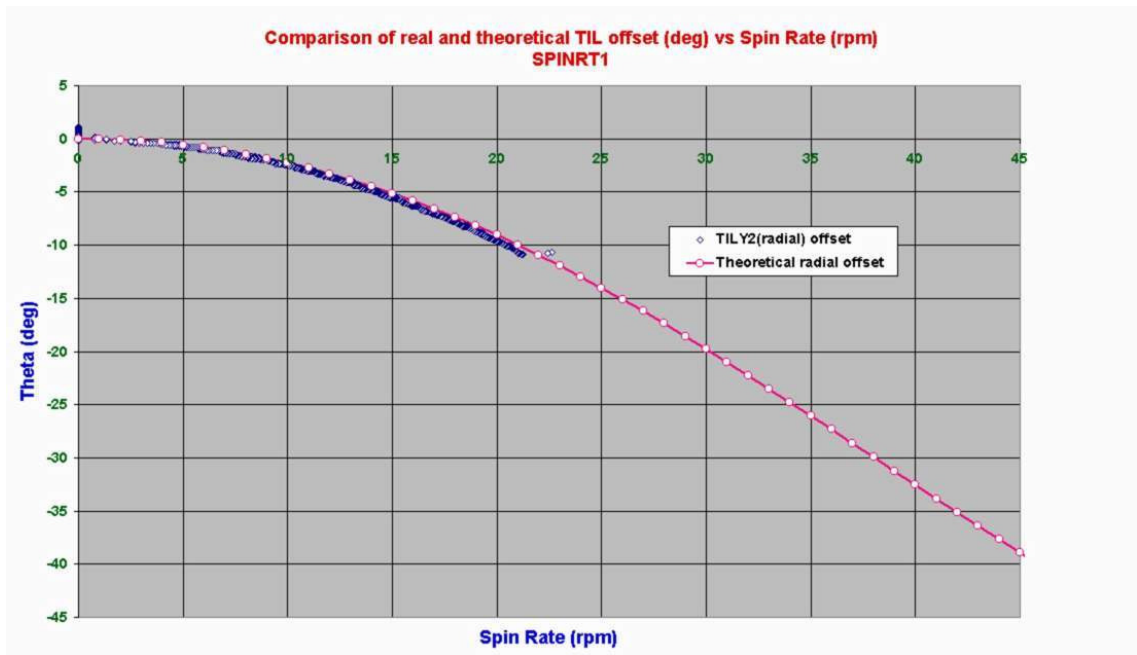


Figure 5.38: SpinRT1 results showing good correlation between spin offset and theory, once the misalignment of the ACC sensor had been taken into consideration

5.5.3 Data analysis: Spin vs. TIL output (as measured by HASI ACC)

The observed levels of the TIL offset against the spin rate as measured by the HASI-ACC sensor showed good agreement with theory, once the misalignment of the ACC sensor was taken into consideration. The agreement departs slightly from theory at the lowest spin rates in Figure 5.37, however consideration of the spin profile shown in Figure 5.31 for the same period show that these were during periods of widely varying spin rates for short periods of time.

Reasonable correlation was also shown in the spin profiles graphs of Figures 5.31 – 5.36 between the HASI-ACC derived spin rates and the spin rates quoted during the flight audio commentary. The spin profile is well represented in the output of the radially sensitive TIL-Y2 sensor. The tangentially sensitive TIL-X2 sensor also yields interesting results, showing the short periods during which moment was applied by hand to increase the table spin rates. Especially well represented by the TIL-X2 sensor were the small regular start-stop rotations being made by hand. Such offsets are induced by the $r(d\Omega/dt)$ accelerations acting tangentially.

Also of note is the aforementioned decrease in the range of inclination measurement whilst spinning, as observed from the TIL-Y1 output. When the centrifugal offset, also measured by the TIL-Y2 sensor, was removed, the TIL-Y1 inclination relative to the platform could usually be reproduced. However as predicted, when the spin rate increased above approximately 20rpm, the combination of inclination and additional centrifugal offset exceeded the sensors specified -60° measurement limit (or around -65° as observed). Whilst it is known from the PSMC program (see section 4.3.4) that a continuous $\pm 50^\circ$ simple harmonic motion amplitude was being executed, the TIL-Y1 sensor indicated a lower amplitude. As would be expected, this only occurred in one direction due to the direction of centrifugal offset.

5.5.4 Spin Table Experiment conclusions

The experiment successfully tested the response of the TIL sensor to spin, and highlighted a limitation on its attitude measurement during periods of high spin rate. The limitations imposed by spin are greater on Titan than on earth due to the reduced level of gravity, and the implications for the probe mission on Titan are discussed briefly in Chapter 6. The operation and use of the HASI-ACC sensor was also a success, although on the Huygens probe the radially oriented sensors are PZR accelerometers rather than the servo tested here.

The experiment successfully demonstrated again the use of the Portable Dynamic Calibration Platform in enabling quick and simple verification and test of sensor performances beyond the confines of the laboratory. No further limitations of the PDCP to those mentioned in the previous experiment discussion were highlighted by the experiment.

Further experimentation has been recommended to test the response of the sensor to a periodic change in the direction of the spin axis. Subsequent tests have recently been performed in conjunction with the Huygens Descent Imager team [Riszk et al., 2001] with a substantially more expensive and sophisticated set-up and have shown results from the TIL sensor in correlation with those described in Chapter 6. The motion of the spin axis was varied at Titan representative rates as would be experienced beneath the Huygens parachute, although the effects of the swing of the TIL sensor housing were not simulated.

Therefore it is strongly recommended that as a next step in accurate representation of the TIL signals that may be expected during the descent phase, experiments are carried out simulating probe swing. An impromptu qualitative investigation was carried out immediately after the spin experiment, due to the availability of a simple child's swing at the recreation ground where the spin table described above was located. Unfortunately the laptop computer power failed after just a few measurements, as did the motor power on the platform. However some interesting qualitative interpretations are possible as discussed briefly below.

5.6 TIL & HASI-ACC Swing test using the PDCP

5.6.1 Swing structure and platform configuration

A schematic of the swing used is shown in Figure 5.39 below, with the key dimension being the length of chain between the seat and the pivot point, L , being measured at approximately (1.35 ± 0.05) m. Thus the period for un-damped oscillations may be predicted at around 2.3 seconds. Note that the HASI-ACC sensor measurement axis remained in its spin experiment configuration, aligned horizontally, and the platform was oriented as shown with the HASI-ACC measurement axes pointing forward and the TIL-Y2 (and TIL-Y1 in the absence of motor motion) indicating angle of swing.

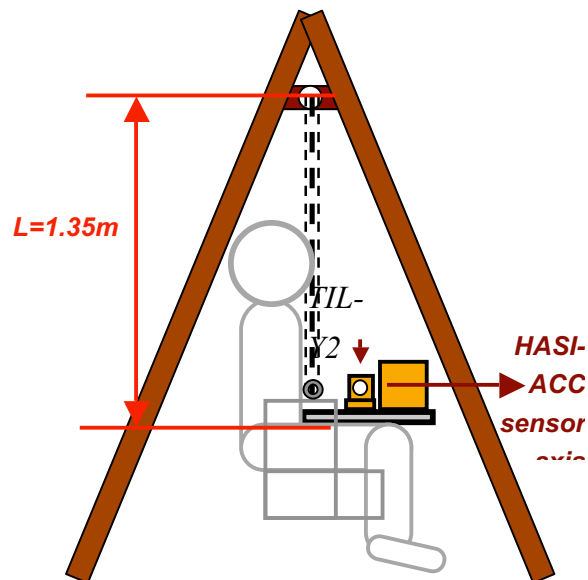


Figure 5.39: Diagram showing swing configuration and platform orientation

5.6.2 Swing Theory

Consideration of equation 3-1 and the accelerations experienced by the TIL sensor when swung as an ideal pendulum mass, indicate, perhaps counter-intuitively, that the TIL fluid surface is likely to remain parallel to the sensor base. This is mainly because, in the absence of drag or friction about the pendulum fixing point, the only acceleration acting on the sensor other than gravity is the tension in the pendulum length, and this has no component acting along the line parallel to the sensor base. If this was the case then from the principle of sensor measurement, the sensor would indicate zero tilt throughout the pendulum motion. The only way the TIL sensor would not act in this way would be in the presence of accelerations on the sensor housing due to drag or friction. This is considered theoretically for the case of the

Huygens probe descent in the next chapter. Since resisting accelerations did exist in the case of such a primitive set-up as the child's swing it was hoped that the TIL sensor would be able to measure some form of inclination angle, and the question existed as to how well the TIL sensor would represent the swing motion. Two sample graphs are shown, with a few brief annotations in Figure 5.40.

5.6.3 Swing Results

The first graph shows a typical plot where the position was held just prior to swing, and a true measure of platform inclination is made by the TIL-Y1 and TIL-Y2 and sensors. The HASI-ACC sensor also represents this inclination well. However upon release, as had been predicted, a significant underestimation of the platform pitch angle was made by both TIL-Y1 and TIL-Y2 sensors, and also the HASI-ACC sensors, due to them essentially perceiving free fall conditions in their respective measurement axes. Additional accelerations due to the operator seating and attempts to prolong the swings, as well as friction, has given rise to some departure from freefall conditions. Therefore reduced inclination measurements have been made although quantitative reconstruction from these was not possible due to the uncontrolled conditions. It was however clearly possible to discern an approximate average period of oscillations as just over 2 seconds, in line with the value predicted above.

5.6.4 Conclusion

Again the calibration platform permitted simple impromptu testing of the TIL and HASI sensors under dynamic conditions that partially resemble those that may exist during the Huygens probe descent. Whilst the experiment clearly needs repeating under vastly improved and controlled conditions for any useful quantitative assessment, a significant area of reduced TIL performance has been highlighted. Future experiments will require some method of providing independent inclination information against which the TIL measurements can be compared.

Attempt is made to investigate the significance of this issue with TIL for the Huygens descent in the next chapter.

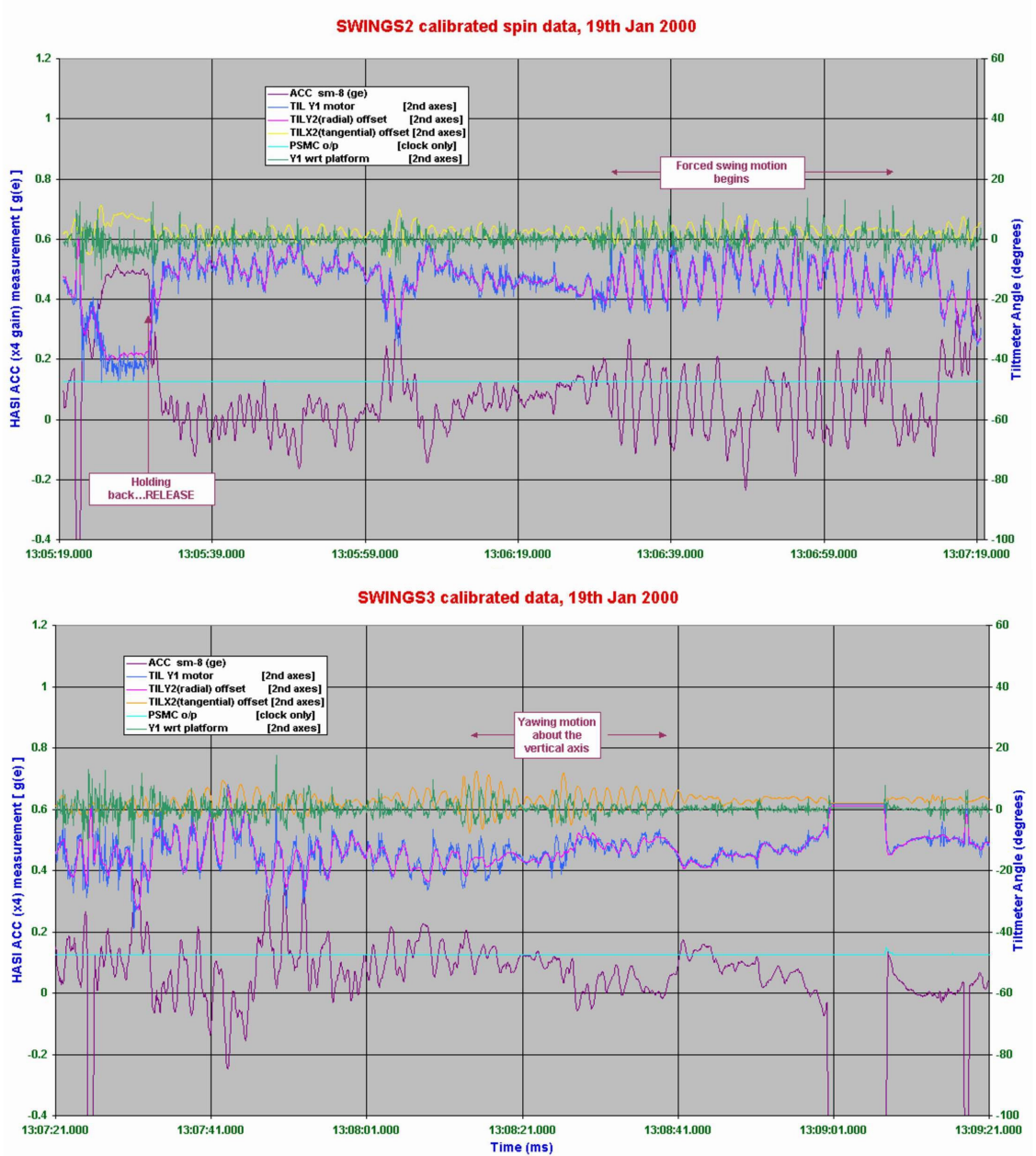


Figure 5.40: Two results files from swing tests carried out showing (a) simple swing and forced swing motion and (b) yawing motion about the vertical axis

5.7 TIL & HASI-ACC PDCP Experiments Conclusion

This concludes the presentation of results, analyses and discussions of three experiments using the TIL and HASI-ACC sensors housed aboard the Portable Dynamic Calibration Platform. Conclusions, discussions and recommendations for further experiments have been addressed at the end of the results sections of each of the experiments and are repeated only briefly here as a guide to the reader.

Successful assessment of the TIL response under Titan gravity, and limited aircraft flight reconstruction has been presented in section 5.3, with recommendations for future flights also offered. The strong sensitivity of the TIL sensor to non-gravitational accelerations has also been demonstrated, of which centrifugal accelerations are but one. Successful reconstruction of spin rate from TIL was demonstrated in section 5.5, and the sensor attitude measurement range was shown to be impacted by the presence of spin. The underestimation of pitch by the TIL sensor during periods of swing was also demonstrated qualitatively in section 5.6 and has highlighted the urgent need for further modelling and experimental verification. The next chapter attempts some preliminary modelling in this area.

Results have shown the Dynamic Calibration Platform to be an extremely useful tool in performing quick and tests of the TIL and HASI-ACC sensors in a range of dynamic environments, some of which would have been complicated to reproduce under laboratory conditions. Its portability and standalone operation make it especially useful in situations where power and data lines are not readily available. The versatility of the programmable stepper motor control board paves the way for a wide range of possible dynamic tests, of which those presented here are but a few. Several recommendations for design improvements that would increase its value have also been made in section 5.4.2.

PAGE INTENTIONALLY BLANK

PAGE INTENTIONALLY BLANK

Chapter 6

TIL sensor aboard the Huygens Probe

6.1 Introduction

Work presented in the previous chapters has made predictions as to the potential surface dynamics that may exist on Titan, modelled the response of the TIL sensor fluid to rapid changes in its equilibrium position under Titan's gravity level, and described experimental observations of the sensor output during periods of aircraft flight, spin, and pendulum type swing. This chapter now briefly considers several issues important for the interpretation of TIL data during the sensor's operation throughout the Huygens descent and surface mission. The TIL sensor has been cited on several occasions (for example [Atkinson, 1998] and [Lebreton & Matson, 1997]) as potentially contributing crucial information towards the reconstruction of probe descent dynamics and trajectory, as well as any dynamics that may be experienced following impact with the surface. It is important therefore to investigate claims that have been made regarding the motions measurable by the sensor.

Firstly, due to the location of the sensor aboard the probe, any requirement for the angles of rotation about the probe axes necessitates a transformation from instrument to probe axes, and a program written for this purpose is discussed. Consideration is then given to the impact of probe spin on the TIL sensor at Titan, with particular focus on the levels of spin resolvable and the reduction in attitude measurement range as observed in the experiment of the previous section. The question of distinguishing between spin-induced and inclination components of the TIL sensor measurement is first discussed for the simple case of spin axis rotation about the point of spin axis and radial vector intersection. The more complex case of TIL measurement of probe spin and swing

during parachute descent is discussed and a simple parachute model, constructed to provide inputs to simulated TIL and HASI-ACC sensors against which their measurable outputs may be compared, is outlined. Discussion is then offered on the impact of the increased TIL response time on Titan and instrument sampling rates in reconstruction of probe motions. Finally brief consideration is given to the measurability of surface dynamics that that could exist in the event of a liquid landing on Titan, using the wave predictions of Chapter 2, before conclusion of the chapter with a summary and recommendations for necessary further modelling.

6.2 Conversion between TIL angles and Probe axes tilts

By virtue of the orientation of the TIL sensor on the Huygens probe, any measurement made by the TIL-X and TIL-Y sensor, whether under static or dynamic conditions, will indicate angles of rotation about sensor axes rather than the probe axes. Whilst motion frequencies will be the same about either sets of axes, the absolute measurement of probe inclination at a particular point in time will require conversion between the two coordinate systems.

6.2.1 TIL position on Huygens Probe

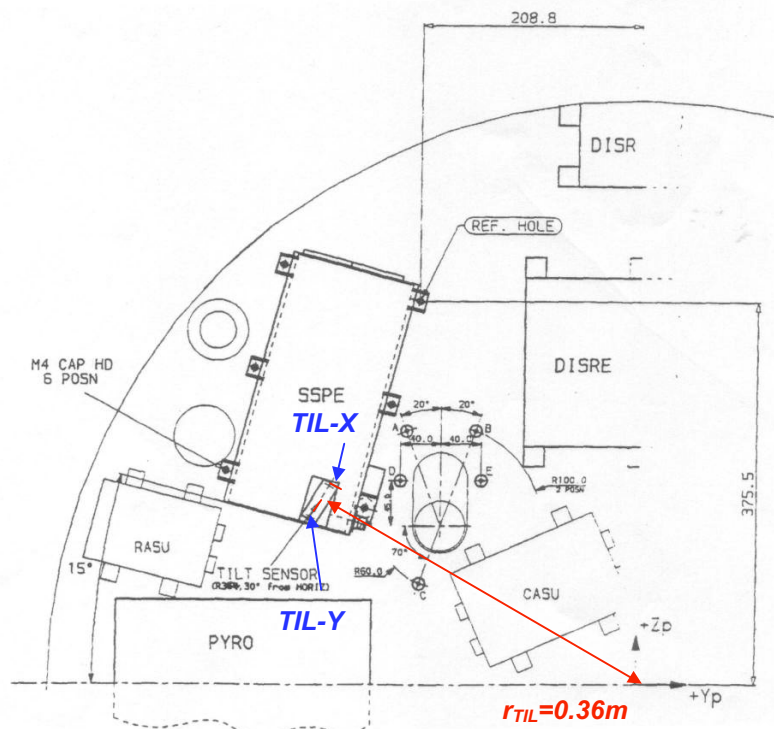


Figure 6.1: Location of the TIL sensor atop SSP Electronics box on Huygens. Note position of probe centre (symmetry) axis bottom right. [taken from and technical drawing included in the SSP Acceptance Data Package, PY-SSP-UKC-AD104]

Figure 6.1 shows the mounting position and orientation of the TIL sensor aboard the Huygens probe, taken from an ESA provided technical drawing. The radial distance from the centre axis of the probe (Probe x -axis, X_p) to the centre of the TIL sensor is 0.36m. The design specification called for the sensor to be oriented such that the measurement axis of the TIL-Y sensor is aligned to within 1° of the probe radial vector [PY-SSP-UKC-AD104] and both sensor axes are perpendicular to the X_p axis.

6.2.2 Transformation between Instrument and Probe axes

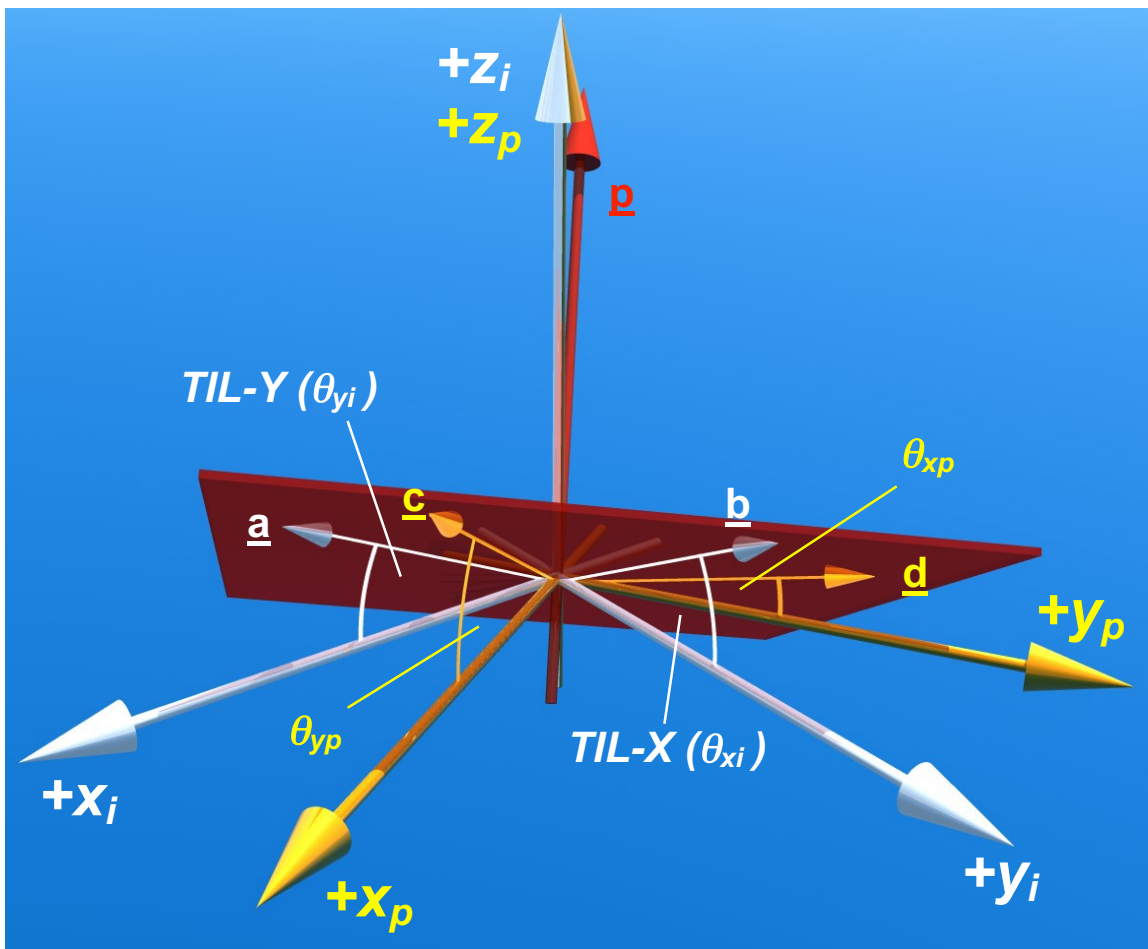


Figure 6.2: Diagram showing instrument and probe coordinate reference frames $x_i y_i z_i$ and $x_p y_p z_p$ respectively, indicating the angles measured by the TIL-X and TIL-Y sensors. Note that the $+x_p +y_p +z_p$ axes above are the $+Y_p +Z_p -X_p$ according to probe convention

The misalignment between the TIL-X and TIL-Y axes, x_i and y_i , and the probe axes y_p and z_p axes means that any rotation about the instrument axes is equivalent to a different rotation about the probe axes, and vice versa. When attempting to transform between the instrument and probe frames of reference a conversion calculation is therefore necessary, as described here. Note that the use of the probe axes convention above may

reduce the clarity of the discussion below. For ease of understanding the conversion method employed, *for the purposes of this section only* the probe axes indicated in the diagram above, +Y_P and +Z_P are renamed +x_p and +y_p. The +X_P axes has been renamed -z_p.

Figure 6.2 illustrates the instrument and probe coordinate reference frames $x_i y_i z_i$ and $x_p y_p z_p$ respectively, and indicates the angles measured by the TIL-X (θ_{xi}) and TIL-Y (θ_{yi}) sensors. The z_i and z_p axes are assumed to be in perfect alignment. **a** and **b** are lines of intersection between the plane of the fluid surface (equivalent to the local horizontal under static conditions) and the $y_i z_i$ and $x_i z_i$ planes respectively. From θ_{xi} and θ_{yi} it is possible to obtain **a** and **b**, and from these the $x_i y_i z_i$ components of the vector normal to the plane, **p**. From the direction cosine matrix relating the two reference frames the $x_p y_p z_p$ components of **p** may be found, and the vectors **c** and **d**, the $x_p y_p z_p$ analogies of **a** and **b**, can be obtained. This then allows angles θ_{xp} and θ_{yp} , the angles of the fluid surface about the probe y_p and x_p axes respectively, to be calculated. It is again reiterated that the axes conventions in this discussion have been used to clarify the conversion algorithm. Probe convention refers adopts +Y_P+Z_P-X_P where $x_p y_p z_p$ has been referred to above.

Two simple MATLAB routines were written to carry out the appropriate reference frame transformations; `ipconvplot.m` for instrument-to-probe axes transformation and `piconvplot.m`, for probe-to-instrument axes transformation. `piconvplot.m` calculates the TIL-X and TIL-Y angles for rotations about the probe Y and Z axes. `ipconvplot.m` makes the reverse calculation and additionally calculates the angle of probe tilt away from the vertical, sometimes referred to as the angle of repose. Figures 6.3 and 6.4 show the conversion plots from the two MATLAB routines. Non-graphical versions of the two routines, `ipconv.m` and `piconv.m` have also been written to simply convert single orientations in one frame to the other, and accept tabulated orientation history as will be received in the Huygens data set.

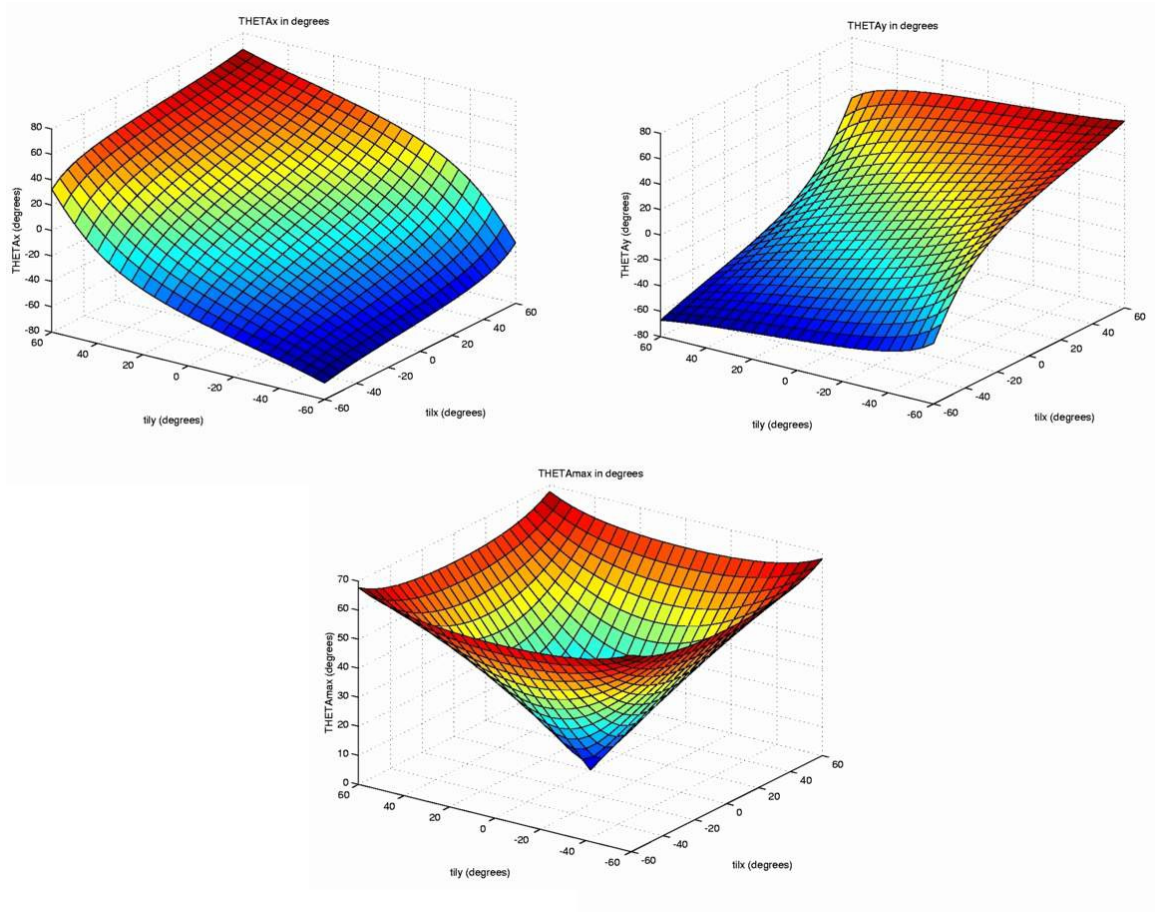


Figure 6.3: Conversion of TIL-X and TIL-Y angles to rotation angles about the probe x_p (left) and y_p (right) axes. Also shown (centre) is the inclination angle of the probe relative to vertical.

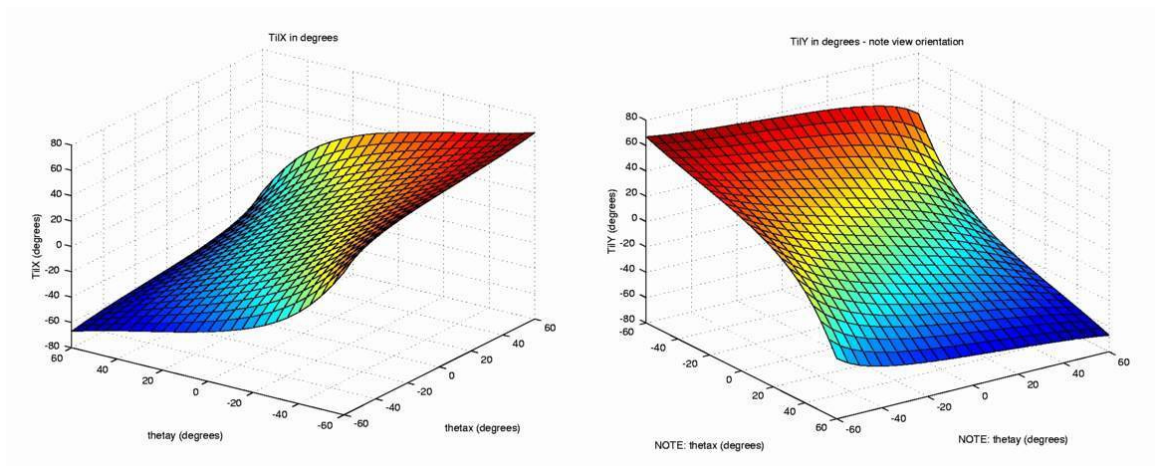


Figure 6.4: Conversion of probe axis rotation angles (horizontal axes) to TIL-X (left) and TIL-Y (right) measured angles (represented on vertical axes).

6.3 Effects of spin on TIL at Titan

As shown theoretically in section 3.2.3 and demonstrated experimentally in section 5.5, the TIL sensor is susceptible to centrifugal acceleration and in the presence of probe spin an inclination of the fluid surface will be induced. Distinguishing between this inclination due to spin and the inclination due to tilt depends upon the exact motion, and several cases are discussed below in section 6.3.3. First however the susceptibility of the TIL sensor to probe spin rates and the limitations imposed on the sensor measurement range are discussed. Brief mention is also given to the smallest spin rates resolvable by the TIL sensor.

6.3.1 TIL measurement range during probe tilt and spin

The centrifugal offset induced in the surface inclination of the TIL sensor fluid was given in equation 5-12. Assuming a value for the Titan gravitational acceleration, g_t , of 1.35m s^{-2} , and radial displacement of the TIL sensor aboard Huygens, r_t , of 0.36m, the centrifugal offset angle θ_{off} varies with probe spin rate on Titan as shown in Figure 6.5 (b). The angular limit of the sensor beyond which linearity breaks down was given in section 3.2.2 as $\pm 60^\circ$ about each of its X and Y axes. Therefore for a given offset angle, the measurable attitude measurement range, θ_{lim} , is offset to

$$\theta_{lim} = +(60^\circ - \theta_{off}) / -(60^\circ + \theta_{off}) \quad (6-1)$$

This may of course mean that for part of a probe revolution attitudes of greater than 60° would be measurable (the inclination measurement varies sinusoidally due to the precession of the gravity vector about the spin axis, viewed from within the probe reference frame, as the probe rotates). However for guaranteed range coverage throughout a revolution the limit of $(60^\circ - \theta_{off})$ is imposed. Conversely for a given probe inclination, a maximum measurable spin throughout one complete revolution of the probe exists. The maximum detectable spin, Ω_{max} , that can exist alongside a probe inclination, θ , before the sensor reaches its limit is then given by

$$\Omega_{lim} = \left[\frac{[g_t \tan(60^\circ - \theta)]^2}{r_t} \right]^{1/2} \quad (6-2)$$

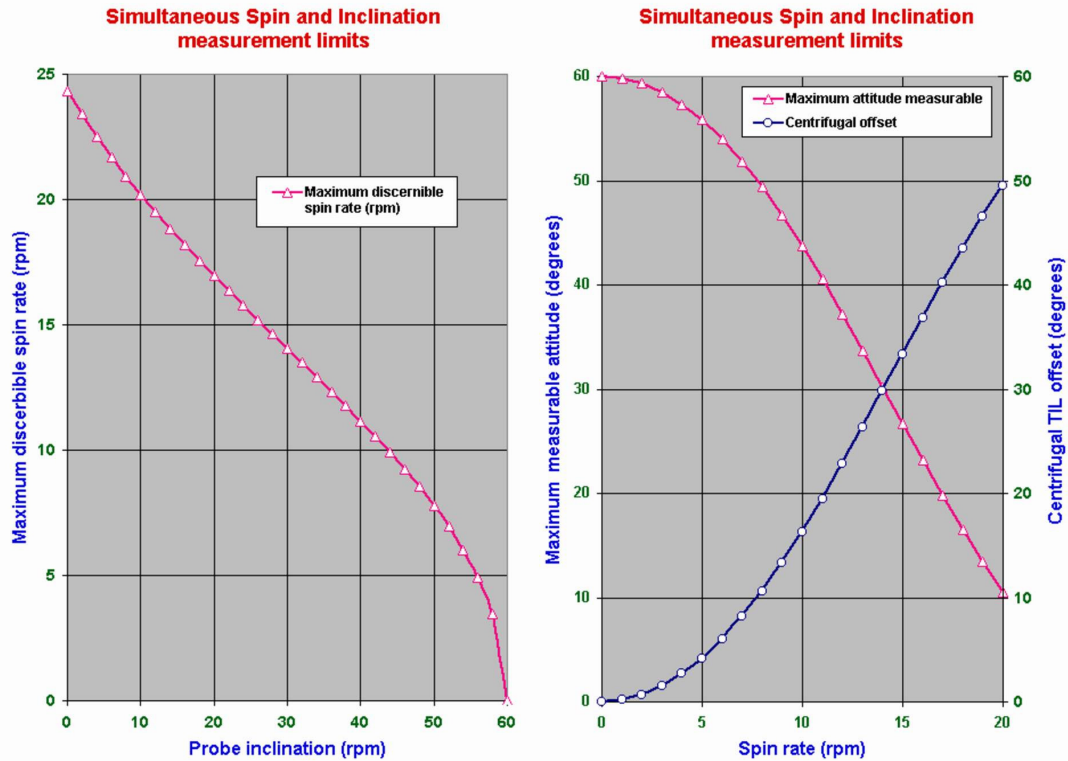


Figure 6.5: (a) & (b) Limits of the TIL sensor measuring spin and inclination simultaneously on Titan. In indicated in blue in (b) is the centrifugal offset

Figure 6.5(a) shows θ_{off} , θ_{lim} against spin rate Ω , and Figure 6.5(b) Ω_{lim} against probe inclination θ . Spin rates of greater than 20rpm have not been considered due to the maximum rates expected during the descent at Titan, as shown in Figure 1.4 [Lebreton & Matson, 1997]. By design of the Huygens parachute system inclinations during descent are expected to be restricted to angles of less than 10° , a requirement driven by probe-orbiter link requirements. As shown, these maxima would suggest saturation of the TIL sensor unlikely. It is interesting to note that for small inclinations the TIL sensor would measure greater spin rates than those measurable by the Huygens RASU unit which has a maximum measurable spin limit of 15rpm. It will also be seen in section 6.3.3 that the centrifugal offset is not necessarily the only method of retrieving the spin rate from the TIL data during descent.

6.3.2 Minimum resolvable spin

The minimum spin discernible with the TIL sensor is calculated using the least bit resolution of the TIL sensor. Using equation 5-12, and knowing that the ADC unit within the SSP electronics for the TIL sensor has a range of $\pm 5V = 10V$ at 12-bit resolution, a least bit resolution for the TIL sensor of 0.08° is calculated. This is finer

than the manufacturers specified accuracy of the TIL sensor, however the value will be used for the sensitivity calculation here. It then follows that the smallest spin rate detectable by TIL-Y, $\delta\Omega_{til_min}$, is approximately 0.7rpm. The manufacturers quoted accuracy of $\pm 0.1^\circ$ in angle measurement however means an error of approximately ± 0.3 rpm in this minimum resolvable value however. Assuming a TIL error of $\pm 0.5^\circ$ due to noise during descent the level of uncertainty would increase to just over 1rpm.

6.3.3 Recognising Spin from the TIL signal

Spin and tilt about probe centre

Whilst the discussion above highlights limits of simultaneous spin and tilt measurement, it does not address the separate question of how to differentiate between the angle measured due to spin and the angle measured due to inclination. The experiment described in section 5.5 verified the spin profile for an oscillating TIL sensor aboard a rotating platform with spin axis vertical. In that case the TIL output was simply the sinusoidal motion being executed by the dynamic calibration platform stepper motor, plus the centrifugal offset. In the case where the spin axis itself is inclined the TIL output profile is slightly different. Figure 6.6 illustrates the motion in question.

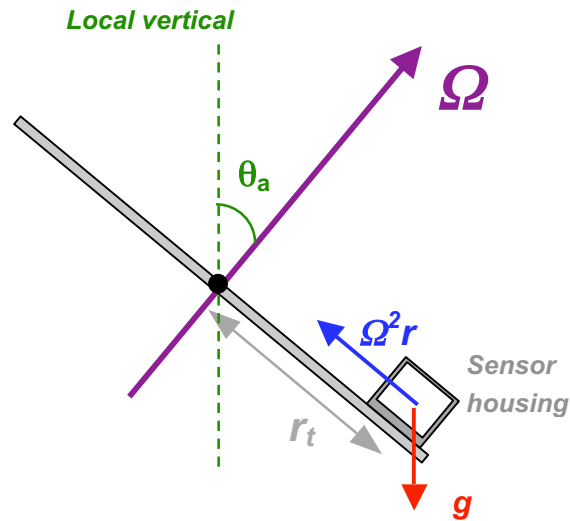


Figure 6.6: TIL sensor spinning about axis through O

For the case shown the platform is taken to be fixed at O. Figure 6.7(a) shows the TIL outputs associated with 10° tilt alone, 10rpm spin alone, an oscillating tilt without spin, and a constant 10° tilt of the spin axis. In the cases of zero spin the plane of the diagram is taken to be perpendicular to the measurement axis of the TIL sensor, and for the calculations of this section the response time of the TIL sensor modelled and calculated

in Chapters 3 and 4 is neglected (mention is given later of the effects of the sensor lag). In the case of oscillating θ , an amplitude of 10° and period of 17s is chosen to represent the approximate natural period of oscillations of a pendulum length 10m on Titan (the approximate parachute-probe distance). However unlike the Huygens case the rotation shown here is about the fixed point O , neglecting linear accelerations associated with the parachute swing.

The sinusoidal variation shown in the case of oscillating tilt and no spin is purely due to inclination change. The sinusoidal variation in the case of spin is due to the fact during one complete revolution of the platform the gravity vector, as viewed from the rotating reference frame, will have precessed once about the spin axis. Therefore, for example, twice per revolution the tilt is directed along the non-measurement axis of the sensor.

In the case of both spin and sinusoidal variation of the inclination of the spin axis, the output is more complex. Again it must be stressed that the spin axis is assumed to rotate about point O . Figure 6.7(b) shows the variation in TIL response for three spin rates: 2, 10 and 20rpm. The resulting signal is of course the sinusoidal variation during spin explained above, modulated by the sinusoidal spin axis inclination, and then offset by the centrifugally induced angle.

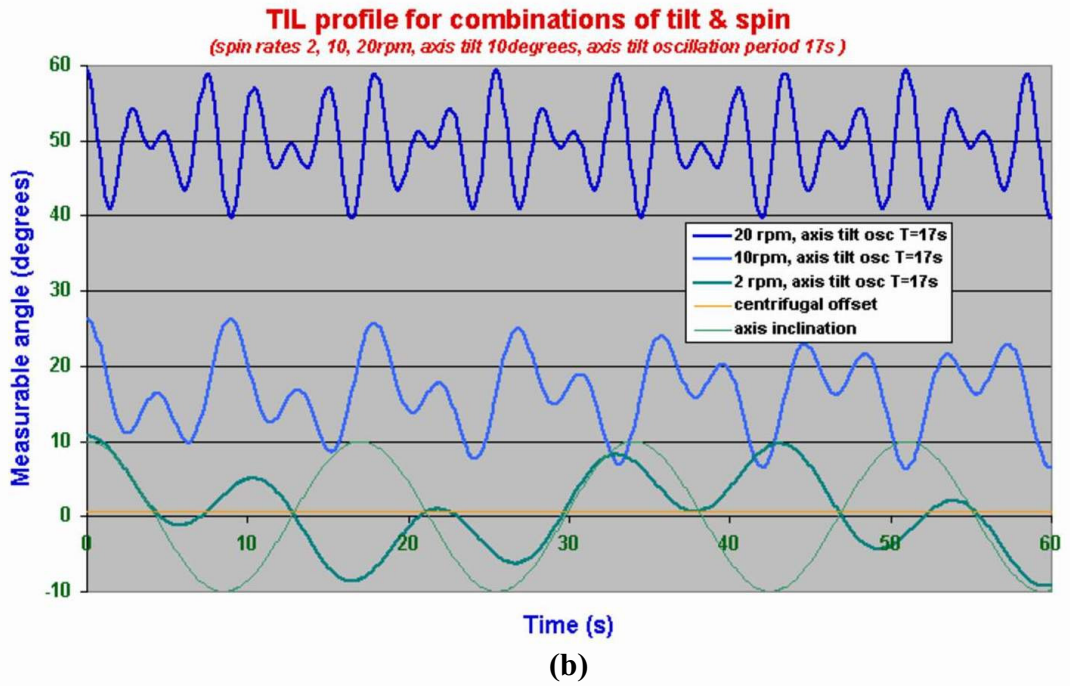
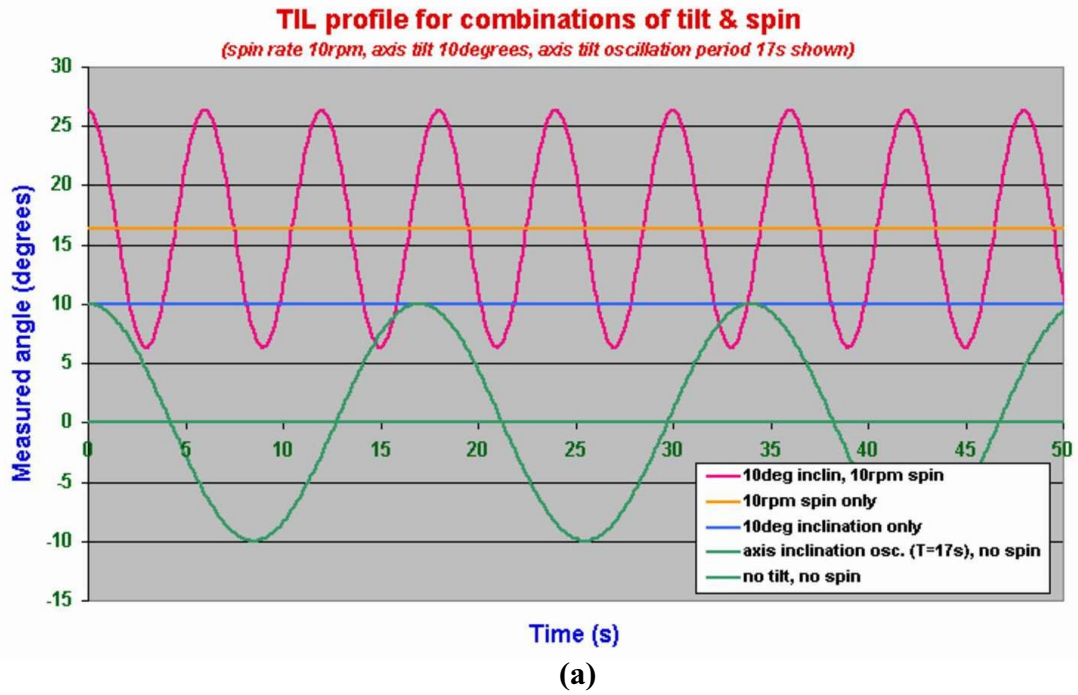


Figure 6.7: Theoretical TIL output angles for combinations of spin and spin axis rotation about fixed point O indicated in Figure 6.6.

Since the angle measured by TIL, θ_{meas} , is given by

$$\theta_{meas} = \theta_a \cos(\omega_a t + \phi) \cos(\Omega t + \psi) + \arctan\left(\frac{\Omega^2 r_t}{g_t}\right) \quad (6-3)$$

where θ_a is the axial tilt, ω_a the axial oscillation frequency, and ϕ and ψ phase constants, and Ω the spin rate it is therefore possible from the oscillations observed to reconstruct the axis inclination history for the arrangement of Figure 6.6. These theoretical profiles were recently verified during an elaborate and useful test by the Huygens Probe DISR imager development team at the University of Arizona [Rizk et al., 2001]. The above set-up however does not model an important aspect of the probe motion known to affect the TIL output, namely that where the spin axis does not rotate about a point within the horizontal plane of the sensor, as is the case during parachute descent, for example. This is considered in the next section.

6.4 Investigating the TIL and HASI-ACC measurement capability of parachute descent dynamics

6.4.1 Introduction

Spin and tilt about point displaced from probe

The above set-up however does not model an important aspect of the probe motion known to affect the TIL output. Consider the probe-parachute system shown in Figure 6.8. The probe and parachute spin axes are decoupled via a unit housed on the main riser. Unlike the arrangement in Figure 6.6 however, the probe spin axis rotates of course not about a point within the probe but some point O within the canopy.

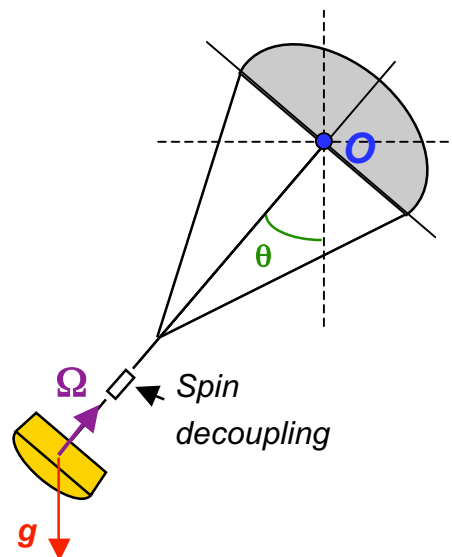


Figure 6.8: Huygens probe beneath parachute showing spin decoupling unit on riser. Direction of gravity, spin rate Ω , and inclination shown. Probe spin axis rotates about O .

This raises issues of TIL measurability discussed in section 5.6.2 for pendulum motion about a fixed point. There it was explained that in the absence of any component of non-gravitational acceleration parallel to the base of the TIL sensor, no inclination would be indicated. Clearly in the case of the probe-parachute system above this model is not satisfactory either since the point about which any pendulum-type swinging motion occurs is not fixed but descending with the parachute. Neither is it satisfactory to consider simply a vertically descending point. Parachute dynamics are highly complex and the motion of the point O in Figure 6.8 above will not necessarily be vertical even with the parachute designed to restrict probe attitude to less than 10° due to probe-orbiter link constraints. Parachutes generate both lift and drag and the motion will depend upon the direction of the wind velocity vector, which will also vary with altitude. Figure 6.9 shows a two-dimensional, simplified representation of the probe-parachute system.

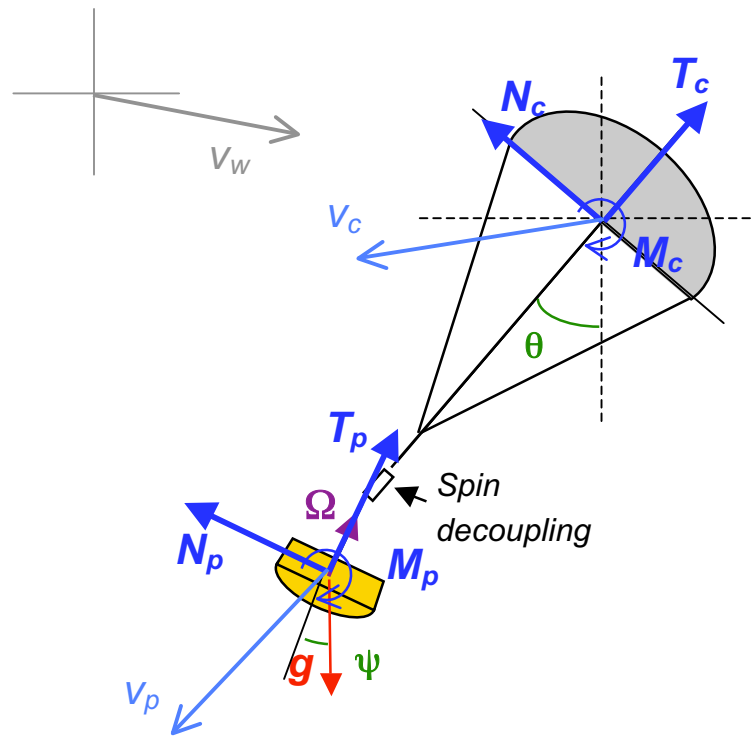


Figure 6.9: Simplified drawing of a six degree of freedom probe-parachute system (2-d) indicating normal and tangential forces and moments on the probe and canopy, probe and canopy attitude and velocity vectors, and wind velocity vector.

The diagram illustrates the drag and lift forces acting on the probe and canopy, resolved along vectors parallel (T) and normal (N) to the probe and canopy axes of symmetry respectively. Subscripts distinguish between the probe and canopy acting forces. A moment (M) may also be generated depending on the parachute and probe aerodynamic

coefficients. Being two-dimensional, such a model as shown in diagram is limited to two rotational and four translational degrees of freedom. In three dimensions therefore the parachute and probe dynamics can only be fully simulated using a twelve degree of freedom model, such as that described by [Underwood, 1993]. Extensive modelling work for Huygens was also carried out by Aerospaziale throughout the development of the probe and parachute system.

Such a complex model is a significant undertaking in its own right, and is not treated here. At the same time the estimation of measurements possible using the TIL and HASI-ACC sensors is an important issue and any predictions that may be made are becoming increasingly valuable as a methodology is developed towards the reconstruction of probe trajectory, vital to the accurate atmospheric profiling of Titan.

To offer insights into TIL and HASI-ACC measurement capabilities during descent therefore, a simplified parachute model was attempted. By generating an approximate parachute descent profile it should be possible to calculate the accelerations experienced by the probe, and from these it should be possible to estimate the accelerations and tilt angle measurements that could be made by the HASI-ACC and TIL sensors. These responses could then be compared with the known inputs and comments made about the possibilities for reconstruction. Clearly the goal of such a model was not to predict accurately the probe trajectory; such a model would require significantly more time and resources than available here. Rather it was to generate a more realistic sequence of accelerations than those described so far, investigate their representation by the two Huygens sensors, and highlight any areas that justify more sophisticated modelling.

6.4.2 3-d.o.f. parachute model for TIL and HASI-ACC measurement predictions

To generate the appropriate range of accelerations a three degree-of-freedom rigid-body model as described by [Cockrell, 1987] was used. This model simulates a two-dimensional parachute and probe, treated together as a single rigid body, with two translational degrees of freedom and one rotational, as indicated in Figure 6.10. Since the model does not simulate spin, the TIL sinusoidal variation and centrifugal offset effects described previously were incorporated separately. This is not a true fourth degree of freedom to the model however, since the combination of probe spin with the moments shown in the diagram would in reality generate forces perpendicular to the plane of the page. Nevertheless, for the purposes of this preliminary investigation it is useful to observe the effects of the simple sinusoidal and centrifugal variations that complicate the sensor outputs even before more complex dynamics are considered, and

these effects are superimposed on the TIL measurement results separately at the end. The parameters used are shown in Figure 6.10.

The model employs body axes coordinates X, Y, Z , with ω_y being the rotation rate about the Y axis. N, T and M are the body-axis normal (along X axis) and tangential (along the Z axis) components of the aerodynamic forces and pitching moment calculated from the respective aerodynamic coefficients C_N, C_T, C_M by

$$\begin{aligned} N &= \frac{1}{2} \rho V^2 S_0 D_0 C_N \\ T &= \frac{1}{2} \rho V^2 S_0 D_0 C_T \\ M &= \frac{1}{2} \rho V^2 S_0 D_0 C_M \end{aligned} \quad (6-4 \text{ a, b \& c})$$

where \underline{V} is the total velocity of the air relative to the body axes ($\underline{v}_w - \underline{v}$), $S_0 D_0$ a reference area, and ρ the atmospheric density. C_N, C_T, C_M are each functions of γ , the angle of attack.

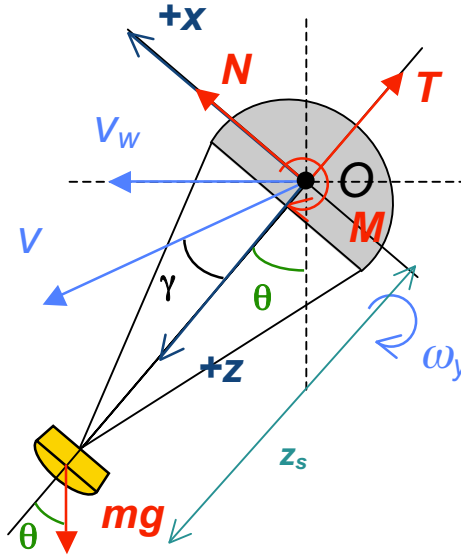


Figure 6.10: Two dimensional, 3 d.o.f, rigid body parachute model

[Cockrell, 1987] gives the equations of motion for the above system as

$$\begin{aligned} (m + \alpha_{11}) \frac{dv_x}{dt} + (mz_s + \alpha_{15}) \frac{d\omega_y}{dt} + (m + \alpha_{11}) \omega_y v_z &= -mg \sin \theta + \frac{1}{2} \rho V^2 S_0 D_0 C_N(\gamma) \\ (m + \alpha_{33}) \frac{dv_z}{dt} + (m + \alpha_{11}) \omega_y v_x + (mz_s + \alpha_{15}) \omega_y^2 &= mg \cos \theta - \frac{1}{2} \rho V^2 S_0 D_0 C_T(\gamma) \end{aligned}$$

$$(I_{yy} + \alpha_{55}) \frac{d\omega_y}{dt} + (mz_s + \alpha_{15}) \left(\frac{dv_x}{dt} + \omega_y v_z \right) - (\alpha_{11} - \alpha_{33}) v_x v_z = -mgz_s \sin \theta + \frac{1}{2} \rho V^2 S_0 D_0 C_M(\gamma)$$

(6-5 a, b & c)

where I_{yy} is the body moment of inertia, m the mass of the probe, z_s the distance between the probe centre of mass and O , assuming the distance of the centre of pressure from the origin is negligible. α_{mn} are ‘added mass’ parameters used by to represent the effects of the air trapped within the parachute, given by $k_{mn} \rho \pi D_0^3 / 12$ where k_{mn} are the added mass coefficients and for a centre of pressure located close to the body-axes origin, O , only k_{11} and k_{33} need be considered [Cockrell, 1987].

Putting $\omega_y = (d\theta/dt)$ the three equations can then be solved, and v_x , v_z , and ω_y obtained. A MATLAB program was written to take as inputs $r_x(0)$, $r_z(0)$, $v_x(0)$, $v_z(0)$, $\theta(0)$, $\omega_y(0)$ and $v_w(0)$, where r_x and r_z are position coordinates and the subscript (0) refers to $t=0$. The program then solves equations 6-5, and provides time histories of r_x , r_z , v_x , v_z , ω_y and θ . The following values were assumed for the model; $m = 201\text{kg}$ [Lebreton & Matson, 1997], $z_s = 10\text{ m}$, $S_0 D_0 = \pi D^2 / 4$ where D is the parachute diameter [Cockrell, 1987], and k_{11} and $k_{33} = 1.1$ and 0.2 respectively [Cockrell, 1987]. C_N , C_T and C_M , each a function of γ , were adapted from C_N , C_T and C_M values for a round flat canopy parachute given in [Tory, 1977]. The results shown were generated for a initial descent velocity of 12 m s^{-1} , i.e. $v_x(0)=0$, $v_z(0)=12\text{ m s}^{-1}$, consistent with an atmospheric density ρ of 0.5 kg m^{-3} at approximately 50km altitude [Flasar et al., 1997]. The wind speed profile was assumed constant over the duration of descent modelled (approximately 200s). At this altitude zonal wind speeds as high as 50 m s^{-1} have been suggested [Flasar et al., 1997] however the results shown here were generated using lower estimates of the same model of 10 m s^{-1} , assumed to be acting horizontally. The model suggests faster damping of parachute-probe oscillations with higher constant wind speed, but a larger steady state inclination θ due to aerodynamic force. Since the model does not treat the parachute and probe separately, to simulate the response following a wind gust an angular velocity $\omega_y(0)$ was imparted to the system as a starting condition, with values of 0 , 3 , 6 and 10° s^{-1} used in the particular results shown. $\theta(0)$ was set to zero for all except the final two plots, where a value of 10° was used.

The MATLAB program produces several plots, a sample of which are shown in Figure 6.11. The first four plots are transformed to a Titan surface reference frame so as to

provide altitude, and show two examples of sample trajectories generated by the parachute model to provide as inputs to the TIL and HASI-ACC measurement models.

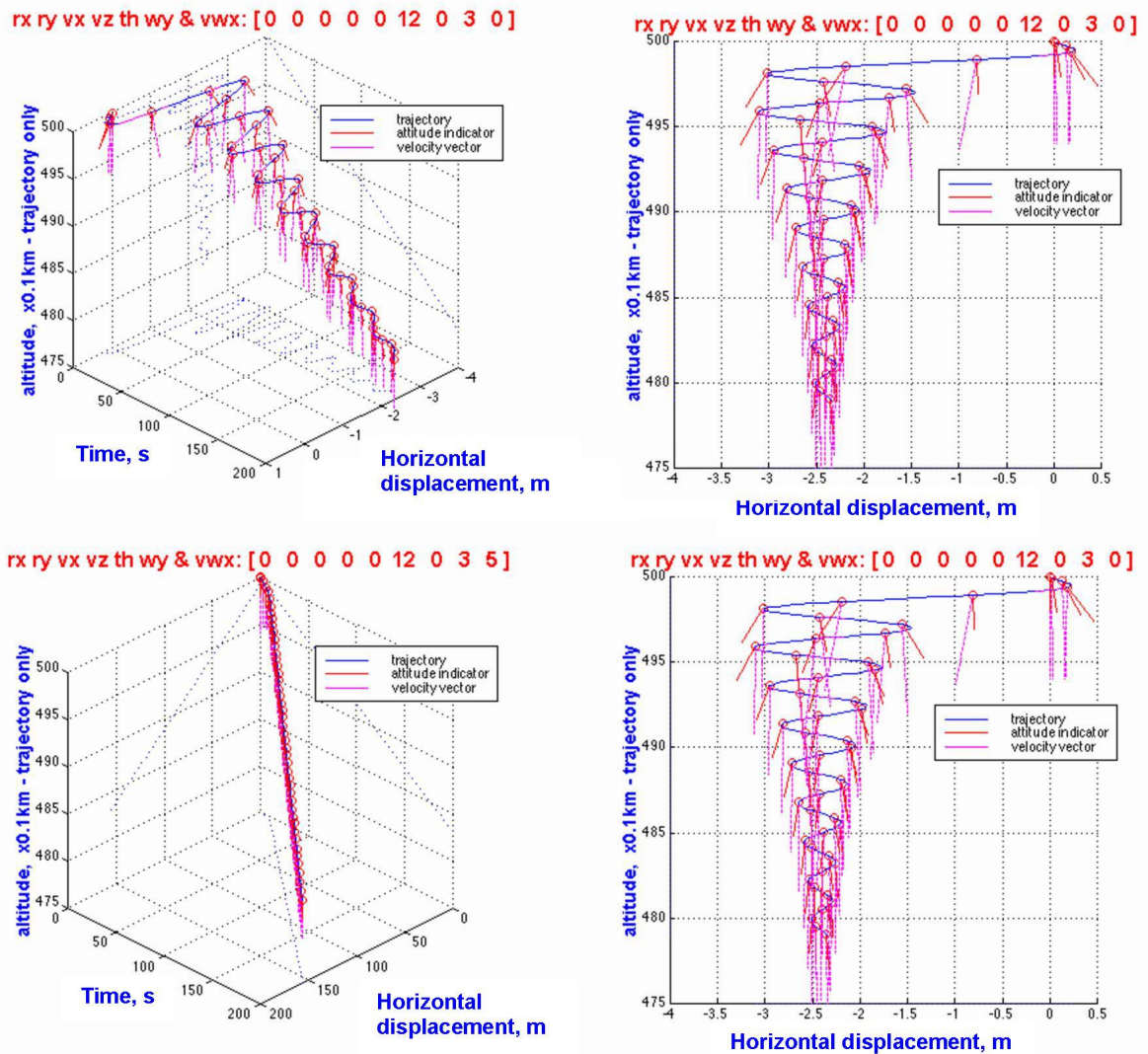


Figure 6.11: Approximation trajectories generated against which TIL and HASI-ACC measurement capability can be tested. Wind velocities 0 and 5 m s^{-1} modelled. (Note: the z-axis altitude uses a x0.1 km scale which applies only to the trajectory. The attitude (red) and velocity (magenta) direction indicators are not scaled)

The left hand graph uses isometric perspective to display the two-dimensional trajectory against time, whereas the right hand graphs show the same trajectory without the time axis. Important to note is the x0.01 km scaling of the vertical axis, i.e. 500 should read 5 km altitude. This scaling however does not apply to the attitude and velocity direction indicators, where the former (marked in red) indicates the direction of the parachute probe +z-axis, and the latter (in magenta) indicates the probe velocity vector, and these

represent the actual angles predicted by the model. As explained above, the goal of the model was not to predict accurately the true probe trajectory but to provide a range of sample parachute descent accelerations to apply to models of the TIL and HASI-ACC sensors. Consequently the detailed modelling of the 10° attitude limit imposed by the actual Huygens parachute was not included. Indeed some of the initial conditions used to generate results shown have exceeded this limit to show more clearly theoretical HASI-ACC and TIL responses. The input conditions for each run of the model are indicated at the top of each graph, using the convention $[r_{x(0)}, r_{y(0)}, r_{z(0)}, v_{x(0)}, v_{y(0)}, v_{z(0)}, \theta_{(0)}, \omega_{y(0)}, v_w]$ where $r_{y(0)}$ and $v_{y(0)}$ are zero due to the dimensionality of the model.

6.4.3 TIL and HASI measurements of probe dynamics as generated with by the 3-d.o.f. parachute model

From the time history of the parachute-probe velocity vector (calculated by the model in body axes) and angular velocity it is relatively straightforward to obtain the accelerations experienced by the accelerometer and TIL sensor by considering their (fixed) positions within the body axes, and the translation and rotational motion of the body axes themselves. Subtracting the acceleration due to gravity, as explained in section 3.2.3, the measured tilt accelerations are thus obtained. At this point a sinusoidal component with angular frequency Ω and a centrifugal offset $[\arctan(\Omega^2 r/g)]$ was introduced to the TIL output to approximate effects of the probe spin (de-coupled from parachute). Again this approximation does not address the cross product forces associated with the moment and spin vectors, but is sufficient to provide useful insights into the resulting sensor signals. Since the descent velocity did not vary significantly over the durations considered and the atmospheric density was assumed constant, the spin rate (aerodynamically induced, as described in section 1.2.3) was also assumed constant. Figures 6.12 to 6.15 show sample results of the model, with the initial conditions again indicated at the top of each graph and using the convention described for Figure 6.11.

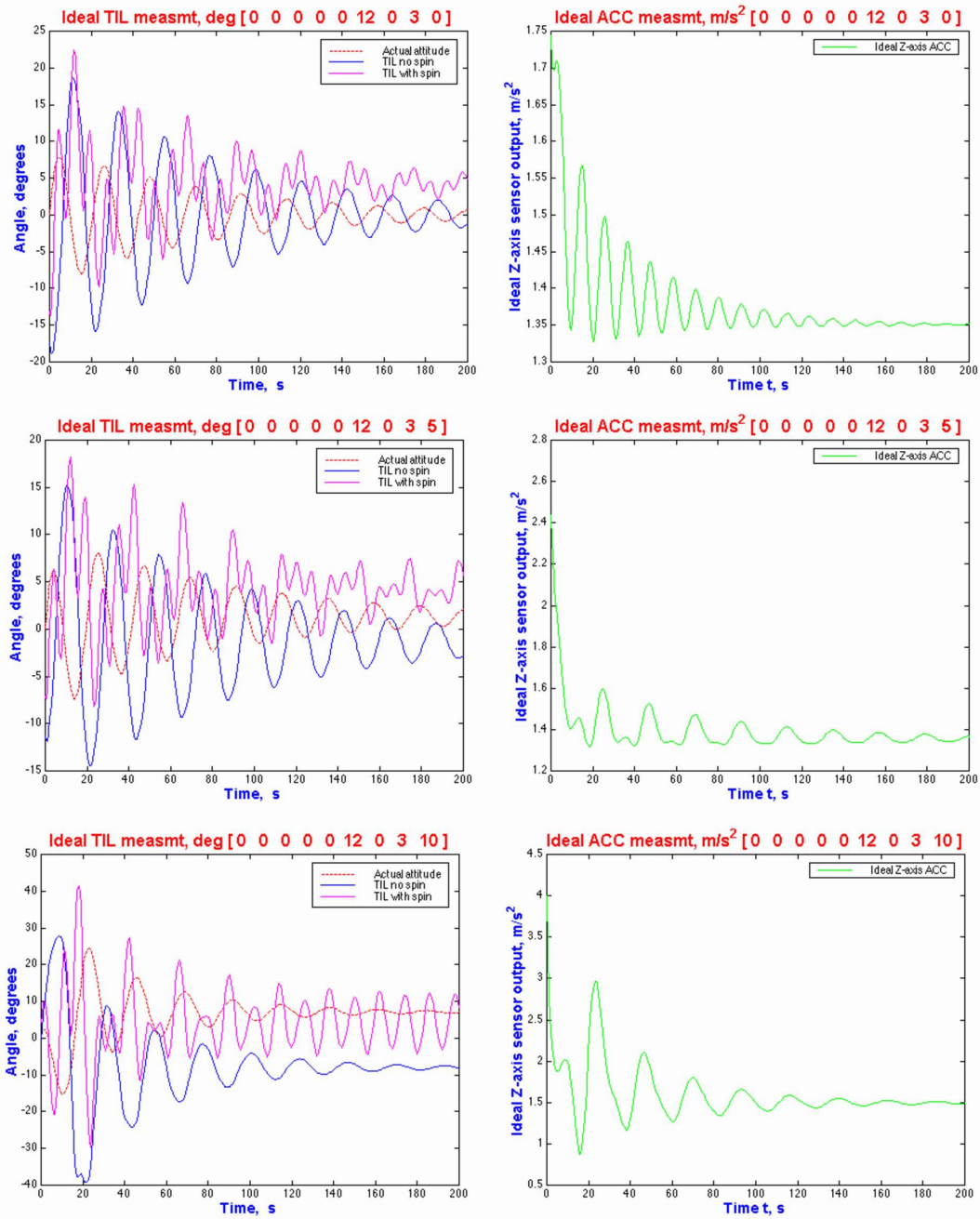


Figure 6.12: Simulated TIL and HASI-ACC measurements for the two dimensional 3-d.o.f parachute model, using initial angular velocity 3° s^{-1} and horizontal wind velocities 0, 5 and 10 m s^{-1} . TIL measured attitude, with and without spin effects, is compared with actual attitude profile.

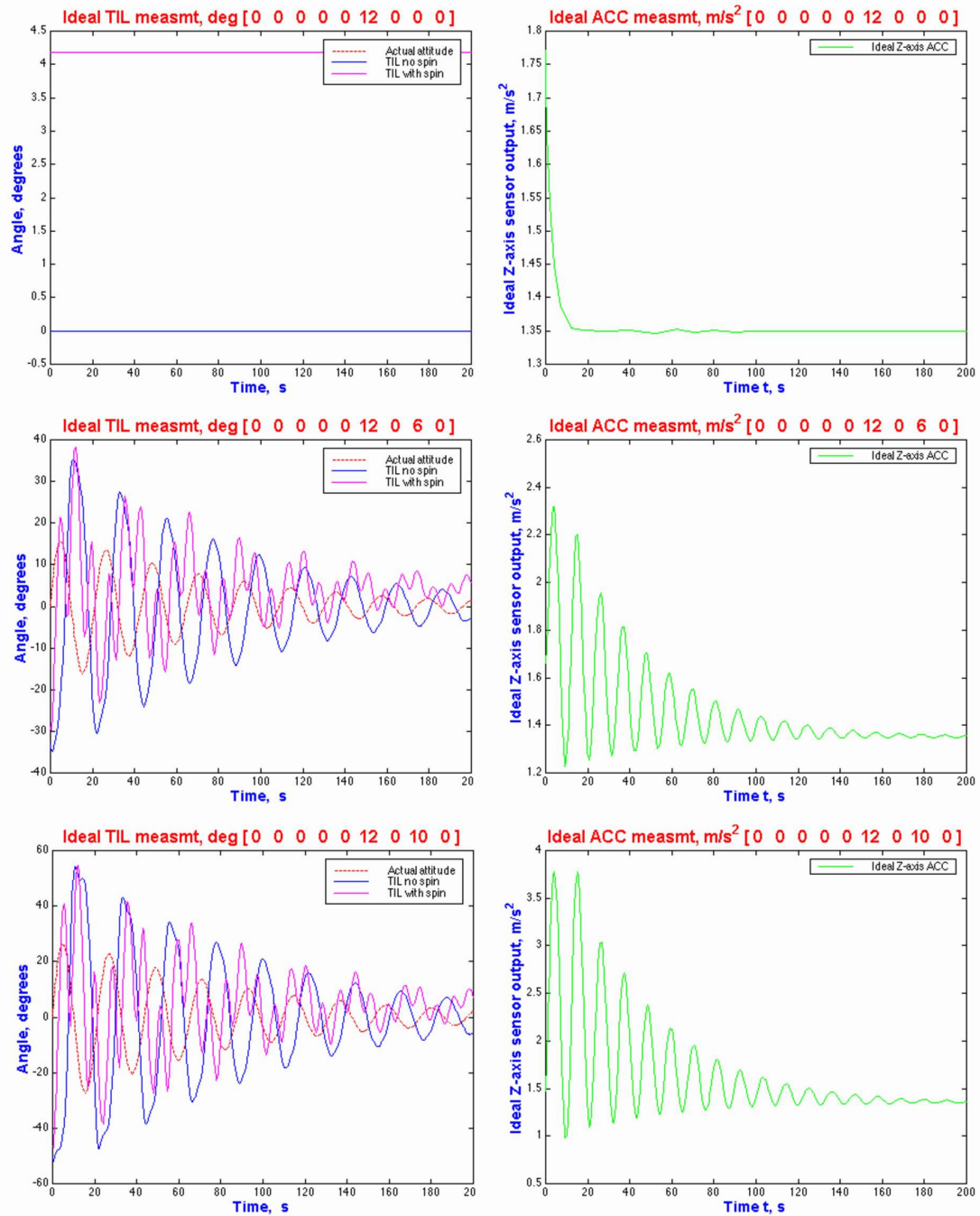


Figure 6.13: Simulated TIL and HASI-ACC measurements for the two dimensional 3-d.o.f parachute model, using horizontal wind velocity $v_w = 0$ and initial angular velocity $\omega_y = 0, 6$ and 10°s^{-1} . TIL measured attitude, with and without spin effects, is compared with actual attitude profile.

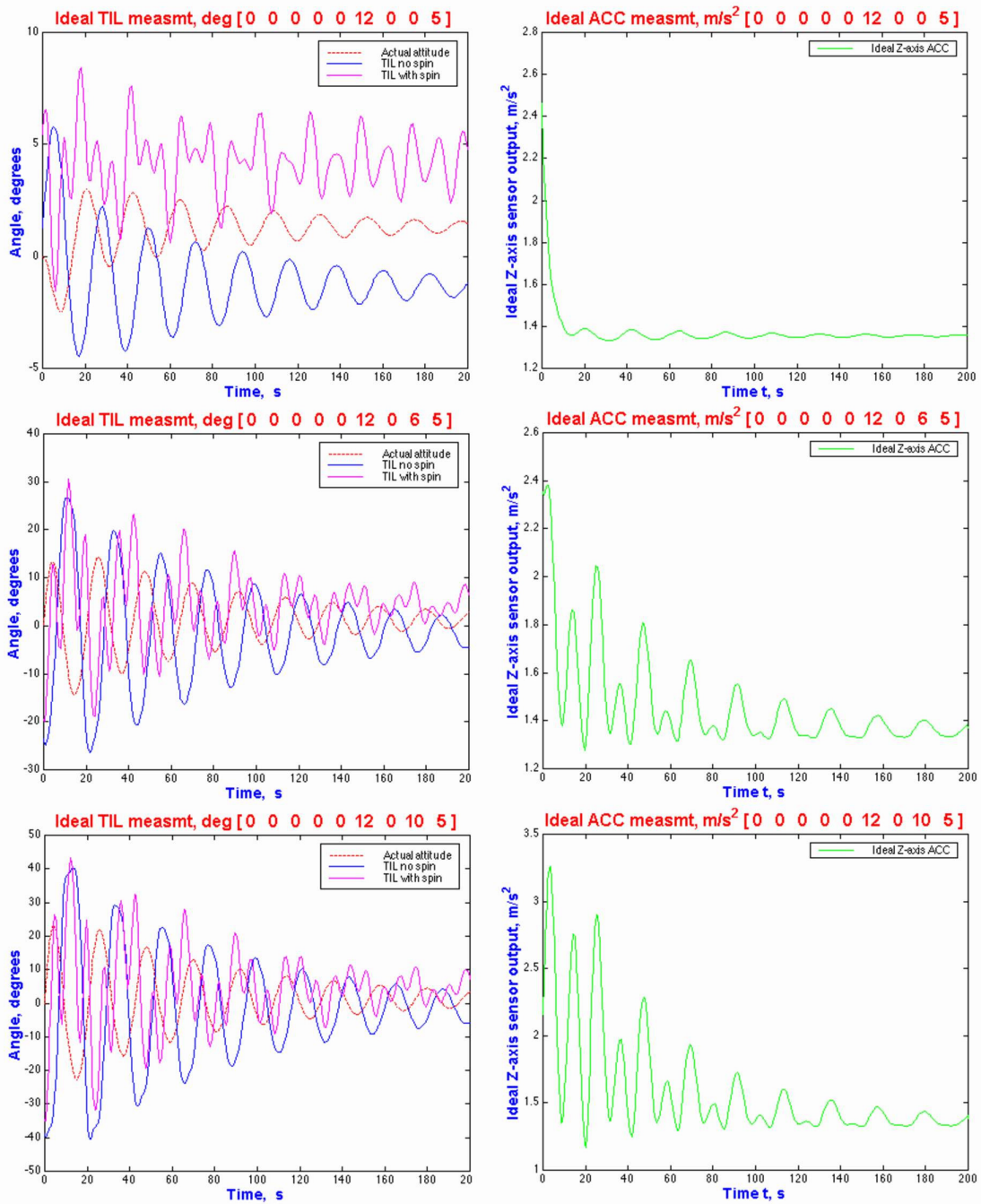


Figure 6.14: Simulated TIL and HASI-ACC measurements for the two dimensional 3-d.o.f parachute model, using horizontal wind velocity $v_w = 5 \text{ m s}^{-1}$ and initial angular velocity $w_y = 0, 6$ and 10°s^{-1} . TIL measured attitude, with and without spin effects, is compared with actual attitude profile.

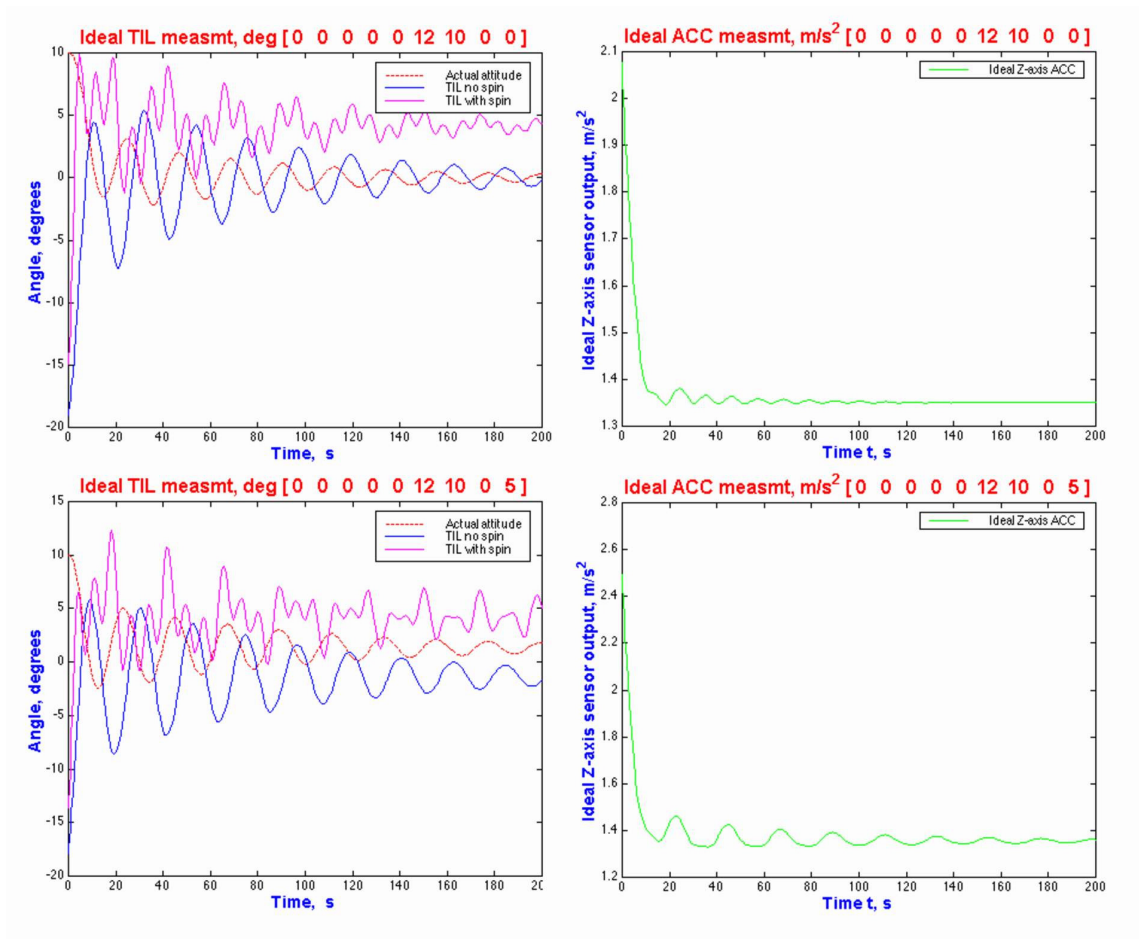


Figure 6.15: Simulated TIL and HASI-ACC measurements for the two dimensional 3-d.o.f parachute model, using initial angular velocity $w_y = 0$, initial inclination angle $\theta = 10^\circ$, and horizontal wind velocities $v_w = 0$ and 5 m s^{-1} . TIL measured attitude, with and without spin effects, is compared with actual attitude profile.

Spin reconstruction with TIL

The model shows clearly the ability to retrieve from the TIL and ACC signals the parachute swing frequency and, from TIL, the probe spin rate. Information may also be deduced concerning the wind velocity from both TIL and ACC (note the steady state value of both sensors in the case of higher winds, in Figure 6.12). As with section 6.3.3 the spin and inclination contributions may be distinguished using any sinusoidal component that appears in both TIL sensor outputs, phased 90° apart. Section 6.3.1 considered the maximum spin rate measurable from the centrifugal offset of the TIL fluid surface and suggested a maximum of approximately 24rpm for no probe tilt, decreasing with the level of probe tilt. This improves on the level of spin measurable with the RASU unit, and indeed it would be possible to measure higher rates of spin still from the frequency of the TIL signal rather than the centrifugal offset. Once the spin rate is calculated it is then possible to remove all spin effects from the TIL signal, and in this case retrieve the ‘TIL no spin’ signal (in blue) in each of Figures 6.12 to 6.15.

Swing reconstruction with TIL

The reconstruction of the probe-parachute swing angle is not so straightforward. The model shows that the TIL response will be out of phase with the actual inclination, although in the real probe case, the specific value of the phase difference will depend on the relative dynamics of the parachute and probe, as indicated in Figure 6.9 by a ‘scissor-mode’ swing for example. Since the rigid-body approximation treats the two as one, such motion cannot be represented, and the phase difference between the probe inclination and the TIL measurement cannot be taken to be accurately represented using this model. Similarly the model succeeds in highlighting the difference between the true probe swing amplitude and that indicated by the TIL sensor. In reality the absolute values of the TIL measured amplitude will again depend on the relative dynamics of the parachute and probe, which in turn are not necessarily those modelled using the rigid body approximation.

Accelerometers

Interesting to note is the fact that whilst the ACC sensor also allows determination of the swing period, and some information on the wind velocity, the use of 3-axis accelerometers would be invaluable in obtaining more information about the directions of the accelerations. The HASI-ACC PZR accelerometers could contribute here, however as the probe descends to lower altitudes the motions become less extreme and therefore the measurable accelerations weaker, as illustrated in the graphs above. With an acceleration measurement resolution of 0.5 m s⁻² [Fulchignoni et al., 1997], some of the motions simulated above may not be resolvable using the PZR.

It should be noted that the work of this section has not treated the higher frequency accelerations generated by smaller scale buffeting of the probe due to turbulence as it descends.

6.4.4 TIL response time

In the predictions made of the TIL sensor response throughout the discussions above, it has been assumed that the fluid surface of the sensor responds immediately to any changing accelerations. The modelling and experimental investigations of Chapters 3 and 5 have shown that this is obviously not the case, and estimates of the time for the sensor to achieve equilibrium level under Titan gravity have ranged from theoretical values of 0.1s to worst case observed values of just under 1s. Calculations of the damped frequency of the TIL fluid have estimated values close to 4Hz and observations have suggested worst case values of between 2 and 3Hz (section 5.3.10). Consideration of the ideal case (infinitely fast) TIL responses modelled in Figures 6.12 to 6.17 show that the acceleration variations likely to be observed on Titan during descent are of significantly longer period than that which would give rise to either resonance or a significant phase lag due to the sensor fluid's frequency response (sections and 3.5.2 and 5.3.10). The model has shown that the highest frequency variations will be those due to spin and even for the highest spin rates predicted on Titan, 20rpm, such oscillations would be an order of magnitude slower than the natural frequency response of the sensor. The TIL response time is therefore not considered to impact significantly the reconstruction of the parachute dynamics as modelled in this section. Particularly high frequency motions associated with the transition through the transonic region during the first part of the probe descent beneath the Main Parachute (section 1.2.3), and impulse type accelerations associated with turbulence and strong wind gusts during the lower parts of the descent have not been modelled here, and it is possible that these motions may necessitate consideration of the TIL response time.

6.4.5 TIL Sampling rates

The TIL sensor is sampled at 1Hz throughout the descent from T_0 until impact with the surface, after which point the sampling rate is doubled to 2Hz. Considering the relatively slow variations of the predicted TIL measurements of this section such a sampling rate during descent should permit reasonable reconstruction of the TIL signal for all but the highest spin rates. For the maximum value for predicted spin of 20rpm, a 1Hz sampling rate would allow three measurements per revolution. In the event of combined spin and swing, consideration of the graphs of this section suggests the accuracy of dynamic

reconstruction using TIL, at the highest predicted spin rates, may be impacted by the data sampling rate.

6.5 Other motions

6.5.1 Surface Waves

Probe motion and gravity-wave measurement with TIL

As shown in Chapter 2, should the Huygens probe impact a liquid surface a range of dynamics may arise. Studies have shown that the probe is likely to remain afloat for the duration of the surface mission and have also made predictions as to its natural buoyant motion, with rocking periods estimated at around 3s [Lorenz, 1994]. The probe motion due to the surface waves discussed in Chapter 2 may be considered similar to that of a wave buoy, and the detailed modelling of such dynamics is complex and will depend upon the local wave spectra. Measurements on earth made using wave buoys have been invaluable in the development of ocean wave research and [Cartwright et al., 1963] discusses methods of reconstructing wave spectra using a wave buoy housing an accelerometer measuring vertical acceleration and gyroscopes measuring pitch and roll. Given the dependence on the local gravity vector of both the TIL sensor fluid and gravity waves on a sea surface, it is not immediately apparent how the TIL sensor would perform in such an environment.

The modelling of sea wave motion is not treated in this work, however early discussions have taken place investigating the possibility of an experiment to observe the sensor's representation of such dynamics [Challenor et al., 2000]. A suitable wave-buoy was identified by the Southampton Oceanography Centre at the University of Southampton, and preliminary design discussions were commenced in August 2000 for the integration of a TIL sensor, and possibly the HASI-ACC servo sensor, for testing atop a sea surface independently characterised by an accelerometer and gyroscope suite as outlined by [Cartwright, 1963]. The sensor sampling rates would be increased relative to the Huygens sampling rates, such that investigation could be carried out firstly into the acceleration induced offsets that would complicate derivation of wave parameters from the TIL data, and secondly into the limitations imposed on spectral reconstruction by the 2Hz surface sampling rate. To date no further progress has been made, and to some extent will depend on the estimated likelihood of a liquid landing by Huygens.

TIL response time and wave frequency

If however it is assumed that the TIL sensor *can* in some way offer some measurement indicating wave frequency, some estimates are possible by given consideration to the wave periods and wavelengths concluded in Chapter 2. If it is assumed that waves shorter in wavelength than the diameter of the Huygens Probe, i.e. 1.3 m, do not significantly affect the motion of the probe, then a lower value for the wave period of measurable peak frequency wind waves may be estimated at 2 seconds using the results of Chapter 2 (consistent with a surface wind speed of approximately 0.5 m s^{-1}). This is sufficiently slow as to avoid resonance for the TIL fluid (4Hz on Titan) and for basic resolution of the peak frequency wave profile using a at 2Hz sampling rate. Longer and slower waves generated by faster surface winds, or greater fetch lengths will be better resolved. However as highlighted in the previous paragraph, a key question is the degree to which the TIL sensor will actually measure the motion due to gravity waves on a sea surface and the case for experimental investigation will likely be influenced by the strength of evidence predicting a liquid landing for the Huygens probe.

6.6 Conclusions

This chapter has considered several aspects of the TIL sensor's dynamic measurement capabilities as relevant to its role in the reconstruction of probe dynamics both during descent and following impact with the surface of Titan. The work of this chapter has drawn from the various analyses and investigations presented throughout this thesis in an attempt to verify claims that have been made regarding the motions measurable by the sensor.

Firstly a program written for transforming between TIL sensor and the more universal probe reference frame was described in section 6.2. The minimum spin resolvable from the centrifugal offset, and limits imposed by the sensor range on measurements of simultaneous inclination and spin were highlighted in section 6.3.1, and the ability of the sensor to indicate spin rates exceeding those measurable by the RASU instrument was demonstrated in section 6.3.3.

The complexity of accurately predicting the TIL and HASI-ACC measurements during parachute descent was discussed in section 6.4, suggesting the need for a twelve degree-of-freedom parachute model for conclusive verification of sensor capabilities. A three degree of freedom parachute model was employed to generate a simple two dimensional parachute descent trajectory against which the TIL and ACC measurements of attitude and acceleration could be compared. A method of incorporating approximate decoupled

probe-spin effects was described and the results were presented in section 6.4.3. Results confirm the complexity of the TIL and ACC measurements, and suggest that whilst spin rate and swing period may be reconstructed using ACC and TIL alone, the sensors do not directly represent the true amplitude or phase of probe swing for the three degree of freedom model. When turbulence and signal noise effects are taken into consideration the complexity of real twelve degree-of-freedom the parachute-probe system on Titan will offer a significant challenge to the accurate reconstruction of probe dynamics and trajectory. In support of the efforts currently underway to coordinate data-sharing between instrument teams for the reconstruction of probe trajectory [Atkinson, 1998] and to maximise the data interpretable from TIL and HASI-ACC sensor measurements, use of a full twelve-degree-of-freedom parachute model is strongly recommended.

The TIL sensor response time, as estimated and observed in Chapters 3 and 5, and sensor sampling rates were discussed in light of the modelled probe motions in section 6.4.4. The degraded TIL response time on Titan is considered sufficiently fast for the representation of most measurable angle variations with the possible exception of those due to significant atmospheric turbulence during the early descent phase. TIL sampling rates are considered sufficient for the reconstruction of motions involving all but the highest predicted spin rates. Brief consideration is given in section 6.5 to the TIL sensor measurement of sea or lake surface motions such as those described in Chapter 2, and recommendation is made for the experimental verification of the TIL sensor's capability in this particular environment.

Chapter 7

Conclusion

This thesis has considered the surface of Titan and the role that may be played by the Huygens Surface Science Package Tiltensor (TIL) throughout the ESA Huygens Mission. Investigations have been presented into both the possible dynamics that may await the Huygens Probe at Titan's surface, and the amount of information that may be contributed by the TIL sensor about the probe's dynamics beneath its parachute during descent. Estimation of the degradation in sensor response time on Titan has also been made, which could be significant when seeking information on any high frequency probe motions, possibly during small scale atmospheric buffeting for example.

The literature on Titan's surface dynamics has been reviewed in Chapter 2 and a gap identified in the treatment of surface waves atop liquid bodies, which remain a possibility at the surface of Titan. Where such bodies exist, the dominance of gravity has been illustrated for free surface waves of wavelengths greater than several centimetres and, under the action of a Titan surface wind, resulting waves have been shown to be longer and slower than their terrestrial counterparts. The extrapolation of terrestrial wind-wave to the Titan case has suggested that surface waves on a Titan sea arising from surface wind speeds of 0.3 ms^{-1} and 1 ms^{-1} will resemble in scale waves on Earth generated by terrestrial winds travelling at 1 ms^{-1} and 3 ms^{-1} respectively. Titan waves will have nearly three times the period and travel almost three times slower than the terrestrial waves however. Issues have been discussed surrounding the applicability of terrestrial models for wind speeds much smaller than 1 ms^{-1} due to the increased influence on Titan of viscous and surface tension effects during both early and latter stages of wave growth. Modelling has suggested that the maximum surface inclinations imparted to the Huygens Probe by waves could be as high as 14° for a 1 ms^{-1} surface wind, and therefore of possible significance to the probe-orbiter link. Careful

measurements of the surface waves made by instruments aboard the Huygens probe could possibly be used to retrieve important planetological information about Titan's surface. Recommendations have therefore been made for a wave buoy experiment to investigate how well the TIL sensor can reconstruct probe tilt atop gravity-dominated surface waves.

A review of the TIL sensor was given in Chapter 3, with consideration given to its mechanical and electrical operational principles, along with the basic static, step response and frequency response calibrations that exist for the sensor. A model for the TIL sensor was described for extrapolating the sensor performance to the environment of Titan, with gravity being the dominant factor. The damped nature of the fluid within the sensor was shown to vary with gravity and whilst the damping time constant remained the same as on Earth, the theoretical time for the sensor to stabilise at its equilibrium value was shown to increase to around 0.3s. Observations made in Chapter 5 suggested a slower response than this, however worst case estimates were still shown to be under 1s and discussions of Chapter 6 showed that this would be sufficient for good representation of most probe motions. Similarly, with a theoretical TIL fluid natural frequency on Titan of around 4Hz, or 2 – 3 Hz based on the worst case experimental observations, the issue of resonance on Titan is considered unlikely for all but the highest frequency probe oscillations possibly due to small scale atmospheric buffeting in the early stages of descent. Such motion may well be better represented then by the 3 axis accelerometers.

A significant factor highlighted with the TIL sensor is its susceptibility to non-gravitational accelerations. This underlined the need for tests of the sensors real performance under real dynamic conditions. The design of a portable dynamic calibration platform (PDCP) which would address this issue as well as permit experimental measurement of the TIL sensor's response time under reduced gravity conditions was outlined in Chapter 4. This platform offers a robust and versatile standalone solution for rapid and impromptu testing of the TIL and HASI-ACC sensors in a wide a range of environments particularly where no other power or data lines are available. A programmable stepper motor system onboard opens up a number of opportunities for dynamic simulation, with only one example, the simulation of simple harmonic motion, being demonstrated in this work. The platform design was validated by three successful experiments, although scope for improvement was identified in the vibration characteristics and data sampling rates for very high frequency motion testing.

Chapter 5 detailed three experiments carried out with the PDCP which provided observational evidence of the TIL sensor response under reduced Titan gravity as well as its susceptibility to linear accelerations. The accurate measurement of spin rate was demonstrated and a limitation in angular range during periods of high spin was highlighted. Of significant value offered by the three field experiments was the observed real-life performance of the TIL sensor when subjected to a range of accelerations and the complexity of motion reconstruction was underlined. Qualitative correlation of the TIL results with the aircraft flight profile was demonstrated, although it is recognised that the aircraft dynamic environment was more adverse than that which might be expected during a balloon flight and it is predicted that useful data may be obtained from the TIL sensor in this latter case. Recommendation is made, in the event of such future experiments, for the independent measurement of attitude and position against which the TIL performance can be compared. In the case of the swing experiment, the representation of swing frequency by TIL was demonstrated although so too was the inability to measure accurately absolute tilt during simple pendulum motion.

In Chapter 6 results from the modelling carried out in Chapters 2 and 3, and from the experiments of Chapter 5, were drawn together and applied to the specific case of the TIL sensor aboard the Huygens probe. A conversion algorithm was demonstrated for transformation between the TIL sensor and Huygens probe axes systems, and the theory behind the angular measurement limit during probe spin, observed in the experiment of Chapter 5, was discussed. It was concluded that, for a nominal descent with spin periods less than 20rpm and inclinations less than 10° the issue would not be of concern for the Huygens mission, although any exceeding either limit necessitates care when interpreting the attitude measurement. The ability of the TIL sensor to indicate spin rates higher than those measurable by the Radial Acceleration Sensor Unit was also discussed, together with the removal of centrifugal TIL offset effects from the TIL data alone subject to a probe tilt greater than zero.

The strong susceptibility of the TIL sensor to linear accelerations, predicted in Chapter 3 and observed in Chapter 5, and impact on measurability of probe swing beneath its parachute was addressed in the second half of Chapter 6. A series of simplified two-dimensional parachute trajectories were generated using a 3-degree-of-freedom rigid-body parachute model, the representation of which by the TIL and HASI-ACC tilt and acceleration measurements could then be investigated. Approximate effects on the TIL measurement due to spin were also incorporated. Results confirm the complexity of the TIL and ACC measurements, and illustrate that whilst spin rate and swing period may be

accurately reconstructed using ACC and TIL alone, the sensors do not directly represent the true amplitude or phase of probe swing for the three-degree of freedom model. The situation will be compounded further due to the additional degrees-of-freedom that exist for the real Huygens descent. Recommendation therefore is made that efforts be undertaken with a full twelve-degree-of-freedom parachute model in support of the efforts currently underway to coordinate data-sharing between instrument teams for the reconstruction of probe trajectory and to maximise the data interpretable from TIL and HASI-ACC sensor measurements.

Discussion was offered concerning TIL sampling rates, and it was concluded that the 1Hz rate would be sufficient for reasonable reconstruction of motions involving all but the highest predicted spin rates. Finally consideration was given at the end of Chapter 6 to the TIL sensor measurement of sea or lake surface wave motions such as those described in Chapter 2, and a brief description offered of an experimental opportunity that exists for verification of the TIL sensor's capability in this particular environment.

Titan represents one of the most mysterious and exciting bodies yet to be explored within our Solar System. When Huygens descends through the aerosol veil 2005 the opportunity will finally exist to ask questions of Titan that have confounded planetary scientists and astronomers for decades, if not centuries. The work presented in this thesis has shown that whilst valuable tools do indeed exist aboard Huygens, work remains to be done if we are to fully understand the answers.

References

Allen, J.R.L., 1985, *Physical Principles of Sedimentology*, Allen & Unwin Press, London

Allison, M.D., “A preliminary assessment of the Titan Planetary Boundary Layer”, *Proceedings Symposium on Titan, Eur. Space Agency Spec. Publ. SP-338*, 113-118, 1992.

Atkinson, D.H., “Report of the Huygens Descent Trajectory Working Group”, ESTEC, June 3, 1998

Bretsznajder, S., 1971, *Prediction of Transport and Other Physical Properties of Fluids*, Pergamon Press, Warsaw

Brewster, E., 1991, “Huygens Tiltensor Subsystem (TIL)”, Third Year Project Report, 1991, University of Kent

Carter, D.J.T., 1982, “Prediction of Wave Height and Period for a Constant Wind Velocity Using the JONSWAP Results”, *Ocean Engineering*, Vol. 9, 1, pp 17-33.

Cartwright, D.E., Longuet-Higgins, M.S., Smith, N.D., 1963, “Observations of the Directional Spectrum of Sea Waves Using the Motion of a Floating Buoy”, *Ocean Wave Spectra*, Proceedings of a Conference sponsored by the US Naval Oceanographic Office, Maryland, 1961

Challenor, P., Ghafoor, N., Srokosz, M., *private communication*, Southampton Oceanography Centre, University of Southampton, April 2000

Cockrell, D.J., 1987, "The aerodynamics of parachutes", NATO AGARDograph No. 295

Comas Solá, J., 1908, *Astronomische Nachrichten*, 4290, 289-290

Combes, M., L. Vapillon, E. Gendron, A. Coustenis, O. Lai, R. Wittemberg, R. Sirdey, 1997, "Spatially Resolved Images of Titan by Means of Adaptive Optics", *Icarus* 129(2), pp482-492.

Dermott, S.F., C. Sagan, 1995, "Tidal effects of disconnected hydrocarbon seas on Titan", *Nature* 374, pp238-240.

Douglas, J.F., Gasiorek, J.M. and Swaffield, J.A., 1985, "Fluid Mechanics", 2nd edition, Pitman Publishing Ltd, London, ISBN 0-273-02134-6

Elachi, C., I. Eastwood, L.E. Roth, C.L. Werner, 1991, "Cassini Titan Radar Mapper", *Proceedings of the IEEE* 79(6), pp867-880.

Ewing, J.A., 1983, "Wind waves: a review of research during the last twenty-five years", *Geophys. J. R. astr. Soc.* 74, pp313-329.

Faber, T.E., 1995, *Fluid Dynamics for Physicists*, Cambridge University Press, Cambridge.

Flasar, F.M., M.D. Allison, J.I. Lunine, 1997, "Titan Zonal Wind Model", In *Huygens: Science, Payload, and Mission*, ed. J.-P. Lebreton, pp287-298, European Space Agency SP-1177.

Fulchignoni, M. et al., 1997, "The Huygens Atmospheric Structure Instrument (HASI)", *Huygens: Science, Payload, and Mission*, ed. J.-P. Lebreton, pp5-24, European Space Agency SP-1177.

Ghafoor, N.A.L., Challenor, P., Srokosz, M.A., Zarnecki, J.C., 2000, "Wind driven Surface Waves on Titan", *J. Geophys. Res.*, 105(5), 12077-091

Ghafoor, N.A., Vleder, G.V., Zarnecki, J.C., 1998, "Winds, Waves and Wave-riders: Titan's Surface and the Huygens Probe", paper presented at the Second International

Titan Symposium, Nantes, April 1998

Ghafoor, N.A., Gourinat, Y., Leese, M.R., Zarnecki, J.C., 1999, "Measurement capability of the Huygens Probe's Surface Science Package Tiltmeter under 1/7th g: simulations in a reduced gravity environment", paper presented at the XXIV Conference of the European Geophysical Society, ESTEC, Noordwijck, April 1999

Gourinat, Y., 1998, *private communication, Reduced-gravity flight coordinator*, ENSICA, Toulouse, France

Gourinat, Y., 1999, *private communication, Reduced-gravity flight coordinator* ENSICA, Toulouse, France

Griffith, C.A., T. Owen, R. Wagener, 1992, "Titan's Surface and Troposphere Investigated with Ground-Based Near-Infra Red Observations", *Icarus* 93(2), pp362-378.

Jones, J.C. & Giovagnoli, F., 1997, "The Huygens Probe System Design", *Huygens: Science, Payload, and Mission*, ed. J.-P. Lebreton, pp5-24, European Space Agency SP-1177.

Kinsman, B., 1965, *Wind Waves*, Prentice-Hall, New Jersey, p297

Koryta, J., Dvorak, J. and Kavan, L., 1993, "Principles of Electrochemistry", 2nd edition, John Wiley & Sons Ltd., England, ISBN 0-471-93838-6

Kuiper, G., 1944, *Astrophys. J.*, 100, 378-383

Lebreton, J.P. & Matson, D.L., 1997, "The Huygens Probe: Science, Payload, and Mission Overview", *Huygens: Science, Payload, and Mission*, ed. J.-P. Lebreton, pp5-24, European Space Agency SP-1177

Lellouch, E. & Hunten, D.M., 1997, "The Lellouch-Hunten Models for Titan's Atmosphere", *Huygens: Science, Payload, and Mission*, ed. J.-P. Lebreton, pp5-24, European Space Agency SP-1177

Lemmon, M.T., E. Karkoschka, M. Tomasko, 1995, "Titan's Rotational Light-Curve", *Icarus* 113(1), pp27-38

Lighthill, J., 1978, *Waves In Fluids*, Cambridge University Press, Cambridge.

Lorenz, R.D., 1994, "Huygens Probe Impact Dynamics", *ESA Journal*, 18, (2), 93-117

Lorenz, R.D., 1994, "Scientific Implications of the Huygens Parachute System", 12th RaeS/AIAA Aerodynamic Decelerator Systems and Technology Conference, May 1993, London

Lorenz, R.D., J.I. Lunine, 1996, "Titan's Surface Reviewed: The Nature of Bright and Dark Terrain", *Planetary and Space Science* 45(8), pp981-992.

Lorenz, R.D., C.P. McKay, J.I. Lunine, 1997, "Photochemically Driven Collapse of Titan's Atmosphere", *Science* 275, pp 642-643.

Lunine, J.I., 1993, "Does Titan Have an Ocean? A Review of Current Understanding of Titan's Surface", *Review of Geophys*, 31(2), pp133-149

Lunine, J.I., 1994, "Does Titan Have Oceans?", *American Scientist* 82, pp134-143.

Marshall, R., 2000, *private communication*, Spectron Glass Inc., 595 Old Willets Path, Hauppauge, NY. 11788

Muhleman, D.O., A.W. Grossman, B.J. Butler, M.A. Slade, 1990, "Radar reflectivity of Titan", *Science* 248, pp975-980

Ori, G., G. Marinangeli, L;Baliva, A;Bressan, M;Strom, 1998, "Fluid dynamics of liquids on Titan's surface", *Planetary and Space Science* 46 (9-10), pp1417-1421

Owen, T., Raulin, F., Lunine, J.I., McKay, C.P., Lebreton, J.P. & Matson, D.L., 1997, "The Relevance of Titan and Cassini/Huygens to Pre-biotic Chemistry and the Origin of Life on Earth", *Huygens: Science, Payload, and Mission*, ed. J.-P. Lebreton, pp5-24, European Space Agency SP-1177.

Pain, H.J., 1993, "The Physics of Vibrations and Waves", 4th edition, John Wiley & Sons Ltd., ISBN 0-471-93742-8

Patel, M., 1999, "Huygens Atmospheric Structure Instrument – A Study of Accelerometers", Final Report, MPhys, University of Kent, 1999

Pierson, W.J., L. Moskowitz, 1964, "A proposed spectral form for fully developed wind seas based on the similarity theory of S. A. Kitaigorodskii", *J. geophys. Res.* 69, pp5181-5190.

Pletser, V., 1994, "Preparation of the EUROMIR missions during parabolic flights with the Ilyushin aircraft, 19th ESA Campaign of July 1994", *µg News*, Vol. 7, No. 3, December 1994, ESA/ESTEC, Noordwijk, The Netherlands

PY-SSP-UKC-AD-104, Huygens SSP TILT Subsystem Acceptance Data Package, Unit for Space Sciences and Astrophysics, University of Kent

Rizk, B., See, C., Doose, L., Bushroe, M., Prout, M., McFarlane, L., Eibl, A., Moncada, P., Tomasko, M., Lorenz, R., Zarnecki, J. and Ghafoor, N., "Using the Surface Science Package Tilt Sensors for Descent Phase Attitude Derivation", *presented at the Huygens 4th DTWG meeting*, August 2001, Open University, UK

Sagan, C., S.F. Dermott, 1982, "The tides in the seas of Titan", *Nature* 300, pp731-733.

Schwarz, L.W., 1974, "Computer extension and analytic continuation of Stoke's expansion for gravity waves" *J. Fluid Mech.* 62, pp553-578

Sears, W.D., 1995, "Tidal Dissipation in Oceans on Titan", *Icarus* 113(1), pp39-56.

Shaw, H., 1997, *private communication / internal documents of original SSP team*, Unit for Space Sciences, University of Kent at Canterbury

Smith, P.H., M.T. Lemmon, R.D. Lorenz, L.A. Sromovsky, J.J. Caldwell, M.D. Allison, 1996, "Titan's Surface, Revealed by HST Imaging", *Icarus* 119, pp336-349.

Sobey, R.J., 1986, "Wind-wave Prediction", *Ann. Rev. Fluid Mech.* 18, pp149-172.

Sohl, F., W. D. Sears, R.D. Lorenz, 1995, "Tidal dissipation on Titan", *Icarus* 115, pp278-294

Srokosz, M.A., P.G. Challenor, J.C. Zarnecki, S.F. Green, 1992, "Waves on Titan", In *Proceedings Symposium on Titan*, Toulouse 1991, pp321-323, European Space Agency SP-338.

Srokosz, M., 2000, *private communication*, Southampton Oceanography Centre, Southampton, England

Stokes, G.G., 1880, "Considerations relative to the greatest height of oscillatory irrotational waves which can be propagated without change of form", *Math. Phys. Papers* 1(1), pp225-228

Tory, C., Ayres, R., 1997, "Computer Model of a Fully Deployed Parachute", *J. Aircraft*, 14 (7), pp675-679

Tucker, M.J., 1991, *Waves in Ocean Engineering*, Ellis Horwood, London, 431pp

Underwood, J. C., 1993, "A 12 degree of freedom parachute-payload simulation of the Huygens probe", AIAA-93-1251

Vago, J. L., 1998, "Parabolic Flight Activities with the Airbus A300 Zéro-G: the European Space Agency's 24th Campaign", *µg News*, 11(1), April 1998, ESA/ESTEC, Noordwijk, The Netherlands

Yeadon, W.H. (*ed*) and Yeadon, A.W., 2001 "Handbook of Small Electric Motors", McGraw-Hill, ISBN 0-070-72332-X

Yelle, R. V., Strobell, D.F., Lellouch, E. & Gautier, D., 1997, "The Yelle Titan Atmosphere Engineering Models", *Huygens: Science, Payload, and Mission*, ed. J.-P. Lebreton, pp5-24, European Space Agency SP-1177.

Zarnecki, J.C., Leese, M.R., Garry, J.R.C., Ghafoor, N. & Hathi, B., "Huygens' Surface Science Package", *Space Science Reviews*, accepted 2001.